

**On the Nature of Scattering from
Isolated Perturbations in Elastic Media
and the Consequences for
Processing of Seismic Data**

Dissertation

zur Erlangung des Doktorgrades
der Mathematisch-Naturwissenschaftlichen Fakultät
der Christian-Albrechts-Universität zu Kiel

vorgelegt von
Christof Müller

Kiel
2000

Referent/in: Prof. Dr. B. Milkereit

Korreferent/in: Prof. Dr. W. Rabbel

Tag der mündlichen Prüfung: 15.11.2000

Zum Druck genehmigt: Kiel, den 15.11.2000

Der Dekan
(Prof. Dr. Th. Bauer)

Abstract

The nature of seismic scattering was investigated by elastic scattering theory and numerical experiment. Seismic scattering situations can be classified by analyzing the amplitude versus scattering angle behavior of the scattered seismic wave field. Significant phase reversals (SPR) within the first arrival scattered seismic wave field from small or sphere shaped scatterers can be utilized as a robust classification criterion. The position of the scatterer has to be known. The concept of SPR classification can in part be extended to the case of scattering from large complex objects, if assuming that scattered energy emanates from scattering centers, i.e. areas of strong curvature. The shape of large objects has a significant impact on the dynamics of the scattered wave field and amplitude versus scattering angle analysis may be difficult. Acquisition geometry should provide sufficient fold, resolution and range of scattering angles.

Seismic acquisition and processing aimed towards resolving position, shape and composition of a single scatterer, has to focus on gaining and preserving as much scattered energy as possible. Scattered seismic energy is weakened by CMP processing. Thus gather oriented as well as prestack methods capable of enhancing the scattering response and assisting in classifying a given scattering situation were developed. A new 3D migration technique based on diffraction stack migration was introduced. The method uses either coherency (DCM) or polarization information (DPM) to enhance the image of scattering centers in the migrated 3D cube over those of reflector elements.

DCM and DPM were applied to marine and crustal seismic data sets:

Multichannel seismic surveying using boomer sources was tested, as a first step in developing a high resolution 3D marine seismic acquisition technique. Boomer sources show sufficient repeatability to be applied in multichannel marine seismic acquisition and processing. For the first time a high resolution multichannel $2\frac{1}{2}$ D seismic survey in the Baltic Sea was conducted. A Pleistocene fluvial channel system situated below a flat cover of unconsolidated sediments was revealed in Kiel Bay. DCM proved to efficiently enhance the image of marine scattering centers.

Crustal VSP data was acquired within the scope of the DSI technology development program which is aimed towards detecting massive volcanogenic ore deposits in the crystalline crust using seismic methods. DCM and DPM were applied to single shot three component VSP data acquired in Matagami, Canada. Due to a lag in azimuthal shot coverage it was not possible to resolve the azimuthal position of the Bell Allard orebody by DCM. DPM reduced imaging ambiguity and a scattering center in vicinity to the orebody was found. DCM was also applied to a crustal multi source VSP data set acquired at Norman West area of the Sudbury impact structure, Canada. The migration image shows significant background noise. Correlation with regional geology is aggravated by similarities between geological structures and the imaging ambiguity imprint on the migration result.

Zusammenfassung

Die Eigenschaften seismischer Streuung wurden mit Hilfe der elastischen Streutheorie und anhand numerischer Experimente untersucht. Seismische Streusituationen können durch die Analyse des Amplitudenverhaltens mit dem Streuwinkel klassifiziert werden. Als robustes Klassifizierungskriterium können signifikante Phasenumkehrungen (SPR) im Ersteinsatz des, von kleinen oder kugelförmigen Streuern, gestreuten seismischen Wellenfeldes ausgenutzt werden. Dazu muß die Position des Streuers bekannt sein. Das Konzept der SPR Klassifizierung kann zum Teil auf den Fall der Streuung von großen komplex geformten Objekten ausgedehnt werden. Die Form großer Objekte hat merklichen Einfluß auf die Dynamik des gestreuten Wellenfeldes und eine Analyse des Amplitudenverhaltens mit dem Streuwinkel wird erschwert. Die Akquisitionsgeometrie sollte eine ausreichende Winkelüberdeckung, -auflösung und -bereich liefern.

Seismische Messungen und Datenbearbeitung die darauf ausgerichtet sind Lage, Form und Zusammensetzung von Einzelstreuern zu ermitteln, müssen so viel gestreute Energie wie möglich sammeln und erhalten. Gestreute seismische Energie wird in der CMP Datenbearbeitung abgeschwächt. Deswegen wurden andere, sowohl an Spurfamilien orientierte, als auch Prestack-Methoden entwickelt, die in der Lage sind, die Streuantwort zu verstärken und eine gegebenen Streusituation zu klassifizieren.

Eine neue 3D Migrationstechnik, die auf der Methode der Diffraktionsstapelung basiert, wurde eingeführt. Die Methode nutzt entweder die Kohärenz (DCM) oder Polarisationsinformationen (DPM), um das Abbild von Streuzentren im migrierten 3D Würfel über das von Reflektorelementen hinaus zu verstärken.

DCM und DPM wurden auf marine und krustenseismische Datensätze angewendet:

Als erster Schritt in der Entwicklung einer hochauflösenden 3D-marineseismischen Registrierungstechnik wurden seismische Mehrkanalmessungen mit Boomer-Quellen getestet. Boomer-Quellen zeigen ausreichende Signalstabilität, um für Mehrkanalregistrierungen und -datenbearbeitung eingesetzt zu werden. Erstmals wurde eine hochauflösende $2\frac{1}{2}$ D-seismische Messung in der Ostsee durchgeführt. In der Kieler Bucht konnte ein pleistozänes fluviales Kanalsystem unterhalb der flachen Schlickbedeckung kartiert werden. DCM konnte das Bild von marinen Streuzentren effektiv verstärken.

Das DSI Technologie-Entwicklungsprogramm hat zum Ziel, vulkanogene Erzlagerstätten in der kristallinen Kruste mit Hilfe seismischer Methoden aufzufinden. DCM und DPM wurden auf einen Einzelschuß-VSP-Datensatz, der im Rahmen von DSI im kanadischen Matagami gemessen wurde, angewendet. Durch einen Mangel an azimuthaler Abdeckung war es nicht möglich die azimuthale Position des Bell Allard Erzkörpers mit DCM aufzulösen. DPM reduzierte die Abbildungsvieldeutigkeit und ein Streuzentrum nahe dem Erzkörper wurde gefunden. DCM wurde ebenfalls auf einen krustenseismischen Mehrschuß-VSP-Datensatz angewendet, der im Norman West Gebiet der Sudbury Impakt Struktur (Kanada) aufgezeichnet wurde. Das Migrationsbild weist erhebliches Rauschen auf. Die Korrelation mit der regionalen Geologie wird durch die Ähnlichkeiten der geologischen Strukturen mit den Störmustern der Abbildungsvieldeutigkeit im Migrationsergebnis erschwert.

Contents

1	Introduction	1
1.1	Motivation	1
1.2	Aims of this Study	3
1.3	Outline	4
2	Theory of Elastic Scattering and Diffraction	6
2.1	Scattering Theory	7
2.1.1	Rayleigh Scattering	8
2.1.2	Born Scattering	13
2.1.3	Scattering from Large Complex Objects	18
2.2	Diffraction Theory	19
2.2.1	Edge Wave Theory	20
2.3	Classification of Scatterers	24
2.3.1	Dynamic Characteristics of Scattered and Diffracted Wave Fields	25
2.3.2	Kinematic Characteristics of Scattered and Diffracted Wave Fields	43
2.4	Conclusions	44
3	Methodology	46
3.1	Gather Oriented Stacking Methods	47
3.1.1	The Common Midpoint Stacking Method	48
3.1.2	A Common Shot Gather Method: Scattering Enhancement Stack	53
3.1.3	A Common Scattering Angle Stacking Method	58
3.1.4	A Common Offset Filter Technique	62
3.2	Prestack Methods	65
3.2.1	Diffraction Stack Migration	66
3.2.2	Diffraction Coherency Migration	71
3.2.3	Migration Ambiguity in Diffraction Stacks	73
3.2.4	Diffraction Polarization Migration	80
3.3	Conclusions	83

4	Field Data Examples	85
4.1	Marine Seismic Case History	86
4.1.1	High Frequency Multichannel Data Acquisition in the Baltic Sea	88
4.1.2	Baltic Sea Scattering Objects: Geological Background	93
4.1.3	Imaging of Marine Scatterers Using Diffraction Coherency Migration	109
4.1.4	Conclusions	113
4.2	Crustal Seismic Case Histories	115
4.2.1	Single Shot 3C VSP Survey in Matagami.	116
4.2.2	Multi Source VSP Survey in Sudbury	124
4.2.3	Conclusions	136
5	Conclusions	138
5.1	Seismic Wave Scattering	138
5.2	Acquisition, Processing and Interpretation	139
5.3	Marine and Crustal Seismic Case Histories	139
5.4	Future Work	140
	References	142
A	Diffraction Stack and Kirchhoff Migration	150
B	Proposed Generic Processing Sequences	151
B.1	A generic processing sequence for marine seismic surveys	152
B.2	A generic processing sequence for VSP surveys	152
C	List of Symbols	154
D	List of Abbreviations	156

Chapter 1

Introduction

1.1 Motivation

Modern geophysics and geology have drastically changed the way scientists look at the earth's interior. It is understood today that the earth is heterogeneous everywhere from the crust and mantle to the core. The scales of these heterogeneities range from the size of rocks to the size of continents (Wu, 1986).

Controlled source seismology is the geophysical tool most suited to investigate the deep and shallow structure of the earth. Seismology is the science of seismic waves as naturally generated by earthquakes, or excited by man-made sources, such as dynamite or even sledge hammers. Seismic sensors (geophones or hydrophones) are used to record the seismic wave field in space and time to image subsurface structures.

Often seismic imaging techniques (which include pre- and poststack migration and CMP processing) assume that the subsurface is composed of laterally continuous lithological contacts. The subsurface is treated as an acoustic or elastic medium. For layered media ray approximations are used to describe seismic wave propagation. It is assumed, that rays are reflected by lithological interfaces following Snell's law (Červený *et al.*, 1977). The layered media and ray approximation holds well for sedimentary basins, the main target of oil prospecting industry (Ostrander, 1984).

However, if the characteristic extent a of a subsurface structure is of the order of the wavelength $\lambda = \frac{2\pi}{k} = \frac{f}{c}$ (k : wavenumber, f : frequency, c : medium velocity) of the incident seismic wave field, the assumptions of the ray approximation break down and scattering occurs. The ratio between dominant wavelength and characteristic extent is generally described by the normalized frequency $k \cdot a$. The ray approximation is valid for the region $ka \gg 10$. Figure 1.1 shows plots for $ka = 1$ and $ka = 10$ as a function of dominant source signal frequency f and background medium velocity c . For smaller values of ka subsurface structures will tend to scatter rather than reflect the seismic wave field.

Ignoring effects of intrinsic absorption (Bohlen, 1998), the nature of seismic scattering is well described by elastic wave theory. In contrast to electromagnetic or acoustic scattering problems, elastic wave scattering includes the difficulty of mode conversion effects (Varadan *et al.*, 1991). In elastic solids longitudinally and transversely polarized wave modes exist and propagate with different speed. Mode conversion occurs if an elastic wave hits a boundary, i.e. a region where the material parameters of the medium change.

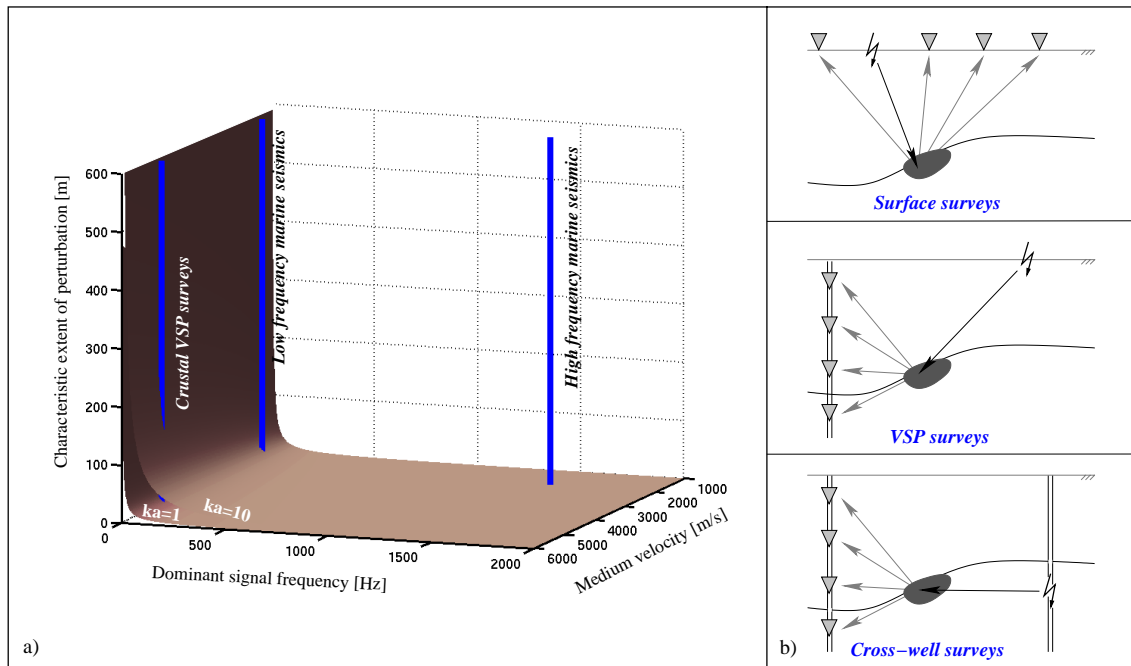


Figure 1.1: a) Surfaces indicating constant normalized frequency ka as a function of frequency, f , velocity, v and scatterer extent, a . For the region $ka < 10$ scattering of seismic waves occurs. Ray approximations are only valid for $ka \gg 10$. Note that for the types of seismic experiments indicated the scattering domain is entered for different values of a . b) Due to the fact that seismic sources and sensors can only be deployed at earth's surface or in boreholes, only three generic types of acquisition geometries suitable for the investigation of scattering problems can be applied: Surface seismic surveys (backscattering), vertical seismic profiling, VSP (side scattering) or cross-well surveys (forward scattering).

Exact and approximate solutions to the scattering problem in elastic media exist:

Mathematical descriptions include exact solutions for scattering from objects which are describable in a closed mathematical form, like spheres, spheroids, cylinders or ellipsoids (Varadan, 1978; Varadan & Varadan, 1979; Korneev & Johnson, 1993a; Korneev & Johnson, 1993a). Approximate mathematical descriptions exist for very small objects ($ka \ll 1$: Rayleigh scattering (Strutt (Lord Rayleigh), 1871)), intermediate sized spheres and spheroids ($0.1 \leq ka \ll 10$) (Mie, 1908; Asano, 1979) and objects with either small extend or material parameter perturbation (Born approximation (Hudson & Heritage, 1981; Gubernatis *et al.*, 1977b; Gubernatis *et al.*, 1977a)).

Numerical solutions of elastic wave equation provide an exact description of the scattering response, such as 3D finite difference (FD) modeling (Bohlen, 1998). The requirements for modeling accuracy have to be accounted for, though. If the scattering problem under consideration includes the simultaneous treatment of structures of significantly different scales, modeling can become computationally very expensive and hybrid methods, e.g.

combining multiple multipole (MMP) and finite element (FE) methods, might be more efficient (Imhof, 1996).

For exploration geophysics, studying subsurface heterogeneities offers greater chances for finding oil, gas or minerals. For example massive volcanogenic ore deposits are of major economical interest and are increasingly investigated using seismic methods (Salisbury *et al.*, 1996; Milkereit *et al.*, 1996; Eaton *et al.*, 1996; Hajnal *et al.*, 1997; Adam, 2000). In engineering, perturbations within an otherwise homogeneous background medium can represent possible hazards to man and equipment (e.g. tunnel construction, Kneib *et al.*, 2000). The detection and classification of scatterers in the marine environment is of great importance for hazard analysis and engineering studies. Possible scattering objects range from ship wrecks to boulders and gas accumulations within the sediments.

1.2 Aims of this Study

In standard seismic data processing the scattered seismic signal is often treated as noise and much effort sometimes is put in removing the signature of scattered energy from seismic sections. However, it includes useful information about composition and shape of the scattering object. Scattered seismic energy is distributed to a wide spatial range, and thus the scattering response is much weaker than reflections from comparable impedance contrasts.

Detecting scattered energy, resolving shape and composition of scattering objects has to focus on gaining and preserving as much scattered energy as possible throughout the seismic data acquisition and processing.

The aim of this study is to develop and investigate a variety of seismic data processing methods that are capable of enhancing either the image of subsurface scattering inclusions or the characteristic signature of scattered seismic energy observed on seismic sections.

Given the position of a scatterer, subsequent analysis of amplitude and phase variations of scattered seismic energy with scattering angle will provide information about the composition of the object. Unlike in seismic inversion application it was not intended to comprise both tasks in one single method. Instead a variety of different processing methods for surface seismics and VSP acquisition geometries are discussed in order to provide a set of flexible modules that can be applied in a processing sequence which might be adapted to the individual acquisition situation.

The nature of scattering from elastic perturbations, i.e. the dynamic and kinematic characteristics of scattered energy is investigated by theoretical consideration and in numerical experiments. It was intended to gain a deeper understanding of the processes of seismic scattering from single geological or man-made subsurface inclusions. The knowledge gained from these considerations was consequently applied to the development of the new processing methods.

The access to the host medium and scattering inclusions is limited due to the fact that seismic sources and sensors can only be deployed at the solid surface of the earth or in boreholes. Since scattering can show pronounced directional behavior it can be crucial to the success of a seismic experiment, whether the layout decided on is able to detect a

maximum of scattered energy or not. Limited directional coverage of the target region can lead to imaging ambiguity.

Basically only three possible seismic acquisition geometries exist as is illustrated in figure 1.1. Surface seismic surveys are applied in land as well as in marine seismic applications. Sources and receivers are arranged along lines or covering a wider area, either providing a two or three dimensional image of the subsurface (2D, 3D seismics). In scattering applications this layout would be most suitable if dominant backscattering is excited by the target objects. The mining industry has long relied on traditional mapping and drilling to locate base metal deposits (Salisbury *et al.*, 1996). This approach is effectively supported by vertical seismic profiling (VSP) acquisition techniques for which receivers are deployed in the borehole at different depths, whereas the source is still located at the surface. Either source or receiver locations are moved during acquisition in order to obtain sufficient ray coverage. VSP surveys are most efficient if steeply dipping structure have to be imaged or strong side scattering is expected. Figure 1.1 shows the schematic of a typical cross-well seismic survey, where shots and receivers are deployed in different boreholes. This technique should be considered, when the scattering process is governed by strong forward scattering. It is however cost intensive and was not investigated in this study.

1.3 Outline

In the first chapter of this study I will review the basic concepts of scattering and diffraction theory. The chapter is subdivided into three major parts:

Section 2.1 reviews the basic concepts of classical elastic scattering theory. Mathematical expressions for the Rayleigh and Born scattering elastic wave fields will be derived. Scattering from large complex shaped objects of arbitrary composition most often can not be described in a closed analytical form. Numerical solution of the elastic wave equation, as in the case in finite difference modeling, helps to understand the scattering process. The finite difference modeling algorithm applied in this study will thus be discussed in the last part of this section. In the first parts of section 2.1 and section 2.3 scattering from small inclusions is always treated first, being followed by a discussion on scattering from larger objects. Since scattering and diffraction generate a comparable signature on seismic sections, they are often treated as the same phenomenon. I will briefly review the main concepts of diffraction theory in section 2.2, as a basis for a follow-up discussion on similarities and differences of both cases. Based on the derived mathematical expression and finite difference modeling results for scattered elastic wave fields in section 2.3 the dynamic and kinematic characteristics of scattered and diffracted wave fields will be discussed. A new approach to classification of scattering phenomena will be given.

In order to account for the characteristic dynamic and kinematic behavior of scattered seismic energy in seismic data processing, several new processing approaches have been developed and tested in the scope of this study. In chapter 3 these methods are treated in two major sections:

It is quite common in seismic processing to group together seismic traces with equal geometrical attributes, such as common source, common receiver or common offset. The newly developed methods which follow this gather orientated approach are considered in section 3.1. The section is subdivided into four parts referring to the individual geometrical attribute used for gathering in each method.

By prestack migration the image of the subsurface is constructed directly from recorded seismic events. In section 3.2 two new migration techniques will be presented, which provide some potential of enhancing the image of subsurface scattering, diffraction locations over images of reflectors. The image obtained for the scattering inclusion by seismic migration can show significant ambiguity. This effect is in part explained by the fact, that scattering is a three-dimensional phenomenon and seismic acquisition layouts will always have limited ray directional coverage. Imaging ambiguity will thus also be discussed here.

The new prestack migration processing techniques will be applied to real seismic data sets in chapter 4. Their performance regarding the task of enhancing scatterer over reflector images will be discussed by example of a multichannel high frequency marine seismic survey that was conducted in shallow waters of the Baltic Sea (section 4.1) and crustal seismic data sets that were acquired by vertical seismic profiling (section 4.2). Target of the investigation will be scattering and diffraction caused by gas accumulations in unconsolidated sediments as well as large base metal ore deposits embedded in earth's crystalline crust. As discussed above, 3D seismic acquisition should provide an optimal basis for effectively gathering scattered seismic energy, because seismic sensors will cover a broad range of source receiver offsets and azimuths. Thus in section 4.1 first steps towards development of a high resolution 3D marine seismic acquisition system will be described.

Chapter 2

Theory of Elastic Scattering and Diffraction

The first chapter of this study is dedicated to the review of theoretical and numerical considerations regarding the scattering and diffraction of seismic waves. Scattering theory provides the necessary means of developing new processing and interpretation approaches to seismic scattering from isolated inclusions in the subsurface. Scattering and diffraction in some aspects are very similar and often treated as equivalent seismic effects. However, they substantially differ if we take a closer look at the dynamics of their scattered and diffracted wave fields. It is thus reasonable to investigate not only the dynamic and kinematic characteristics of scattered but also of diffracted seismic energy.

The following chapter is subdivided into three main sections. In each section an introductory review of the major contributions from other scientists will be given:

In the first section I will review the basic principles of scattering theory. Starting with Rayleigh scattering theory, scattering from inclusions of arbitrary material parameters which are much smaller than the seismic wavelength will be described. Rayleigh scattering provides the means of understanding the dynamic characteristics of the scattered wave field also for larger inclusions (section 2.1.1). Subsequently, the theory of the Born approximation will be discussed. Although it is limited in its validity and applicability, the Born approximation is widely used in active and passive source seismology today. Scattering from inclusions comparable to the size of the seismic wavelength can be described by this linearized perturbation theory, provided that the contrast in material parameters of the scatterer is sufficiently small (section 2.1.2). If scattering objects become large compared to the seismic wavelength and possibly exhibit strong material parameter perturbations, numerical methods have to be used in order to describe the scattered wave field. Thus finalizing this section a description of a finite difference algorithm will follow which was later used to model the exact scattering response from large complex objects of arbitrary material parameter perturbation (section 2.1.3).

The second section of the chapter will review the theory of seismic diffraction, in its realization of the Edge Wave theory (EWT, section 2.2.1). EWT is commonly applied to

model and investigate diffractions, caused by abrupt changes in otherwise smoothly varying subsurface structures. Since EWT is a ray approximation solution to the wave equation the concept of seismic ray tracing will also be reviewed. It builds the basis for understanding the concept of EWT.

In the last section of this chapter I will investigate the dynamic and kinematic characteristics of scattered and diffracted seismic wave fields as it follows from the theoretical considerations discussed. Several examples will be used which relate to the marine and crustal seismic case histories discussed in chapter 4). At first the dynamic characteristics of seismic waves scattered from very small inclusions, i.e. Rayleigh scatterers will be investigated. Subsequently the effects of shape and composition of larger inclusions within the scope of the Born approximation will be discussed. following this a review of results from modeling the seismic scattering response from large complex objects using the finite difference algorithm mentioned above will be given. The given examples will only relate to the crustal seismic case histories of chapter 4. A short discussion about the dynamic characteristics of the diffracted seismic wave field will follow (section 2.3.1).

The equal kinematic characteristics of diffracted and scattered seismic wave fields are important for the development of seismic imaging and interpretation methods for scattered seismic wave fields and will be discussed finalizing the current chapter (section 2.3.2).

2.1 Scattering Theory

Scattering occurs if the wavelength is comparable to or much larger than the extent of a subsurface heterogeneity. The relative size of a scattering inclusion is best described by the normalized frequency $k \cdot a$, which is defined as the product between the wave number of the incident wave field and the inclusions size.

If $ka \ll 1$, i.e. the wavelength of the incident wave field is much greater than the inclusion itself, the scattered power will be proportional to k^4 and can be described by the Rayleigh scattering theory (Strutt (Lord Rayleigh), 1871).

If the wavelength gets smaller compared to the size of the object, i.e. $ka \approx 1$, we enter the regime of resonance or Mie scattering. A complete mathematical-physical theory of the scattering of electromagnetic radiation by spherical particles, was developed by G. Mie in 1908. In this context it is defined as scattering produced by spherical particles without special regard to comparative size of radiation wavelength and particle diameter. The Mie approximation assumes that the inclusion is composed of numerous small non-interacting parts, each of which causes a scattered field of the Rayleigh scattering type. Only in 1979 this approach was extended to spheroids by Ansano. Scattering in this regime is often referred to as Mie scattering even though the scattering inclusion is not of spherical symmetry.

An exact solution to the problem of scattering from spheres of arbitrary size and contrast can be found in e.g. Korneev & Johnson (1993a; 1993b). The use of a spherical vector expansion restricts this boundary matching approach (BMA) to the spherical symmetry of the scatterer. It can, however, be expanded by the use of a different set of basic functions as

shown in Pao & Varadarajulu (1976). This so called T-matrix or scattering matrix approach yields the mathematical instruments of describing the scattered wave field for objects with strong parameter perturbation and for a broad variety of shapes (Varadan, 1978; Varadan & Varadan, 1979). The success of the method is, however, dependent on the convergence of the expansion series used and is only applicable to shapes that are describable in a closed mathematical form, i.e. spheres, cylinders and ellipsoids (Wu, 1989a). The approach is described in detail by Varadan & Varadan (1978).

If the scattering object is comparable to or smaller than the wavelength of the incident wave field, and the contrast in material parameters is sufficiently weak, an approximate description of the scattering is widely used. This so called Born approximation, of which the first derivations were given by Bhatia (1959) and Miles (1960), provides the means of separately describing the influence of composition and shape of the scattering inclusion. It was comprehensively derived by Gubernatis, *et al.* (1977b; 1977a) and reviewed by Wu (1989b).

If the scatterer is of arbitrary shape and contrast in its material parameters and tends to be even larger than the seismic wavelength scattering can only be described using exact numerical solutions, such as finite difference algorithms (e.g. Bohlen, 1998 and Bohlen *et al.*, 2000)

The interest of seismology in scattering, diffraction phenomena is mainly restricted to two cases. First, scattering attenuation as it occurs in random media (Aki, 1980; Sato, 1982; Shapiro, 1993) and second, scattering/diffraction at earth core-mantle boundary (Haddon & Buchen, 1981).

Only few authors have been interested in investigating scattering from isolated impedance contrast regarding the possibility of imaging the scatterer itself (e.g. Belfer *et al.*, 1998; Landa & Keydar, 1998).

A comprehensive review of the different scattering regimes and their relevance for modern seismology can be found in Wu (1986).

In the following I will review the theory of scattering from spheres of arbitrary size and material parameter perturbation as it was derived by Korneev and Johnson (1993a,b). Rayleigh scattering can be regarded as a special case of scattering from spheres, i.e. when the sphere is very small. The equations for the far field scattered amplitudes of small inclusions for either arbitrary and low parameter contrast will be derived. Following this, I will discuss the theory of the Born approximation as it is found in Gubernatis *et al.* (1977b; 1977a). The equations for the far field scattered amplitudes in the limits of the Born approximation will be derived. The validity criterion as it was investigated by Hudson & Heritage (1981) will be given. Finally I will briefly describe the finite difference algorithm (Bohlen, 1998) that is used in the section 2.1.3 in order to model the scattering response from large complex objects of arbitrary material parameter contrast.

2.1.1 Rayleigh Scattering

The process of scattering from small inclusions of arbitrary strong material parameter contrast compared to a given background medium is called Rayleigh scattering. A small object in this regard shows a characteristic extend a much smaller than the wavelength of the incident wave field. In this section I will follow a solution for scattering from spheres of ar-

bitrary size and material parameter contrast as derived by Korneev and Johnson (1993a,b), since Rayleigh scattering can be described as a special asymptotic case of scattering from a sphere.

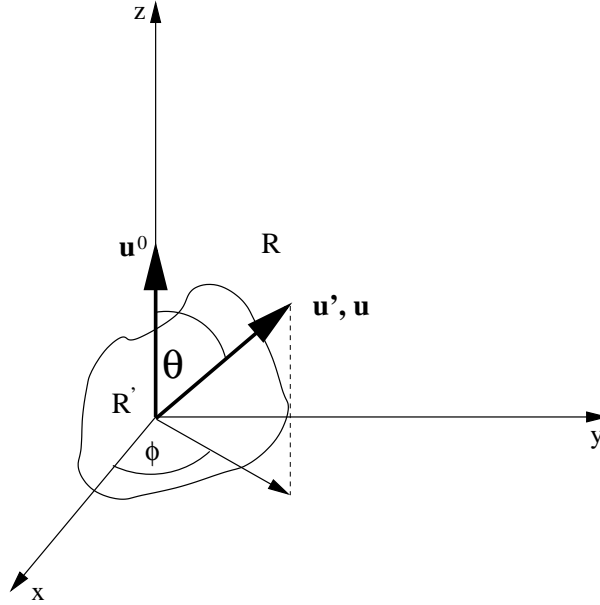


Figure 2.1: *Coordinate system and scattering geometry for a generic scattering experiment. The forward scattering direction is defined by $\theta = 0$. Please note, that the angle of seismic reflection κ in contrast is defined as the angle between a reflector surface normal and the incident or emerging ray. It is assumed that the region R' compared to the background medium carries a perturbation of material parameters.*

In order to solve the scattering problem for the sphere the incident and scattered wave fields are written as a series of spherical vector systems, which was derived by Petrashen (1945; 1949):

$$\begin{aligned} \mathbf{Y}_{lm}^0 &\equiv \mathbf{Y}_{lm}^0(\theta, \phi) = \mathbf{r} \times \nabla Y_{lm}(\theta, \phi) \\ \mathbf{Y}_{lm}^+ &\equiv \mathbf{Y}_{lm}^+(\theta, \phi) = (l+1)\hat{r}Y_{lm}(\theta, \phi) - r\nabla Y_{lm}(\theta, \phi) \\ \mathbf{Y}_{lm}^- &\equiv \mathbf{Y}_{lm}^-(\theta, \phi) = l\hat{r}Y_{lm}(\theta, \phi) + r\nabla Y_{lm}(\theta, \phi) \end{aligned} \quad (2.1)$$

where \hat{r} is the unit vector in radial direction. Y_{lm} denote the spherical harmonic functions:

$$Y_{lm}(\theta, \phi) = e^{im\phi} P_l^m(\cos \theta), \quad l \geq 0, \quad (-l \leq m \leq l) \quad (2.2)$$

with $P_l^m(x)$ being the Legendre functions:

$$\begin{aligned} P_l^m(x) &= (1-x^2)^{m/2} \frac{d^{l+m}}{dx^{l+m}} \frac{(x^2-1)^l}{2^l l!}, \quad (m \geq 0) \\ P_l^m(x) &= (-1)^{|m|} \frac{(l-|m|)!}{(l+|m|)!} P_l^{|m|}(x), \quad (m < 0) \end{aligned} \quad (2.3)$$

The incident (\mathbf{u}^0) and scattered wave fields (\mathbf{u}' , \mathbf{u}) must satisfy the elastodynamic equations of motion for both the background medium R and inside the scatterer R' :

$$(\lambda + 2\mu)\nabla^2\mathbf{u} - \mu\nabla \times \nabla \times \mathbf{u} + \rho\omega^2\mathbf{u} = 0 \quad (2.4)$$

which here is written in the frequency domain. λ , μ , ρ denote the Lamé-parameters and the density. The wave fields must also satisfy the boundary conditions, i.e. the displacement and traction on the sphere's surface have to be continuous:

$$\begin{aligned} \mathbf{u}' &= \mathbf{u}^0 + \mathbf{u} \\ \mathbf{t}'_r[\mathbf{u}'] &= \mathbf{t}_r[\mathbf{u}^0 + \mathbf{u}] \end{aligned} \quad (2.5)$$

The traction for the inner and outer region is given by :

$$\mathbf{t}_r(\mathbf{u}) = \lambda\nabla \cdot \mathbf{u}\hat{r} + 2\mu\frac{\partial\mathbf{u}}{\partial r} + \mu_r[\hat{r} \times \nabla \times \mathbf{u}] \quad (2.6)$$

The wave field inside the sphere has to stay finite and the scattered field has to satisfy a radiation condition:

$$\mathbf{u} \approx \frac{\mathbf{c}(\theta, \phi)}{r} e^{-ikr}, \quad (r \rightarrow \infty) \quad (2.7)$$

$$k_p = \frac{\omega}{v_p}, \quad k_s = \frac{\omega}{v_s}, \quad (2.8)$$

$$v_p = \sqrt{\frac{\lambda + 2\mu}{\rho}} = \alpha^{-1}, \quad v_s = \sqrt{\frac{\mu}{\rho}} = \beta^{-1}, \quad \text{for both regions} \quad (2.9)$$

$\mathbf{c}(\theta, \phi)$ is a vector quantity only depending on the polar and azimuthal angles θ and ϕ , respectively, ω the circular frequency of the incident wave field.

A plane compressional wave propagating in positive z-direction, i.e.

$$\mathbf{u}^0 = e^{-i\omega\alpha z} \hat{z} \quad (2.10)$$

(α denoting the slowness of the background medium, \hat{z} the unit vector in z-direction, $e^{i\omega t}$ is omitted), expressed in terms of the spherical vector expansion given above reads as follows:

$$\mathbf{u}^0 = \sum_{l \geq 0}^{\infty} \{j_{l+1}(\omega\alpha r) \mathbf{Y}_{l0}^+ - j_{l-1}(\omega\alpha r) \mathbf{Y}_{l0}^-\} \exp\{-i[\pi/2(l+1)]\} \quad (2.11)$$

$j_k(x)$ are spherical Bessel functions.

Solving the wave equation for the inner and outer scattered fields \mathbf{u}' and \mathbf{u} then yields:

$$\begin{aligned}\mathbf{u}' &= \sum_{l \geq 0}^{\infty} \{ [\alpha'_l j_{l+1}(\omega \alpha' r) + l b'_l j_{l+1}(\omega \beta' r)] \mathbf{Y}_{l0}^+ \\ &\quad + [-a'_l j_{l-1}(\omega \alpha' r) + (l+1) b'_l j_{l-1}(\omega \beta' r)] \mathbf{Y}_{l0}^- \} \\ &\quad \exp\{-i[\pi/2(l+1)]\} \\ \mathbf{u} &= \sum_{l \geq 0}^{\infty} \{ [\alpha_l h_{l+1}(\omega \alpha r) + l b_l h_{l+1}(\omega \beta r)] \mathbf{Y}_{l0}^+ \\ &\quad + [-a_l h_{l-1}(\omega \alpha r) + (l+1) b_l h_{l-1}(\omega \beta r)] \mathbf{Y}_{l0}^- \} \\ &\quad \exp\{-i[\pi/2(l+1)]\}\end{aligned}\quad (2.12)$$

$h_k(x)$ are the spherical Hankel functions of the second kind. The spherical Bessel function $j_k(x)$ are used to represent the scattered field inside the scatterer and satisfy the condition of finite. The spherical Hankel function satisfy the radiation condition. \mathbf{u} can be written in an explicit and more convenient form (Gritto *et al.*, 1995):

$$\begin{aligned}\mathbf{u} &= \mathbf{u}_p + \mathbf{u}_s \quad (2.13) \\ \mathbf{u} &= \sum_{l \geq 0}^{\infty} e^{-i\frac{\pi}{2}(l+1)} (2l+1) \\ &\quad \left\{ a_l \left[\left((l+1) \frac{h_l(k_p r)}{k_p r} - h_{l-1}(k_p r) \right) P_l(\cos \theta) \hat{r} - \frac{h_l(k_p r)}{k_p r} \frac{\partial P_l(\cos \theta)}{\partial \theta} \hat{\theta} \right] \right. \\ &\quad \left. + b_l \left[l(l+1) \frac{h_l(k_s r)}{k_s r} P_l(\cos \theta) \hat{r} + \left(h_{l-1}(k_s r) - \frac{h_l(k_s r)}{k_s r} \right) \frac{\partial P_l(\cos \theta)}{\partial \theta} \hat{\theta} \right] \right\}\end{aligned}$$

\hat{r} and $\hat{\theta}$ are unit vectors in r and θ direction, respectively. \mathbf{u}_p and \mathbf{u}_s are the scattered compressional and shear wave fields, respectively. The unknown coefficients a_l and b_l (for both regions) can be found by satisfying the boundary conditions of the scattering problem (boundary matching approach). Both coefficients are available in analytical form and can thus be calculated for any order of l . For the special case of the Rayleigh approximation ($kR \ll 1$) equation 2.13 can be restricted to only those terms which are lowest in frequency (Gritto *et al.*, 1995) and the following expressions for a_l and b_l are obtained:

$$a_0 = i \frac{\xi^3}{6} \frac{\frac{3}{2}(\lambda' - \lambda) + \mu' - \mu}{\frac{1}{2}(\frac{3}{2}\lambda' + \mu') + \mu} \quad (2.14)$$

$$a_1 = -i \frac{\xi^3}{9} \left[\frac{\rho'}{\rho} - 1 \right], \quad b_1 = i \frac{\eta^3}{9} \left[\frac{\rho'}{\rho} - 1 \right], \quad (2.15)$$

$$a_2 = i \xi^3 \frac{4}{45} \left[\frac{\mu'}{\mu} - 1 \right] \frac{\gamma^2}{D}, \quad b_2 = -i \eta^3 \frac{2}{45} \left[\frac{\mu'}{\mu} - 1 \right] \frac{\gamma}{D} \quad (2.16)$$

with

$$\xi = k_p R, \quad \eta = k_s R, \quad (2.17)$$

$$\gamma = \frac{v_s}{v_p}, \quad D = 1 + \frac{2}{15} \left[\frac{\mu'}{\mu} - 1 \right] (3 + 2\gamma^2) \quad (2.18)$$

As can be seen from the above equations, a_l and b_l depend on the wavenumber of the wave field as well as on the physical properties of the sphere and the background medium. If we insert these coefficients into equation 2.13, we arrive at a low frequency, Rayleigh scattering approximation for the sphere with arbitrary contrasts in the material parameters. This solution is valid for the near and far scattered wave fields \mathbf{u}_p and \mathbf{u}_s , respectively (Korneev & Johnson, 1993b):

$$\mathbf{u}_p = A \left\{ -\frac{1}{2} \frac{\frac{3}{2}(\lambda' - \lambda) + \mu' - \mu}{\frac{1}{2}(\frac{3}{2}\lambda' + \mu') + \mu} + \left(\frac{\rho'}{\rho} - 1 \right) \cos \theta + \frac{2}{3} \left(\frac{\mu'}{\mu} - 1 \right) \frac{\gamma^2}{D} (1 - 3 \cos^2 \theta) \right\} \hat{r} \quad (2.19)$$

$$\mathbf{u}_s = B \left\{ - \left(\frac{\rho'}{\rho} - 1 \right) \sin \theta + \left(\frac{\mu'}{\mu} - 1 \right) \frac{\gamma}{D} \sin 2\theta \right\} \hat{\theta} \quad (2.20)$$

with

$$A = k_p^2 \frac{V}{4\pi} \frac{e^{-ik_p r}}{r}, \quad B = k_s^2 \frac{V}{4\pi} \frac{e^{-ik_s r}}{r} \quad (2.21)$$

If the parameter perturbations are small, i.e.:

$$\frac{|\delta\lambda|}{\lambda} = \frac{|\lambda' - \lambda|}{\lambda} \ll 1; \quad \frac{|\delta\mu|}{\mu} = \frac{|\mu' - \mu|}{\mu} \ll 1; \quad \frac{|\delta\rho|}{\rho} = \frac{|\rho' - \rho|}{\rho} \ll 1 \quad (2.22)$$

the coefficients a_l , b_l can be expressed in a converging binomial series expansion, where only the linear term is kept (Gritto *et al.*, 1995). The expressions for the scattered wave field in equations 2.19 and 2.20 then read:

$$\begin{aligned} \mathbf{u}_p &= A \left\{ -\frac{1}{2} \frac{\frac{3}{2}\delta\lambda + \delta\mu}{\frac{1}{2}(\frac{3}{2}\lambda + \mu) + \mu} + \frac{\delta\rho}{\rho} \cos \theta + \frac{2}{3} \frac{\delta\mu}{\mu} \gamma^2 (1 - 3 \cos^2 \theta) \right\} \hat{r} \\ \mathbf{u}_s &= B \left\{ -\frac{\delta\rho}{\rho} \sin \theta + \frac{\delta\mu}{\mu} \gamma \sin 2\theta \right\} \hat{\theta} \end{aligned} \quad (2.23)$$

or after some algebra:

$$\mathbf{u}_p = A \left\{ -\frac{\delta\lambda}{\lambda + 2\mu} + \frac{\delta\rho}{\rho} \cos\theta - \frac{2\delta\mu}{\lambda + 2\mu} \cos^2\theta \right\} \hat{r} \quad (2.24)$$

$$\mathbf{u}_s = B \left\{ -\frac{\delta\rho}{\rho} \sin\theta + \frac{\delta\mu}{\mu} \sin 2\theta \right\} \hat{\theta} \quad (2.25)$$

In case of an incident S-wave the derivation is analogous and will arrive at:

$$\mathbf{u}_p = A \left\{ \frac{\delta\rho}{\rho} \sin\theta - \frac{\delta\mu}{\mu} \sin 2\theta \right\} \cos\phi \hat{r} \quad (2.26)$$

$$\begin{aligned} \mathbf{u}_s = B \left\{ \frac{\delta\rho}{\rho} \cos\theta - \frac{\delta\mu}{\mu} \cos 2\theta \right\} \cos\phi \hat{\theta} \\ + B \left\{ -\frac{\delta\rho}{\rho} \cos\theta \right\} \sin\phi \hat{\phi} \end{aligned} \quad (2.27)$$

Equations 2.24 through 2.27 are equivalent to the Born-Approximation for small inclusions of low contrast as will be described in the following section.

2.1.2 Born Scattering

If wavelength of the incident field is comparable to the size of the scattering object, the Rayleigh scattering approximation is no longer valid. The upper limit for the Rayleigh approximation, i.e. $kR \ll 1$, is not exactly known, but inclusions with relative size of $\frac{a}{\lambda} \leq 17\%$ generally carry an error of less than 5% (Gritto *et al.*, 1995). Gubernatis (1977a,b) derived a solution for the elastic scattered wave field for an arbitrarily shaped inclusion of sufficiently low contrast in material parameters.

Derivation of the Born approximation

The scattering problem was formulated in the form of an integral equation that was derived from the equivalent elastodynamic differential equation of motion (equation 2.4). The total wave field \mathbf{u}^t is formulated as a sum of incident \mathbf{u}^0 and scattered wave fields \mathbf{u}^s ,

$$u_i^t = u_i^0 + u_i^s = u_i^0 + (u_i' + u_i) \quad (2.28)$$

u_i' and u_i are vector components of inner and outer scattered wave fields, respectively.

The scattered wave field can be expressed in terms of an integral over the volume R of the inclusion¹:

$$u_i^t = u_i^0 + \delta\rho\omega^2 \int_R g_{ij}(\mathbf{r} - \mathbf{r}') u_j(\mathbf{r}) d\mathbf{r}' + \delta C_{jklm} \int_R g_{ij,k}(\mathbf{r} - \mathbf{r}') u_{l,m'}(\mathbf{r}') d\mathbf{r}' \quad (2.29)$$

$\delta\rho$ and δC_{jklm} are the perturbations in density and elastic tensor components of the scattering object compared to the background medium, and are defined as:

$$\begin{aligned} \delta\rho &= \rho' - \rho \\ \delta C_{jklm} &= C'_{jklm} - C_{jklm} \end{aligned} \quad (2.30)$$

$g_{ij}(\mathbf{r} - \mathbf{r}')$ is the Greens function of an arbitrary background medium. $u_j(\mathbf{r}')$ is the wave field inside the scatterer, which is generally unknown. The notation $f_{,k'}$ stands for $\delta f / \delta x'_{k'}$. Figure 2.1 shows the geometry of the problem.

Equation 2.29 is a general result and valid for any perturbation $\delta\rho$ and δC_{jklm} and any kind of background medium. A solution for the general case of equation 2.29 is not available, but can be formulated for the scattered far field by making use of the Born approximation:

Starting with equations 2.28 and 2.29 the scattered wave field can be written as:

$$u_i^s = \delta\rho\omega^2 \int_R g_{im} u_m d\mathbf{r}' + \delta C_{jklm} \int_R g_{ij,k} u_{l,m'} d\mathbf{r}' \quad (2.31)$$

in the far field $r \rightarrow \infty$ this takes on the approximate form (Gubernatis *et al.*, 1977a,b):

$$u_i^s = A_i \exp(ik_p r)(r^{-1}) + B_i \exp(ik_s r)(r^{-1}) \quad (2.32)$$

with

$$\begin{aligned} A_i &= \hat{r}_i \hat{r}_j f_j(\mathbf{k}_p) \\ B_i &= (\delta_{ij} - \hat{r}_i \hat{r}_j) f_j(\mathbf{k}_s) \end{aligned} \quad (2.33)$$

\hat{r}_i are the Cartesian components of the unit vector in ray direction and

$$f_i(\mathbf{k}) = \delta\rho\omega^2 \int_R g_{ij} u_j \exp(-i\mathbf{k} \cdot \mathbf{r}) d\mathbf{r}' + \delta C_{jklm} \int_R g_{ij,k} u_{l,m'} \exp(-i\mathbf{k} \cdot \mathbf{r}) d\mathbf{r}'. \quad (2.34)$$

A_i and B_i are the far field scattering amplitudes polarized in ray direction and perpendicular to it, respectively. They describe the mode conversion into P- and S-waves that is produced by scattering. For an isotropic homogeneous background medium the Greens function g_{ij} is known analytically. This special case is now assumed and we use:

$$g_{ij}(\mathcal{R} = \mathbf{r} - \mathbf{r}') = \frac{1}{4\pi\rho\omega^2} \left[k_s^2 \frac{\exp(ik_s \mathcal{R})}{\mathcal{R}} \delta_{ij} - \frac{\partial}{\partial x_i} \frac{\partial}{\partial x_j} \left(\frac{\exp(ik_p \mathcal{R})}{\mathcal{R}} - \frac{\exp(ik_s \mathcal{R})}{\mathcal{R}} \right) \right] \quad (2.35)$$

¹Einstein summation convention is used in the following

In order to solve equation 2.29 the wavefield inside the scatterer has to be known, which is generally not the case. It can, however, be approximated by the incident wavefield itself. Thus an iterative series expansion can be initialized, if equation 2.29 is formally written as:

$$u_i = u_i^0 + \int_R G [u_i(\mathbf{r}'), u_{i,j'}(\mathbf{r}')] d\mathbf{r}' \quad (2.36)$$

where $G[u_i(\mathbf{r}'), u_{i,j'}(\mathbf{r}')] d\mathbf{r}'$ describes the complete integral of equation 2.29. The iteration procedure is defined by:

$$u_i^{(n+1)} = u_i^0 + \int_R G [u_i^{(n)}(\mathbf{r}'), u_{i,j'}^{(n)}(\mathbf{r}')] d\mathbf{r}' \quad (2.37)$$

and is initialized by $\mathbf{u}^{(0)} = \mathbf{u}^0$.

This series is known as the Born series and converges if $|u_i^{(n+1)} - u_i^{(n)}| \rightarrow 0$ if $n \rightarrow \infty$ (Gubernatis *et al.*, 1977a). It then is an exact solution for the scattering problem formulated by equation 2.29. The number of iterations is equivalent to the order of the scattering process. If the series 2.37 is truncated after the first member, the scattering process is only described by its first order, often referred to as *single scattering*. This approximation is then called first order Born approximation or just Born approximation. Because of the nature of the iteration, the Born approximation replaces the field inside the object by the incident wave field. It must be noted, that the Born approximation is only valid for weak *single scattering* and small sized objects. The accuracy of the approximation was extensively investigated by Hudson and Heritage (1981), who derived a mathematical criterion for the validity of the Born approximation. It is given by:

$$\Delta p = \frac{|\delta\rho|}{\rho} + \frac{|\delta\lambda| + 2|\delta\mu|}{\lambda + 2\mu} \ll (k_s a)^{-1} \quad (2.38)$$

k_s is the shear wavenumber in the background medium.

We can now derive the expressions for the far field scattered amplitudes for incident plane compressional and shear waves:

Starting with the case of an incident longitudinally polarized plane wave traveling in positive z-direction, i.e.

$$u_i^0 = \hat{a}_i \exp(ik_p z) \quad (2.39)$$

where \hat{a}_i are the components of a unit vector in z direction and inserting into equation 2.34 we find:

$$\begin{aligned} f_i(k\hat{r}) &= \frac{k^2}{4\pi\rho\omega^2} [(\delta\rho\omega^2 - 2k_p k \delta\mu \cos\theta)\hat{a}_i - k_p k \delta\lambda \hat{r}_i] \\ &\times \int_R \exp [i(k_p \hat{z} - k\hat{r})\mathbf{r}'] d\mathbf{r}' \end{aligned} \quad (2.40)$$

where k has to be replaced by either k_p or k_s depending on the type of scattering mode conversion.

For the far field scattered amplitudes A_i and B_i by substituting equation 2.40 into equation 2.33 we obtain:

$$A_i = \frac{k_p^2}{2\pi} \left(\frac{\delta\rho}{\rho} \cos\theta - \frac{\delta\lambda + 2\delta\mu}{\lambda + 2\mu} \cos^2\theta \right) \int_R \exp [i(k_p\hat{z} - k_p\hat{r}) \cdot \mathbf{r}'] d\mathbf{r}' \cdot \hat{r}_i \quad (2.41)$$

$$B_i = \frac{k_s^2}{4\pi} \left(\frac{k_p\delta\mu}{k_s\mu} \sin 2\theta - \frac{\delta\rho}{\rho} \sin\theta \right) \int_R \exp [i(k_p\hat{z} - k_s\hat{r}) \cdot \mathbf{r}'] d\mathbf{r}' \cdot \hat{\theta}_i \quad (2.42)$$

The integral factor is called shape factor, because it only depends on the shape of the inclusion and not on its composition. It also depends on the angle θ between \hat{r} and \hat{z} , which is the scattering angle. The shape factor represents the three dimensional Fourier transform of the spatial distribution of the object. The first terms in equations 2.41 and 2.42 only depend on the composition of the object and on the scattering angle and is thus called composition factor.

For the case of an incident transversely polarized plane wave traveling in positive z direction, i.e.

$$u_i^0 = \hat{b}_i \exp(ik_s z) \quad (2.43)$$

where \hat{b}_i are the components of a unit vector perpendicular to the z-direction, equation 2.34 reads:

$$f_i(\gamma\hat{r}) = \frac{\gamma^2}{4\pi\rho\omega^2} \left[(\delta\rho\omega^2 - k_s\gamma\delta\mu \cos\theta)\hat{b}_i - \gamma k_s\delta\mu\hat{r}_1\hat{b}_1\delta_{1,3} \right] \times \int_R \exp [i(k_s\hat{z} - \gamma\hat{r}) \cdot \mathbf{r}'] d\mathbf{r}' \quad (2.44)$$

with the corresponding scattering amplitudes:

$$A_i = \frac{k_p^2}{4\pi} \left(\frac{\delta\rho \sin\theta \cos\phi}{\rho} - \frac{\delta\mu}{\lambda+2\mu} \frac{k_s}{k_p} \sin 2\theta \cos\phi \right) \times \int_R \exp [i(k_s\hat{z} - k_p\hat{r}) \cdot \mathbf{r}'] d\mathbf{r}' \cdot \hat{r}_i \quad (2.45)$$

$$B_i = \frac{k_s^2}{4\pi} \left[\left(-\frac{\delta\rho \sin\phi}{\rho} + \frac{\delta\mu \sin\phi \cos\theta}{\mu} \right) \hat{\phi}_i + \left(\frac{\delta\rho \cos\theta \cos\phi}{\rho} - \frac{\delta\mu \cos^2\theta \cos\phi}{\mu} \right) \hat{\theta}_i \right] \\ \times \int_R \exp [i(k_s \hat{z} - k_s \hat{r}) \cdot \mathbf{r}'] d\mathbf{r}'$$

(2.46)

Shape factor for different geometrical objects

For shapes that are describable in a closed analytical form, such as spheres, cylinders and ellipsoids, the shape factor can explicitly be calculated by integration (Gubernatis *et al.*, 1977a):

$$S(p, q) = \int_R \exp [i(p\hat{z} - q\hat{r}) \cdot \mathbf{r}'] d\mathbf{r}' \quad (2.47)$$

For a sphere of a radius a , $S(p, q)$ will then read as:

$$S = 4\pi a^3 \frac{\sin(a\Delta k) - a\Delta k \cos(a\Delta k)}{(a\Delta k)^3} \quad (2.48)$$

with

$$\begin{aligned} \Delta k &= |\Delta \mathbf{k}| = |p\hat{z} - q\hat{r}| && \text{in general} \\ \Delta k &= 2k \sin \frac{\theta}{2} && \text{for non mode conversion scattering} \\ \Delta k &= \sqrt{k_p^2 + k_s^2 - 2k_p k_s \cos\theta} && \text{for mode conversion scattering} \end{aligned} \quad (2.49)$$

If the normalized frequency $a\Delta k$ approaches zero, i.e. the sphere gets very small compared to the wavelength, S approaches unity for all scattering directions. Equations 2.41, 2.42, 2.45 and 2.46 will then equal equations 2.24 through 2.27 derived in section 2.1.1, as they should.

For a cylinder of a radius b , length $2a$ and cylinder axis aligned along the z axis, S reads as follows:

$$S = 4\pi a b^2 \frac{\sin a(\Delta k)_z}{a(\Delta k)_z} \frac{j_1[b(\Delta k)_x]}{b(\Delta k)_x} \quad (2.50)$$

$(\Delta k)_x$ and $(\Delta k)_z$ are the projections of $\Delta \mathbf{k}$ onto the x and z axes, respectively and $j_1(x)$ is the Bessel function of order unity.

The shape factor for an ellipsoid with its axis a_1, a_2 and a_3 aligned along the x, y and z axes of the coordinate system, is:

$$S = 4\pi a_1 a_2 a_3 \frac{(\sin \Delta K) - \Delta K \cos \Delta K}{\Delta K^3} \quad (2.51)$$

where $\Delta K = (\Delta k_1^2 a_1^2 + \Delta k_2^2 a_2^2 + \Delta k_3^2 a_3^2)^{1/2}$ with Δk_i representing the projection of $\Delta \mathbf{k}$ onto the \hat{a}_i axis. It equals that of a sphere in case of $a_1 = a_2 = a_3$. Equation 2.47 can be integrated numerically for more complex objects, which makes the Born approximation an attractive tool for modeling the scattering response of single isolated inclusions.

2.1.3 Scattering from Large Complex Objects

In the preceding section I described the mathematical approach to the description of scattering phenomena for objects which are either small or of spherical symmetry or which show sufficiently small perturbations in their elastic parameters with respect to the reference medium. If the object is of comparable size or greater than the wavelength of the incident wave field, or possibly shows large perturbations in its material parameters, a closed mathematical solution can only be obtained for a limited range of shapes and contrasts.

To describe and understand scattering from large objects with arbitrary shape and arbitrary elastic parameters a different approach was used instead. As already applied by Bohlen (1998), a finite difference algorithm was utilized to model the complete scattered wave field for a broad variety of objects. Numerical solutions of the elastic wave equation 2.4 naturally provide the full wave field response of the subsurface including the direct arrival as well as scattered and reflected energy.

By definition (equation 2.28), the scattered wave field is the difference between the total and the incident wave fields. In order to obtain the scattering response as such, we thus have to subtract the wave field obtained for a model without scatterer from that obtained for a model with scatterer. The procedure is illustrated in figure 2.2.

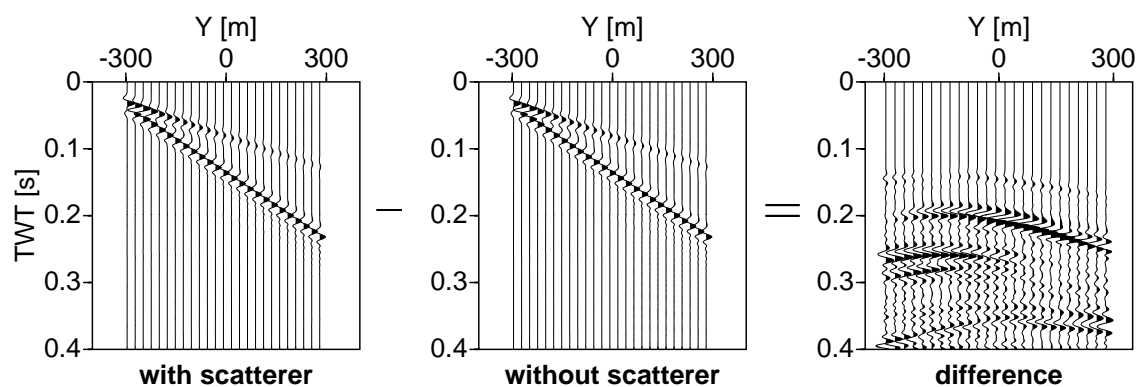


Figure 2.2: The pure scattering response by definition (e.g. equation 2.28) is obtained by subtracting the finite difference wave field simulation without inclusion from a simulation with inclusion (energy balanced for display).

The main results obtained by Bohlen et al. (in preparation 2000) using a model for scattering from mineral deposits embedded in the crystalline crust will be reviewed in section 2.3.1.

The FD algorithm used, is a 3D extension of the 2D viscoelastic and elastic finite difference algorithms described by Robertsson et al. (1994b) and Levander (1988). In the algorithm the velocity-stress formulation of the 3D viscoelastic wave equation is solved on a staggered grid. The accuracy of the finite difference operators are of fourth order in space and of second order in time ($O(4,2)$).

Finite difference modeling is commonly regarded as an exact modeling method for arbitrary complex models. Inaccuracies, i.e. numerical grid dispersion and grid anisotropy, may occur if the spatial and temporal sampling is not fine enough. For the applied $O(4,2)$ scheme the

spatial grid spacing h must be less than $\lambda_s^{min}/6$ where λ_s^{min} denotes the minimum shear wavelength within the model. This guarantees that the error due to numerical dispersion is smaller than 5 percent (Robertsson *et al.*, 1994b). The 3D-FD algorithm is stable as long as the time-step Δt fulfills the criterion (Blanch, 1995):

$$\Delta t \leq \frac{6h}{7\sqrt{3}v_p^{max}} \quad (2.52)$$

where v_p^{max} is the maximum P-wave velocity within the model.

2.2 Diffraction Theory

The theory of diffraction is based on the original concept of Huygens, which describes the disturbance at a point P in space due to an existing wavefront which emanates from a source \mathbf{x}_s , as the superposition of an infinite number of secondary waves, which are emitted on the wavefronts surface.

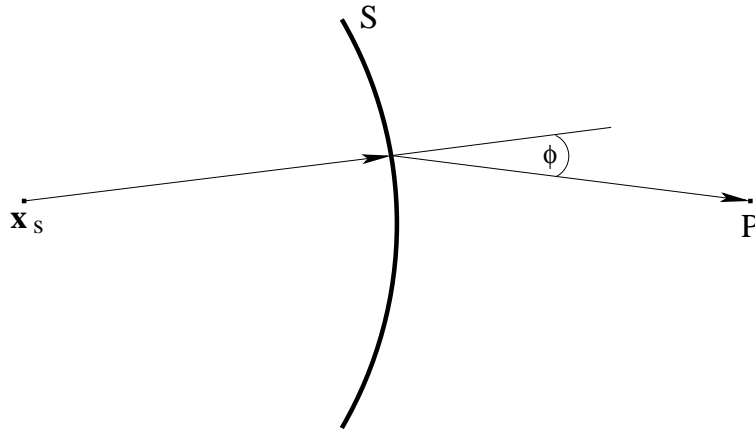


Figure 2.3: *Huygens-Fresnel-Principle. Each element of the wavefront S that has emanated from a source \mathbf{x}_s , can be regarded as the center of a secondary disturbance which is propagated in form of a spherical wave. Interference of all secondary waves which are tuned by an obliquity factor depending on Φ contribute to the resulting disturbance in point P .*

It was put on a mathematical basis by Kirchhoff in 1882. The first rigorous solution to a diffraction problem was given by Sommerfeld in 1896, when he discussed the diffraction of a plane wave by a perfectly conducting semi-finite plane screen. Because exact solutions for general diffraction phenomena are accompanied by mathematical difficulties, the approximate methods based on Huygens, Fresnel and Kirchhoff must be used in most cases of practical interest (Born & Wolf, 1980). Keller (1962) gave a kinematic description of the diffraction phenomenon in his geometrical theory of diffraction, which however will fail in predicting the dynamical behavior of the diffracted wave field. Since the paper of Hilterman (1970) Kirchhoff diffraction theory (KDT) has found a wide acceptance in reflection seismology (Kampfmann, 1988). KDT simultaneously provides a solution for reflected and

diffracted seismic wave fields. In geophysical applications it is widely used to model seismic reflection and diffractions from planar, curved and/or interrupted geological interfaces. KDT is often applied in its acoustic representation, although there is no principle restriction in the approach to the use of the scalar wave equation. A formulation for the elastic wave equation was for example given by Pao and Varatarajulu (1976).

In KDT it is generally assumed, that the seismic wavelength is much smaller than the extent of any of the subsurface structures. The relative size of subsurface discontinuities is thus given by a normalized frequency $k \cdot a \gg 1$.

Edge Wave method (EWT) is closely related to the Kirchhoff integral method and differs only in the approximations of the integral (Klem-Musatov & Aizenberg, 1989). This theory, as derived by Klem-Musatov (1985), provides a convenient way of describing reflected and diffracted seismic waves as two linear independent ray approximation solutions of the wave equation.

I will now review basic principles of ray tracing which build the basis for understanding the main results of the edge wave theory. The theory itself will be discussed subsequently.

2.2.1 Edge Wave Theory

The concept of ray theory builds the basis for understanding the Edge Wave theory and shall now be reviewed. An overview of this theory can, e.g., be found in Rabbel (1987). Subsequently, the basic concepts of the Edge Wave theory itself will be described.

Basic principles of ray tracing

The basic concept of ray theory is to expand the elastic wave field in a "ray series", which can be truncated to its leading terms in the case of a high frequency approximation. Through this approach the equation of motion leads to a system of differential equations, which allows for separation into longitudinal and transverse components of the wave field, with waves speed v_p and v_s respectively. In two dimensional media the transverse components further separate into vertically and horizontally polarized rays with respect to the plane of the medium. The system of differential equations also yields the well known eikonal and transport equations:

$$[\nabla_x \tau(\mathbf{x}, \mathbf{y})]^2 = c_0^{-2}(\mathbf{x}) \quad (2.53)$$

$$A(\mathbf{x}, \mathbf{y}) \nabla_x \tau(\mathbf{x}, \mathbf{y}) 2 \nabla_x A(\mathbf{x}, \mathbf{y}) \nabla_x(\mathbf{x}, \mathbf{y}) = 0, \quad (2.54)$$

c_0 is the velocity of seismic waves in the background medium (either v_p or v_s).

The eikonal equation gives the travel time τ_R^Ω of the ray, also called phase or eikonal, which obeys Fermat principle. In ray notation used here Ω denotes the ray itself and R stands for "reflection". The transport equation determines the complex amplitude of the traveling rays a_R^Ω , which also carries phase information. Energy transport is assumed to be mainly in direction of the ray excluding transverse diffusion (e.g. Rabbel, 1987).

The ray theoretical wave field $\mathbf{u}_R(\mathbf{x}_s, \mathbf{x}_r, t)$ is the amount of all rays \mathbf{u}_R^Ω that have traveled through the subsurface from the source to the receiver:

$$\mathbf{u}_R(\mathbf{x}_s, \mathbf{x}_r, t) = \sum_{(\Omega)} \mathbf{u}_R^\Omega(\mathbf{x}_s, \mathbf{x}_r, t) \quad (2.55)$$

\mathbf{x}_s and \mathbf{x}_r denoting the position of source and receiver, respectively.

The amplitude u_R^Ω of the particle displacement $\mathbf{u}_R^\Omega = u_R^\Omega \cdot \hat{u}_R^\Omega$ (\hat{u}_R^Ω is the unit vector in direction of particle motion) along each ray can be separated in a spatial and a temporal part:

$$u_R^\Omega(\mathbf{x}_s, \mathbf{x}_r, t) = \text{Re} \left\{ a_R^\Omega(\mathbf{x}_s, \mathbf{x}_r) W_s \left[t - \tau_R^\Omega(\mathbf{x}_s, \mathbf{x}_r) \right] \right\} \quad (2.56)$$

The complex function $W_s(t)$ is an analytical expression for the source waveform:

$$W_s(t) = w_s(t) + i\mathcal{H}[w_s(t)] \quad (2.57)$$

with $\mathcal{H}[w_s(t)]$ being the Hilbert transform of the source waveform. The transport equation was solved e.g. by Červený (1987) and yields the amplitude a_R for a ray that has been transmitted or reflected by N interfaces as in the following expression:

$$\begin{aligned} a_R(\mathbf{x}_s, \mathbf{x}_r) &= \frac{1}{L_{sr}} g(\kappa_s) r(\kappa_r) \left(\frac{v_s \rho_s}{v_r \rho_r} \right)^{1/2} \\ &\times \prod_{k=1}^N C_k \left[\frac{v_k^+ \rho_k^+ \cos(\kappa_k^+)}{v_k^- \rho_k^- \cos(\kappa_k^-)} \right]^{1/2} \end{aligned} \quad (2.58)$$

L_{sr} is a spreading term describing the divergence of the ray amplitude while passing either freely through the medium or being refracted at same interface. If the ray passes through a caustic its phase is shifted by $\pi/2$, so that one may introduce the so called KMAH-index, which counts the number of caustics along the ray path and divides L_{sr} into a pure divergence and a phase shift term:

$$L_{sr} = L(\mathbf{x}_s, \mathbf{x}_r) = |L_{sr}| \exp\left(-i \frac{\pi}{2} K_{sr}\right) \quad (2.59)$$

where K_{sr} counts the number of caustics passed. In order to calculate the divergence term L_{sr} in equation 2.58 one has to consider divergence of the wavefront as well as focusing effects and caustics (Červený, 1987; Hoffmann, 1995). $g(\kappa_s)$ and $r(\kappa_r)$ are source and receiver characteristics with $\kappa_{s,r}$ being the take off angle and angle of incidence, respectively. The coupling term, which is the next term in the equation, depends on impedance contrast present at the source and the receiver. And finally we have a term describing the transmission loss due to reflections and/or transmissions of the ray while traveling through the heterogeneous earth. There is no principle limit in expanding the complexity of equation 2.56, so that e.g. terms for absorption can be added (Rabbel, 1987).

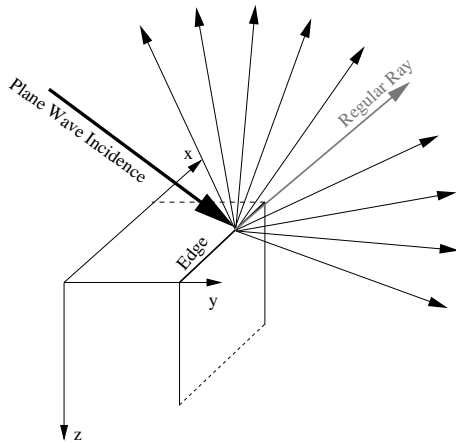


Figure 2.4: Special case of 2D diffraction: A ray incident in the plane perpendicular to the edge of an otherwise continuous reflector is diffracted to a fan of rays. This fan also lies in the plane of the incident wave field. In the general situation of arbitrary incidence direction rays are diffracted to a cone.

Dealing with diffractions: Edge Wave Theory

The ray tracing method by itself is not able to describe diffractions, but is very useful to calculate the wave field in a convenient way up to a point in the subsurface where it is either reflected or diffracted. It is reasonable to search for a method that provides the means of dealing with inevitable shadow zones in the ray wave field, which are produced by discontinuities in the subsurface layering, by edges, wedges or pinch outs. Keller (1962) gave a kinematic description of the diffraction phenomenon in his geometrical theory of diffraction:

A ray cone will emerge from any discontinuity, which in the case of plane rays (2D-situations) will degenerate to a fan that lies within the ray-plane itself (see figure 2.4) .

Keller's theory will fail in predicting the dynamical behavior of the diffracted wave field in the vicinity of the boundary layer, which is defined by the last regularly reflected ray. This drawback is overcome by the Edge Wave theory, which provides the means of smoothing discontinuities in the ray wave field by adding the Edge Wave solution to the classical ray solution. In contrast to Kirchhoff theory the Edge Wave method yields the advantage of two linearly independent solutions for the reflected and the diffracted wave fields:

$$\mathbf{u} = \mathbf{u}_R + \mathbf{u}_D \quad (2.60)$$

The wave equation is reduced asymptotically to a Kummer's equation (differential equation of second order) with two linearly independent solutions, of which the first one is the common solution for zero-order ray theory described above and the second one yields the wave field for the diffracted wave (Edge Waves). The theory is reviewed in Rabbel (1987); Klem-Musatov (1989) and Klaeschen (1995) and only main results will be repeated here. The reflected wave field \mathbf{u}_R is given by equation 2.56. It is zero in the shadow zone (see figure 2.5). The diffracted wave field is given by:

$$u_D^\Omega(\mathbf{x}_s, \mathbf{x}_r, t) = \pm Re \left\{ a_D^\Omega(\mathbf{x}_s, \mathbf{x}_r) W_s \left[t - \tau_D^\Omega(\mathbf{x}_s, \mathbf{x}_r) \right] \right\} \quad (2.61)$$

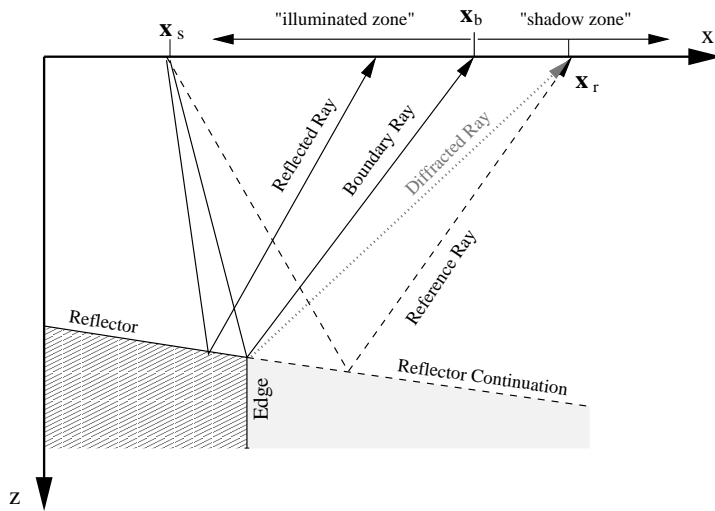


Figure 2.5: The boundary ray is the last ray that is reflected regularly. The amplitude of the diffracted ray at the boundary is a function of the travel time distance between diffracted and reference ray. The reference ray is calculated by virtual continuation of the reflector (equation 2.64 and 2.65).

τ_D is the travel time of the diffracted ray. Compared to the reflected wave field the phase of u_D is negative in the illuminated zone and positive in the shadow zone. a_D is the amplitude of the diffracted wave field and given by:

$$a_D(\mathbf{x}_s, \mathbf{x}_0, \mathbf{x}_r, \mathbf{x}_b) = a_R(\mathbf{x}_s, \mathbf{x}_b) d_{EW}(\mathbf{x}_s, \mathbf{x}_0, \mathbf{x}_r, \mathbf{x}_b) \quad (2.62)$$

\mathbf{x}_0 denotes the position of the diffracting edge, \mathbf{x}_b the boundary to the shadow zone and $d_{EW} = d_{EW}(\Delta\tau)$ the weakening function which depends on the travel time difference

$$\Delta\tau = \tau_D(\mathbf{x}_s, \mathbf{x}_0, \mathbf{x}_r) - \tilde{\tau}_R(\mathbf{x}_s, \mathbf{x}_r). \quad (2.63)$$

$\tilde{\tau}_R$ is the travel time of the reference ray shown in figure 2.5 and can be calculated in a paraxial approximation (Rabbel, 1987; Kläschen, 1995).

The Edge Wave theory yields for the weakening function (Klem-Musatov & Aizenberg, 1985; Klem-Musatov & Aizenberg, 1989):

$$\begin{aligned} d_{EW} &= \pm W(w) \\ &= \pm \frac{1}{2\sqrt{\pi}} \Gamma\left[\frac{1}{2}, -\frac{i\pi w^2}{2}\right] \exp\left(-\frac{i\pi w^2}{2}\right) \end{aligned} \quad (2.64)$$

with $w = w(\tau_D, \tilde{\tau}_R, \omega)$ defined by:

$$w = \sqrt{\frac{2\omega\Delta\tau}{\pi}} \quad (2.65)$$

and the incomplete gamma function:

$$\Gamma\left(\frac{1}{2}, z\right) = \int_z^\infty \frac{\exp(-t)}{\sqrt{t}} dt \quad (2.66)$$

2.3 Classification of Scatterers

Since the early work of Zoeppritz (1919) the analysis of amplitude variation as a function of source receiver offset (AVO) has evolved to become one of the most appreciated classification methods for stratified seismic reflection horizons in exploration seismology. It found broad acceptance within modern oil and gas exploration industry (Ostrander, 1984). Today it is used for example as one of the favored techniques in order to investigate the petrophysical properties of so called bottom simulating reflectors (BSR) (Hyndman & Spence, 1992; Ecker, 1998).

AVO analysis, however can not be applied to isolated localized geological or man made inclusions in the earths subsurface, because in such situations the assumption of lateral continuity is violated. Such inclusions are of academical or financial interest, or even represent potential security risks. They range from large scale objects such as the earths inner core or pronounced velocity perturbations in the mantel (plumes, hot spots) to small scale geological features such as boulders or gas accumulations in unconsolidated marine sediments. Other targets of interest for geophysical exploration are man made caverns in salt diapirs, used for storing large amounts of production resource materials, localized oil and gas accumulations found in traps at salt dome flanks, or massive volcanogenic ore deposits as situated in the upper, mining accessible part of the crystalline crust. Among others, there are potentially hazardous objects such as abandoned or lost ammunition originating from former military altercations, or ship wrecks.

From a theoretical point of view all these inclusions represent perturbations in the Lamé parameters and density of the elastic medium they are embedded in. The Lamé parameters are related to the compressional and shear wave velocities v_p and v_s of the medium by equation 2.9. Thus the scattering process is also governed by perturbations in seismic velocities and density of the background medium, i.e. $\delta v_p = v'_p - v_p$, $\delta v_s = v'_s - v_s$ and $\delta \rho = \rho' - \rho$. The scattering process can be classified by these parameters. Analyzing the characteristic dynamic behavior of the scattered seismic wave field as it is state of the art in AVO analysis, can thus possibly help in gaining information about the composition of a scattering object.

First approaches to the classification of seismic scatterers where given by Wu (1989a). He introduced the notion of velocity and impedance scattering, which was later extended by the notion of density scattering through Eaton (1999). Both considerations, however, are based on the concept of the Born approximation, which is not generally valid. Here I present a classification approach which is based on the theory of Rayleigh scattering, and, as will be discussed below, can in part be extended to characterize the scattering from large complex shaped objects of arbitrary material parameter contrast.

In the following I will describe the dynamic behavior for a number of examples of scattering objects situated in crystalline host rock or marine unconsolidated sediments. The examples chosen are referring to the seismic processing case histories as described in chapter 4 towards the end of this study.

Not only the dynamic, but moreover the kinematic characteristics of the seismic wave field scattered from isolated inclusions is of interest for developing new processing approaches in order to image the inclusion itself and to analyze the characteristic dynamic behavior of scattered seismic waves. Thus subsequently to the investigation of the dynamic features of

scattering a brief description of its kinematic characteristics will be given. The discussion will be accompanied by short appreciation of the dynamic and kinematic behavior of diffracted seismic wave fields, due to the close relatedness of both phenomena.

2.3.1 Dynamic Characteristics of Scattered and Diffracted Wave Fields

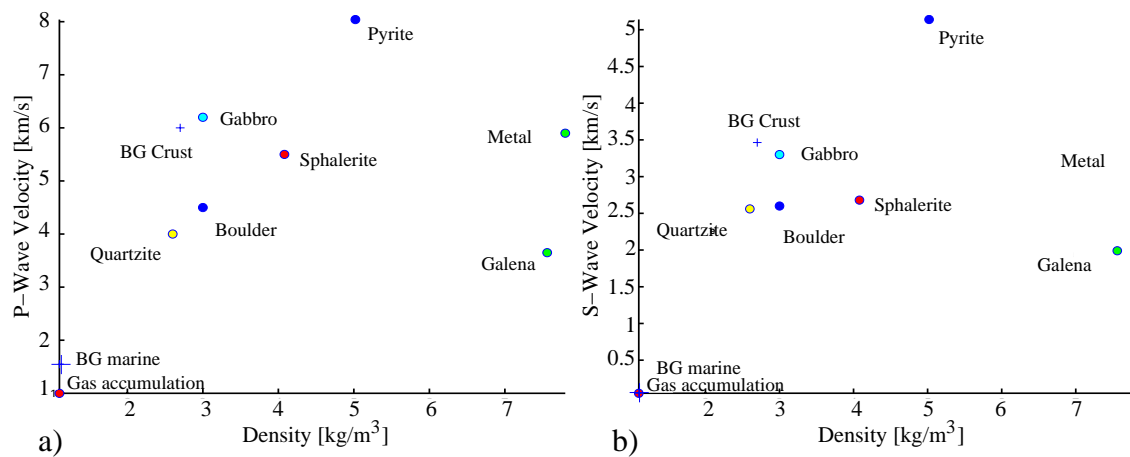


Figure 2.6: Material parameters of possible scattering objects and the two background media (BG-) considered here. The material parameters span a three dimensional vector space, which will be called the material parameter space. The display represents the projection of each material parameter vector onto the v_p, ρ (a) and v_s, ρ (b) planes, respectively. The dynamic characteristics of the scattered wave field will generally depend not only on the position of the scatterer in the material parameter space, but also on the position off the background medium. The combination of background and scatterer material parameters is defined as the scattering situation.

In order to interpret the scattering signature recorded in seismic measurements, it is important to know how the composition of the scatterer influences the dynamics of the scattered wave field.

Mineral ore deposits in the crystalline crust as well as several different objects, such as boulders, metal objects or gas accumulations situated in an unconsolidated marine sediment background medium, will serve as an example. The elastic parameters of these example inclusions are summarized along with the parameters for the background medium in tables 2.1 and 2.2, respectively. The examples are chosen because they relate to the case histories discussed in chapter 4.

Figure 2.6 shows the position of the assumed inclusions as two cross plots through the three dimensional *material parameter vector space*, spanned by the seismic velocities v_p and v_s and the mass density ρ . The display represents the projection of each material parameter vector onto the v_p, ρ (a) and v_s, ρ (b) planes, respectively. The dynamic characteristics of the scattered wave field will generally depend not only on the position of the scatterer in

	$v_p[m/s]$	$v_s[m/s]$	$\rho[kg/m^3]$
Pyrite	8040	5140	5020
Sphalerite	5500	2680	4080
Galena	3650	1990	7560
Gabbro	6200	3300	3000
Quartzite	4000	2560	2600
Crystal. crust	6000	3000	2700

Table 2.1: Average P -wave velocity (v_p), S -wave velocity (v_s), and density (ρ) for the five types of inclusions and for the crystalline background medium considered here. (Salisbury et al., 1996; Schön, 1996).

	$v_p[m/s]$	$v_s[m/s]$	$\rho[kg/m^3]$
Gas accumulation	1000	50	1100
Granite boulder	4500	2600	3000
Metal object	5900	3200	7800
Uncons. sediments	1550	50	1100

Table 2.2: Average P -wave velocity (v_p), S -wave velocity (v_s) and density (ρ) for three types of possible scattering object immersed in unconsolidated sediments background.

the material parameter space, but also on the position of the background medium (see e.g. equations 2.19 and 2.20). The combination of background and scatterer material parameters will be defined as the *scattering situation*. Figure 2.6 is the graphical representation of tables 2.1 and 2.2.

In the following I will first focus on the dynamic characteristics of the scattered wave field emanating from small inclusions (Rayleigh scattering). Subsequently I will discuss the dynamics of scattering from larger objects as it can be described within the limits of the Born approximation. And finally, results from finite difference modeling of the scattered wave field from large objects of complex shape will be given. The influence of the shape and composition of these objects on the dynamics of the scattered wave field will be investigated.

Dynamic characteristics of Rayleigh scattering

In figure 2.7 the far field scattered amplitudes for $p \rightarrow p$ and $p \rightarrow s$ scattering from a sphere (equations 2.19 and 2.20) are plotted as a function of scattering angle for different mineral ores (pyrite, galena, sphalerite) and some rocks (gabbro, quartzite) which are typically found in the crystalline crust. Figure 2.8 shows the same plots for the marine examples, i.e. a gas accumulation, metal object and a typical boulder submerged in unconsolidated sediments. The elastic parameters are summarized in table 2.1 and 2.2, respectively.

As is evident from the figure, $p \rightarrow p$ as well as $p \rightarrow s$ scattered amplitudes show different dynamic behavior for different materials.

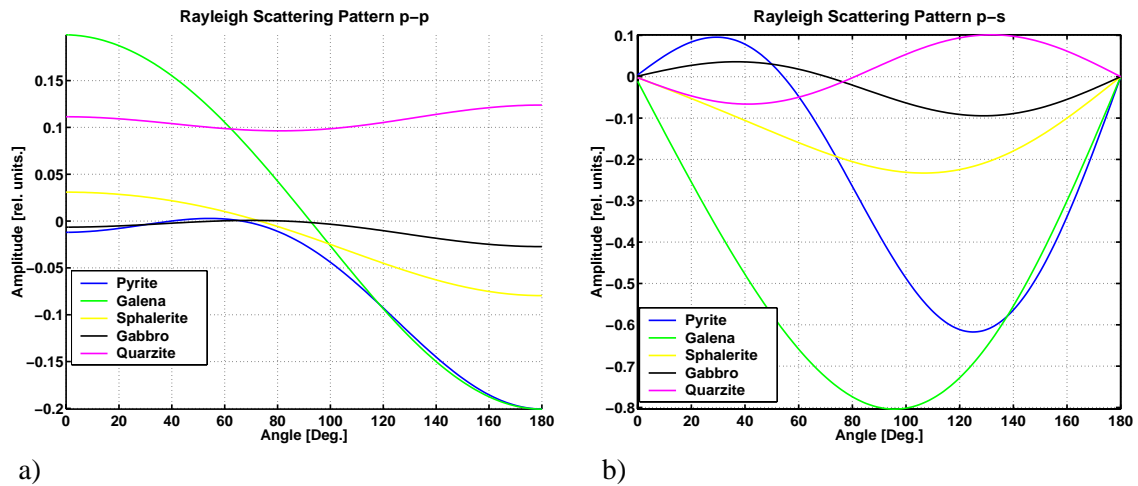


Figure 2.7: Far field Rayleigh scattering amplitudes for the individual inclusions and crustal background model as listed in table 2.1 plotted as a function of scattering angle θ for the cases of $p \rightarrow p$ (a) and $p \rightarrow s$ (b) scattering. The overall scattering strength is proportional to the square of the incidence wave fields frequency and the volume of the inclusion. The directional behavior of the scattered wave field is governed by the elastic perturbations of the scattering situation in question (equations 2.24 and 2.25). The scattered wave field shows phase reversals that only depend on the scattering situation. They are thus called significant phase reversal (SPR). Phase reversals for $\theta = 0^\circ$ and $\theta = 180^\circ$ in the case of $p \rightarrow s$ scattering are merely of geometrical origin.

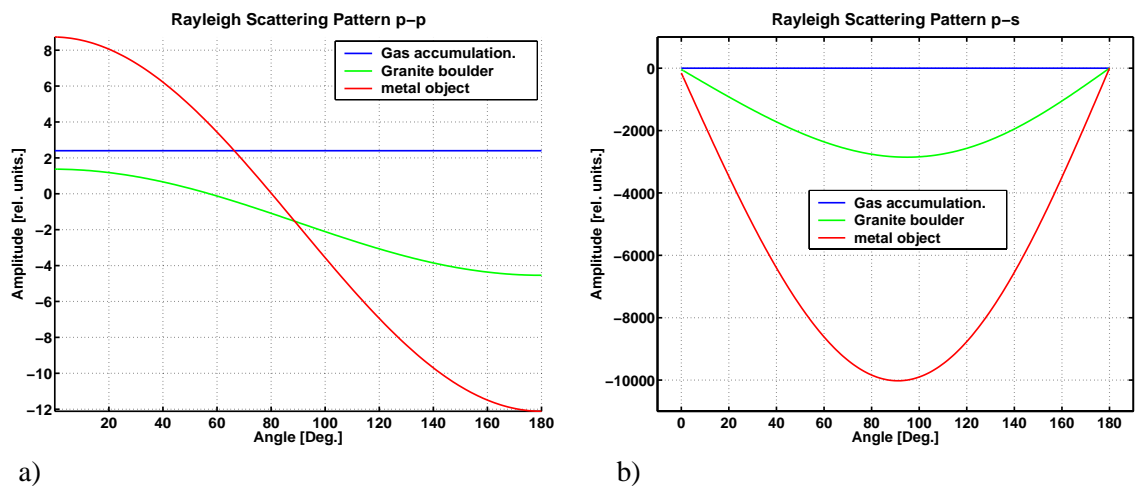


Figure 2.8: Far field Rayleigh scattering amplitudes for the individual inclusions and marine background model as listed in table 2.2 plotted as a function of scattering angle θ for the cases of $p \rightarrow p$ (a) and $p \rightarrow s$ (b) scattering. Please note that the gas accumulation shows a constant angular trend for both $p \rightarrow p$ and $p \rightarrow s$ scattering.

For $p \rightarrow p$ scattering the plotted functions are of the type:

$$\mathcal{A} \cos^2 \theta + \mathcal{B} \cos \theta + \mathcal{C} \tag{2.67}$$

and for $p \rightarrow s$ scattering of type:

$$\mathcal{D} \sin 2\theta + \mathcal{E} \sin \theta \tag{2.68}$$

Thus the dynamic characteristics are governed by the parameters \mathcal{A}, \mathcal{B} and \mathcal{C} for $p \rightarrow p$ scattering and \mathcal{D} and \mathcal{E} for $p \rightarrow s$ scattering respectively. The explicit expressions for these parameters are summarized in table 2.3 for convenience.

Rayleigh Approximation	Born Approximation
<p>p → p</p> $\mathcal{A} = -2 \left(\frac{\mu'}{\mu} - 1 \right) \frac{\gamma^2}{D}$ $\mathcal{B} = \frac{\rho'}{\rho} - 1$ $\mathcal{C} = -\frac{1}{2} \frac{\frac{3}{2}(\lambda' - \lambda) + (\mu' - \mu)}{\frac{1}{2} \left(\frac{3}{2}\lambda' + \mu' \right) + \mu} + \frac{2}{3} \left(\frac{\mu'}{\mu} - 1 \right) \frac{\gamma^2}{D}$ <p>with</p> $\gamma = \frac{v_s}{v_p}$ $D = 1 + \frac{2}{15} \left(\frac{\mu'}{\mu} - 1 \right) (3 + 2\gamma^2)$	<p>p → p</p> $\mathcal{A} = -2 \frac{\mu' - \mu}{\lambda + 2\mu}$ $\mathcal{B} = \frac{\rho'}{\rho} - 1$ $\mathcal{C} = -\frac{\lambda' - \lambda}{\lambda + 2\mu}$
<p>p → s</p> $\mathcal{D} = \left(\frac{\mu'}{\mu} - 1 \right) \frac{\gamma}{D}$ $\mathcal{E} = -\left(\frac{\rho'}{\rho} - 1 \right)$	<p>p → s</p> $\mathcal{D} = \left(\frac{\mu'}{\mu} - 1 \right) \gamma$ $\mathcal{E} = -\left(\frac{\rho'}{\rho} - 1 \right)$

Table 2.3: Parameters that govern the far field scattered amplitudes for the Rayleigh- and Born-Approximation, respectively.

The main features of the far field scattering amplitudes are the number and the angular position of the zero crossings, which correspond to polarity reversals in the scattered wave field and the amplitude extrema.

In order to classify different scatterers it is interesting to investigate the number and type of zero crossings observed in figures 2.7 and 2.8. Equation 2.67 has two possible roots that depend on all three parameters ($\mathcal{A}, \mathcal{B}, \mathcal{C}$). In equation 2.68 zero crossings for $\theta = 0^\circ$ and $\theta = 180^\circ$ do not depend on the material properties. We thus can conclude that for both $p \rightarrow p$ and $p \rightarrow s$ conversion, reversals in the polarity of the scattered wave field (except for $\theta = 0^\circ$ and $\theta = 180^\circ$) do depend on the composition of the scatterer and the background it is embedded in (*scattering situation*). I will call these types of phase reversals "significant phase reversal" (SPR). If observed in a seismic section, the number and angular position of SPR's can serve as a characteristic and robust dynamic feature to aid in the classification of a scatterer. The number and position of SPR's for the inclusions considered here are summarized in tables 2.4 and 2.5.

	SPR [Deg.] $p \rightarrow p$	SPR [Deg.] $p \rightarrow s$	sign(δv_p)	sign(δv_s)	sign($\delta \rho$)
pyrite	37;66	53	+	+	+
galena	92;-	-	-	-	+
sphalerite	72;-	-	-	-	+
gabbro	82;52	70	+	+	+
quartzite	-;-	80	-	-	-

Table 2.4: Angular position and sign of perturbations for the investigated crustal inclusions. The number and angular position of SPR's (significant phase reversals) in the scattered seismic wave field change depending on the composition of the scattering inclusion. When observed in seismic recordings SPR's can serve as a robust criterion for the classification of scattering objects. Please compare with figure 2.7.

	SPR [Deg.] $p \rightarrow p$	SPR [Deg.] $p \rightarrow s$	sign(δv_p)	sign(δv_s)	sign($\delta \rho$)
Granite boulder	59	-	+	+	+
Metal object	80	-	+	+	+
Gas accumulation	-	-	-	0	0

Table 2.5: Angular position and sign of perturbations for the investigated inclusions hosted in a background medium of unconsolidated sediments. The gas accumulation shows neither an S-wave velocity nor a density contrast. It thus shows a constant angular trend for either $p \rightarrow p$ and $p \rightarrow s$ scattered waves and thus no SPR. Please compare with figure 2.8 and table 2.4.

Figure 2.9 shows the angular position of the first order SPR's for $p \rightarrow p$ scattering as a function of compressional wave velocity and mass density of the inclusion, for the crustal (a) and marine (b) examples. $v_p/v_s=2.0$ was assumed for the crustal and $v_p/v_s = \sqrt{3}$ for the marine inclusions and background media.

Please note that each plot represents a two dimensional cross-section through the three dimensional material parameter space. The positions given for the individual scattering inclusions and the background media, have to be interpreted as projections of their material parameter vectors onto the cross sectional planes plotted here. They do not exactly obey the assumptions for the velocity ratios ($v_p/v_s=2.0$, $v_p/v_s = \sqrt{3}$) given above. We will thus observe slight deviations between the SPR's indicated in figure 2.9 and those given in tables 2.4 and 2.5 or figures 2.7 and 2.8. Also, should all isolines focus at the location of the background parameters, since no scattering will occur if background and inclusion material parameters are equal. For the same reason as above this is not found for the marine case. This discussion is valid for any function of the material parameters which is displayed in a crosssectional plot such as in figure 2.9. It must thus also be considered in subsequent examples.

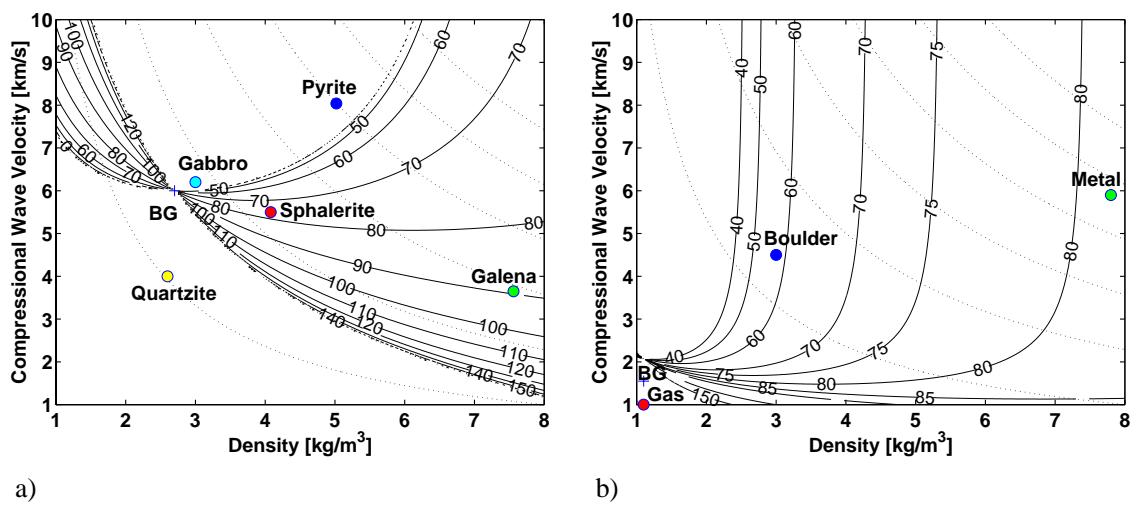


Figure 2.9: Rayleigh scattering angle of first order significant phase reversal (SPR, solid lines) for crustal (a) and marine (b) scattering situations, respectively, plotted for p-p scattering as a function of P-wave velocity and density. $v_p/v_s = 2.0$ was assumed for the background and the perturbations in the crustal scenario, whereas in the marine case it was $v_p/v_s = \sqrt{3}$. For a broad range of perturbations a phase reversal is observed. Since it only depends on the composition of the scatterers and the background medium, it may serve to classify the scattering situation in question. Dashed lines indicate constant impedance.

For a given background medium however, we can clearly distinguish several scatterers from just knowing the SPR's scattering angle. For the crustal model, e.g. Galena ($SPR = 92^\circ$) can obviously be distinguished from Pyrite ($SPR1 = 37^\circ$, $SPR2 = 66^\circ$). The same is true for the marine example. A metal object submerged in unconsolidated sediments ($SPR = 80^\circ$) should clearly be distinguishable from a typical granite boulder ($SPR = 59^\circ$). Even though the angular position of SPR's cover a wide range of scattering angles, their accessibility in seismic measurements depends on the used acquisition layout. The SPR's for both examples are primarily found in forward scattering direction (towards $\theta = 0^\circ$) and it will be difficult to access them through a classical surface seismic experiment.

The type and number of zero crossings does not directly correlate with the set of signs of

perturbations that is given in tables 2.4 and 2.5. If the complete angular trend of equations 2.19 and 2.20 is included in an inversion approach only the parameters given in table 2.3 can be inverted. The table also summarizes the parameters $\mathcal{A}, \mathcal{B}, \mathcal{C}$ and \mathcal{D}, \mathcal{E} for the Born-Approximation. Beylkin and Burridge (1990) presented a linearized Born inversion approach, which is based on similar considerations.

In general the access of seismic experiments to the host medium and scattering inclusions is limited due to the fact that seismic sources and sensors can only be deployed at the solid surface of the earth or in boreholes (figure 1.1b). Scattering is weak compared to diffraction or reflection from interfaces with comparable impedance contrast. Furthermore, the far field scattered amplitude is a function of scattering angle (equations 2.19, 2.20). It can thus be crucial to the success of a seismic scattering experiment whether the deployed acquisition layout is able to cover significant range of scattering angles for which maximum scattered amplitudes can be measured or not. Also it should be considered if an expected SPR is accessible with a specific layout.

The amplitudes $u_f = u(\theta = 0^\circ)$, $u_s = u(\theta = 90^\circ)$, $u_b = u(\theta = 180^\circ)$, referring to forward, side and back scattering, respectively, can thus be used as another classification attribute for seismic applications. They can be seen from figures 2.7 and 2.8.

Surface seismic surveys would be most suitable if dominant back scattering is exhibited by the target objects. If strong side scattering is expected in a scattering application a VSP experiment should be considered. Cross-well seismic surveys, where shots and receivers are deployed in different boreholes, should be used, when the scattering process is governed by strong forward scattering.

As we can see from figure 2.7 the decision about the acquisition layout utilized in a scattering seismic experiment also should include considerations about mode conversion. $p \rightarrow p$ scattered modes are generally weaker than $p \rightarrow s$ scattered modes and the directions of maximum scattered amplitudes for both modes are not the same.

Another important dynamic feature, apart from the angular radiation characteristics of a scattering inclusion is its total scattering strength. It is described by the normalized scattering cross section σ_N . The normalized scattering cross section is the ratio of the flow of total scattered energy, which includes scattered P- as well as scattered S-wave energy, to the flow of incident wave energy through a cross sectional area of the scattering object (geometrical shadow of the object). Figure 2.10 illustrates the notion in a sketch.

For a sphere Korneev and Johnson (1993) derived the following expression for σ_N :

$$\begin{aligned} \sigma_N &= 4 \sum_{l \leq 0}^{\infty} (2l + 1) \left\{ \left| \frac{a_l}{k_p R} \right|^2 + l(l + 1) \gamma_2 \left| \frac{b_l}{k_s R} \right|^2 \right\} \\ &= \sigma_{N_p} + \sigma_{N_s} \end{aligned} \quad (2.69)$$

where a_l , b_l and γ are the parameters given in equations 2.14 through 2.16 and 2.18.

In figure 2.11 σ_N is shown as a function of compressional wave velocity v_p and mass density ρ (solid lines) for a cross section through material parameter space. Crystalline crust was assumed as background medium (see table 2.1). As in figure 2.9 a fixed velocity ratio of

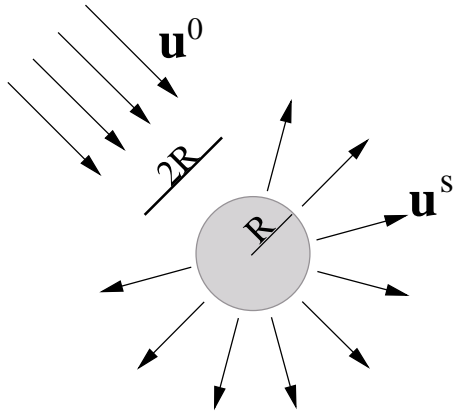


Figure 2.10: The normalized scattering cross section (NSC) is the ratio of the flow of total scattered energy u^s , to the flow of incident wave energy u^0 through a cross sectional area of the scattering object.

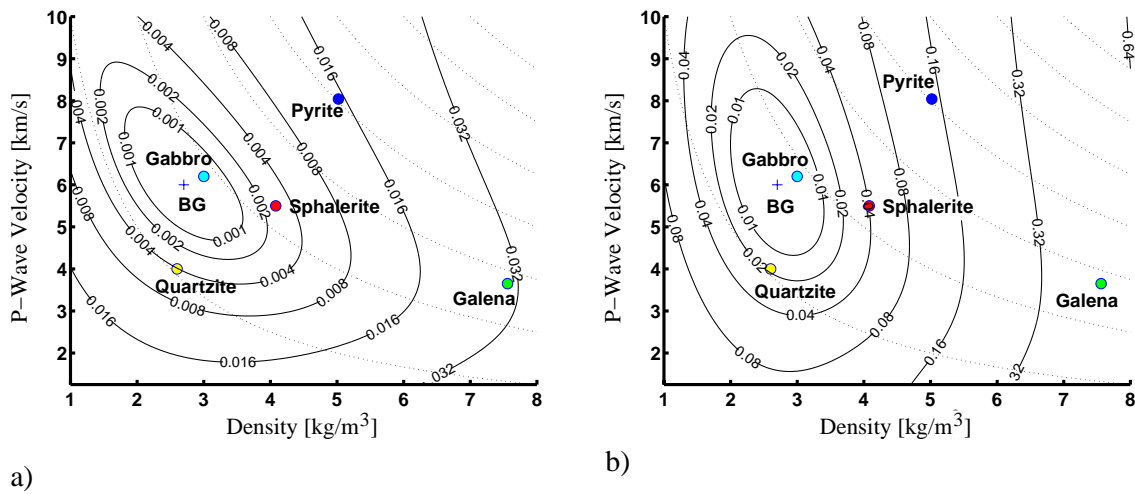


Figure 2.11: Normalized scattering cross section (NSC, solid lines) P- (a) and S-wave component (b) as a function of P-wave velocity and density of the inclusion. In contrast to the plane wave concept of impedance (impedance isolines dashed) the NSC increases with increasing distance from the background medium in material parameter space. Inclusion of low impedance contrast to the background medium can thus very well be strong scatterers.

$v_{p0}/v_{s0} = v_p/v_s=2.0$ was assumed for both inclusions and background medium. Example inclusions are plotted to give a general impression of their scattering strength. Impedance isolines are plotted as a reference (dashed lines).

As we can see from the plot, scattering strength is not controlled by the impedance contrast. Objects with an impedance comparable to that of the background can very well be strong scatterers, if sufficient contrast to the background is provided for any of the material parameters. In the figure, the compressional and shear wave scattering cross sections σ_{N_p} and σ_{N_s} are plotted separately. We observe that σ_{N_s} is nearly one order of magnitude greater than σ_{N_p} , which is due to the fact, that Rayleigh scattering energy is proportional to ω^4 (e.g. equation 2.21).

The considerations presented above are restricted to scattering from objects that are small compared to the size of the seismic wavelength. In the scope of this investigation however,

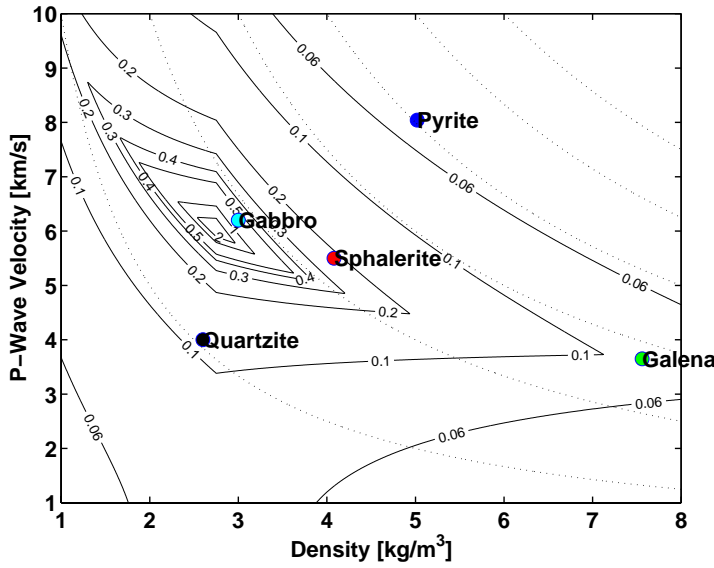


Figure 2.12: Validity of the Born approximation for large inclusions. The lines indicate the maximum valid inclusion size a/λ_s as a function of average P-wave velocity v'_p and density ρ' of the scatterer (equation 2.70). A ratio of $v_p/v_s = \sqrt{3}$ with regard to the crystalline background medium was assumed inside and outside the inclusion (Bohlen et al., 2000).

we are mainly interested in scattering from objects that are of comparable size or even greater than the seismic wavelength. In these cases not only the composition but also the shape of the scatterer will have an influence on the dynamics of the scattered seismic wave field. These effects will be discussed in the following sections.

Dynamic characteristics of Born Scattering

The results obtained above partly hold for the case of scattering from large complex objects. As described in section 2.1.2 this case can be treated with the Born approximation, if size and material parameter contrast of the inclusion obeys the limits given by equation 2.38. Using relation 2.9 and writing equation 2.38 as an equality, we can estimate an upper limit for the relative inclusion size $\frac{a}{\lambda_s} = \frac{k_s a}{2\pi}$ as a function of perturbations $\delta v_p, \delta v_s, \delta \rho$:

$$\frac{a}{\lambda_s} = [2\pi \Delta p(\delta v_p, \delta v_s, \delta \rho)]^{-1} \quad (2.70)$$

Figure 2.12 shows a plot of isolines for this upper limit in relative inclusion size as a cross section $v_p/v_s = \sqrt{3}$ inside and outside the inclusion through the material parameter space. As a qualitative picture, that can be drawn from the plot, the size of the inclusion has to get smaller with increasing size in perturbation to keep the Born approximation valid. For a pure sphalerite inclusion e.g., we can find $a/\lambda_s = 0.2$. To stay within the region of validity of the Born approximation we have to consider cases with $a/\lambda_s \ll 0.2$. In a crystalline background medium as given above, we thus find that the size of the inclusion must be much smaller than $a = 600m$. It is worth noting that for an inclusion of relative size $a/\lambda_s \ll 0.3$, with an elastic behavior of the background assumed, i.e. $\lambda_p/\lambda_s \approx \sqrt{3}$, we obtain:

$$\frac{a}{\lambda_p} \ll 0.17 \quad (2.71)$$

Inclusions of this size can readily be described by Rayleigh scattering theory, with an error less than 5% (Gritto *et al.*, 1995).

Another, heuristic approach of measuring the validity of the Born approximation can be applied by direct numerical comparison with exact solutions:

The composition factor can be regarded as the Rayleigh scattering pattern for a small low contrast inclusion (section 2.1.1 equation 2.24-2.27). It is plotted in Figure 2.13 as a function of scattering angle along with the Rayleigh scattering pattern (compare with figure 2.7) for the case of $p \rightarrow p$ and $p \rightarrow s$ scattering.

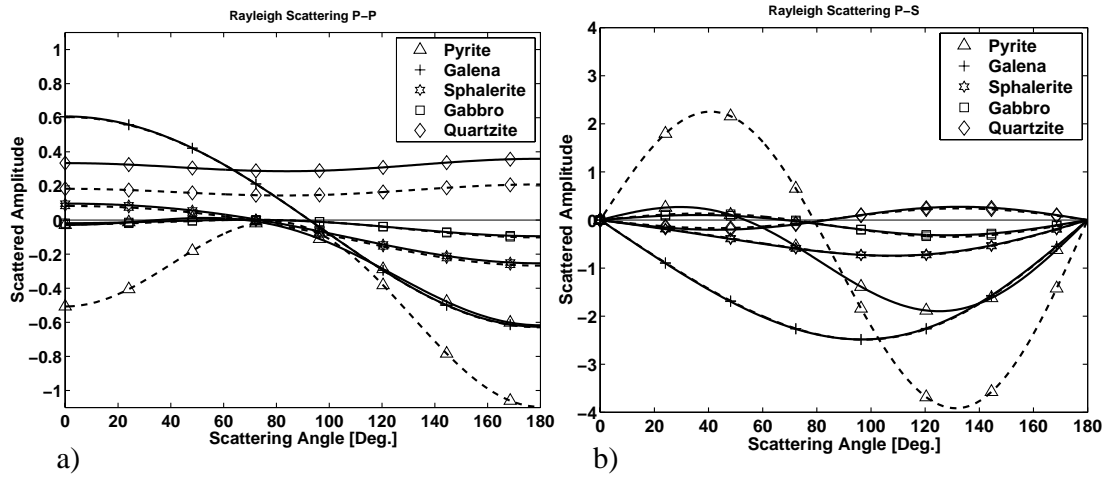


Figure 2.13: Far field amplitudes of $p \rightarrow p$ (a) and $p \rightarrow s$ (b) scattered waves for small inclusions embedded in a crystalline host rock (for material parameters please refer to table 2.1). Calculations are carried out for an incident wave field frequency of $f = 50\text{Hz}$ and a sphere of radius $a = 5\text{m}$, which corresponds to a normalized frequency of $ka \approx 0.26$. Solid lines correspond to the exact Rayleigh scattering solution for the sphere (equation 2.13 with 2.14 - 2.16), dashed lines to the Rayleigh-Born approximation (equations 2.24 and 2.25). Especially for pyrite the Rayleigh-Born approximation shows severe deviations from the exact solution (Bohlen *et al.*, 2000).

From the plots we can conclude that the dynamic characteristics of the scattered wave field that are influenced by the composition of the scatterer are very similar to those of Rayleigh scattering. However, because the Born approximation is not an exact solution to the scattering problem and only valid for small, low contrast inclusion, the composition factor in some cases shows significant deviation from the Rayleigh scattering pattern (e.g. for pyrite).

The error E of the Born approximation can be calculated as integral over differences in scattering amplitudes for all scattering angles between the Born approximation and the Rayleigh scattering approximation:

$$\begin{aligned}
 E_{pp} &= \frac{1}{2\pi} \int_0^{2\pi} \left\{ u_{pp\text{Rayleigh}}(\theta) - u_{pp\text{Born}}(\theta) \right\} d\theta \\
 E_{ps} &= \frac{1}{2\pi} \int_0^{2\pi} \left\{ u_{ps\text{Rayleigh}}(\theta) - u_{ps\text{Born}}(\theta) \right\} d\theta
 \end{aligned} \tag{2.72}$$

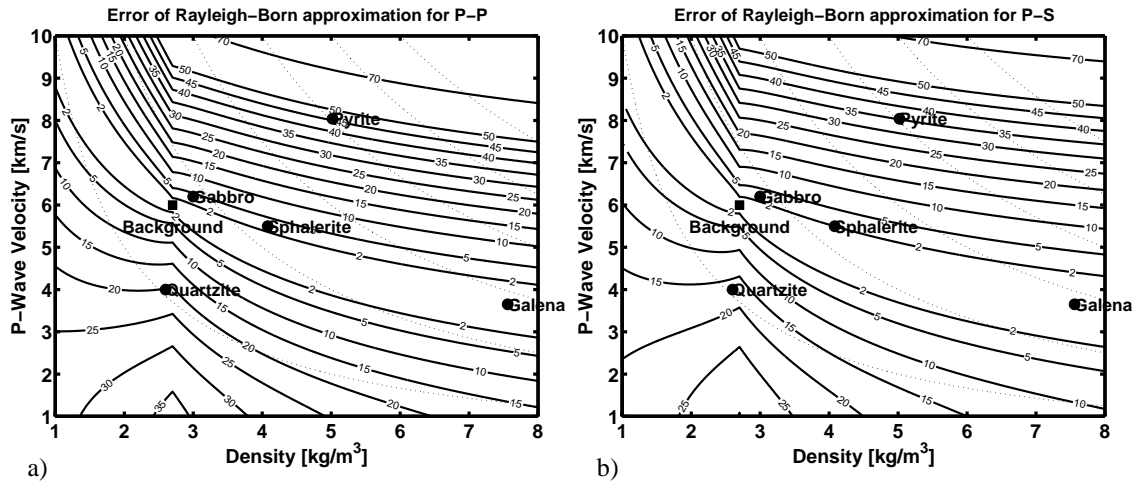


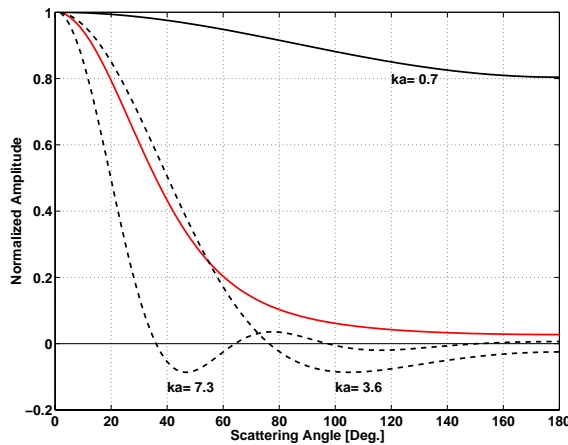
Figure 2.14: Error of the Rayleigh-Born approximation for (small) crystalline inclusions ($\alpha/\beta = \sqrt{3}$ assumed). Isolines give mean relative error (averaged over all scattering angles) in percent. a) Error for $p \rightarrow p$ scattering, b) Error for $p \rightarrow s$ scattering (Bohlen et al., 2000).

Figure 2.14 displays the error 2.72 as a function of density and compressional wave velocity, where again $v_{p0}/v_{s0} = v_p/v_s = \sqrt{3}$ was assumed. The error patterns for scattered p-waves and converted s-waves are very similar. Generally, we see that a perturbation in seismic velocities leads to much stronger inaccuracies than a perturbation in mass density. We also observe a corridor with errors less than 2%, for very small impedance contrasts compared with the background medium. However, a perturbation of just a few percent can lead to a significant error in the Born approximation, even for very small inclusions. We can conclude that both requirements, i.e.: a) the inclusion being sufficiently small and b) being of low contrast in its elastic parameters compared to the background medium, are quite restrictive and the Born approximation should be applied carefully.

Within its validity limits, however, the Born approximation provides a convenient mathematical instrument for independently treating influence of shape and composition by writing the scattered wave field as the product of a form- or shape factor (also referred to as distribution factor in the literature) and a composition factor.

The shape factor can be regarded as the spatial Fourier transform of the objects shape (Section 2.1.2, equation 2.47). Like the composition factor it is a function of scattering angle, but also depends on the difference in wave numbers of incident and scattered wave fields (section 2.1.2, equation 2.49). Dynamic characteristics will thus depend on the wavelength of the incident wave field. Figure 2.15 shows the normalized shape factor S_n of a sphere as a function of scattering angle for different wavelength of the incident wave field. The graphs are labeled with corresponding values for the normalized frequency ka . For values of ka significantly larger than 1, i.e. the sphere being much larger than one wave length, the shape factor will produce phase reversals in the scattered wave field. The oscillatory character of the shape factor increases with increasing normalized frequency. For values of ka significantly smaller than one, S_n has no zero crossing anymore and approaches unity for all scattering angles, thus scattering is not influenced by shape, or in

Figure 2.15: Shape factor as a function of scattering angle for different normalized frequencies (dashed lines: em monochromatic shape factor) and as integrated over a frequency range of $0 - 180Hz$ (solid line: integral shape factor). Inclusion size was assumed to be $a = 69.4m$ and background medium velocity was $6000m/s$. The integration was weighted with a Ricker type wavelet of $50Hz$ dominant frequency:



With decreasing scatterer size the monochromatic shape factor approaches unity for all scattering angles. For large inclusions the shape factor confines the scattered wave field to the forward scattering direction. The monochromatic shape factor generates an increasing number of phase reversals in the scattered wave field with increasing inclusion size ($ka = 3.6; ka = 7.3$). The integral shape factor generates no phase reversal.

this case, size of the sphere anymore.

Seismic sources (apart from vibrator seismic applications) emit an impulse which covers a broad frequency range.

The shape factor in this case should exhibit an integral effect over the whole frequency content of the seismic signal. Figure 2.15 also shows the shape factor S_I for a sphere as resulting from weighted integration over the frequency content of a Ricker type wavelet with $50Hz$ dominant frequency. S_I generates no phase reversal.

It can thus be concluded that in seismic scattering experiments and within the limits of the Born approximation, the shape factor not necessarily produces a phase reversal in the scattered wave field. The effect however depends on the frequency content of the incident wave field. It could not finally be shown that this result has general validity.

Whenever the above considerations hold, SPR's can also serve as a classification attribute in the case of scattering from large complex objects.

Large complex objects

As we have seen in the preceding section, scattering from objects other than spheres or spheroids can be treated with the Born approximation, but only for a very limited range of perturbation and sizes of scatterers. However, large inclusions with sizes comparable or even larger than the seismic wavelength can be of importance in exploration seismology (e.g. mineral ore deposits, which often are of great economic interest). Only few tools exist for numerical investigation of the scattered wave field and exact theoretical solutions are not available (please see also section 2.1.3). In order to gain a better understand-

ing of dynamic characteristics of scattered wave fields from large inclusions with realistic parameter perturbation, the scattering response was modeled using a (visco)elastic finite difference approach (Bohlen, 1998; Bohlen *et al.*, 2000). Following the formalism of the Born approximation the separate influence of composition and shape was investigated in two generic numerical experiments:

1. Six sphalerite inclusions with different shapes

- (a) A point scatterer: a small sphere serving as a reference example for Rayleigh scattering.
- (b) A sphere with a radius of approx. 70m: serving as a reference for scattering from spheres.
- (c) A highly complex shaped object: geological structures can often be of very complex or even fractal shape.
- (d) A parabolic lens: parabolic lenses were also investigated by other authors (e.g. Eaton, 1999).
- (e) A model resembling an existing volcanogenic massive sulphide ore deposit: the Bell Allard orebody in the Matagami mining camp, Quebec, Canada (Adam, 2000).
- (f) A dike model: dikes represent abrupt changes in lithology of often strong impedance contrast and are of planar, elongated shape.

Except for the point scatterer all objects occupy approximately the same volume.

2. Four differently composed inclusions

- (a) typical gabbro
- (b) sphalerite
- (c) galena
- (d) pyrite

as given in table 2.1 were modeled in the shape of a parabolic lens.

Influence of shape Figures 2.16 and 2.17 show snapshots of the scattered wave field obtained by building the difference between the total wave field and the wave field from a model without scatterer (section 2.1.3, figure 2.2), for the $p \rightarrow p$ and $p \rightarrow s$ scattering modes respectively.

The inclusions were assumed to be composed of sphalerite and to be situated in a crystalline background medium with elastic parameters as given in table 2.1. From these snapshots we can conclude that the shape of the inclusion has a strong influence on the dynamics of the scattered wave field. The point scatterer in figure 2.16 e.g. shows slightly stronger back- than fore scattering as in good agreement with Rayleigh scattering theory (figure 2.7) whereas the sphere has a pronounced sharply focused fore scattering amplitude. The dike

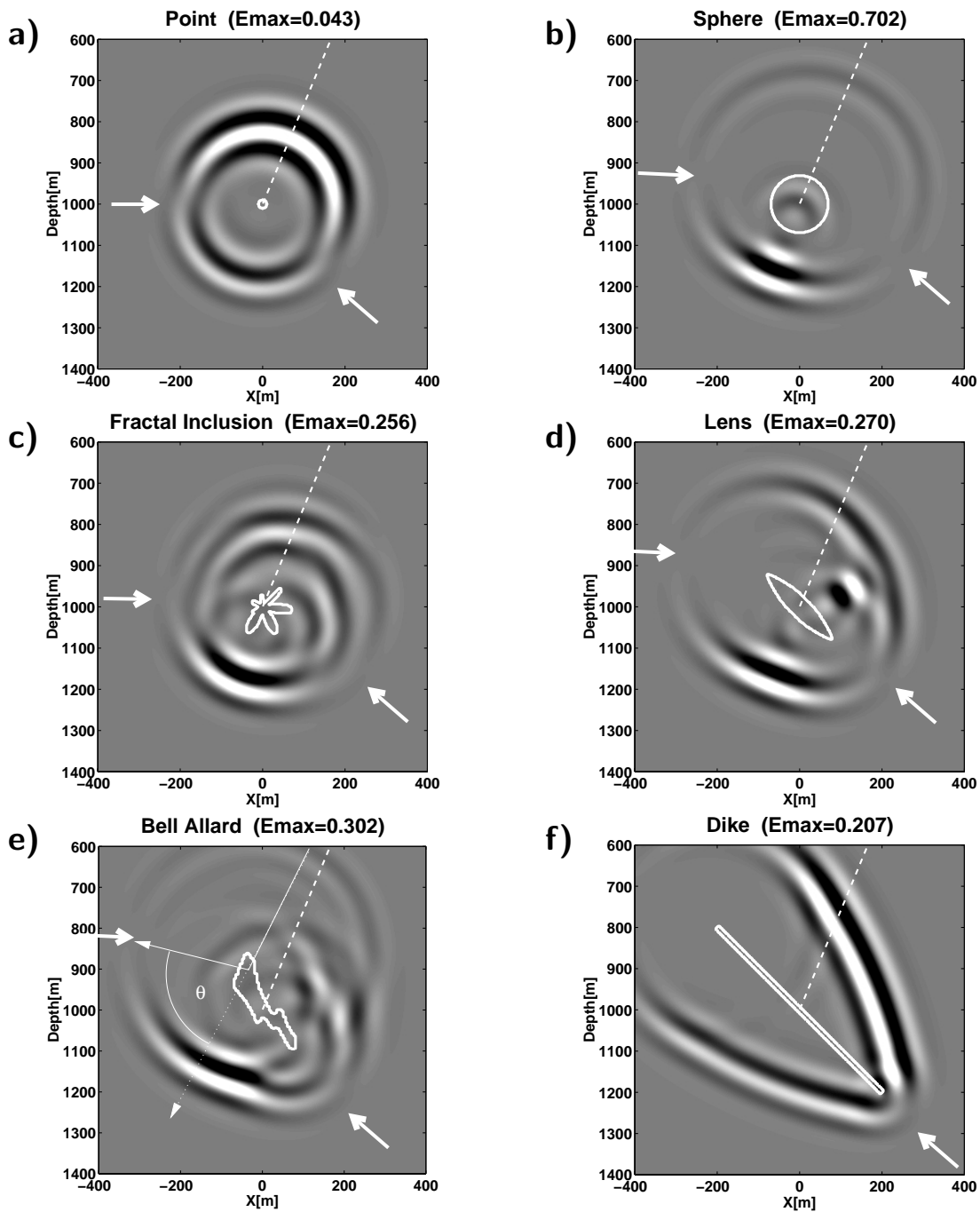


Figure 2.16: Finite Difference snapshots at $T = 0.24s$ of scattered energy of compressional waves for six Sphalerite inclusions in crystalline background with different shapes. The dashed lines indicate the incident ray direction. E_{max} is the maximum energy of a snapshot normalized to the energy of the incident P-wave. Single phase reversals (white arrows) at approximately 76° scattering angle occur irrespective of the shape (Bohlen et al., 2000). Please note that the angle is measured from the scattering center and not from the center of the object, as indicated by the additional lines in the "Bell Allard" example (e).

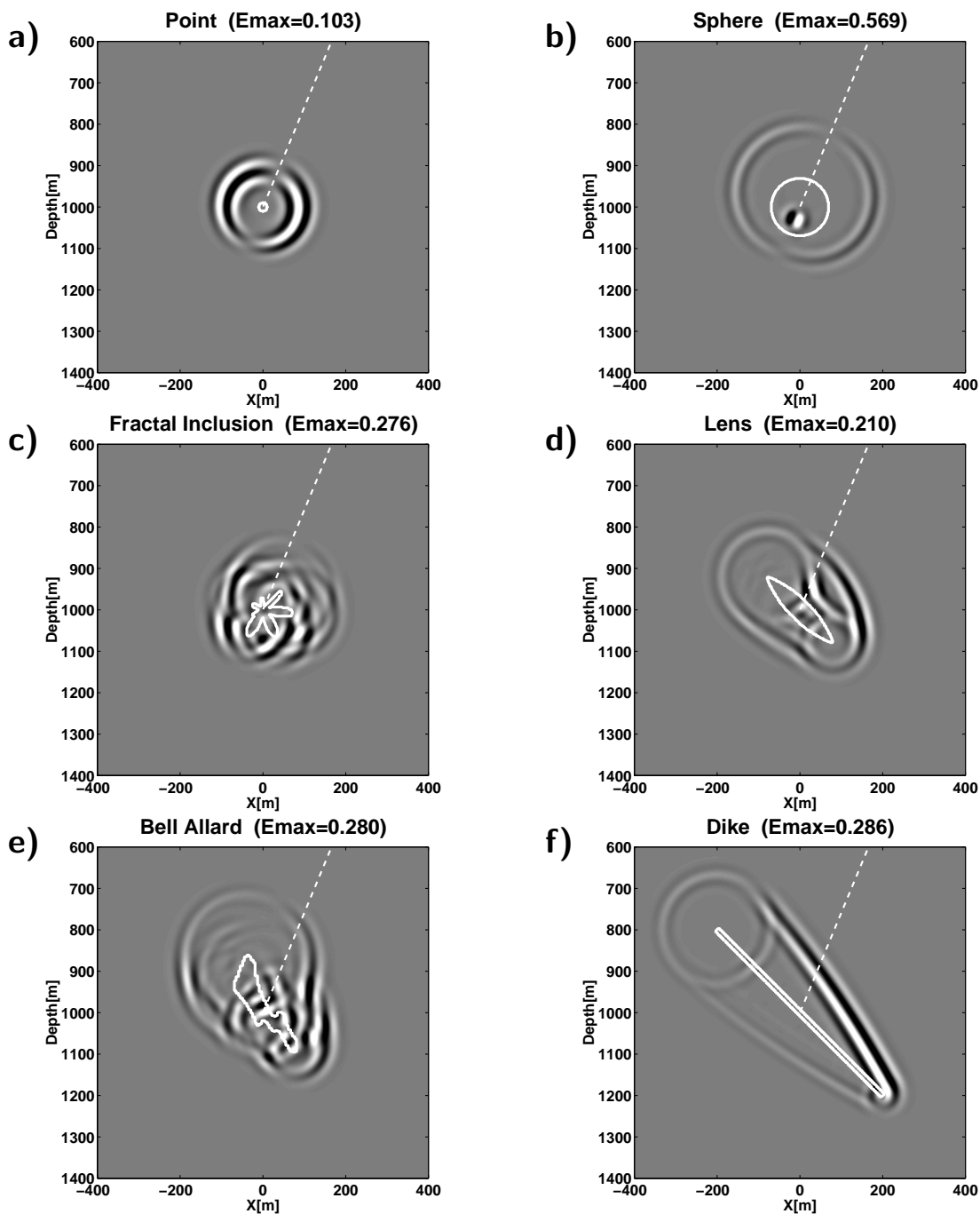


Figure 2.17: Snapshots of scattered energy of shear waves for six spherulite inclusions in crystalline background with different shapes. Please compare with Figure 2.16 (Bohlen et al., 2000).

example on the other hand behaves like a reflector element and thus contributes maximum amplitudes in the direction of the reflection angle. Generally speaking, the complexity of the response strongly depends on the complexity of the inclusions shape e.g. as seen in figure 2.16 c and e. In addition to this, focusing effects cause very different maximum amplitudes as displayed in the individual figures. The very low maximum amplitude of the point scatterer has to be explained by its size, since the scattering amplitudes are proportional to the volume of the inclusion (equation 2.19). All modeled inclusions generate a significant phase reversal (SPR) of scattered $p \rightarrow p$ events (first arrivals) at a scattering angle of approximately 76° (see white arrows in figure 2.16). The phase reversal seems to show slight fluctuations in its angular position. The corresponding $p \rightarrow p$ scattering however, does not take place at the center of the inclusions, but at areas with strong curvature, e.g. at the top of the Bell Allard ore body model (figure 2.16e). The angular position of the SPR in fact agrees quite well with Rayleigh scattering theory, if we assume that scattering takes place at a scattering center, i.e. the position where incident and scattered ray intersect. Measured from these scattering centers the angle of the SPR is found to be 76° with just little error. We thus can conclude, that even for large complex objects the SPR is an overall characteristic dynamic feature which is independent of the shape of the inclusion and only depends on its composition. The above still holds for $p \rightarrow s$ converted wave fields, although S-wave scattering has a higher resolution than P-wave scattering. Structural features of the inclusions thus exhibit a stronger effect on the wave field (figure 2.17 c,d and e). Sphalerite has no SPR for the $p \rightarrow s$ scattering mode. In excellent agreement with Rayleigh scattering theory only geometrical phase reversals at $\theta = 0^\circ$ and $\theta = 180^\circ$ are observed. They are independent of the composition of the scatterer.

Influence of composition Figure 2.19 shows seismograms of the pure scattered wave field for an ellipsoidal inclusion with four different compositions.

The scattered wave field as such again was obtained by taking the difference of the wave fields from a model with and one without scatterer (section 2.1.3). The geometry of the numerical experiment is shown in figure 2.18.

The inclusion was assumed to be situated in a depth of 500 m, rotated 45 degrees about the y-axis and to have a size of 400m x 100m x 200m. The receiver line was chosen to lie parallel to the x-axis and centered about the origin of the y-axis. One shot point was simulated with coordinates $\mathbf{x}_s = (-300, 0, 0)$. Figure 2.19 shows vertical component seismograms of the wave field for a typical gabbro (a), sphalerite (b), galena (c) and pyrite (d), corrected for geometrical spreading and normalized to their maximum amplitudes. The kinematic behavior is comparable for each example. Compressional wave responses can clearly be distinguish from shear wave response by their different apparent velocities.

The complexity of the scattered wave field is shown by the synthetic seismograms. It shows different dynamic characteristics due to diverse compositions of the scatterers.

The source that was modeled in the experiment was purely compressional, but produced a strong shear wave component in the incident wave field by conversion at the free surface. We thus observe not only $p \rightarrow p$ and $p \rightarrow s$ scattering modes (early arrivals in the seismograms), but also $s \rightarrow p$ and $s \rightarrow s$ modes (late arrivals).

Except for the very first arriving $p \rightarrow p$ scattered mode most other modes interfere with each other, which makes the overall picture even more complex. We can however extract

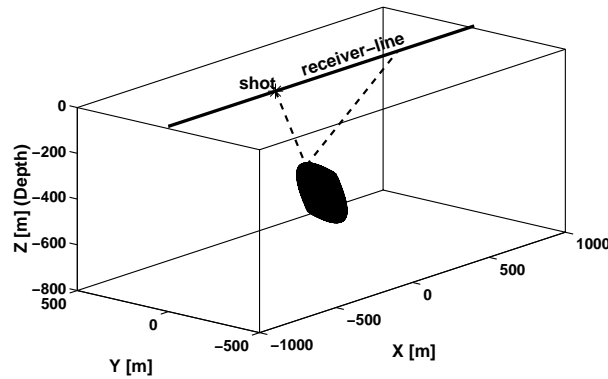


Figure 2.18: 3 D model of an inclusion (black) embedded in a homogeneous crystalline background. See table 2.1 for the considered perturbations. The inclusion is a parabolic lens with a size of $400m \times 100m \times 200m$ in x -, y -, z -direction, respectively. It is rotated 45 degrees about the y -axis, and is centered at a depth of $500m$ (Bohlen et al., 2000).

some general dynamic features from the seismograms. The influence of composition is noticeable, because the distribution of energy to different modes varies for each example. Although every modeled composition supports all possible scattering modes, they are not equally developed. Galena e.g. shows very pronounced $p \rightarrow s$, $s \rightarrow p$ and $s \rightarrow s$ scattering and produces strong reverberations (coda in figure 2.19 c), whereas pyrite and gabbro show more pronounced single scattered modes (i.e. no coda in figure 2.19 a and d). We note that the amplitude distribution observed in all seismograms has a tendency to be higher for traces that are situated in direction perpendicular to the dip of the scatterer. This is most reasonably explained as a focusing effect and thus depends on the shape and not on the composition of the scatterer. From the modeled acquisition geometry we would expect SPR's as predicted by Rayleigh scattering theory (figure 2.7) for Sphalerite and Galena to be found in the range between $x = 0m$ and $x = 1000m$ (figure 2.19b and c). They are difficult to observe, because the seismograms only display the vertical component of modeled seismic sensors. The recorded amplitudes are tuned by the cosine of the incidence angle. As a consequence for a realistic investigation of the angular position of SPR's in recorded seismograms, all three recorded geophone components would have to be projected onto the direction of the scattered ray. This procedure needs a priori information about the position of the scattering center and is not straight forward. Considerations about finding these positions and the treatment of three component seismic data in processing and interpretation of scattered seismic energy will be discussed in section 3.

We can conclude that, although the scattering pattern in the seismograms are quite complex, effects can be isolated that are due to the composition of the scatterer. There are however pronounced dynamic features that are caused by the shape of the scattering inclusion or the geometry of the acquisition geometry and which are not a priori distinguishable from composition effects. Consequently, composition and shape effects will be difficult to distinguish in surface seismic field experiments.

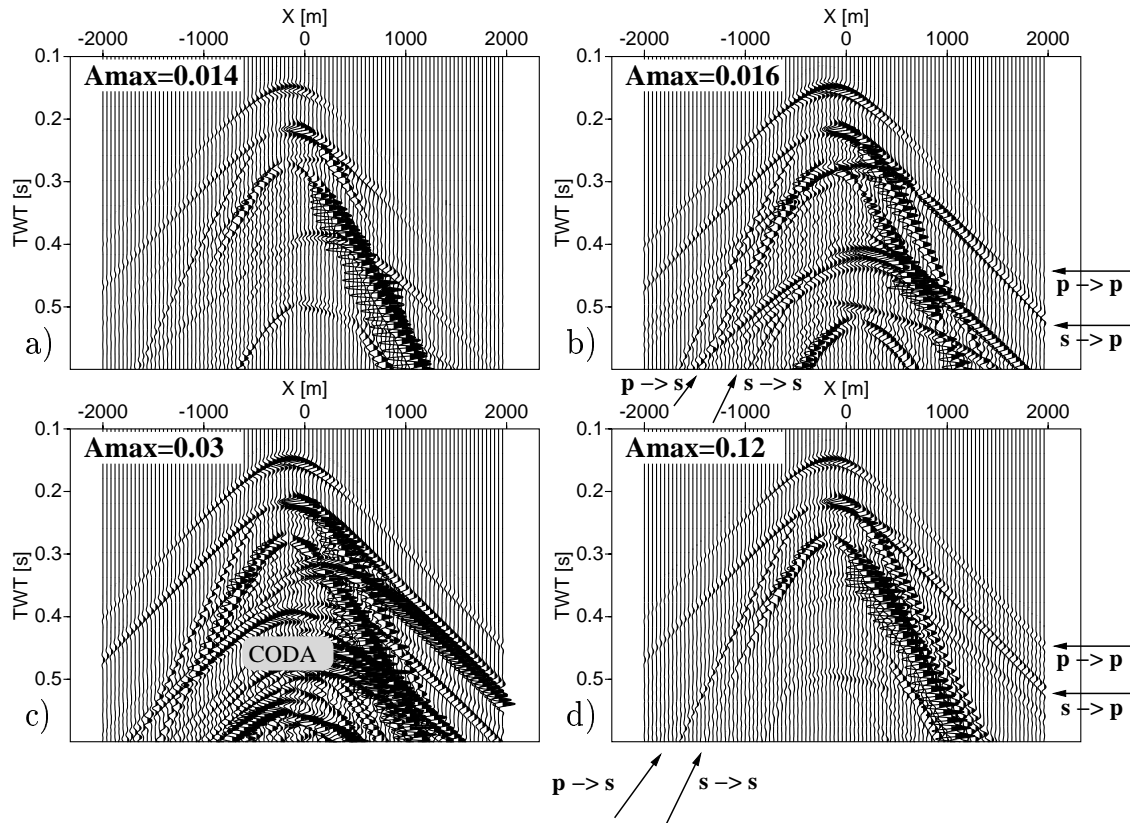


Figure 2.19: Seismograms of the scattered wave field for four different lens shaped scattering objects: gabbro (a), sphalerite (b), galena (c) and pyrite (d), after spherical spreading correction and normalization to maximum amplitude. Dynamic characteristics of scattered wave field change with composition. The modeled source was compressional, but since a significant S-wave was generated at the free surface of the model, not only $p \rightarrow p$ and $p \rightarrow s$, but also $s \rightarrow p$ and $s \rightarrow s$ scattering modes can be observed (Bohlen et al., 2000).

Diffracted wave fields

Diffraction can be regarded as diffusion of seismic energy transversal to the direction of the last regularly reflected ray. The dynamic characteristics of diffractions are described by the weakening function, or diffraction coefficient, which follows e.g. from Edge Wave theory (equation 2.64). The diffraction response itself will have half of the amplitude of the regularly reflected ray in its close vicinity and show a phase reversal of 180° when passing from the illuminated into the shadow zone. In the illuminated zone the phase of the diffraction response is opposite to that of the reflection. The weakening function only depends on frequency and a kinematic parameter, i.e. the travel time difference between a reference ray and the diffracted ray. Since the elastic parameters of the truncated reflector or the edge only enter in the form of the reflection coefficient for the regular ray, no additional information on the composition of the reflector or the edge can be drawn from the dynamics of the diffraction response. Also the phase reversal predicted for the diffracted wave field is merely of geometrical nature. It is worth noting that an isolated diffraction response as

described by the Edge Wave theory is never observed on a seismic section as such, it always is accompanied by the primary wave field, i.e. the reflection, which causes the diffraction.

2.3.2 Kinematic Characteristics of Scattered and Diffracted Wave Fields

Even though dynamic characteristics of the scattered and diffracted wave fields substantially differ, we find that their kinematic behavior is similar. This is due to the fact that both, scattering and diffracting disturbances, can be regarded as secondary sources in the subsurface. The scattering, diffracting response is excited by an incident wave field that travels through the background medium until it reaches the point of perturbation. From this position in space secondary wave fields emanate in all spatial directions. Thus we find for the travel time from the source \mathbf{x}_s via the disturbance \mathbf{x}_0 to the receiver \mathbf{x}_r :

$$t(\mathbf{x}_s, \mathbf{x}_0, \mathbf{x}_r) = t_s(\mathbf{x}_s, \mathbf{x}_0) + t_r(\mathbf{x}_0, \mathbf{x}_r) \quad (2.73)$$

The travel times t_s and t_r depend on the field of wave propagation velocity $v = v(\mathbf{r})$ for incident and scattered or diffracted seismic energy in the background medium. Equation 2.73 is valid for any acquisition geometry and any background medium. In the case of a homogeneous background medium ($v = v_0 = \text{const}$) equation 2.73 can be written as:

$$t = \frac{|\mathbf{x}_s - \mathbf{x}_0|}{v_0} + \frac{|\mathbf{x}_0 - \mathbf{x}_r|}{v_0} \quad (2.74)$$

We also can assume the subsurface velocity structure to change with depth only, so that $v = v(z)$. In this case the travel time from the source \mathbf{x}_s to the disturbance can be written as:

$$t_s = \int_0^{z_0} \frac{dz}{v(z)[1 - (p_s v(z))^2]^{\frac{1}{2}}} \quad (2.75)$$

z_0 is the depth of the disturbance with the source assumed to be located at the surface ($z_s = 0$) and at a horizontal offset Δ_s from the disturbance:

$$\Delta_s = \int_0^{z_0} \frac{p_s v(z) dz}{[1 - (p_s v(z))^2]^{\frac{1}{2}}}. \quad (2.76)$$

p_s denotes the ray parameter which is related to the takeoff angle κ_s at the source by:

$$\kappa_s = \sin^{-1}(p_s v(z = 0)) \quad (2.77)$$

Two analogous integrals can be written for the travel time and horizontal offset between the disturbance and the receiver, assumed to be situated in a depth $z = z_r$:

$$\begin{aligned} t_r &= \int_{z_r}^{z_0} \frac{dz}{v(z)[1 - (p_r v(z))^2]^{\frac{1}{2}}} \\ \Delta_r &= \int_{z_r}^{z_0} \frac{p_r v(z) dz}{[1 - (p_r v(z))^2]^{\frac{1}{2}}} \end{aligned} \quad (2.78)$$

where p_r is the ray parameter for the scattered ray, traveling from the disturbance to the receiver. By this formalism the total travel time from a source situated at the surface to a disturbance in the subsurface and back to a receiver can readily be calculated. The receiver and the source can either be situated in a borehole or at the surface.

For the general case of a velocity field $v = v(\mathbf{r})$ the travel times can be derived by solving the eikonal equation 2.53.

Although the above discussion is strictly valid only for point scatterers and planar diffractors, it can be concluded that scattered and diffracted wave fields will show no characteristic differences in their kinematic behavior. It should thus not be possible to distinguish both effects by their kinematics.

2.4 Conclusions

Even though convenient, classification approaches using the Born approximation suffer from its limited validity, and cannot generally be applied. Instead a different classification approach was followed in the above discussion:

Scattering from small scale seismic inclusions not only depends on their composition, but also on the composition of the background medium. The material parameters of the object, i.e. seismic velocities and mass density and also those of the background medium can be assigned to a point in a *material parameter space*. The absolute value of the difference between the background parameter vector and the scattering objects parameter vector is called a *scattering situation*. This scattering situation can be classified by analyzing the amplitude versus scattering angle (AVSA) behavior of the scattered seismic wave field. When observed on seismic sections, a significant phase reversal (SPR) within the first arriving scattered seismic wave field can be utilized as a robust criterion in order to classify the current scattering situation. In order to enhance the signal to noise ratio, it is probably necessary to stack the recorded scattered seismic wave field within a common scattering angle gather as will be described in section 3.1.3.

The concept of SPR classification can in part be extended to the case of scattering from large complex objects with arbitrary contrast in their material parameters compared to the background medium. It can be assumed that scattering takes place at *scattering centers*, which behave in good approximation like Rayleigh scatterers, as has been shown by FD modeling. The shape of large objects however has a significant impact on the dynamics of the full scattered wave field, and it can not be ignored. Also scattering and diffraction can be intertwined and dynamical analysis may be difficult. An AVSA analysis demands the knowledge about the position of the scattering center, for which it would be necessary to image the scatterer as such. First approaches to the imaging of scatterers on the cost of reflectors will be presented in chapter 3.

The equality of the kinematic characteristics of the scattered and diffracted wave field makes it impossible to distinguish between them. It will thus be a challenge to new seismic processing approaches to include their different dynamic behavior into imaging procedures in order to separate them. The difference in the kinematic characteristics of the reflected compared to the scattered, diffracted seismic wave field is an excellent chance to distinguish

between them, as will be discussed in section 3.2.2.

Diffraction represents the diffusion processes of reflected seismic energy into the zones close to the last regularly reflected seismic ray. Thus diffractions from interrupted, otherwise continuous seismic reflectors have to be expected to be stronger than pure scattering from structures with comparable parameter perturbations.

Seismic acquisition and processing should thus focus on acquiring and preserving as much scattered energy as possible. In any case the phase information of the scattered wave field has to be preserved since it is vital to provide the possibility of AVSA analysis.

The acquisition layout governs the accessible range of scattering angles and their coverage in seismic measurements. Thus, when planning a seismic survey that is aimed towards detecting and interpreting scattering from isolated inclusions a layout with sufficient angular coverage has to be used. In three component seismic data processing it might also be necessary to project the recorded scattered wave field onto the direction of the scattered ray in order to clearly emphasise the position of the SPR. In order to do so, the position of the scattering inclusion or the scattering center has to be known.

Chapter 3

Methodology

Scattered seismic energy is weak compared to reflections from laterally continuous subsurface structures of comparable impedance contrast. Detecting scattered energy, resolving shape and composition of scattering objects has to focus on gaining and preserving as much energy as possible throughout the seismic processing sequence.

Modern seismic imaging techniques which among others include pre- and poststack migration and CMP processing, generally assume that the subsurface is composed from laterally continuous lithological contacts. CMP-Processing has evolved to become the most robust and best known processing methodology in controlled source reflection seismology. It is applied to generate zero offset equivalent seismic sections and to enhance the signal to noise ratio of the reflection response. The signature of scattered or diffracted seismic events is attenuated. Thus it is necessary to develop new processing techniques that account for the kinematic and dynamic characteristics of the scattered wave field.

In the following chapter, I will describe several different processing approaches that utilize knowledge gained from elastic scattering theory in order to enhance scattered seismic energy on seismic sections:

The chapter consists of two major sections. At first (section 3.1), I will focus on gather oriented processing methods. Gathering traces of common geometrical attributes and stacking after suitable travel time correction is aimed towards increasing the signal to noise ratio of the seismic response.

The most prominent example is the CDP or CMP processing method, which will be discussed in the first section (3.1.1). The CDP method is not suited for the enhancement of scattered energy on seismic sections. Thus several different other methods were developed which will be discussed subsequently.

Section 3.1.2 describes the Scattering Enhancement (SES) or Common Profile Point (CPP) stacking method, which uses a statical travel time correction tailored to correct for the move out of a seismic scattering response. Based on a similar travel time correction but with gathering traces of common scattering angle is the Common Scattering Angle (CSA) stacking method, which will be described thereafter (section 3.1.3). To finalize this first section of the following chapter, I will introduce a Common Offset Filter method, taking advantage of the kinematic characteristics of scattering in order to suppress the signature from direct arriving and reflected seismic events (section 3.1.4).

The second main section is dedicated to the enhancement of the image of seismic scatterers by utilizing prestack processing methods (section 3.2). As opposed to the methods described above, prestack seismic processing omits the step of gathering traces of common geometrical attributes. An image of the subsurface is directly build from the available seismic data by migration. A variety of prestack migration methods exist. Diffraction Stack Migration (DSM) is reviewed in section 3.2.1 to build the basis of two newly developed prestack migration approaches, that focus on enhancing the image of an isolated seismic scatterer over that of continuous reflectors. It is especially suited for this task, because it is derived from a simple geometrical interpretation of Huygens principle, which closely relates to the scattering process.

Diffraction Coherency Migration (DCM) will be introduced in section 3.2.2. The method is based on the concept of DSM. It measures the coherency of recorded seismic signals along the scattering signature in seismic data space enhancing the migrated image of subsurface discontinuities.

Especially in VSP experiments the number of applied seismic sources and receivers is limited. The image resulting from any applicable migration procedure will show a certain degree of ambiguity, if only the scalar wave field is recorded in VSP surveys. Imaging ambiguity in DCM/DSM migration is thus discussed in section 3.2.3.

In the case of three component registration this ambiguity can significantly be reduced by incorporating polarization information in the migration procedure, as it is implemented in Diffraction Polarization Migration (DPM) and will be described in section 3.2.4.

3.1 Gather Oriented Stacking Methods

The use of gather oriented stacking methods is motivated by the desire to enhance the scattering hyperbola as a characteristic signature e.g. observed on CMP processed zero offset sections. A scattering hyperbola is recognized much easier than a collapsed point, as it would be produced by migration.

The classical CMP approach, however, shows some major drawbacks in reproducing the scattering signature. The approximation to a zero offset section, which is generated by classical CMP processing (Mayne, 1962), produces a subsurface representation, which shows reflection and diffraction response in the same display. It thus sometimes serves as the very first indicator for the presence of scatterers or subsurface discontinuities. The CMP approach, however, shows some major drawbacks in reproducing the scattering signature. In the following section, I will introduce several different gather orientated processing approaches, which are aimed towards enhancing the scattering signature over that of reflections.

In order to investigate the performance of these methods, two different synthetic marine models and one crustal model were calculated using the Born approximation modeling software package BMOD 3D as provided by Eaton (1997). The material parameters for the modeled scatterers and the background media are listed in table 3.1.

For the two marine examples unconsolidated sediments were assumed as background medium. The first marine model was designed to resemble a metal sphere of $1m$ diameter situated $2.5m$ below the $20m$ deep seafloor. The second marine model was a sphere shaped gas

Material parameters	v_p [m/s]	v_s [m/s]	ρ [kg/m ³]
Marin examples:			
Gas accumulation	1000	50	1000
Metal object	5890	3200	7100
Seafloor	2000	50	1100
Background (uncons. sediments)	1550	50	1000
Crustal example:			
Ore inclusion	5670	3360	4125
Background (crystalline crust)	6300	3200	2750

Table 3.1: *In order to illustrate the performance of the processing approaches discussed in the following section, three different model seismic data sets were generated. In two marine examples a sphere shaped inclusion, a gas accumulation and a metal object were assumed to be situated below the seafloor. In a third example, a spherical volcanogenic ore inclusion embedded in a crystalline host rock was modeled.*

accumulation positioned as above. A Ricker wavelet with a center frequency of $f_c = 800Hz$ was used as source signal. Traces were simulated to be recorded by a moving streamer array with 48 channels and $2m$ group separation. A constant offset between source and first receiver was assumed. The shot interval was $\Delta x_s = 2m$. Both datasets were modeled to represent a typical high frequency multichannel marine seismic survey, as it can be related to the marine seismic case histories described in section 4.1.

In the crustal example a Ricker wavelet with a center frequency of $f_c = 50Hz$ was used. A sphere shaped scatterer of $40m$ radius situated in $500m$ depth was assumed to be embedded in a crystalline host rock background. A shot spread ($2000m$ range) centered above the scatterer was simulated. The model relates to the crustal seismic case histories discussed in section 4.2.

It must be said that the Born approximation is not strictly valid in all considered examples. Especially in case of the assumed metal sphere, dynamic characteristics of the scattered wave field will strongly deviate from the exact solution. Amplitude information was thus only used to investigate the ratio of processing input to output. The orebody model, however, should be in good agreement with the requirements for Born scattering (please refer to figure 2.12). Whenever modeled travel time information was used, the obtained results are nonetheless valid, because travel time calculations are not based on the Born approximation in BMOD 3D.

3.1.1 The Common Midpoint Stacking Method

The CMP processing approach is a very robust and widely used method to enhance reflected seismic energy in multichannel reflection seismic recordings. Seismic traces are sorted into gathers of common midpoints (CMP). After being corrected for travel time differences caused by different source-receiver offsets (NMO correction), they are stacked to enhance the signal-to-noise-ratio of the resulting section (see e.g. Yilmaz, 1987). The final CMP

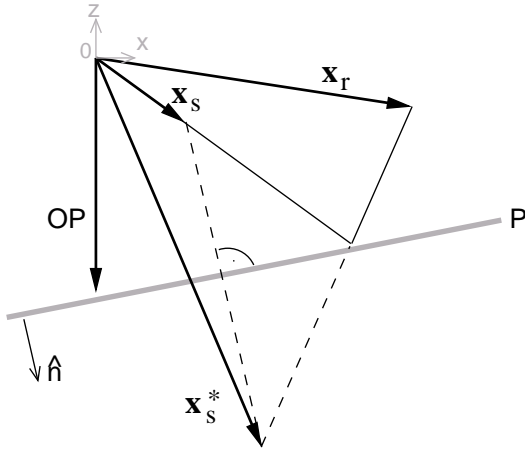


Figure 3.1: Vector diagram of a generic seismic reflection scenario. The reflection response for an arbitrarily dipping plane P , can be calculated using the image point method. The reflecting plane is defined by a point \mathbf{OP} on the plane and a normal vector \hat{n} (O , origin). A ray emitted from the source at \mathbf{x}_s will be reflected to the receiver position \mathbf{x}_r . The position of the reflecting point on the surface of P is found by connecting the image source at \mathbf{x}_{s^*} (which has the same perpendicular distance to P as \mathbf{x}_s) with \mathbf{x}_r .

processed section is a good approximation of a zero offset experiment, with coinciding positions for source and receiver. Even though applied travel time corrections are calculated under the assumption that all contributions to the seismogram emanate from reflecting interfaces, usually scattering/diffraction signatures can be observed in form of diffraction hyperbolas in the resulting section. This is due to the fact that for small source-receiver offsets the differences in travel time for a horizontally layered reflector and a scatterer or a diffracting edge are similar. It can be shown that up to a certain degree even the dynamic behavior of diffractions is correctly accounted for in a CMP stacked section (Berryhill, 1977). However, with increasing distance between source and receiver differences in travel time become more severe, so that the applied travel time correction and the increasing NMO stretch will prevent far offset scattered energy from being stacked correctly. As was shown in section 2.3.1 scattered seismic energy can significantly contribute to the far offset domain and will be lost, if the travel time corrections applied in seismic processing are not exact. For a generic reflection scenario the misfit between the commonly applied NMO correction and a correction that would be necessary to correct for move out of a scattered seismic signal can be calculated (Jäger, 1998). Figure 3.1 shows the geometry of the problem. The travel time t_r for a ray emanating from a source \mathbf{x}_s , being reflected at a plane P to the receiver \mathbf{x}_r can be calculated by assuming an image source in \mathbf{x}_{s^*} (see e.g. in Cosma & Heikkinen, 1996). P is parameterized by the normal vector \hat{n} and a point \mathbf{OP} . For a homogeneous background medium we find for t_r :

$$t_r(\mathbf{x}_s, \mathbf{x}_r, \hat{n}) = \frac{|\mathbf{x}_r - \mathbf{x}_s + 2\mathbf{x}_{sn} - 2\mathbf{OP}_n|}{c_0} \quad (3.1)$$

\mathbf{x}_{sn} is the projection of \mathbf{x}_s on \hat{n} : $\mathbf{x}_{sn} = \hat{n}(\hat{n} \cdot \mathbf{x}_s)$ and \mathbf{OP}_n results from the projection of \mathbf{OP} on \hat{n} : $\mathbf{OP}_n = \hat{n}(\hat{n} \cdot \mathbf{OP})$. The travel time for the scattered/diffracted wave field is repeated here for convenience (equation 2.74):

$$t_s(\mathbf{x}_s, \mathbf{x}_r, \mathbf{x}_0) = \frac{|\mathbf{x}_r - \mathbf{x}_0| + |\mathbf{x}_0 - \mathbf{x}_s|}{c_0} \quad (3.2)$$

The most simple case for which we can specialize equation 3.1 is the case of a horizontal reflector as depicted in figure 3.2. The geometry for a scatterer D assumed to lie in P is

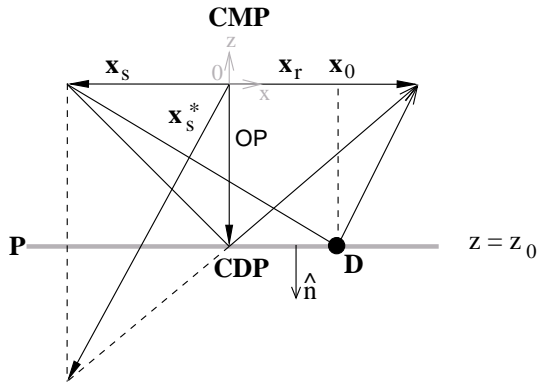


Figure 3.2: Special case of figure 3.1. The common midpoint (CMP) is defined as the lateral position half way between the source x_s and the receiver x_r . It is located exactly above the common depth point (CDP). The coordinate system was shifted to coincide with the CMP. In common CDP processing a normal move out (NMO) correction is applied to correct for the travel time difference caused by increasing source receiver offsets. In order to correct the NMO of a scattering response, generally a different correction time has to be assumed.

also shown.

Equations 3.1 and 3.2 for this case read:

$$\begin{aligned}
 t_r &= \frac{|\mathbf{x}_r - \mathbf{x}_s - 2\mathbf{OP}_n|}{c_0} \\
 &= \frac{\sqrt{(x_r - x_s)^2 + 4z_0^2}}{c_0}
 \end{aligned} \tag{3.3}$$

and

$$t_s = \frac{\sqrt{(x_r - x_0)^2 + z_0^2} + \sqrt{(x_s - x_0)^2 + z_0^2}}{c_0} \tag{3.4}$$

The normal move out correction for either the scattered and reflected seismic rays can now be defined as:

$$t_{rNMO} = t_r - t_{r_0} \tag{3.5}$$

and

$$t_{sNMO} = t_s - t_{s_0}, \tag{3.6}$$

For the common midpoint coordinate system (CMP=0), we find:

$$t_{r_0} = \frac{|2\mathbf{OP}_n|}{c_0} = \frac{2z_0}{c_0} \tag{3.7}$$

and

$$t_{s_0} = 2 \frac{\sqrt{x_0^2 + z_0^2}}{c_0} \quad (3.8)$$

Equations 3.7 and 3.8 are the zero offset two way travel times to and from the reflector and the scatterer respectively. $t_{r_{NMO}}$ equals $t_{s_{NMO}}$ only in two cases:

1. $x_0 = 0$, i.e. when the midpoint between \mathbf{x}_r and \mathbf{x}_s (CMP) and the lateral position of the scatterer coincide.
2. $x_s = x_r$, i.e. the zero offset case where both $t_{r_{NMO}}$ and $t_{s_{NMO}}$ are zero and no normal move out correction has to be applied in either case.

Figure 3.3 shows the difference between both corrections (NMO misfit) along with the NMO stretch factor $\Delta f/f = t_r/t_{r_0}$. A scatterer was assumed to be situated in a homogeneous background medium at 1500m depth. A background medium velocity $c_0 = 6000m/s$ was chosen to resemble the situation found for the crystalline crust.

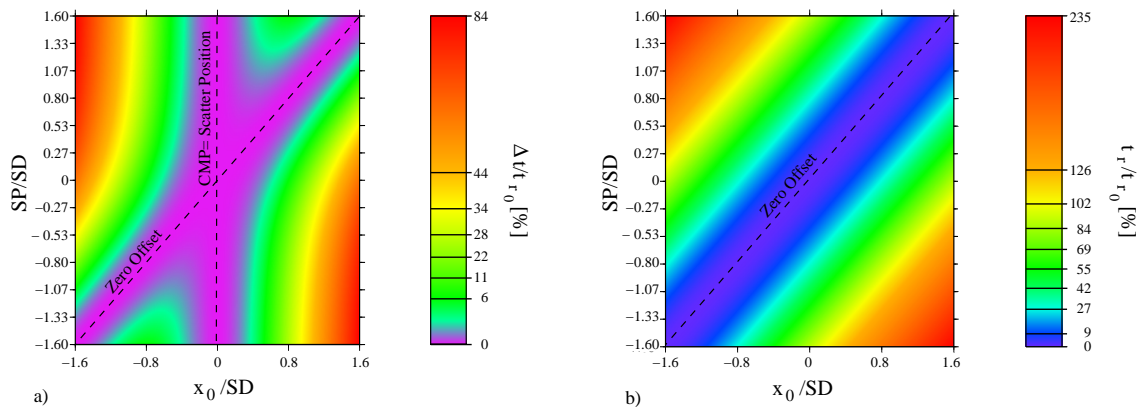


Figure 3.3: a) Difference Δt between $t_{s_{NMO}}$ and common $t_{r_{NMO}}$ normalized to minimal two way reflector travel time t_{r_0} and b) NMO-Stretch for common reflection NMO in percent as a function of lateral scatterer (x_0) and shot point (SP) position. Considered is the generic case of a horizontal reflector embedded in a homogeneous background medium ($c_0 = 6000m/s$). Positions are normalized to scatterer depth (SD) and given in the CMP coordinate system (Jäger, 1998).

The plots show the individual quantities normalized to t_{r_0} as a function of shot point (SP) and scatterer positions (x_0) measured in the CMP coordinate system and given in units of scatterer/reflector depth (SD).

CDP processing and stack will not enhance the far offset scattered or diffracted wave field contributions due to the misfit in the applied NMO correction. This problem is in part accounted for in DMO processing (see e.g. Yilmaz, 1987). But still, NMO stretch will occur and valuable portions of the scattered wave field will be lost.

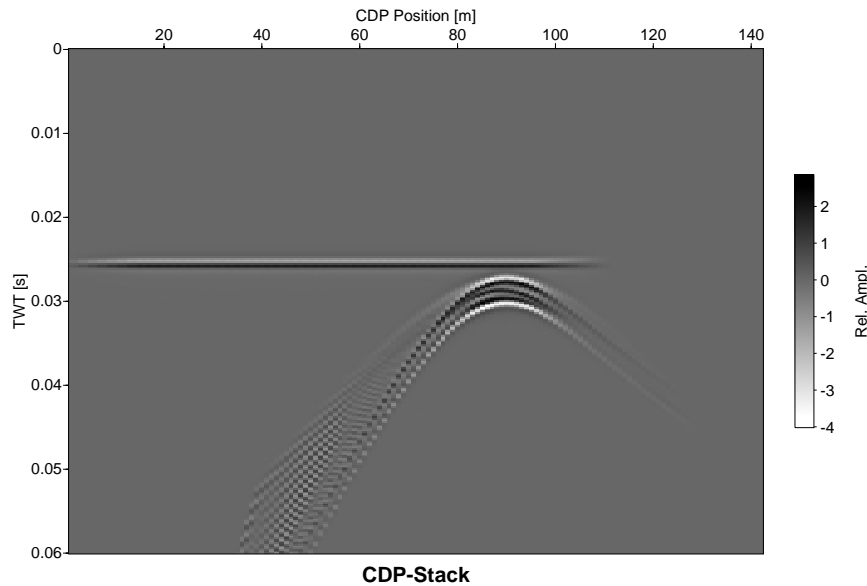


Figure 3.4: *CMP stacked seismic section of a simple travelt ime model. A seafloor reflection was modeled along with a scattering response from a solid metal sphere using the Born approximation (Eaton, 1997). Due to NMO correction misfit the far flanks of the scattering hyperbola are not stacked in phase. The seafloor, as expected, was mapped properly.*

In order to illustrate the effects of the travel time correction misfit, a travel time simulation was carried out for either the marine metal object and gas scattering models as introduced above.

Figure 3.4 shows the CDP processed zero offset stack for the metal object model. The scattering response of the sphere is very strong compared to the seafloor reflection. The example was chosen, to illustrate the drawbacks of the CMP processing method regarding the treatment of seismic scattering:

The far flanks of the scattering response are not stacked in phase due to the misfit caused by the applied reflection NMO travel time correction. The only portion of the scattering response that was "imaged" sufficiently, is the apex of the hyperbola, which results from stacking near offset contributions of the scattered seismic wave field. Energy scattered to the far offset is lost.

In a real seismic experiment the scattering response in most cases can be expected to be much weaker, as depicted in figure 3.5 which shows the same result for the gas inclusion model. The reflection response "overpowers" the scattering response and it can hardly be seen in the section ($u_{Scat}^{max}/u_{Ref}^{max} \approx 0.2$).

It is worth noting that the scattering response can be enhanced in a CMP section by applying a gradient velocity field in the NMO correction. In such a case, however, reflections with travel times comparable to those of the scattering response far flanks will not be imaged properly (e.g. Jäger, 1998).

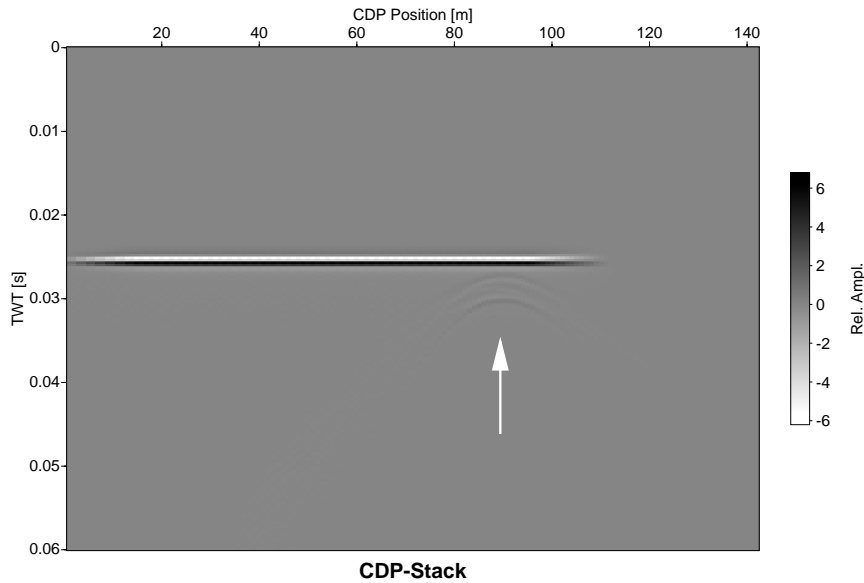


Figure 3.5: CMP stacked seismic section of a simple traveltime gas inclusion model. The scattering response (indicated by the arrow) of the modeled gas inclusion is weak and "overpowered" by the strong reflection response. It can hardly be seen in the section ($u_{Scat}^{max}/u_{Ref}^{max} \approx 0.2$). Please compare with figure 3.4.

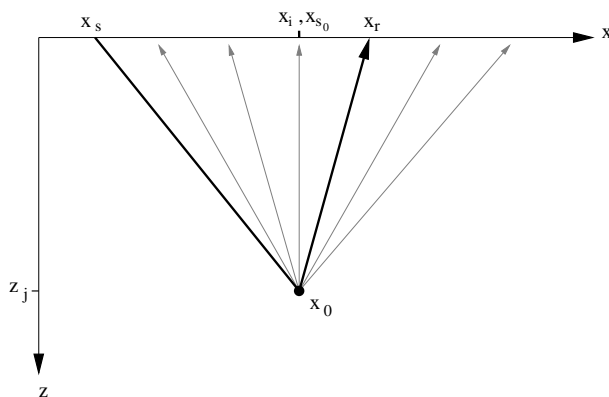


Figure 3.6: Geometry of a generic surface seismic experiment for a homogeneous background medium. The correct travel time correction to generate a SES-stack depends on the possible position $x_0 = (x_i, z_j)$ of a scatterer.

The above examples illustrate the need for a processing approach that on one hand enhances the scattering response by applying an specific scattering NMO correction and on the other hand suppresses the usually strong response from layered seismic interfaces.

3.1.2 A Common Shot Gather Method: Scattering Enhancement Stack

As illustrated above, the CMP processing approach can destroy the far flanks of the scattering response due to a misfit in NMO correction and NMO stretch. The aim of avoiding these drawbacks can readily be met by applying corrections adapted to the specific scat-

tered wave field travel times.

I will now describe the method of the so called scattering enhancement stack (SES). It is applicable to land reflection seismic surveys and can easily be adapted to the case of marine reflection seismic applications. We start with the assumption of a two dimensional land seismic model with constant background velocity $c(\mathbf{x}) = c_0$. The adaption to models with depth varying velocity or even more complex situations is straight forward. The method will subsequently be adapted to a marine acquisition geometry.

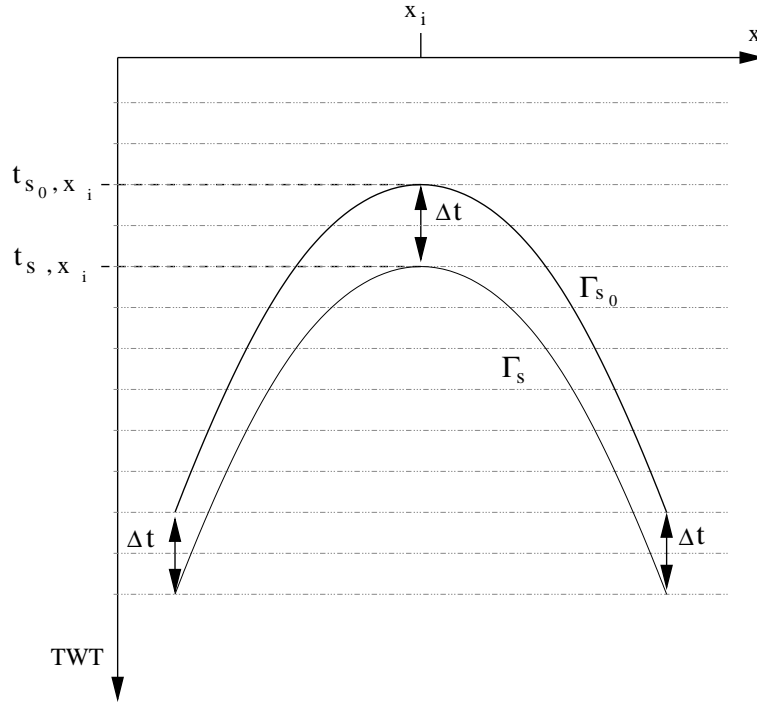


Figure 3.7: The time shift $\Delta t(x_i, x_s)$ of the scattering hyperbola defined as the difference in apex travel time between Γ_{s_0} and Γ_s , is constant for all receiver positions x_r . The shape $d\Gamma/dx_r$ of the scattering signature does not depend on the location of the shot point.

Figure 3.6 shows the geometry of this scattering problem. A spread of geophones is assumed to be laid out at the surface at their horizontal position $\mathbf{r} = (x_r, 0)$ with a number of shot points fired from their positions $\mathbf{s} = (x_s, 0)$. The scatterer location is $\mathbf{x}_0 = (x_i, z_j)$. The scattering travel time curve Γ in a shot gather, i.e. the recorded amplitude field $f_{s_k}(x_r, t)$, is a function of the velocity model $c(\mathbf{x})$, the location of the scatterer and the shot/receiver locations:

$$\Gamma = \Gamma(x_r, x_s, x_i, z_j, c(\mathbf{x})) \tag{3.9}$$

The energy emanating from \mathbf{x}_0 is distributed along Γ . For a homogeneous background medium $\Gamma(x_r, t)$ in f_{s_k} has the form of a hyperbola with its apex (position of minimum travel time) at x_i . If the shot location equals the lateral position of the scatterer, i.e. $x_s = x_i$ the apex travel time is calculated to be:

$$t_{min} = 2t_{s_0, x_i} \quad (3.10)$$

where t_{s_0, x_i} is the travel time from \mathbf{x}_{s_0} to \mathbf{x}_0 . If the shot is not located above the scatterer, the apex travel time and thus the complete travel time curve Γ will be shifted by:

$$\Delta t(x_i, x_s) = t_{s, x_i} - t_{s_0, x_i} \quad (3.11)$$

Please note that the shape $d\Gamma/dx_r$ of the travel time curve does not depend on the location of the shot. In other words: a variation in the shot location will only lead to a time shift Δt of Γ . This shift for a given shot location x_s is a constant for all receiver locations x_r (figure 3.7).

In order to stack the scattering response found in individual shot gathers, knowledge about the explicit shape of Γ is thus not required and only a correction for the shift Δt has to be applied. In a homogeneous background medium Δt can be calculated to be:

$$\Delta t(x_i, x_s) = \frac{1}{c_0} \left(\sqrt{z_j^2 + (x_s - x_i)^2} - z_j \right) \quad (3.12)$$

The rule for the stack then reads:

$$F_{SES}(x_r, t, x_i, z_j) = \sum_{k=1}^m f_{s_k}(x_r, t + \Delta t(x_i, x_s)) \quad (3.13)$$

where F_{SES} is the final SES-stacked section and f_{s_k} are the individual shot gathers each shifted by Δt and m is the number of shots. F_{SES} still depends on the scatterer position (x_i, z_j) and the explicit form of Δt . The position of the scatterer is generally unknown, so that x_i and z_j have to be varied (in a systematic fashion or using an optimization algorithm) until the stacked amplitude in F_{SES} is maximized. This maximum can be evaluated by calculating the total power of the stacked section (like e.g. proposed by Ronen and Clearbout, 1985) or since we intentionally tried to keep up and enhance the characteristic scattering response with the SES method, by interactive human decision (Rechenberg, 1994; Schwefel, 1995).

The discussion can readily be adapted to the case of marine seismic acquisition layouts, where usually the source and each receiver are moving and towed in a fixed distance to each other and to the boat. Γ will experience not only a temporal shift Δt in the individual shot gathers, but also will "move" sideways by the spatial shot interval Δx_s . This is due to the fact that the receivers are moving across the lateral position of the scatterer x_i . Every receiver will have a new position $x_{r'}$ which is related to the shot position by:

$$x_{r'} = x_s - \Delta x_{s,r} \quad (3.14)$$

where $\Delta x_{s,r}$ is the fixed distance between x_s and $x_{r'}$. Also correcting for this effect the stacking rule now reads:

$$F_{SES}(x_r, t, x_i, z_j) = \sum_{k=1}^m f_{s_k}(x_s - \Delta x_{s,r}, t + \Delta t(x_i, x_s)) \quad (3.15)$$

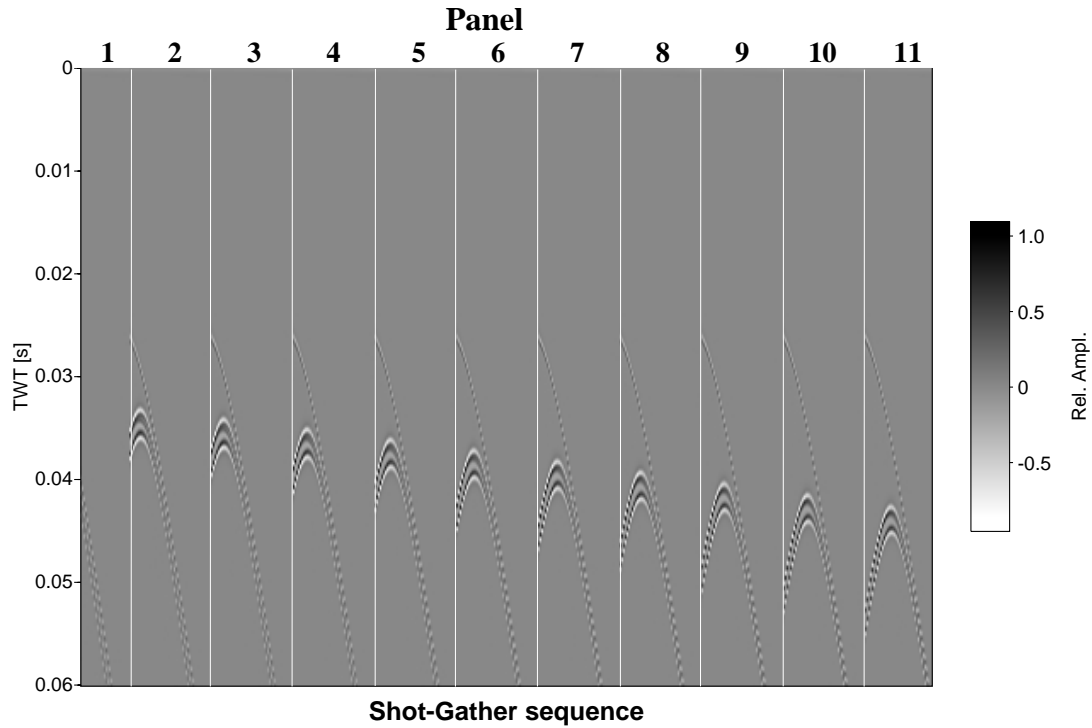


Figure 3.8: Sequence of shot gathers illustrating the temporal τ and lateral shift Δx_s due to the moving acquisition layout in a marine seismic survey. Please note, that the flanks of the scattering response show variable coverage and amplitudes from shot to shot.

Figure 3.8 shows the individual shot gathers $f_{s_k}(x_r, t)$ for the metal sphere model described in section 3.1. The temporal and lateral shifts are evident. Please note that since Γ “moves“ in each shot gather by an amount of Δx_s to the side also the flanks of the scattering response do. Thus, maximum coverage is only achieved for the apex itself. In the final section $F_{SES}(x_r, t, x_i, z_j)$, depicted in figure 3.9, we thus observe that the far flanks show much weaker amplitudes than the apex.

The complete dataset was normalized to one before stacking . We now observe a maximum relative amplitude of 30 in the SES stack, which is $30/4 = 7.5$ times the stacked amplitude of the CMP stack. Although the stacking success is superior to that found for the CMP stack, the lateral resolution r_x of the SES stack is only $r_x = 2m$ which is exactly the spatial shot interval and has to be compared with $r_x = 1m$ for the CMP stack (please compare with figure 3.4).

As we have expected most of the energy coming from the reflector is smeared out over the SES stack, which is due to the specific travel time correction applied. In the far offset range, the travel time for the scattering response and the modeled sea floor reflection approach asymptotically. This effect is generally observed for scattering and reflecting interfaces that are situated close to each other. In this case it results in the fact, that in the SES stack part of the signatures flanks is immersed in reflector noise. Figure 3.10 shows the result for

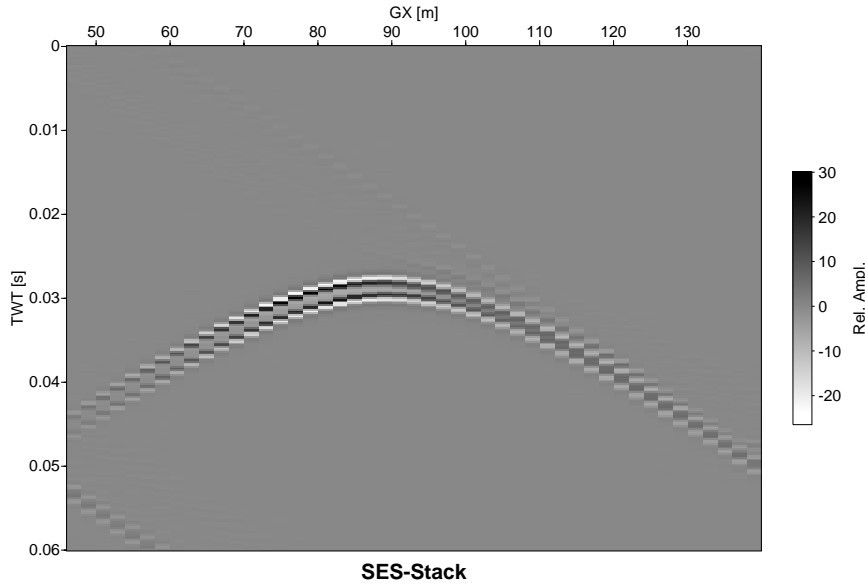


Figure 3.9: Resulting SES stack from the metal object model. The applied travel time correction and SES stack has enhanced the scattering response over that of the modeled seafloor reflection response. The maximum stacked amplitude is 7.5 times that of common CMP processing and stack. Please note that the lateral resolution of the SES stack equals the spatial shot interval.

the modeled gas accumulation.

In contrast to the CMP stack (figure 3.5) we now clearly see the scattering response, although the disturbance due to reflector noise naturally is much more severe than in figure 3.9.

It should be mentioned that the SES method can be implemented in complete analogy in the common receiver gather domain (f_{r_k}). Due to the movement of receivers in marine acquisition geometries the notion "common receiver" actually refers to gathers off common profile points (CPP's). The SES method in the case of a marine application will thus be called CPP method. Figure 3.11 shows the analog acquisition geometry for comparison with figure 3.6.

Receivers positioned in x_r now play the role of the shot points and vice versa. In each common receiver gather we will find a scattering travel time curve $\Gamma = \Gamma(x_s, x_r, x_i, z_j, c(\mathbf{x}))$. Γ will have its minimum apex travel time in the gather formed for the receiver positioned exactly above the scatterer $x_r = x_i$ (please compare with equation 3.10 ff):

$$t_{min} = 2 \cdot t_{r_0, x_i} \quad (3.16)$$

and will experience a shift of

$$\Delta t(x_i, x_r) = t_{r, x_i} - t_{r_0, x_i} \quad (3.17)$$

so that for a homogeneous background medium Δt can be calculated to be:

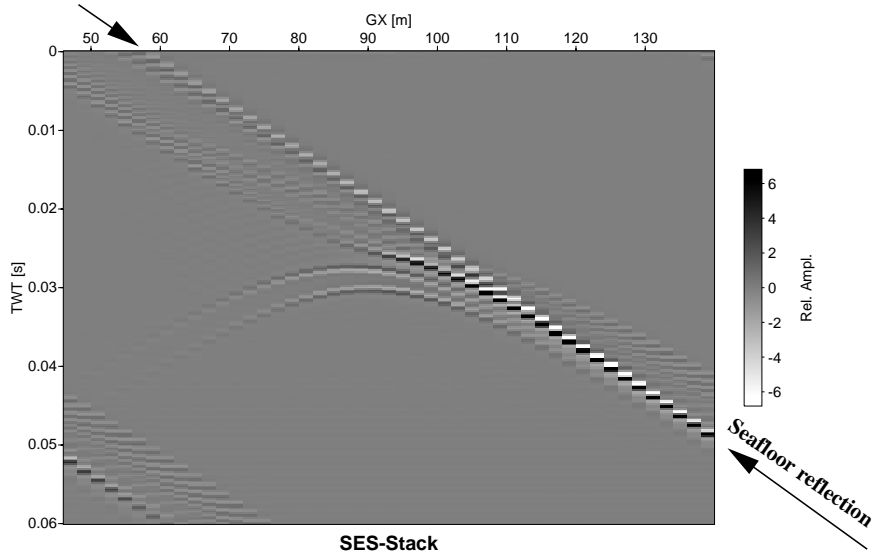


Figure 3.10: SES stacking result from the modeled gas accumulation. Compared to figure 3.5, the gas diffraction signature is now obviously enhanced. The modeled seafloor reflection contributes as smeared noise to the section. Please see also figure 3.9.

$$\Delta t(x_i, x_r) = \frac{1}{c_0} \left[\sqrt{z_j^2 + (x_r - x_i)^2} - z_j \right] \quad (3.18)$$

The stacking rule for the land seismic application then reads:

$$F_{CPP}(x_s, t, x_i, z_j) = \sum_{k=1}^m f_{r_k}(x_s, t + \Delta t(x_i, x_r)) \quad (3.19)$$

which for marine applications will be:

$$F_{CPP}(x_s, t, x_i, z_j) = \sum_{k=1}^m f_{r_k}(x_r + \Delta x_{s,r}, t + \Delta t(x_i, x_r)) \quad (3.20)$$

The SES stacking method has two major drawbacks. First, it only can be used to interpret one scattering response at a time and second, it does not account for the dynamic behavior of the scattering response such as amplitude and phase variations with scattering angle. As discussed in section 2.3.1 depending on the scattering situation it is not unlikely to find complete phase reversals in the scattered wave field along Γ , which would cause destructive interference of the amplitudes in the resulting SES stack.

In the following section a gather orientated processing method which accounts for the dynamic characteristics of the scattering response will be discussed.

3.1.3 A Common Scattering Angle Stacking Method

In the case that the scatterer is of spherical symmetry, the $p \rightarrow p$ and $p \rightarrow s$ scattering response will only depend on the angle between the incident and the scattered wave field,

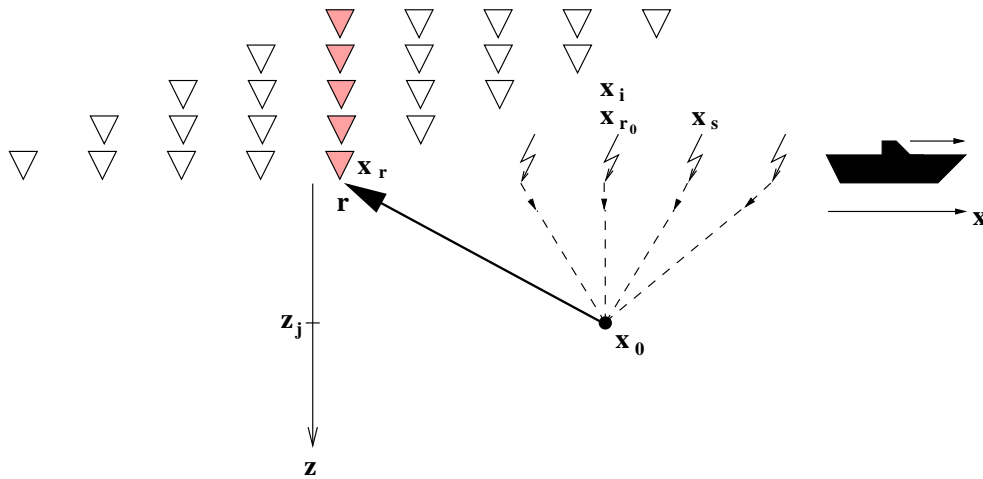


Figure 3.11: Geometry of the CPP gather stacking method. Traces belonging to one common profile point are gathered. After applying a lateral shift to correct for the movement of the acquisition spread $\Delta x_{s,r}$, a static travel time correction is applied. The procedure is comparable to building a common receiver gather in land seismic applications.

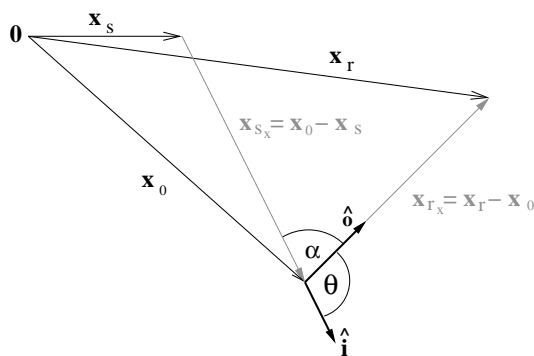


Figure 3.12: Generic acquisition geometry, defining the scattering angle θ in vector notation. θ is the angle between the unit incident $\hat{i} = \mathbf{x}_0 - \mathbf{x}_s / |\mathbf{x}_0 - \mathbf{x}_s|$ and unit scattered $\hat{o} = \mathbf{x}_r - \mathbf{x}_0 / |\mathbf{x}_r - \mathbf{x}_0|$ seismic ray vectors. It is given by: $\cos \theta = \mathbf{x}_{sx} \cdot \mathbf{x}_{rx} / |\mathbf{x}_{sx}| |\mathbf{x}_{rx}|$.

i.e. the scattering angle θ . This holds for pure Rayleigh scattering as well as for scattering in the limits of the Born approximation (please compare equations 2.19, 2.41, 2.42 and 2.48 in section 2.1).

In order to calculate the scattering angle for a given acquisition geometry the scattering position has to be known. For complex background media we would have to determine this angle by ray tracing (section 2.2.1).

For a homogeneous background medium the calculation is straight forward and it follows from simple geometry that (figure 3.12)

$$\cos \theta = \cos(180^\circ - \alpha) = \left(\frac{\mathbf{x}_{sx} \cdot \mathbf{x}_{rx}}{|\mathbf{x}_{sx}| |\mathbf{x}_{rx}|} \right), \tag{3.21}$$

where α is the complementary scattering angle.

The scattering response \mathbf{u}^s is the same for all traces with the same scattering angle $\theta(\mathbf{x}_s, \mathbf{x}_0, \mathbf{x}_r)$.

Figure 3.13 shows the situation for a surface seismic experiment. Traces of common scattering angle can be stacked in phase after applying corrections for spherical divergence and travel time corrections adapted to scattering in order to avoid NMO stretch. This procedure is equivalent to projecting shots and receivers onto a sphere with radius $r = z_0$. The travel time correction to be applied is thus given by:

$$\Delta t = \frac{|\mathbf{x}_r - \mathbf{x}_0| + |\mathbf{x}_0 - \mathbf{x}_s|}{c_0} - \frac{|z_0|}{c_0} \quad (3.22)$$

where z_0 is the depth of the scatterer.

Stacking traces of common scattering angle (CSA) will improve the signal to noise ratio of the scattered wave field. The resulting CSA stacked section (CSA stack) shows amplitude and phase trends of the scattered wave field u^s with scattering angle which are only influenced by the composition of the scatterer. As discussed in section 2.3.1 the angular position of the significant phase reversals (SPR) in the scattered wave field in particular can be used to classify the scattering situation in question. In order to illustrate the performance of the CSA stack, it was applied to a synthetic seismic dataset. As described in the introduction the scattering response from a spherical mineral inclusion embedded in an otherwise homogeneous crystalline crust background medium was modeled. The assumed material parameters are listed in table 3.1. The final CSA stack and intermediate results for CSA-gathers with $\alpha_1 = 20^\circ$ and $\alpha_2 = 100^\circ$ are depicted in figure 3.14.

The enhancement in signal to noise ratio in the stacked scattered wave field is governed by the amount of angular fold provided by the acquisition geometry. Figures 3.15a and 3.15b show histograms of the angular distribution $h(\alpha)$ for a typical marine seismic and VSP survey, respectively. The VSP example was chosen, because the CSA histograms for marine

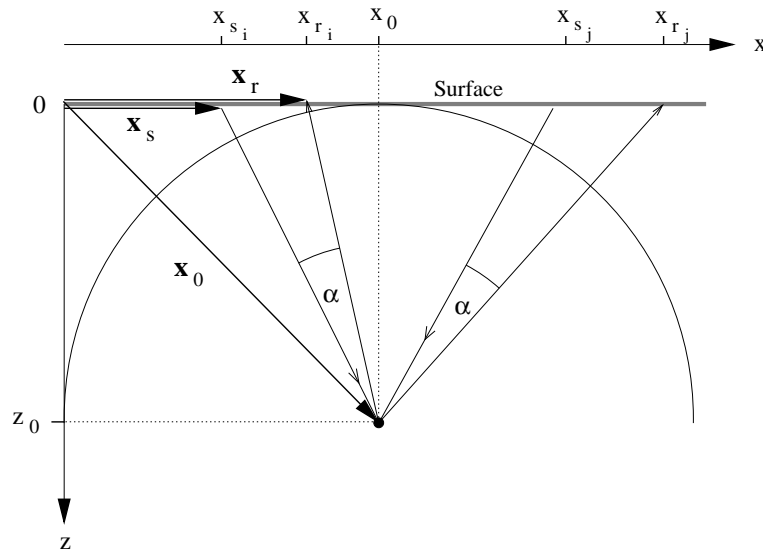


Figure 3.13: Common Scattering Angle (CSA) gather geometry. For a given scattering position \mathbf{x}_0 traces of common scattering angle $\alpha = 180^\circ - \theta$ are gathered. Seismic scattering events are corrected for NMO by applying the static shift $\Delta t = \frac{|\mathbf{x}_r - \mathbf{x}_0| + |\mathbf{x}_0 - \mathbf{x}_s|}{c_0} - \frac{|z_0|}{c_0}$. This correction is equivalent to projecting sources \mathbf{x}_s and receivers \mathbf{x}_r onto a sphere.

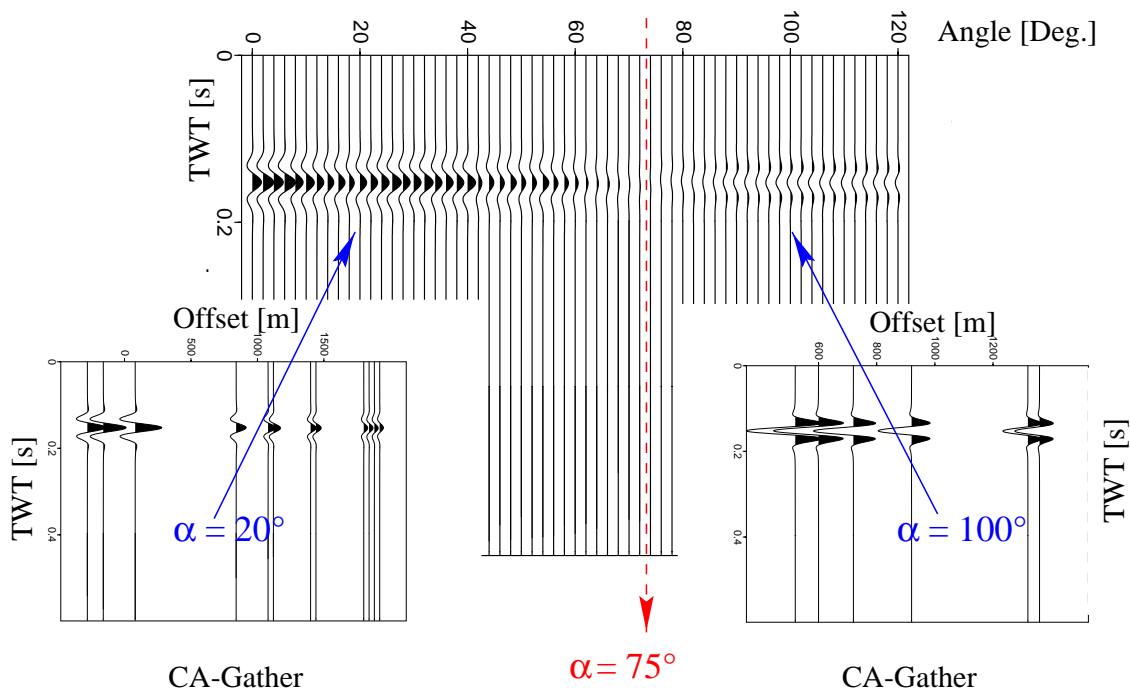


Figure 3.14: Two exemplary CSA-gathers ($\alpha = 20^\circ$ and $\alpha = 100^\circ$) and stacking result for the modeled scattering situation as listed in table 3.1. Traces of common scattering angle stack in phase. In a realistic field data example the signal to noise ratio of the scattering response would be enhanced in the stacked section. The interpretation of the observed SPR ($\theta = 75^\circ$, this example) becomes more reliable.

and land seismic surveys are quite similar. According to the synthetic examples discussed throughout this chapter, for the marine acquisition scenario a scatterer in 22.5m water depth was assumed to be investigated with an 48 channel streamer array. The calculation of scattering angles was restricted to source and receiver positions no farther than eight times the scatterer depth, in order to limit the number of scattering angles α close to zero. For the VSP common angle histogram a scatterer situated at the end of a 1400m deep straight borehole was assumed to be investigated with 140 receivers distributed equally across its complete depth range. The shot point was situated at 300 meters lateral offset to the borehole. The scatterer was positioned 150m away from the bottom of the borehole. The histograms are comparable to the common fold diagrams or stacking charts used in reflection seismic applications. The angular fold can be increased by increasing the bin size for the CSA stack which, however, also will decrease the angular resolution. The histogram not only shows the angular fold of the acquisition layout but also its angular coverage. In order to classify a certain scattering situation, by e.g. detecting a significant phase reversal the angular position of the SPR should be covered by the acquisition layout with sufficient fold. Marine and land seismic survey histograms show apparent similarities. Small scattering angles are covered more frequently than larger ones and the angular range is limited to scattering angles less than $\alpha = 180^\circ$. In marine and surface seismic applications

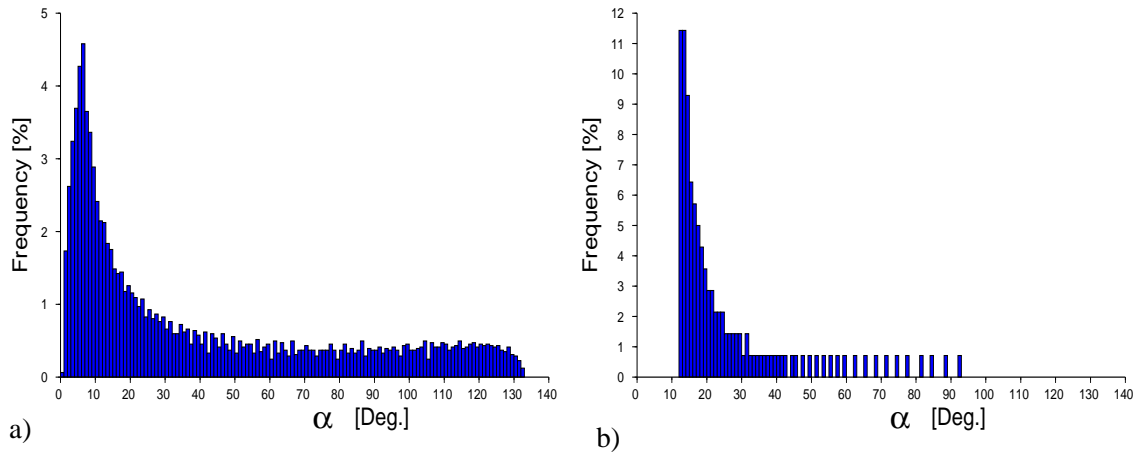


Figure 3.15: Scattering angle histograms $h(\alpha)$ for a) a shallow marine seismic acquisition layout and b) a typical VSP survey. In case (a) a scattering inclusion at 22.5m water depth was assumed to be measured with a 48 channel streamer array with 2m of geophone distance. Scattering angles were only considered for source or receiver position no further than eight times the inclusion depth. A 1400m deep straight borehole with 140 receivers distributed every 10m along the borehole with a shot point 300m away from the collar and a scatterer 150m away from the bottom of the borehole was assumed in case (b). Both layouts span a significant number of low scattering angles. The angular coverage and range of the marine layout is however much higher than that of the VSP.

low scattering angles generally correspond to shots and receivers being located at large distances from the scatterer position.

The angular range of VSP surveys also depends on the offset from source to borehole and the assumed depth of the scatterer. The plot shows poor coverage for most of the calculated scattering angles. The situation can be improved by applying multiple sources with different offsets which probably could be deployed at different depth (cross-well VSP). The CSA stack method can be applied to analyze the dynamic characteristic of the scattering response of a spherically symmetric inclusion. It was shown in section 2.1.3 for large inclusions of arbitrary shape that the position of the SPR is always found at the same scattering angle, when measured from the corresponding scattering center. If the position of the scattering center is known, a CSA processing approach should thus also be applicable to larger objects with complex structure.

3.1.4 A Common Offset Filter Technique

As discussed in the preceding sections, the success of enhancing the scattering signature is partly prevented by the strong reflector noise in the SES or CPP stacked section. It is possible however to take advantage of the fact that the scattering response changes its spatial and temporal position within the seismogram, in order to suppress seismic energy from horizontal reflectors and the direct arrival. This approach, as described in the following, was adapted from image processing methods (see e.g. Jähne, 1997). The scattering

response can be regarded as a moving object in a sequence of images (subsequent shot gather, receiver gather). It can be enhanced by the following simple procedure:

Let $\Gamma_{rh} = \Gamma_{rh}(\mathbf{x}_r, \mathbf{x}_s, z_j, c(\mathbf{x}))$ be the travel time curve of a horizontally layered reflector, $\Gamma_{rd} = \Gamma_{rd}(\mathbf{x}_r, \mathbf{x}_s, \hat{n}, \mathbf{OP}, c(\mathbf{x}))$ that of any dipping reflector, $\Gamma_d = \Gamma_d(\mathbf{x}_r, \mathbf{x}_s, c(\mathbf{x}))$ the direct arrival and $\Gamma_s = \Gamma_s(\mathbf{x}_r, \mathbf{x}_s, \mathbf{x}_0, c(\mathbf{x}))$ be the curve of a point scatterer. For simplicity we now assume a homogeneous background medium with $c(\mathbf{x}) = c_0$ and a surface marine seismic survey where $\mathbf{x}_r = (x_r, 0, 0)$ and $\mathbf{x}_s = (x_s, 0, 0)$. The fixed distance between the individual receivers and the source is given by $\Delta x_{s,r} = x_s - x_r$. We then find for the travel times of the individual arrivals described above:

$$\begin{aligned} t_{rh}(\mathbf{x}_s, \mathbf{x}_r, z_j) &= \frac{\sqrt{\Delta x_{s,r}^2 + 4z_j^2}}{c_0} \\ t_{rd}(\mathbf{x}_s, \mathbf{x}_r, \hat{n}, \mathbf{OP}) &= \frac{|\mathbf{x}_r - \mathbf{x}_s + 2\mathbf{x}_{sn} - 2\mathbf{OP}_n|}{c_0} \\ t_s(\mathbf{x}_s, \mathbf{x}_r) &= \frac{\Delta x_{r,s}}{c_0} \end{aligned} \quad (3.23)$$

and finally:

$$t_s = \frac{\sqrt{(x_r - x_0)^2 + z_0^2} + \sqrt{(x_s - x_0)^2 + z_0^2}}{c_0} \quad (3.24)$$

The travel times t_{rd} and t_s will change from shot to shot since \mathbf{x}_{sn} as well as $(x_r - x_0)$ and $(x_s - x_0)$. t_s and t_{rh} in contrast are no function of x_s and thus will be constant. The "motion" of Γ_s and Γ_{rd} can be used to construct a filter that removes the direct arrival and reflected energy from horizontal reflectors. Figure 3.16 gives an overview of the filter process. The filter is constructed by stacking traces with common offset for a number n of subsequent shots and normalizing by the number of stacks:

$$F_j(x_r, t) = \frac{1}{n} \sum_{k=j}^n f_{s_k}(x_r, t) \quad (3.25)$$

In figure 3.16 this procedure corresponds to steps 1 to 3. Direct arriving seismic energy and energy from horizontal reflectors will have a constant travel time signature Γ_d, Γ_{rh} in each individual shot gather, whereas the travel times of scattered energy and dipping reflector response will be a function of the current shot position. Thus stacking of traces with common offset will enhance the signal of the direct arrival and the events from horizontal reflectors. Other signals, i.e. from dipping reflectors and diffractions, will be weakened by destructive interference or smeared out. Normalizing the stack will yield a filter operator that shows the averaged direct arrival and horizontal reflections. The distorted signal from dipping reflectors and scattered energy will be weakened by a factor of n , i.e. the number of common offset traces stacked to construct the filter operator. In the next step the filter operator will be subtracted from the current shot gather. The performance of the filter depends on the number of stacks used and on the spatial shot interval Δx_s .

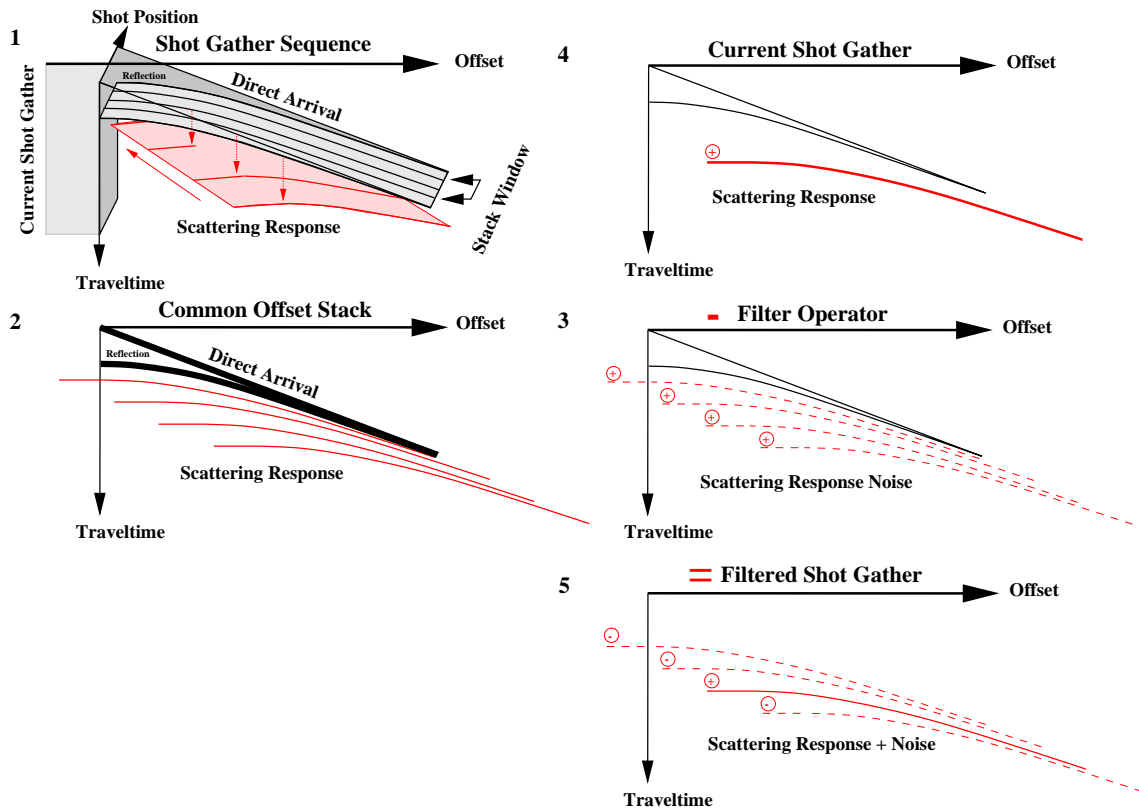


Figure 3.16: The principle of the difference filter technique. For a given sequence of shot gathers (1) the signature of a possible scattering response will change its apex travel time within the recorded seismograms from shot to shot. Responses from horizontal reflectors and the direct arriving wave field will have constant travel time throughout the sequence. Stacking traces of common offset and normalizing by the number of traces stacked (2), will generate a filter operator (3) which can be subtracted from a current shot gather (4). Applying this procedure as a moving filter on a sequence of shot gathers will result in a section, only showing the scattering response and weak filter noise (5).

The whole section will be filtered by constructing the filter operator for a moving window of width n in the common offset domain:

$$f'_{s_j}(\mathbf{x}_r, t) = f_{s_j}(x_r, t) - \frac{1}{n} \sum_{k=j}^n f_{s_k}(x_r, t) \quad (3.26)$$

In the following the filter will be called a *difference filter* (DF) due to the subtraction procedure described by equation 3.26. It is worth noting that the method is comparable to other difference filter techniques commonly applied in seismic acquisition and processing. In VSP data processing the direct arrival is usually removed using a moving window median filter. The filter is constructed by calculating the median of the direct arrival amplitudes within a given trace window and subtracting it from a current trace. On board quality control techniques in marine airgun seismic surveys also utilize such techniques. Subsequent source signals are recorded and subtracted from each other to provide a readily perceived

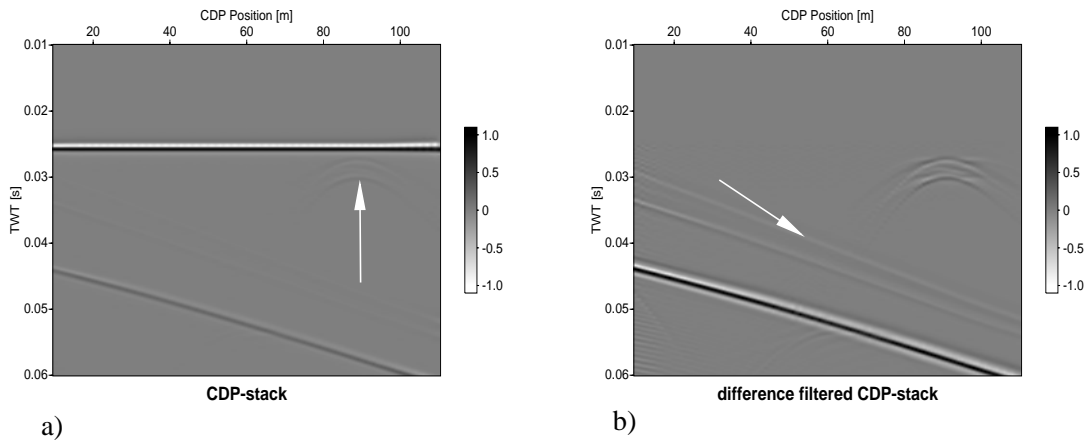


Figure 3.17: CDP stacked section for the gas accumulation model. A dipping reflector was introduced. a) section without and b) with a difference filter (DF) applied prior to CDP sorting, NMO correction and stacking. The DF clearly suppresses the strong reflection from the horizontal sea floor, while sustaining the weak scattering of the modeled gas accumulation and the dipping reflector response. The white arrow in figure a) shows the weak scattering response. The white arrow in figure b) indicates "dipping" numerical noise, which is also preserved. The DF is applied prestack and thus still permits the application of e.g. prestack migration after filtering.

peak signal, if the source should fail.

In figure 3.17a a common CDP stacked section of the modeled gas accumulation as already described above is shown. A dipping reflector was introduced to the model in order to illustrate the performance of the DF. Figure 3.17b shows the CDP stacked section, after prestack difference filtering for the same data set. Horizontal reflections are perfectly suppressed, whereas the scattering response and the dipping events are preserved.

3.2 Prestack Methods

In order to apply the travel time corrections required for most of the gather oriented methods discussed in the preceding section, the position of the scattering object in the subsurface has to be known. This position is often the main target of the investigation itself. As mentioned in the section 3.1.2, it can e.g. be found by iteratively varying an assumed position and successively applying e.g. SES or CPP gather and stack. The correct position would then have to be delineated by either applying a mathematical criterion or through human evaluation of the stacking result. However, except for the proposed common offset filter technique (section 3.1.4), reflector noise is present in all of the proposed gather oriented methods and selecting an optimum stacking result is even more aggravated. Ambiguity of the obtained position is another problem as will be discussed in this section.

Kanasewich *et al.* (1988) presented the Common Fault Point stacking (CFP) technique as a complementary approach to the CMP method. Aimed towards imaging of subsurface discontinuities, diffraction signatures are collapsed to points indicating their origin on the

resulting seismic section. A comparable approach was investigated by Hoffmann (1995), who accounted for the dynamic characteristics of diffracted seismic energy in prestack migration. The method was called Common Fault Point (CFP) migration.

Diffraction Stack Migration as first developed by Hagedorn (1954) is based on a geometrical interpretation of Huygens principle. It shall serve as starting point for the development of prestack scattering enhancement imaging techniques. The method provides the means of separating scattered and reflected seismic events by their different travel time characteristics. It was formalized and put on a sound theoretical basis by French *et al.* (1975) or Miller *et al.* (1983, 1984, 1987),, by relating it to linearized seismic inversion and the generalized Radon transform (GRT). An explicit treatment of the elastic case of this formalism can be found in Beylkin and Burridge (1990).

By implementing coherency criteria into Diffraction Stack Migration an image of the subsurface can be obtained, which emphasizes the position of the scatterer over that of reflectors. The use of coherency measures is very common in the literature:

Neidell and Tanner (1971) investigated the performance of several possible types of coherency measures in velocity analysis applications, e.g. unnormalized cross correlation and semblance (normalized output to input energy ratio). Gelchinsky *et al.* (1985) proposed a procedure of automatic wave detection on the basis of measuring the coherence along phase and group travel time curves. They also investigated the performance of several different statistical measures in applications of seismic velocity analysis. Milkereit (1987) used localized semblance as slowness weights in order to enhance the migrated image of noisy crustal seismic data. Landa and Keydar (1998) and Landa *et al.* (1987) proposed and applied semblance as a coherency measure to extract scattered and diffracted seismic energy from seismic sections.

In the following I will review the concept of the GRT as the theoretical foundation for diffraction stack migration and also for the newly developed methods described thereafter. Subsequently I will introduce the concept of Diffraction Coherency Migration (DCM), which implements the use of coherency measures into Diffraction Stack Migration.

In the case of scalar wave field registration and if in seismic acquisition layouts only a limited number of sources and/or receivers is deployed, e.g. in VSP surveying, migration can show significant imaging ambiguity. This problem will be investigated by numerical examples in section 3.2.3.

The concept of Diffraction Polarization Migration (DPM) will be introduced finalizing this section. DPM is an alternative approach to DCM. It images scatterers by including polarization information into the migration process. It also provides the means of effectively reducing imaging ambiguity for acquisition geometries with only few shot points.

3.2.1 Diffraction Stack Migration

The early formulations of the diffraction stack migration were merely geometrical interpretations of Huygens principle. It is assumed that the subsurface is composed of an infinite number of scatter points contributing to the observed wave field. Each subsurface point can carry a certain perturbation compared to the background medium, either being a point scatterer or part of some arbitrarily shaped object or a laterally continuous reflector.

The image of the subsurface is then constructed by summing all recorded wave field samples

that could have arrived at the receiver from a given subsurface point and assigning the resulting value to a corresponding point in the image space. Repeating this procedure for all image space positions will give the final image. The image space is formed by a regular grid. There is no restriction in principle on the complexity of the velocity distribution in the background medium. For travel time calculations ray tracing methods can be used. The advantage of the method is that there is no a priori requirement to fulfill demands of the wave equation like in Kirchhoff migration.

Following Miller *et al.* (1987) I will now describe the imaging process of the diffraction stack in a formal way:

Back projection:

The data value $u(\tau)$ recorded at a given travel time τ in a seismic trace $u(\mathbf{x}_{r_i}, \mathbf{x}_{s_j}, t)$ carries contributions from several points $\mathbf{y} = (y_1, y_2, y_3)$ in the subsurface. $\tau = \tau(\mathbf{x}_s, \mathbf{y}) + \tau(\mathbf{y}, \mathbf{x}_r)$ is the travel time from the source \mathbf{x}_s to \mathbf{y} and back to the receiver \mathbf{x}_r . These points in image space lie on the surface $I_\tau(\mathbf{x}_s, \tau, \mathbf{x}_r)$, which for a background medium with constant velocity distribution $c(\mathbf{x}) = c_0$, is an ellipsoid with shot and receiver of the corresponding seismic trace in its foci. The surface is called an isochrone surface, i.e. Hagedorn's curve of maximum concavity (figure 3.18a).

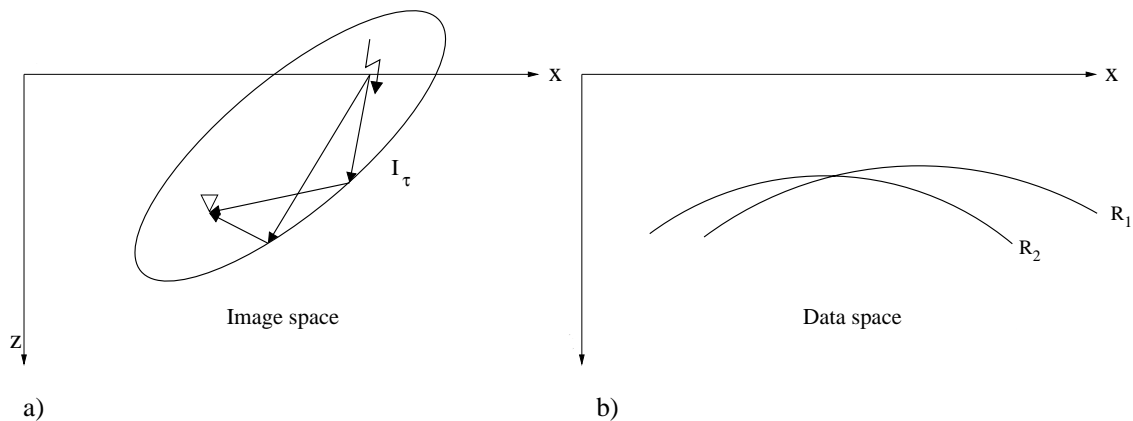


Figure 3.18: a) Locations with equal travel time lie on an isochrone image I_τ in image/subsurface space building an ellipsoid (for $c_0 = const$) with shot and receiver in its foci. b) A fixed image point \mathbf{y} will contribute seismic energy to the reflection time surface R in data space.

In other words:

For a given travel time $\tau(\mathbf{x}_{s_j}, \mathbf{y}_0, \mathbf{x}_{r_i})$ the data value $u(\mathbf{x}_{r_i}, \mathbf{x}_{s_j}, \tau)$ is assigned to the isochrone surface in subsurface space (*back projection*). Every data value contributes to exactly one such surface. They are all added up to build the migrated image, which benefits from interference and thus depends on the periodicity of the seismic signal.

Projection:

A given subsurface point $\mathbf{y} = (y_1, y_2, y_3)$ on the other hand will contribute seismic energy to the data space, i.e. the seismic traces, that lies on the travel time curve $R_{\mathbf{y}}(\mathbf{x}_s, \mathbf{y}, \mathbf{x}_r)$. This curve is called a reflection time surface (RTS) (French, 1975) and is equivalent to Hagedorn's curve of maximum convexity (figure 3.18b). One travel time can belong to different image points, of course as indicated in the figure by the intersection of R_1 and R_2 .

The process of image building can thus also be achieved by adding the data values along the RTS and assigning their sum to the image point \mathbf{y} (*projection* or *diffraction stack*). Diffraction stack and back projection are thus the same procedure, only that the data values are added in a different order. The isochrone surface I_τ is parameterized by the travel time τ and the reflection time surface $R_{\mathbf{y}}$ by the image position \mathbf{y} . They are subsets of the data and image space, respectively (Miller *et al.*, 1987):

$$I_\tau = \{\mathbf{y} : \tau(\mathbf{x}_s, \mathbf{y}, \mathbf{x}_r)\} \quad (3.27)$$

$$R_{\mathbf{y}} = \{\tau : \mathbf{y}(\mathbf{x}_s, \tau, \mathbf{x}_r)\} \quad (3.28)$$

As described above the data recorded in a seismic trace at a certain time τ can be regarded as the integral contribution from subsurface points lying on an isochrone surface I_τ , thus:

$$\hat{u}(\tau) = \int_{I_\tau} u(\mathbf{y}) dI \quad (3.29)$$

$u(\mathbf{y})$ is the object function defined by the scattering potential (either acoustic or elastic) in the earth subsurface, while $\hat{u}(\tau)$ is the resulting data function, represented by the recorded seismic data. Similarly we have:

$$\hat{f}(\mathbf{y}) = \int_{R_{\mathbf{y}}} f(\tau) dR \quad (3.30)$$

with $f(\mathbf{y})$ again being the object function, which can be recovered by applying a diffraction stack on the recorded seismic data $f(\tau)$ along the reflection time surface $R_{\mathbf{y}}$. The integral operation in equation 3.29 and 3.30 resemble the process of recording a seismic response (projection) and the process of imaging (back projection) in terms of a corresponding pair of projection operators (Miller, 1983). Thus diffraction stack migration is formulated in terms of an inversion procedure.

Like already shown in chapter 2.1 the scattered wave field i.e. the field giving rise to the data function in equation 3.29 can be expressed in terms of the Born approximation. Obeying the assumptions that have to be made in order to keep this approximation valid, the scattered wave field (for the acoustic case, to simplify matters) can be written as (Miller, 1983):

$$u^s(\mathbf{x}_r, \mathbf{x}_s, \omega) = \omega^2 \int G_0(\mathbf{x}_r, \mathbf{y}, \omega) G_0(\mathbf{x}_s, \mathbf{y}, \omega) f(\mathbf{y}) d^3\mathbf{y} \quad (3.31)$$

where the wave field inside the scatterer has been replaced by the incident wave field as usual, which in this case is represented by the Greens function $G_0(\mathbf{x}_s, \mathbf{y}, \omega)$. G_0 is chosen to be the first order approximation given by geometrical optics:

$$G_0(\mathbf{x}, \mathbf{y}, \omega) = A(\mathbf{x}, \mathbf{y}) e^{i\omega\tau(\mathbf{x}, \mathbf{y})} \quad (3.32)$$

The travel time function τ satisfies the eikonal equation 2.53 and the amplitude or geometrical spreading term satisfies the transport equation 2.54 along the ray connecting the points \mathbf{x} and \mathbf{y} . Substituting G_0 from equation 3.32 in equation 3.31 and transforming into the time domain yields:

$$u^s(\mathbf{x}_r, \mathbf{x}_s, t) = -\frac{\partial^2}{\partial t^2} \int A(\mathbf{x}_s, \mathbf{y})A(\mathbf{y}, \mathbf{x}_r)\delta[t - \tau(\mathbf{x}_s, \mathbf{y}) - \tau(\mathbf{y}, \mathbf{x}_r)]f(\mathbf{y})d^3\mathbf{y} \quad (3.33)$$

The delta function restricts integration to points that lie on the isochrone surface and thus obey the travel time relation:

$$\tau = \tau(\mathbf{x}_s, \mathbf{y}) + \tau(\mathbf{y}, \mathbf{x}_r) \quad (3.34)$$

Equation 3.33 relates the scattered acoustic pressure emitted by the source at \mathbf{x}_s and recorded by the receiver at \mathbf{x}_r to the second time derivative of the weighted integral of $f(\mathbf{y})$ over the isochrone surface I_τ (projection) (Miller *et al.*, 1987).

For the case of a constant velocity background medium, G_0 will be the free space Greens function with $A(\mathbf{x}, \mathbf{y}) = 1/(4\pi|\mathbf{x} - \mathbf{y}|)$ representing simple spherical spreading and $\tau = |\mathbf{x} - \mathbf{y}|/c_0$ the travel time on a straight line path. The projection 3.33 becomes an integral over an ellipsoid for every seismic trace, with source and receiver in its foci.

If we compare equation 3.33 with the classical Radon transform in its filtered version (Radon, 1917)

$$\frac{\partial^2}{\partial p^2} f^\nabla(\hat{\xi}, p) = \frac{\partial^2}{\partial p^2} \int \delta(p - \hat{\xi}\mathbf{y})f(\mathbf{y})d^3\mathbf{y} \quad (3.35)$$

a direct analogy between equation 3.33 and equation 3.35 can be drawn:

The integration is taken along planes $p = \hat{\xi}\mathbf{x}$. In equation 3.33, a source-receiver pair plays the role of $\hat{\xi}$, thus describing a family of "parallel" isochrone surfaces, whereas t plays the role of p , i.e. fixing one such surface within that family (Figure 3.19).

An inversion formula can be suggested for 3.33 by comparison with the inversion for the filtered Radon transform (Radon, 1917), i.e.

$$\begin{aligned} f(\mathbf{y}_0) &= -\frac{1}{8\pi^2} \int \frac{\partial^2}{\partial p^2} \int \delta(\hat{\xi}(\mathbf{x} - \mathbf{y}_0))f(\mathbf{x})d^3\mathbf{x}d^2\hat{\xi} \\ &= -\frac{1}{8\pi^2} \int \frac{\partial^2}{\partial p^2} f^\Delta(\hat{\xi}, p = \hat{\xi}\mathbf{y}_0)d^2\hat{\xi} \end{aligned} \quad (3.36)$$

and compares to:

$$\begin{aligned} \langle f(\mathbf{y}_0) \rangle &= \int \frac{\partial^2}{\partial t^2} \tilde{f}(\mathbf{x}_r, \mathbf{x}_s, t = \tau(\mathbf{x}_r, \mathbf{y}_0, \mathbf{x}_s))dW(\mathbf{x}_r, \mathbf{y}_0, \mathbf{x}_s) \\ &= \int u^s(\mathbf{x}_r, \mathbf{x}_s, t = \tau(\mathbf{x}_r, \mathbf{y}_0, \mathbf{x}_s))dW(\mathbf{x}_r, \mathbf{y}_0, \mathbf{x}_s) \end{aligned} \quad (3.37)$$

Equation 3.37 is a weighted diffraction stack along the reflection time surface $R_{\mathbf{y}}$. The weights $dW(\mathbf{x}_r, \mathbf{y}_0, \mathbf{x}_s)$ depend on the source and receiver positions as well as on the position of the image point \mathbf{y}_0 . $\langle f(\mathbf{y}_0) \rangle$ estimates the value of the object function in

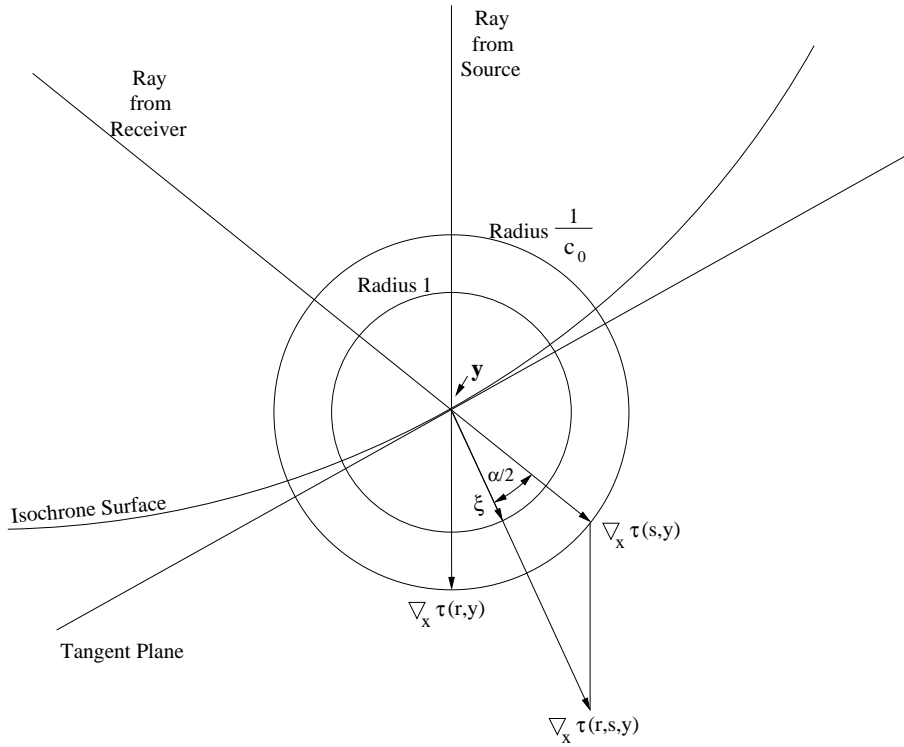


Figure 3.19: *Geometry of the backprojection procedure: By assuming that the isochrone surface in the vicinity of the image point can be approximated by planes with normals $\hat{\xi}$ that are parameterized by the travel time τ , inverse GRT can be used for the backprojection step (Miller et al., 1987).*

the image point y_0 . Thus, the back projection step formalized by equation 3.37 is equivalent to an inversion of $f(y)$ (Miller et al., 1987).

By assuming that the isochrone surface in the vicinity of the image point can be approximated by planes with normals $\hat{\xi}$ that are parameterized by the travel time τ it can be shown (Miller et al., 1987) that the weighting function takes on the form:

$$dW(\mathbf{x}_r, \mathbf{y}_0, \mathbf{x}_s) = \frac{1}{\pi^2}(\mathbf{x}_r, \mathbf{y}_0, \mathbf{x}_s) \frac{|\cos^3 \alpha(\mathbf{x}_r, \mathbf{y}_0, \mathbf{x}_s)|}{c_0^3(\mathbf{y}_0)A(\mathbf{x}_r, \mathbf{y}_0, \mathbf{x}_s)} d^2 \hat{\xi} \quad (3.38)$$

For reconstructing the object function, we thus need the measured wave field, which is projected back to the position of the image point y_0 and finally integrated over all possible directions of local planes defined by $\hat{\xi}$. The wave field is corrected by an obliquity factor $|\cos^3 \alpha(\mathbf{x}_r, \mathbf{y}_0, \mathbf{x}_s)|$ and for spreading effects by $1/A(\mathbf{x}_r, \mathbf{y}_0, \mathbf{x}_s)$. α is the angle between the incident and the scattered ray and as defined in section 2.1 is zero for backward scattering. Equation 3.37 is closely related to Kirchhoff migration (please refer to appendix A).

The possible values of $\hat{\xi}$ are dictated by the acquisition geometry. In an ideal case $\hat{\xi}$ would cover the whole directional range. However in a real seismic experiment the directional coverage of $\hat{\xi}$ is limited. The effect of this limitation will be discussed in section 3.2.3.

Also in a typical seismic experiment the scattered wave field u^s (which in terms of this discussion includes the reflected wave field as well) is "contaminated" by the direct arriving wave field. A method of removing the direct arrival from marine seismic sections was already discussed in section 3.1.4.

By incorporating coherency measures into the process of diffraction stack migration, we can take advantage of the characteristic kinematic behavior of the scattered and diffracted seismic energy in order to separate it from the direct arriving and reflected wave fields. This approach will be described in the following section.

3.2.2 Diffraction Coherency Migration

As pointed out in section 2.3.2 scattered and diffracted wave fields show quite different kinematic behavior compared to that of reflections. Expressed in terms of DSM, the wave field emerging from a point scatterer contributes coherent energy to the whole "reflection time surface" (RTS), whereas the reflected wave field only contributes energy to the RTS, where the reflection condition is satisfied (figure 3.20).

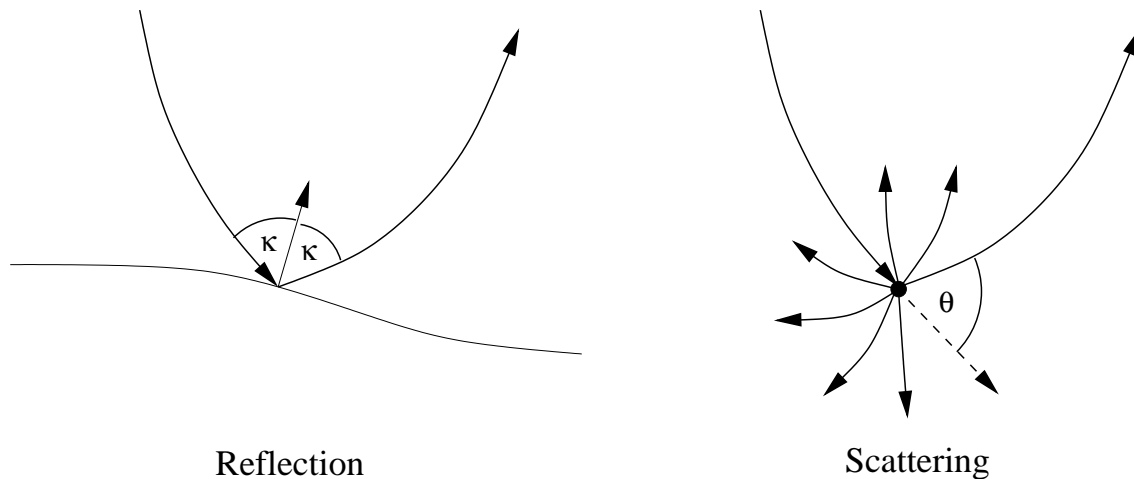


Figure 3.20: *Scattering and reflection can be distinguished by their different kinematics. κ denotes the reflection angle, like it is commonly defined in seismic applications and θ the scattering angle.*

Thus if the coherence of seismic energy is measured along the RTS, and in DSM this measure is used instead of the stacked amplitude, an image of the subsurface should be obtained, that emphasizes the position of scatterers and diffractors over that of reflectors. In the following I will refer to this procedure as "diffraction coherency migration" (DCM). I will briefly review the concept of multichannel cross correlation and semblance, as well as their possible performance in the task of separating scattered and reflected seismic energy:

Assuming a seismic experiment where data is recorded on M independent data channels (seismic traces) and identifying the lag trajectory $k(i)$, $i = 1, \dots, M$ as defined by Neidell and Taner (1971), with the travel time $\tau_R(\mathbf{x}_r, \mathbf{y}_0, \mathbf{x}_s)$ corresponding to the reflection time

surface, i.e. $k(i) \approx \tau_R/dt$ (dt being the sampling rate), the unnormalized cross correlation sum (CC) can be written as the sum of all possible unnormalized cross correlations between traces i and traces $i + p$ (Neidell & Taner, 1971):

$$CC = \sum_{p=1}^{M-1} \sum_{i=1}^{M-p} \frac{1}{N+1} \sum_{j=k(i)-(N/2)}^{k(i)+(N/2)} f_{ij(i)} f_{i+p,j(i+p)} \quad (3.39)$$

$N + 1$ is the number of samples in the gate centered about the sample $k(i)$ in the i th trace and $f_{ij(i)}$ is the amplitude assigned to that sample in trace i . The width of the gate has to be chosen by the interpreter and should usually be of the length of the source signature. Equation 3.39 can be normalized in two different ways. On one hand we can choose a normalizing denominator which equals to the geometric mean of the energy in the specific time gate of the traces i and $i + p$:

$$NCC = \frac{2}{(M-1)M} \sum_{j=k-(N/2)}^{k+(N/2)} \sum_{p=1}^{M-p} \sum_{i=1}^{M-p} \frac{f_{ij} f_{i+p,j(i+p)}}{\sum_{j=k-(N/2)}^{k+(N/2)} f_{ij}^2 \sum_{j=k-(N/2)}^{k+(N/2)} f_{i+p,j(i+p)}^2} \quad (3.40)$$

This is a statistical normalization approach. Equation 3.40 is called the normalized cross correlation sum (NCC).

On the other hand an arithmetic average can be chosen for the normalization of equation 3.39. After some algebra Neidell and Taner (1971) arrive at the equation for the energy normalized cross correlation sum (ECC):

$$ECC = \frac{\sum_{j=k-(N/2)}^{k+(N/2)} \{ \{ \sum_{i=1}^M f_{ij(i)} \}^2 - \sum_{i=1}^M f_{ij}^2 \}}{(M-1) \sum_{j=k-(N/2)}^{k+(N/2)} \sum_{i=1}^M f_{ij}^2} \quad (3.41)$$

The values ECC vary between $\frac{-1}{M-1} \leq ECC \leq 1$. Equation 3.41 is related to the semblance coefficient NE by

$$ECC = \frac{1}{M-1} (M \cdot NE - 1) \quad (3.42)$$

where

$$NE = \frac{\sum_{j=k-(N/2)}^{k+(N/2)} \{ \sum_{i=1}^M f_{ij(i)} \}^2}{M \sum_{j=k-(N/2)}^{k+(N/2)} \sum_{i=1}^M f_{ij}^2} \quad (3.43)$$

The values of NE range from $0 \leq NE \leq 1$. The semblance coefficient is equivalent to the energy normalized cross correlation sum (3.41). Both functions 3.43 (or 3.41) and 3.39 can be used to measure coherence along the reflection time surface. They are sensitive to changes in shape of the seismic signal from trace to trace. Semblance in contrast to normalized cross correlation penalizes variations in RMS amplitude. For weak seismic signals, like it is the case for scattered and diffracted seismic energy, we can expect that the noise portion of the signal leads to significant RMS variations. Thus it is worth investigating the performance of CC, NCC in comparison with a semblance measure, either ECC or NE, on the task of separating scattered from reflected seismic signals.

The implementation of coherency measures into DSM can be achieved by using the following analogy:

For DSM the image $\langle f(\mathbf{y}_0) \rangle$ is obtained by integrating recorded data values along the RTS $R_{\mathbf{y}_0}$. This compares to the image $C(\mathbf{y}_0)$ obtained by measuring coherency C along the RTS in DCM. In both cases the RTS is a function of shot, receiver position $\mathbf{x}_s, \mathbf{x}_r$ and the image point \mathbf{y}_0 . Integration and measuring coherency in both cases is carried out over all the available data. The difference between DSM and DCM lies in the fact that in order to calculate the coherency a gate centered about the RTS travel time values τ_R is needed. Furthermore the oscillatory nature of the source signal is not transferred to the DCM image as it is the case for DSM. In order to be able to compare the performance of DSM with that of DCM, in the following stacking in DSM was conducted using a time gate like in DCM. The image was obtained by calculating the energy contained in the stacked gate.

Figure 3.21 compares the result of this modified version of DSM with that of DCM in a synthetic data example. In order to model the seismic response a simple travel time algorithm was used. The geometry of the model was taken from a real VSP field experiment carried out in Sudbury, Canada at the Norman West mining camp in 1998 (Perron & Snyder, 1998) (please also refer to section 4). In the investigated scenario a point scatterer (A) at 1400m depth was modeled along with a plane dipping 30° and striking at 30° from the North. The plane was assumed to have infinite extension and to intersect the borehole at 1000m depth. Due to the limited spatial coverage of the acquisition layout only portions of the planes were imaged (B). The circular distribution of secondary events around the primary image is caused by the imaging ambiguity of the acquisition layout (please refer to section 3.2.3). The modeled scattering response was scaled down to be a factor of 10 less the amplitude of the reflection response prior to migration. The data was contaminated with random noise to yield a signal to noise ratio of $s/n = 10$.

The DCM image of the scatterer is brighter than that of the plane ($C_{Scat}^{max}/C_{Refl}^{max} \approx 1.25$), whereas the DSM image of the plane is brighter than that of the scatterer ($C_{Scat}^{max}/C_{Refl}^{max} \approx 0.4$). It can thus be concluded that in contrast to DSM, DCM enhances the image of point scatterers over that of reflecting interfaces.

3.2.3 Migration Ambiguity in Diffraction Stacks

In seismic investigations 3D effects, such as side swipes are often ignored. The subsurface is assumed to be composed of interfaces, with their normal vectors pointing parallel to the image plane. Such an assumption, however, is not valid if scattering from single isolated objects is considered. We then have to take into account that a significant amount of energy originates from the side of the seismic line. Generally speaking, energy can be contributed to the acquisition spread from the complete subsurface half space.

I will discuss the effects of imaging ambiguity and the consequences for acquisition design by the example of a vertical seismic profiling survey. The investigation will be restricted to the imaging ambiguity regarding scatterers. The investigated acquisition geometry is that of a multiple source offset VSP. A number of shots is applied from different surface locations, and the seismic response is measured with a much larger number of receivers deployed in

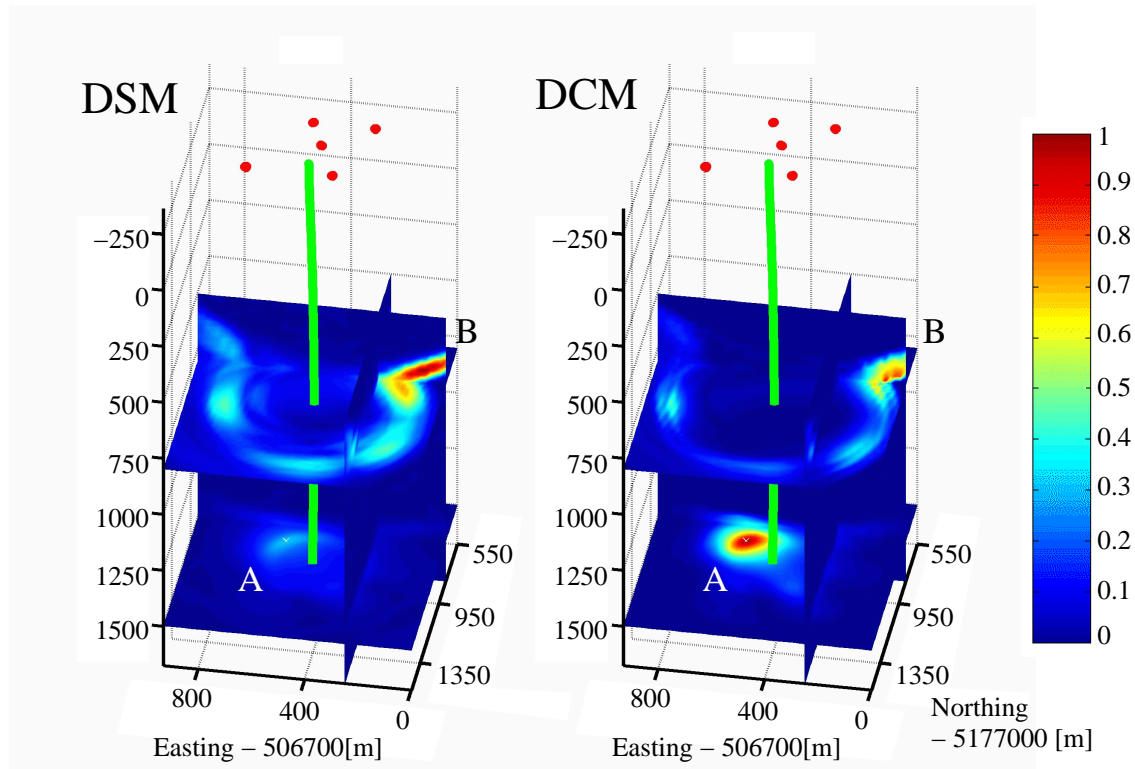


Figure 3.21: Common diffraction stack migration (left panel) compared with diffraction coherency migration (right panel). The DCM image of the scatterer (A) is brighter than that of the plane (B) ($C_{Scat}^{max}/C_{Refl}^{max} \approx 1.25$), whereas in DSM the image of the plane is brighter than that of the scatterer ($C_{Scat}^{max}/C_{Refl}^{max} \approx 0.4$).

a borehole. Such surveys were used e.g. for "investigations for the final disposal of spent nuclear fuel" (Cosma & Heikkinen, 1996) in the past and are currently used in developing a method for detecting massive volcanogenic ore deposits in Canada (Eaton *et al.*, 1996; Salisbury *et al.*, 1997). The latter application is part of chapter 4.

Figure 3.22 shows a cross section through the subsurface. It intersects one shot point located at the surface and a straight line of receivers thought to be deployed in a borehole. Plotted are the isochrone lines for each shot receiver combination and the sample position of an image point, e.g. the position of a scatterer.

As we can see from the plot, the image point is intersected by a number of isochrones, which equals the number of shot and receiver combinations, i.e. the number of seismic traces. Equations 3.37 and 3.38 describe the back projection or imaging procedure as accomplished by an integration over all directions $\hat{\xi}$ (please compare with figure 3.19). $\hat{\xi}$ is the normal vector to tangent planes of ellipses intersecting the image point. The ambiguity of the back projected image depends on the amount of spatial directions covered by $\hat{\xi}$ and thus on the acquisition geometry.

Figure 3.23 shows isochrone lines for the VSP experiment of figure 3.22 as a horizontal slice intersecting the image space in the depth of the scatterer. All tangents to the isochrone

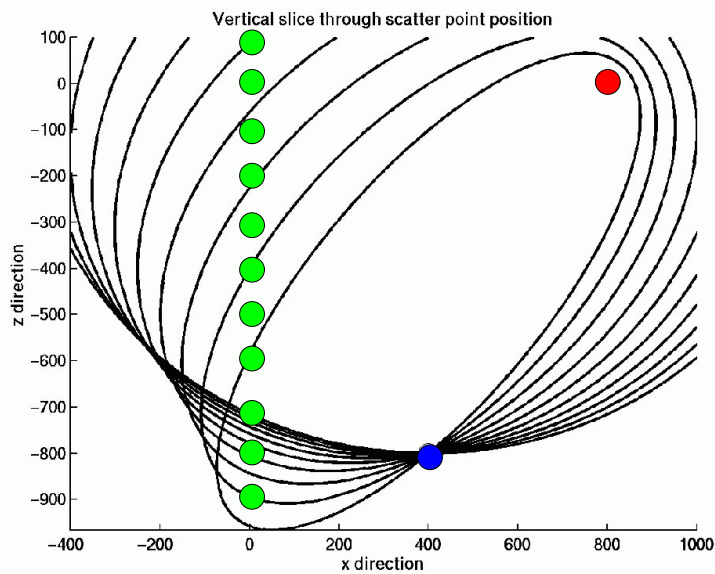


Figure 3.22: Isochrone lines in the plane intersecting one shot point located at the surface and a straight line of receivers in a borehole. The quality of the back projected image obtained by DCM/DSM depends on the amount of spatial directions covered by $\hat{\xi}$ (please compare with figure 3.19).

surfaces are parallel at the position of the scatterer. The directional coverage of the vector $\hat{\xi}$ in this plane is poor. For this acquisition geometry $\hat{\xi}$ only covers spatial directions that lie in the plane going through source and receivers. As a result only the distance of the image point to the borehole and its depth are more or less constrained. Its azimuthal position with respect to the receiver line is highly ambiguous.

Figure 3.24 shows the image that resulted from migrating synthetic data modeled for an acquisition layout with the same symmetry as depicted in figures 3.22 and 3.23. The migrated energy is confined to the depth of the scatterer, whereas its azimuthal position could not be reconstructed.

Please note the slightly skew appearance of the depth image, which is due to the local orientation of the individual isochrone surfaces, that add up to build the migrated image (please compare with figure 3.22). There will thus also be slight uncertainty in the depth and distance to the borehole that is obtained for the scatterer position. This situation will become more severe if the offset from source to borehole collar is increased.

This drawback can be overcome by e.g. applying more sources distributed in a circular arrangement on the surface, as shown in figure 3.25.

However for economical reasons VSP surveys are most often limited to a small number of shot points i.e. 5 to 6. It is then desirable to reduce the imaging ambiguity by varying the positions of the sources rather than applying a large number of them. It is neither a simple task to predict the imaging ambiguity that is produced by a given acquisition layout (survey design), nor is it easy to say which design will be the best. Figure 3.26 shows a compilation of images that were obtained after coherency migration of synthetic datasets.

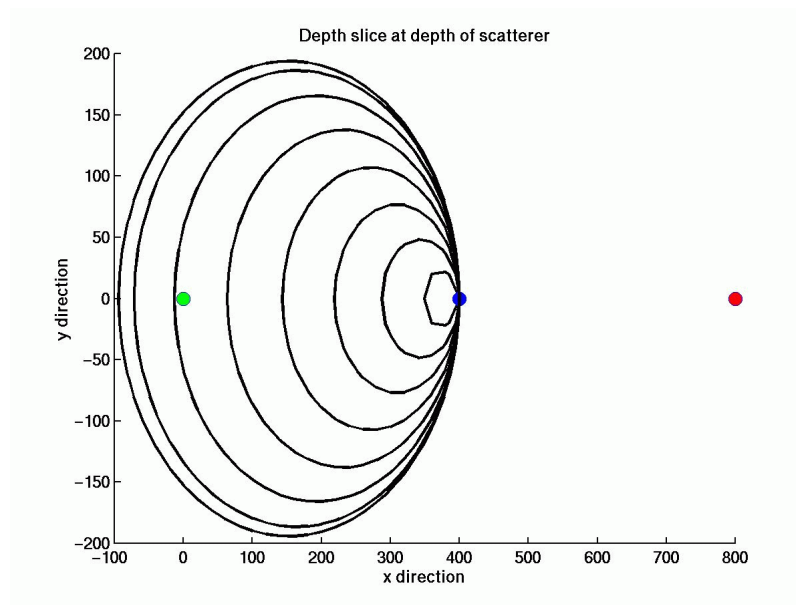


Figure 3.23: Depth slice intersecting the image space at the position of the scatterer, where tangents to the isochrone surfaces are parallel. Thus the azimuthal position with respect to the receiver line is ambiguous

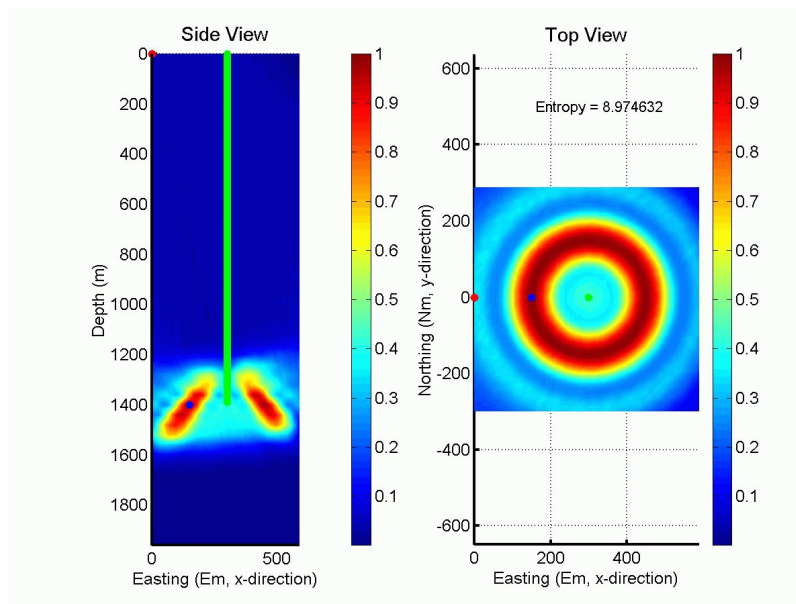


Figure 3.24: Synthetic data migration result modeled for an acquisition layout as depicted in figures 3.22 and 3.23. Energy is confined to the depth of the scatterer, whereas its azimuthal position could not be constrained.

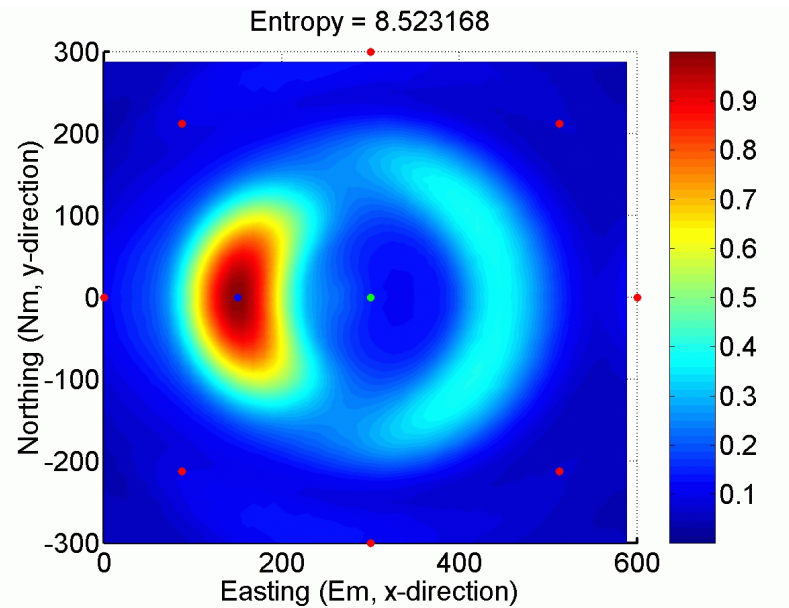


Figure 3.25: *Improving imaging ambiguity by applying more sources distributed in a circular arrangement on the surface. It is, however, desirable to reduce the imaging ambiguity by varying the positions of the sources rather than applying a large number of them.*

The data were calculated for several different shot distributions at the surface. Receivers and scatterer depth were held constant as in the configuration shown in figure 3.24.

Figure 3.26a shows a configuration with one shot point positioned $300m$ off the plane passing through the scatterer and the receiver line resulting in the same degree of imaging ambiguity as for the setup of figure 3.24. As discussed above (figure 3.22) for a single shot VSP the isochrones passing through the position of the scatterer up to a certain degree constrain its vertical position and the distance to the receiver line. High uncertainty regarding the azimuthal position of the scatterer is obtained, though. It can be expected that the deployment of more shot points increases the constraints on vertical and azimuthal position of the scatterer in the migration image. VSP acquisition geometries with different numbers of shots and different shot distributions shall now be discussed:

Azimuthal ambiguity is reduced with increasing number of shot points (e.g. figure 3.26b,c,d). The configuration shown in figure 3.26e uses six shot points and highly constrains the azimuthal position of the scatterer.

If we break the radial symmetry of the shot distribution like in figure 3.26f, ambiguity seems to be even more reduced. In contrast to the setup shown in figure 3.26e only four shot points were used.

In order to judge which acquisition layout shows highest certainty, while using as few shots as possible, a quantitative description of imaging ambiguity in DCM/DSM is required.

One single amplitude maximum found exactly in the position of the scatterer with all other amplitudes being comparably small, would rate a migration result as non ambiguous. If more than one possible position for the scatterer is found in the migrated image, the amount

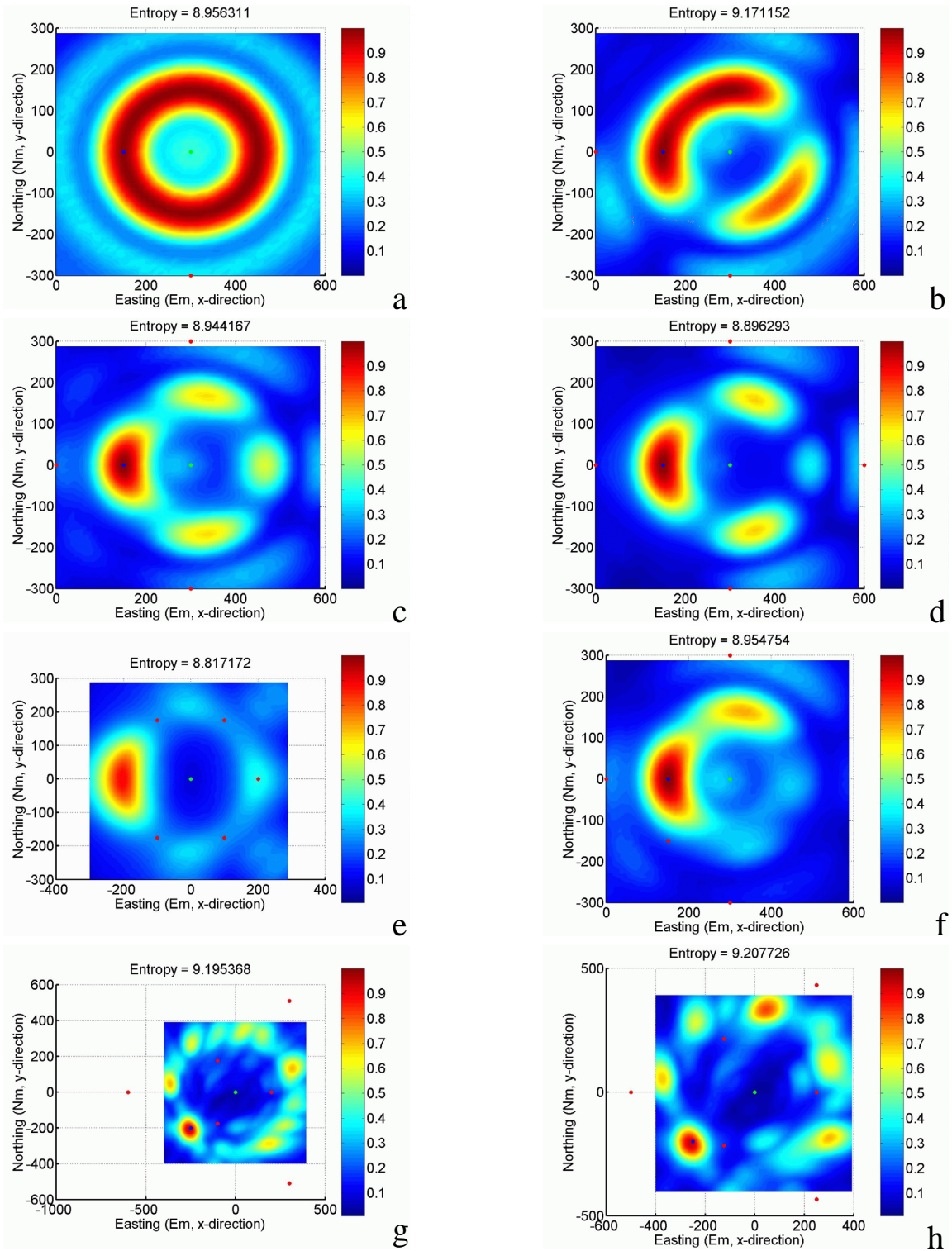


Figure 3.26: Compilation of images obtained after migrating synthetic datasets calculated for several different shot distributions at the surface with receivers and scatterer depth held constant as in figure 3.24. Entropy H is introduced as a measure for the degree of ambiguity and plotted along with each configuration.

of ambiguity has increased. A state of high ambiguity thus corresponds to a state of high disorder and a state of low ambiguity to a state of order in image space.

As a possible measure for the degree of ambiguity in DCM/DSM images I propose to use entropy H , which measures order and disorder in a set of data values (e.g. Press *et al.*, 1994; Goltz, 1998).

If N is the number of grid points of the image space Ξ and N_k is the number of amplitude classes k found in the image then $p_k = \frac{N_k}{N}$ is the probability of k in Ξ . The entropy of Ξ is defined by:

$$H = - \sum_{k=1}^{k_{max}} p_k \cdot \ln(p_k) \quad (3.44)$$

its minimum value is $H = 0$, corresponding to complete order and its maximum value is $H = \ln(k_{max})$, corresponding to complete disorder in Ξ .

Considering the example with no ambiguity in the migration image, one amplitude maximum at the position of the scatterer is given which can be normalized to one. All other image points carry very small amplitudes, which can be set to zero. Only two amplitude classes are found, i.e. $k_1 = 1$ and $k_2 = 0$. For an image space of N grid points, we then find $N_{k_1} = 1$ and $N_{k_2} = N - 1$. Thus we have:

$$\lim_{N \rightarrow \infty} H = - \left(\frac{N-1}{N} \ln\left(\frac{N-1}{N}\right) + \frac{1}{N} \ln\left(\frac{1}{N}\right) \right) \quad (3.45)$$

$$= 0 \quad (3.46)$$

Entropy will also go to zero for the case of all amplitudes being equal, i.e. having only one amplitude class in Ξ .

In figure 3.26 entropy is plotted along with each migration result. Amplitude values were normalized and rounded to $1/N$, to provide comparable conditions for all migration volumes. Amplitude classes with zero probability were removed from the dataset. In all cases entropy was calculated for the complete 3d image cube.

Entropy is of the same order of magnitude for all configurations. For the radial symmetric configurations (figures 3.25 and 3.26b,c,d,e) it can generally be said that entropy is reduced with an increasing amount of shot points used.

Breaking the symmetry of the shot point distribution seems not to significantly reduce imaging ambiguity (figure 3.26f).

Some of the distributions yield good results even if only a small number of shot points is used (please compare figure 3.26g,h with figure 3.26d). It can thus be concluded that investigating the ambiguity in DSM/DCM images by automated survey design optimization can help in reducing acquisition costs.

In the next section I will describe, how polarization information can be included into the concept of DSM as an additional approach towards reducing imaging ambiguity. The method that will be described (diffraction polarization migration, DPM) is a migration technique in its own right and thus was not treated in this section.

3.2.4 Diffraction Polarization Migration

Another characteristic feature of the scattered wave field is the directional behavior of the particle motion relative to the scattered ray, i.e. its polarization. In DSM the position of the image point is known, so that the polarization of the scattered ray is known for a given background velocity model. If we know how the ray should be polarized when arriving at the receiver after it left the image point (expected polarization), we can compare it with the actually measured wave fields polarization (measured polarization). The bigger the deviation, between expected and measured polarization is, the less likely did the measured seismic energy come from the image point under consideration.

As a measure for this likeliness any suitable function $h(\beta, \mathbf{u})$ of the angle β between expected \hat{p} and measured polarization \mathbf{u} can be applied (Duveneck, 2000). Incorporating the function $h(\beta, \mathbf{u})$ into a diffraction stack will penalize all measured amplitudes which little likely have emerged from the image point in question. Imaging ambiguity, as discussed in the preceding section (see e.g. figure 3.24), can be effectively decreased since the polarization of the scattered wave field will only fit for image points that really host a scatterer. A migration procedure based on this idea will now be discussed and will be called diffraction polarization migration (DPM). $h(\beta, \mathbf{u})$ will be called the polarization alignment measure (PAM).

In order to estimate the expected polarization, we can assume, that the scatterer is composed out of several non interacting point scatterers. \hat{p} will then be given by simple Rayleigh scattering theory (equations 2.19 and 2.20). The validity of this approximation is supported by numerical modeling studies as described in section 2.3.1 and by Bohlen et al. (2000).

For the sake of simplicity and because we often have to deal with compressional wave sources in crustal and marine seismic investigations I will restrict the following discussion to the cases of $p \rightarrow p$ and $p \rightarrow s$ scattering. Figure 3.27 shows the situation for both cases as found at the receiver. In the case of $p \rightarrow p$ scattering the expected polarization \hat{p} is

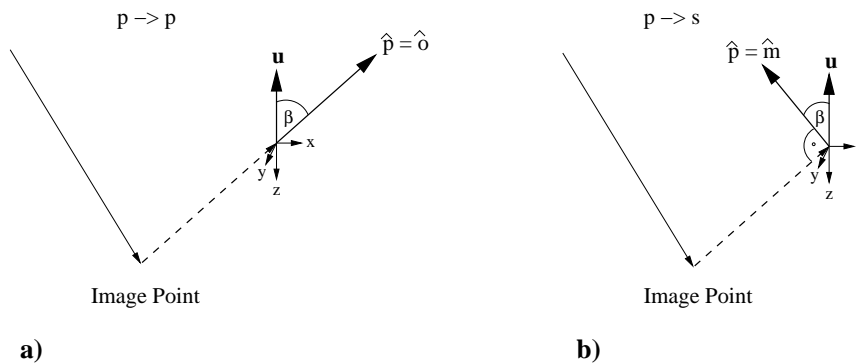


Figure 3.27: In the case of $p \rightarrow p$ scattering (a) the expected polarization \hat{p} is parallel to the direction of the emerging ray \hat{o} . For the case of $p \rightarrow s$ scattering (b) we find $\hat{p} = \hat{m}$ perpendicular to it.

parallel to the direction of the emerging ray \hat{o} . For the case of $p \rightarrow s$ scattering we find $\hat{p} = \hat{m}$, the meridian direction.

DPM is implemented into the formalism of DSM in analogy like it was done in the case of DCM (section 3.2.2):

The DSM image $\langle f(\mathbf{y}_0) \rangle$ is obtained by integrating recorded data values along the RTS $R_{\mathbf{y}_0}$. This compares to the image $\langle f'(\mathbf{y}_0) \rangle$ obtained by summing the values of the function $h(\beta, \mathbf{u})$ along the RTS. In both cases the RTS is a function of shot, receiver position s, r and the image point in question \mathbf{y}_0 . Integration is carried out over all available data. In contrast to DCM, the resulting DPM image will show the oscillatory nature of the source signal.

The migration procedure can thus be described by the following equation:

$$\langle f'(\mathbf{y}_0) \rangle = \frac{1}{MN} \sum_{i=1}^M \sum_{j=1}^N h(\beta_{ij}^m(\mathbf{y}_0, \mathbf{u}_{ij}(\tau_{ij}^m(\mathbf{y}_0))), \mathbf{u}_{ij}(\tau_{ij}^m(\mathbf{y}_0))) \quad (3.47)$$

where \mathbf{u}_{ij} is the scattered wave field recorded at the receiver \mathbf{r}_j with the source in s_i .

m is the type of scattering mode conversion assumed, e.g. $p \rightarrow p$ or $p \rightarrow s$.

$\tau_{ij}^m(\mathbf{y}_0)$ is the travel time from the source s_i via the point \mathbf{y}_0 to the receiver \mathbf{r}_j for mode m .

$\beta_{ij}^m(\mathbf{y}_0, \mathbf{u}_{ij}(\tau_{ij}^m(\mathbf{y}_0)))$ is the angle between expected and measured polarization as found in \mathbf{r}_j .

M and N are the number of shots and receivers, respectively.

Several different explicit forms for $h(\beta, \mathbf{u})$ were suggested and investigated by Duveneck, (2000):

$$\begin{aligned} h_I &= \mathbf{u} \cdot \hat{p} = u \cos(\beta) \\ h_{II} &= \cos^9(\beta) \\ h_{III} &= \begin{cases} \cos^9(\beta) & \text{if } |\cos^9(\beta)| > 0.95 \\ 0 & \text{else} \end{cases} \\ h_{IV} &= \begin{cases} \mathbf{u} \cdot \hat{p} |\cos^9(\beta)| & \text{if } |\cos^9(\beta)| > 0.95 \\ 0 & \text{else} \end{cases} \end{aligned} \quad (3.48)$$

Figure 3.28b shows the model of a massive volcanic ore deposit related to the crustal seismic case history discussed in section 4.2. The seismic response as depicted in figure 3.28a was calculated using the finite difference algorithm as described in section 2.1.3 and provided by Bohlen (1998). An acquisition geometry with one shot point and a straight receiver line deployed in a bore hole was simulated (crustal VSP survey). Modeling parameters are given in table 3.2.

Figure 3.29a shows the image that results when applying DPM to the synthetic seismic data set. As the polarization alignment measure h_I (equation 3.48) was used.

Strong events (marked as S in figure 3.28) heavily distort the image of the scatterer, because a single high amplitude data value will produce a very strong isochrone contribution in image space. In real seismic data we would have to deal with strong reflections in addition. The imaging approach has thus to be refined by a normalizing procedure during or prior to migration that scales down strong events in the seismogram to approach those of scattered or diffracted waves.

Background medium	Orebody	Perturbation
$v_p = 6000 \text{ m/s}$	$v_p = 5500 \text{ m/s}$	$\delta v_p/v_p = \delta v_s/v_s = -0,083$
$v_s = 3000 \text{ m/s}$	$v_s = 2750 \text{ m/s}$	$\delta \lambda/\lambda = \delta \mu/\mu = 0,34$
$\rho = 2,7 \text{ g/cm}^3$	$\rho = 4,3 \text{ g/cm}^3$	$\delta \rho/\rho = 0,59$

Table 3.2: Material parameters of the orebody model depicted in figure 3.28b as were used in the finite difference simulation.

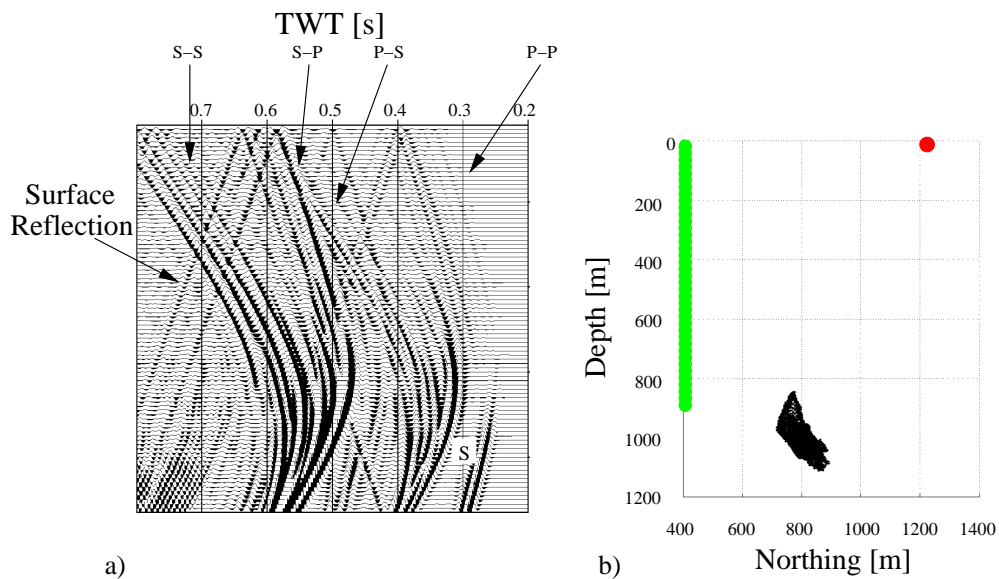


Figure 3.28: a) 2D finite difference seismogram (a) and input model (b) for a synthetic single shot VSP. The scattered wave field shows strong dynamic variations (S), that have to be normalized prior to or during the imaging procedure.

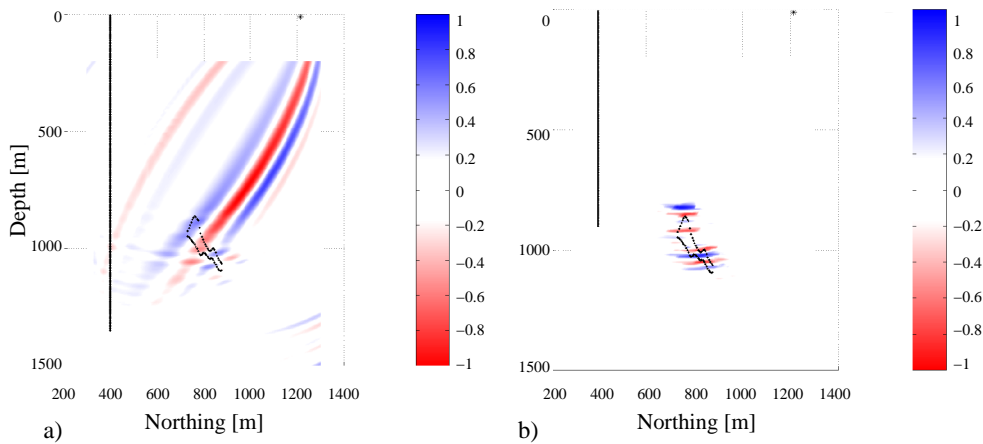


Figure 3.29: a) resulting image after applying DPM to the model depicted in figure 3.28. The polarization alignment measure was chosen to be $\mathbf{u} \cdot \hat{\mathbf{p}} = u \cos(\beta)$ (h_I in equation 3.48). b) DPM result after limiting the receiver range and introducing a strict aperture rule into the PAM (h_{III} in equation 3.48) (Duvneek, 2000).

Within the migration process this can be accomplished by dropping the amplitude information in the function $h(\beta, \mathbf{u})$, like it is done for h_{II} and h_{III} in equation 3.48

Normalization can also be achieved by applying a moving window gain prior to migration, which is simultaneously applied to all three components for each shot receiver combination and preserves their directional information.

Figure 3.29b shows the result of DPM after limiting the receiver range and using the function h_{II} as the polarization alignment measure. The image of the assumed scattering body is now confined to its outline.

3.3 Conclusions

Several different processing methods that are capable of enhancing the seismic response of isolated scattering objects were discussed in this section. Two new concepts, based on common geometrical attributes and prestack migration were introduced.

A processing method that is aimed at resolving shape and composition of a single scatterer has to focus on gaining and preserving as much scattered energy as possible, since the scattered seismic signal is weak by nature.

The CDP processing approach does not account for the kinematic and dynamic characteristics of the scattered wave field. Due to the NMO correction applied in individual CDP gathers prior to stacking, only near offset scattered or diffracted energy will be enhanced. Strong portions of scattered seismic energy however can contribute to the far offset domain, e.g. by dominant side or forward scattering. Even in DMO processing, NMO stretch will still destroy this part of the scattered wave field.

For most of the gather orientated methods such as the SES, CPP and CSA approaches the position of the scatterer has to be known a priori, or has to be iteratively determined. In

all the cases discussed in detail a reliable velocity model of the background medium has to be given in order calculate the travel time of scattered energy and to apply static travel time corrections.

A new 3D migration technique based on diffraction stack migration (DSM) was introduced. The method uses either coherency (DCM) or polarization information (DPM) of the scattered wave field.

In case of scalar wave field registration coherency measured along reflection time surfaces in the dataset, detects scattered energy (DCM). The resulting migrated cube enhances images of scattering centers over those of reflector elements. Since the image is composed from resulting coherency values, true amplitude information is lost. The image obtained by applying DSM to scalar VSP and surface seismic surveying data is ambiguous. The degree of ambiguity depends on the spatial distribution and the number of shot points being used in the survey. Entropy is proposed as an ambiguity measure and can serve as object function for an automated survey design optimization algorithm.

For three component seismic data sets, the comparison of measured and expected polarization is another possible way to distinguish scattered from reflected or non coherent seismic energy (DPM). Imaging ambiguity is greatly reduced if such information is included in the DSM process. High amplitude seismic events need to be scaled down by normalization during or prior to migration, so that true amplitude information is lost, as in DCM.

Chapter 4

Field Data Examples

In order to evaluate the processing approach discussed in chapter 3 the processing sequences proposed in appendix B were applied to marine and crustal seismic data sets.

High frequency seismic surveys were conducted in the Baltic Sea in the northern area of Kiel Bay, Germany, utilizing a boomer source and a multichannel streamer array. Several surveys were carried out between 1997 and 1999. Data were acquired by the former Institute of Geophysics (IFG-Kiel), which is now the Department of Geophysics within the Institute of Geosciences at Kiel University. Since the size of possible scattering objects in the Baltic Sea is expected to be of the order of one up to a few meters, a Boomer was used as seismic source. On one hand it was intended to study the feasibility of using a boomer source in multichannel marine seismic acquisition and in a high resolution 3D seismic survey. On the other hand these surveys were aimed towards finding seismic scattering objects and test the algorithms described in the preceding section.

The second data set was acquired by the Continental Geosciences Division (CGD) of the Geological Survey of Canada (GSC) in Ottawa. The GSC hosted a workshop on September 6, 1996 from which a joint research program was initiated. This research has focused on the new application of vertical seismic profiling (VSP) techniques to mineral exploration problems. The Downhole Seismic Imaging (DSI) consortium intends to reconstruct an image of the subsurface from reflected and scattered seismic waves. The main target of their investigations are massive volcanogenic ore deposits hosted in crystalline felsic and mafic background rocks.

In the following I will describe the performance of the proposed processing sequences for both, the marine and the crustal seismic data sets.

The marine case history (section 4.1) will include a description of performance of the boomer source when deployed in multichannel marine seismic data acquisition (section 4.1.1). Scattering is a three dimensional phenomenon by nature and thus, in order to image seismic scatterers the need for 3D seismic data acquisition and processing arises. In section 4.1.2 first tests towards high frequency 3D seismic surveying using Boomer sources will be discussed. The information obtained from area mapping is used as a basis for regional (section 4.1.2) and local (section 4.1.2) geological interpretation. Finally results from DCM as ap-

plied to high frequency multichannel seismic data will be given (section 4.1.3).

In section 4.2 a review of the geological settings, seismic acquisition and processing from two different VSP surveys aimed towards imaging of massive volcanogenic mineral (VMS) ore deposits will be given. The first case history describes a single source three component VSP survey conducted in Matagami, Quebec (section 4.2.1). Since it is well documented that the Matagami Bell Allard VMS deposit generates a measurable scattering response, DCM as well as DPM was applied to the acquired data set, to serve as a benchmark for the performance of both algorithms. The second crustal seismic case history (section 4.2.2) is dealing with a multi source multi offset three component VSP survey, which was conducted in Sudbury, Ontario. It serves as a very recent DSI research example. Only DCM was applied to this data set for the first time providing a 3D image of possible scattering centers in the crystalline crust obtained from VSP/DSI surveying. Since DCM is a scalar migration technique only the vertical component was used for migration. Arising imaging ambiguity will be discussed.

4.1 Marine Seismic Case History

Figure 4.1 shows the area of the Baltic Sea that was subject to marine seismic investigations carried out between 1997 and 1999. In shallow marine environments high-resolution seismic surveys commonly apply boomer sources in combination with a single channel hydrophone streamer to map horizontally stratified sedimentary interfaces in a two dimensional profiling fashion. Diffraction events found in single channel recordings are interpreted as scattering responses from shallow, isolated objects or sharp discontinuities of otherwise continuous geological features. Possible scattering objects range from ship wrecks and old ammunition to boulders and gas accumulations within the sediments. The typical size of these objects (man made or geogenic) range from less than one meter up to several meters and are often found buried in Holocene horizons and thus in direct vicinity to the sea floor. To make them the target of marine seismic investigations a broadband seismic source like the boomer with an appropriate wavelengths spectrum ranging from a few up to several meters and a penetration depth of up to fifty meters thus is a natural choice. Since scattered seismic energy is distributed to all spatial directions, it is necessary to deploy a large offset multichannel hydrophone array as sensor in order to record as much scattered energy as possible.

The aim of the investigation was to study the feasibility of applying high frequency Boomer sources in multichannel marine seismic data acquisition and to proceed step by step towards 3D seismic acquisition technologies. The area of investigation was selected due to scattering observed on earlier acquired 2D seismic sections.

In a first approach, between 1997 and 1998 seismic acquisition, was conducted along a wide spread grid of long 2D profiles (indicated by lines in figure 4.1). The collected data was used to investigate repeatability of the Boomer source and to establish regional settings of the geology in the study area (Riedel, 1998; Brughmans, 2000). During the experiments different types of boomers and multichannel streamer arrays were used. A much denser grid

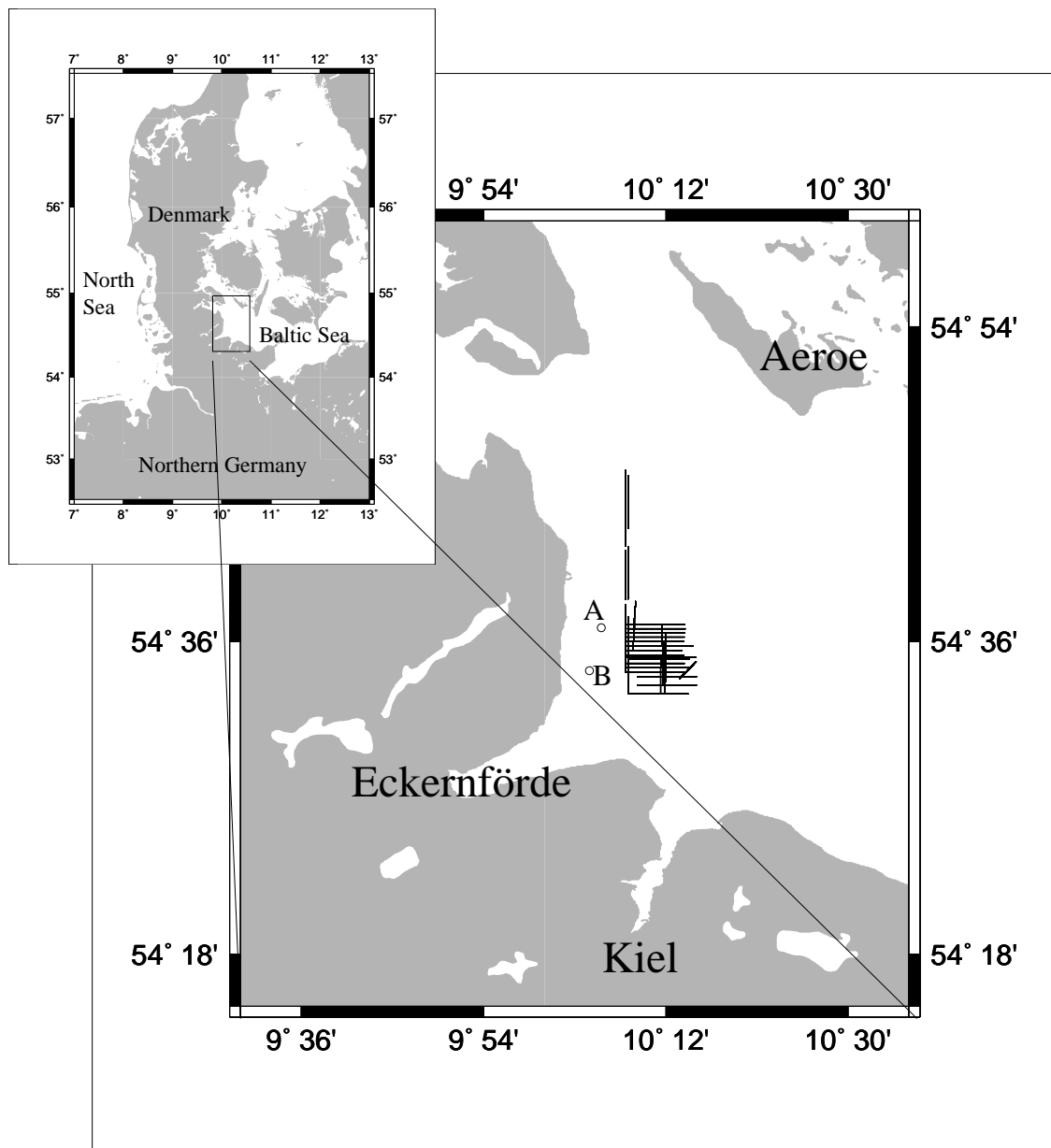


Figure 4.1: Overview of the area subject to high resolution multichannel marine seismic surveys conducted between 1997 and 1999. The lines in the enlargement indicate the position of a wide grid of 2D profiles that were sailed in a first approach towards developing a 3D seismic acquisition system using Boomer sources. A and B are locations of two oil platforms in the area.

of parallel seismic lines was acquired in a survey conducted in 1999. This high resolution $2\frac{1}{2}$ D survey served as the next step towards 3D seismic acquisition. In the following I will discuss technical details such as source stability/repeatability and the influence of the streamer array effect on the recorded seismic signal. Following this, I will briefly review the main results from conventional 2-D seismic data acquisition and processing. Results from the $2\frac{1}{2}$ D survey and corresponding 3D structural interpretation will be discussed subsequently. Finally I will investigate the performance of diffraction coherency migration (DCM) in comparison with diffraction stack migration (DSM) regarding the task of enhancing the image of seismic scatterers and structural discontinuities in the subsurface.

4.1.1 High Frequency Multichannel Data Acquisition in the Baltic Sea

The use of multichannel streamer arrays in conjunction with boomer sources is not common in marine seismic acquisition. Group length and number of hydrophones within a group in available streamers are most often tuned to suppress the direct arrival of air gun seismic sources. The streamers used for the discussed investigations were thus not explicitly constructed to be applied with boomer sources. The array characteristic that is imprinted on the recorded seismic data severely distorts the signal shape, as will be discussed in the following section.

In multichannel reflection seismology the stability/repeatability of the applied source is an important issue. Subsequent processing depends on the source to be stable enough to make estimates on the source signals shape that are valid for at least reasonably large portions of the survey. If the shape of the source signal changes significantly from shot to shot, deconvolution, CDP-sorting and stacking or migration may fail or perform poorly. Thus the stability of the boomer source was investigated, as will be described subsequently.

Data in all individual surveys was recorded with a shot rate between 1 Hz and 0.5 Hz. This corresponds to a shot to shot distance of 1-2 m, when accounting for the average vessel speed of 2 m/s. The sampling rate was set to $250\mu s$ in order to ensure for recording unaliased signals up to 2000 Hz frequency content. All seismic data were recorded using an 48 channel BISON seismograph.

Streamer Array Effects

During the surveys carried out between 1997 and 1999 two different types of streamers were used, whose geometrical parameters are listed in table 4.1.

The grouping effect or array characteristic effect (AE) is governed by the following law (see e.g. in Sheriff & Geldart, 1982):

$$AE(\kappa, f) = \left| \frac{\sin\left(N\frac{\pi df}{v} \cdot \sin(\kappa)\right)}{N \sin\left(\frac{\pi df}{v}\right)} \right| \quad (4.1)$$

with f being the frequency of the seismic wave field incident in an angle κ to the streamer, which has N hydrophones spaced by hydrophone interval d . v is the velocity of the background medium. The amplitude characteristic of a grouped streamer thus depends on the

assigned designations	streamer A	streamer B
number of channels	48	12
length of streamer	100m	50m
group spacing	2.0m	3.8m
group length	1.8m	0.25m
hydrophone interval	0.26m	0.09 m
hydrophones per group	8	3

Table 4.1: Geometrical parameters of streamers used for seismic surveys conducted between 1997 and 1999 in the Baltic sea.

frequency content of the seismic signal and the angle of incident at the streamer. Figure 4.2 shows a plot of equation 4.1, for streamers A and B, respectively.

A zero value of equation 4.1 corresponds to destructive interference of the grouped signals. If the frequency range of the source signal extends into this region of the plotted characteristics severe pulse shape alteration will result. In other words, if the grouping length is bigger than the wavelength of the signal as projected onto the streamer axis, a temporal interference of the signal with itself will result and lead to an alteration of the frequency and phase content of the signal.

For further processing acquired seismic data had to be band limited to frequencies smaller than 700 Hz whenever the 48 channel streamer or both streamers were used (figure 4.2 straight line). Using the seismic traces "as recorded" would result in poor performance of any typical multichannel processing step, such as stacking or migration. A great portion of useful seismic signal was lost.

Source Stability/Repeatability

Verbeek and Mc Gee (1995) investigated the signal characteristics of high resolution marine reflection profiling sources. They found that the Boomer is one of the most stable sources available. Encouraged by their work, I investigated the repeatability of two different Boomer sources that were applied during the marine surveys concerned here. The sources were a currently traded EG&G Boomer (source A) and an older one (source B) which had been rebuilt several times and thus must be regarded as costume-made. Figure 4.3 shows source spectra estimated from measured first arrivals at streamer A for both sources, 10 subsequent shots and two different offsets, 10 m and 50 m, respectively.

Predominantly we observe the interference effect of the streamer array characteristics. Direct arrivals correspond to an incident angle at the streamer of 90° , for which we find destructive interference at approximately 700 Hz and 1500 Hz signal frequency. From the spectra we can already estimate that for near offsets the low frequency part of the spectra is more stable than for large offsets. Source B appears to be more stable than source A. In order to get a more quantitative estimate of the repeatability I calculated the repeatability index RI as given by Verbeek and Mc Gee (1995):

$$RI = \min |S(k)| \quad (4.2)$$

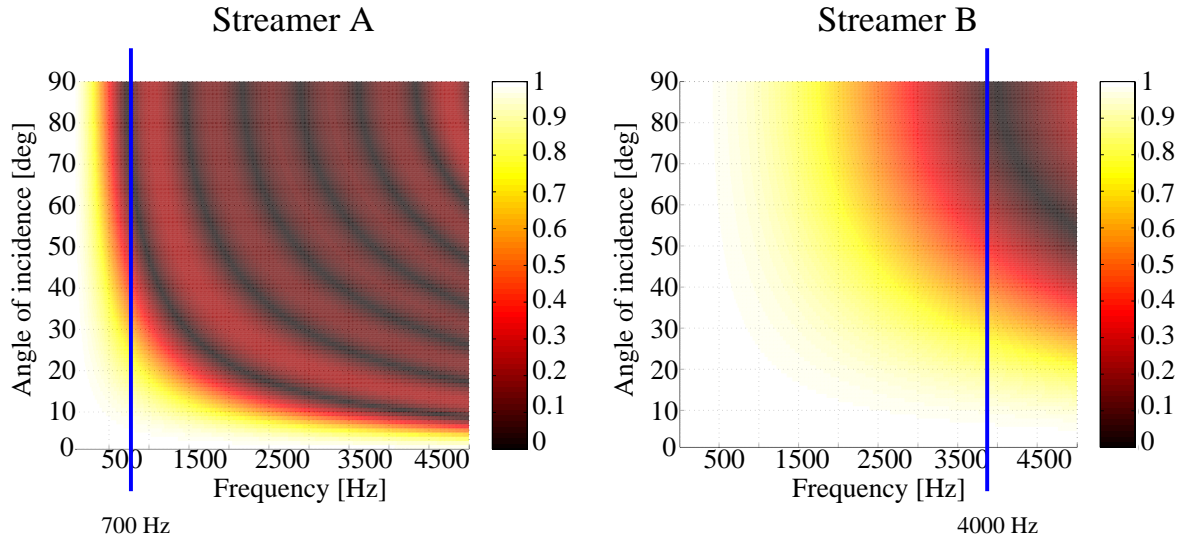


Figure 4.2: Streamer characteristics (equation 4.1) for streamer A and B with geometrical parameters as listed in table 4.1. The boomer source emits a broad spectrum of frequencies. Sampling was designed for a frequency content up to 2000 Hz. A zero value of equation 4.1 corresponds to destructive interference of the grouped signals. If the frequency range of the source signal extends into this region of the plotted characteristic severe pulse shape alteration will result. Seismic data have to be band limited (as indicated by the lines at 700 Hz and 4000 Hz) in order to avoid streamer array effects.

where

$$S(k) = \frac{\sum_{i=0}^N |S_{1i} - S_{2(i-k)}|}{\max |S_{1i}| \cdot N} \quad (4.3)$$

$S_{1(i)}$ and $S_{2(i)}$ represent two subsequent pulses digitized by samples $i=1..N$. RI gives the mean relative deviation between the two sampled signals normalized to the maximum amplitude of the reference signal (chosen to be S_1). If S_1 and S_2 are very much alike, RI will be close to zero. Poorer repeatability is indicated by larger RI values. RI is given in percent deviation from the maximum reference signal amplitude.

For each source (A, B) RI was calculated from shot to shot for a sequence of 1000 shots. As input for the analysis the direct arrival was chosen as an estimate for the source signal. Parameters varied during the investigation were offset and frequency content of the input signals.

Since the data used in this investigation was recorded in a real marine seismic experiment swell noise introduces a randomly varying static shift on the input wavelets. Veerbek and Mc Gee (1995) calculated the minimum of $S(k)$ to derive RI. This step was modified here. Static shifts of individual signals were determined and corrected by cross-correlation with an averaged source signal. RI not only measures changes in the shape of the signal but also overall amplitude fluctuations. To delineate whether deviations were introduced by variations in source strength or in signal shape, RI was calculated for either true amplitude recorded and energy balanced signals. The median (RI*) and standard deviation (STD) of each set was calculated.

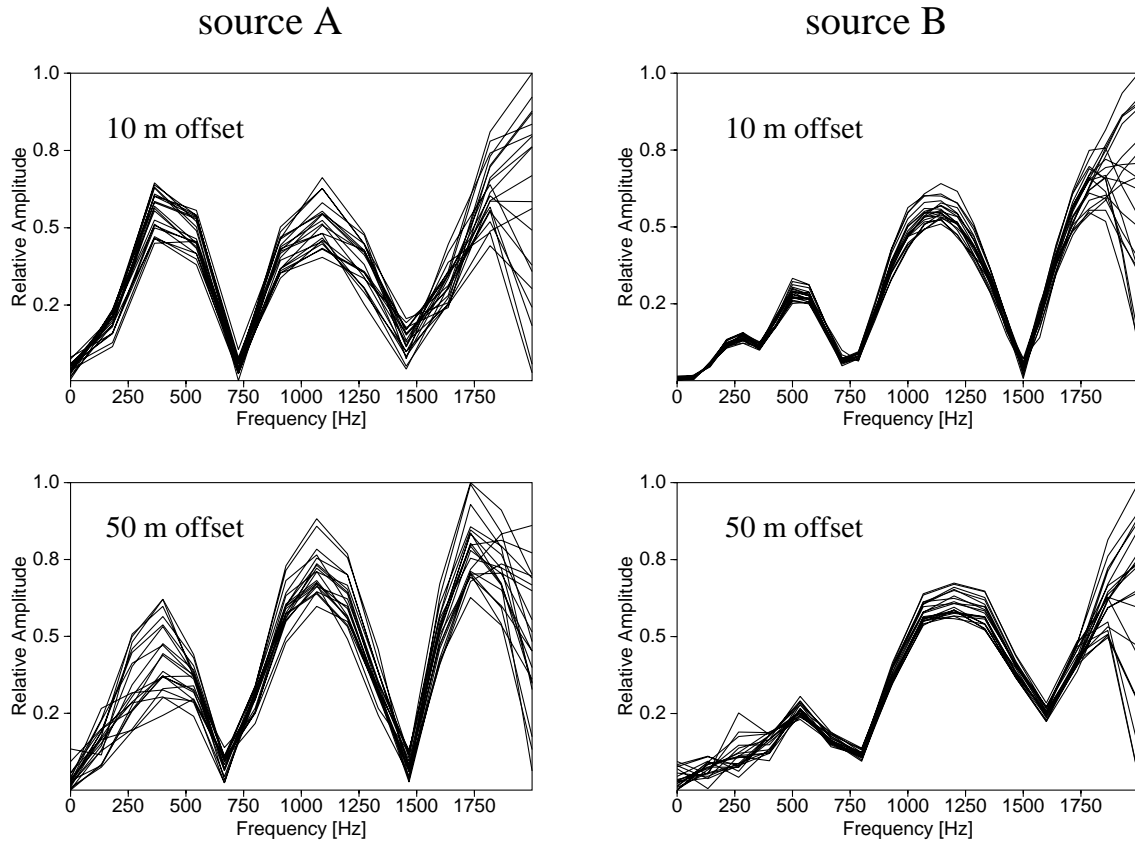


Figure 4.3: Source spectra estimated from the measured first arrival at the streamer for both sources, 10 subsequent shots and offsets 10m and 50m, respectively. The effect of the streamer array characteristics is predominantly observed in both spectra (drop outs at ≈ 700 Hz and 1500 Hz). Source A shows a broader frequency content than source B.

Figure 4.4 shows histograms of RI calculated for both sources. The signals were band limited by applying a trapezoidal band pass filter with gate frequencies $f_i = (100, 200, 600, 700)$ Hz. The chosen source receiver offset was approximately 10 m for both sources. The upper panel shows the RI histogram for true amplitude source signals and the lower panel shows histograms for energy balanced input.

For both sources RI shows smaller values and standard deviation when energy balanced input was used. The shape of the emitted boomer signals is thus more stable than the source strength. An effect that might be explained by power supply fluctuations. RI^* ranges from 0.04 and 0.08 for both sources and is significantly greater than the results obtained by Verbeek and Mc Gee.

Figure 4.5 shows histograms for RI calculated from source signals measured at 50 m offset which were filtered to contain the same frequency range as in the example above. Again, the upper and lower panels show the results for true amplitude and energy balanced input signals, respectively. The effect of energy balancing is still evident. The values for RI^* range from 0.09 for source B to 0.2 for source A and their distribution is broader than in figure 4.4. It can thus be concluded that repeatability/stability of the source signal decreases

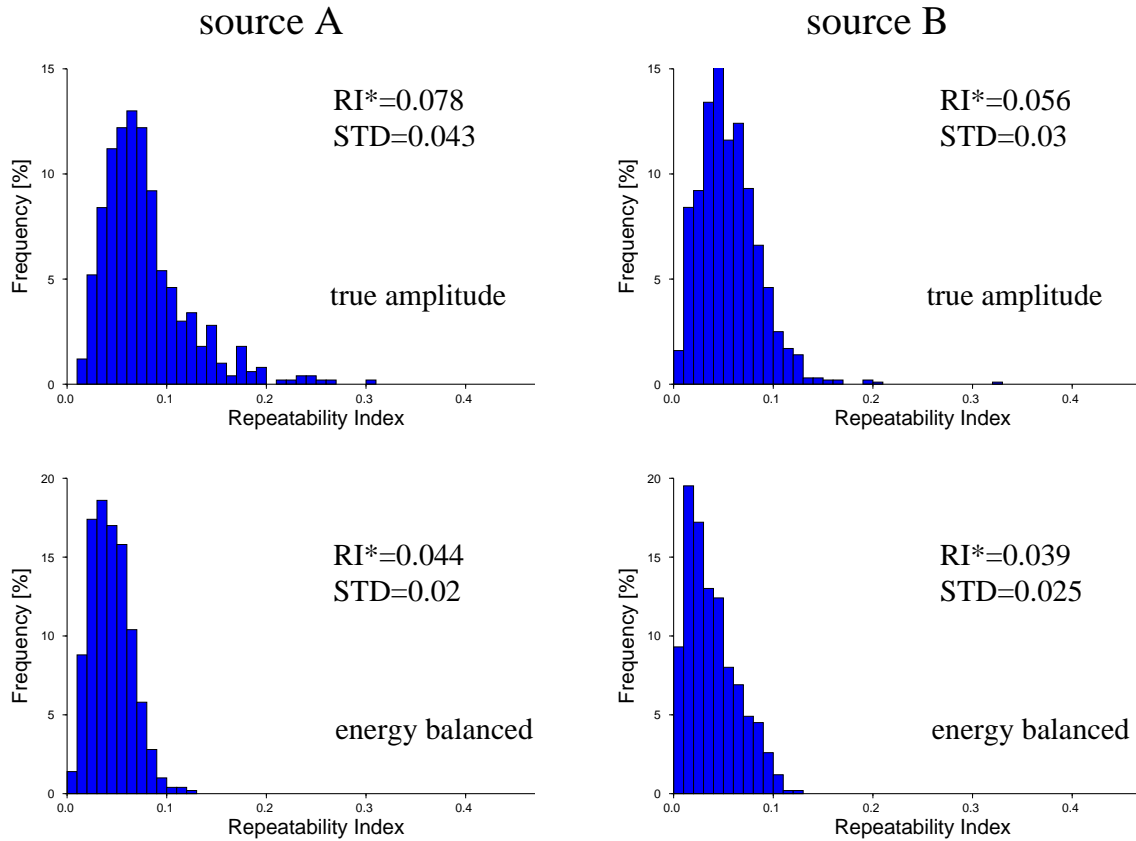


Figure 4.4: Repeatability index (RI) histograms for sources A and B. Source receiver offset was 10 m. True amplitude, as well as, energy balanced bandpass filtered signals where input to the analysis ($f_i=(100,200,600,700)$ Hz). The energy balanced signals show higher repeatability.

with increasing offset. This effect can possibly be explained by the increasing influence of the moving water surface on direct arriving seismic energy. The wave length of the Boomer signal in water is approx. 1.5m and thus could be affected by waves.

Finally figure 4.6 shows the RI histograms for energy balanced signals and an offset of 10 m. Here a broader frequency range was preserved in the input signal. The gate frequencies where set to $f_i=(100,200,1400,1600)$ Hz. We can conclude that for near offsets the lower frequency content of the source spectrum is more stable than the high frequency content (please compare with figure 4.4 lower panel). This observation still holds for greater offsets but becomes less prominent.

Summarizing it can be said that RI increases with decreasing offset and with decreasing frequency content. Variations in source strength seem to be more severe than variations in the spectra. Verbeek and Mc Gee arrive at much better RI values for the boomer source. To explain this discrepancy we have to consider, that the source signals in Verbeek's and Mc Gee's investigation were recorded with a hydrophone positioned at depth, with a offset ranging from only 2 to 20 m. No swell noise and no near surface disturbances were present as in the examples given here. In addition RI values where corrected for noise contributions,

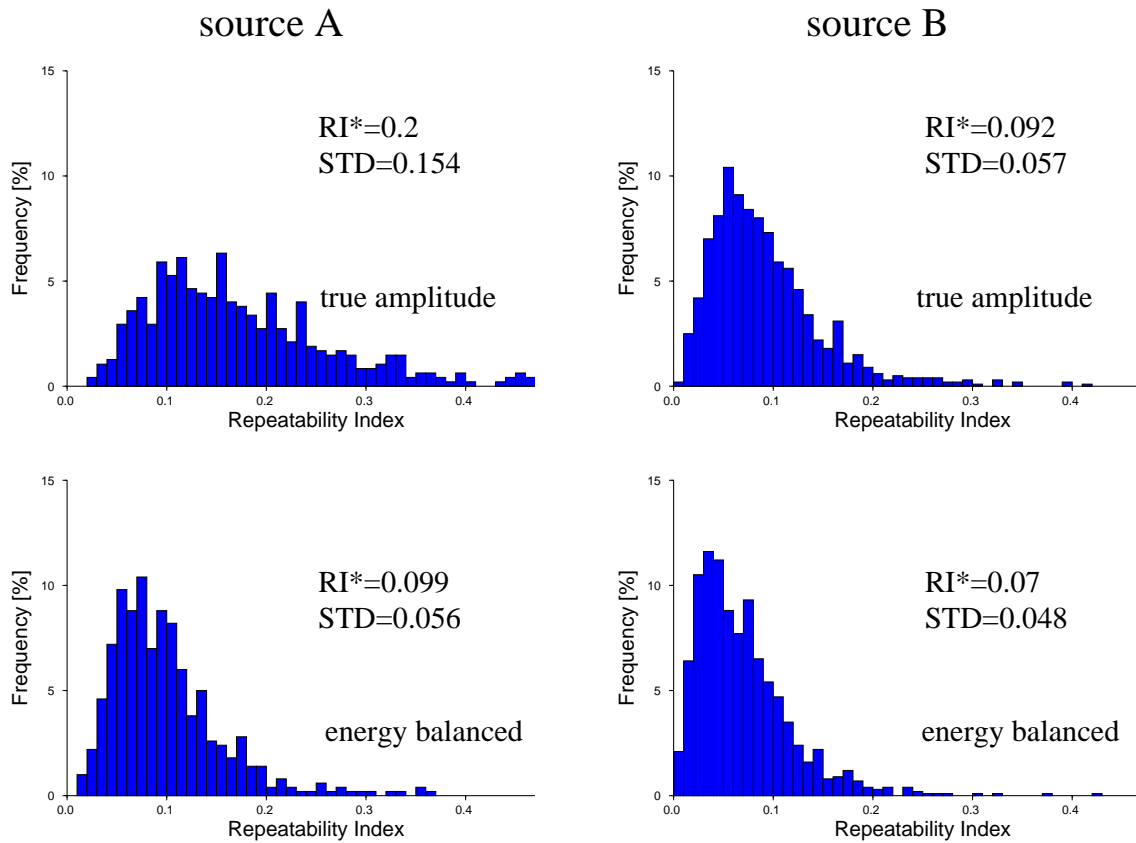


Figure 4.5: Repeatability index (RI) histograms for sources A and B. Source receiver offset was 50 m. Bandpass gate frequencies where $f_i=(100,200,600,700)$ Hz; Repeatability decreases with increasing offset.

which was avoided here, since noise will certainly decrease repeatability of the seismic signal and should be considered when RI values are calculated. The values obtained are comparable to those given for airguns. Airguns are commonly used in seismic data acquisition and have proven to be stable enough to conduct typical multichannel processing steps. We can thus expect that the boomer source will be suitable for real multichannel marine seismic field experiments and data processing.

4.1.2 Baltic Sea Scattering Objects: Geological Background

As an approach towards high frequency multichannel 3D seismic acquisition, three marine surveys were conducted 1997 and 1999. Figure 4.7 gives an overview of the sailed profiles. The data was acquired using different combinations of Boomer sources and streamer arrays. In a first step, a wide grid of 2D profiles was acquired in order to evaluate the possibility of area wide seismic mapping and geological interpretation using conventional acquisition geometry with large inter profile distances. A single Boomer source in conjunction with a multichannel streamer array was used. A regional geological interpretation was performed on the basis of the acquired seismic data and will be discussed in the following.

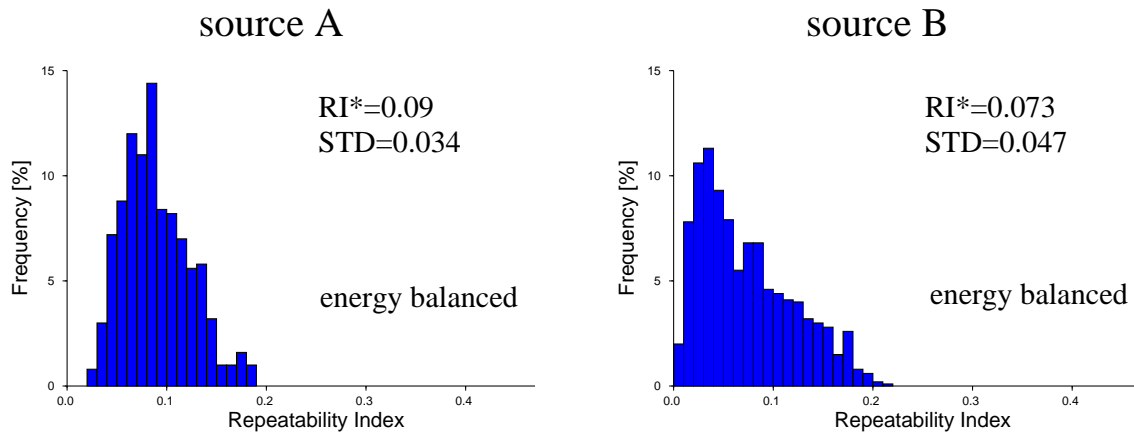


Figure 4.6: Repeatability index (RI) histograms for sources A and B. Source receiver offset was 10 m. Bandpass gate frequencies where $f_i=(100,200,1400,1600)$ Hz. Low frequencies of the signals are more repeatable than high frequencies, please compare with figure 4.4, lower panel.

Due to strong lateral variations of deeper geological features, only the sea floor could satisfactorily be mapped. Thus two additional surveys were conducted each using a different combination of streamer arrays and boomer sources. Inter profile distances were significantly reduced. For the first time a high resolution seismic data cube was acquired in the Baltic sea, providing the means for local structural 3D interpretation of local geological features. In the second part of this section, these first results from $2\frac{1}{2}$ D seismic surveying as well as the performance of two different acquisition layouts will be discussed.

Coarse Grid Geological Interpretation

Coarse grid 2D seismic acquisition surveys conducted between 1997 and 1998 were sailed using only one boomer and one streamer at a time. A set of conventional 2D marine seismic profiles was acquired. Figure 4.8 shows a sketch of the acquisition geometry the used recording equipment. Navigational information was recorded by hand at the beginning and the end of each profile. No real time processing was conducted. Multichannel data were directly recorded onto DLT tape using an 48 channel BISON seismograph. Near trace profiles were continuously recorded in order to monitor source and sensor activity and data quality.

In order to document the quality of the acquired data, figure 4.9a shows an unprocessed single shot seismogram recorded on profile 18.

As discussed in the preceding chapter, the recorded seismic data had to be band limited to the frequency range ≤ 700 Hz. Panel b of figure 4.9 is filtered with a bandpass filter ($f_i=(100,200,600,700)$ Hz) to suppress the effect of the streamer array characteristics. The gap at about 55 m is due to a link connecting two main streamer elements that built the actual 48 channel array. The enlargements shown for both panels illustrate, that the sea floor response splits up into a double pulse with increasing offset albeit a band limit to

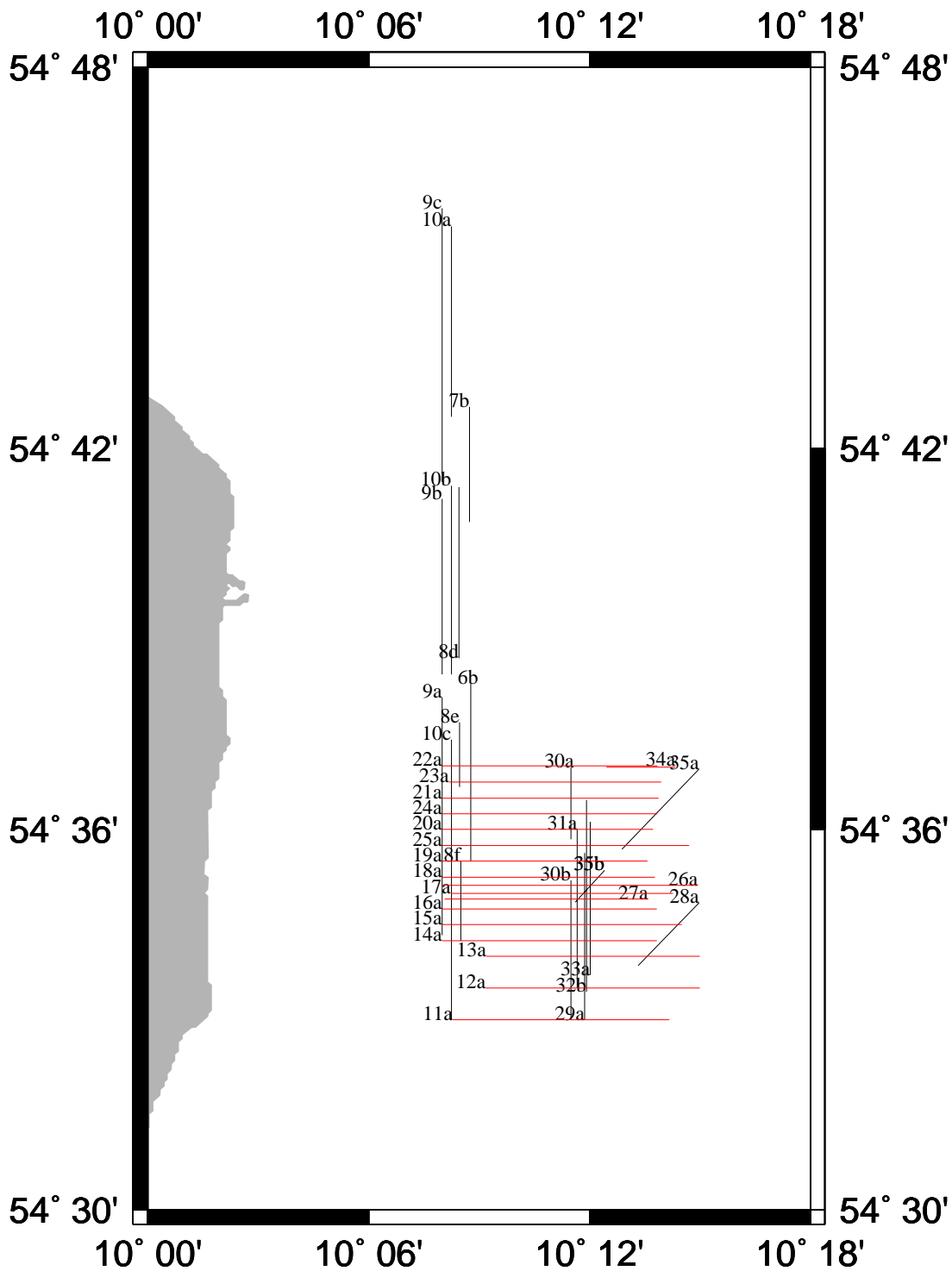


Figure 4.7: Outline of the profiles sailed as a first approach to 3D seismic data acquisition with high frequency seismic sources. The acquired seismic sections were interpreted by hand. Picked horizons on profiles plotted in red (east-west profiles) were combined to generate maps of the observed horizons (please refer to figure 4.13).

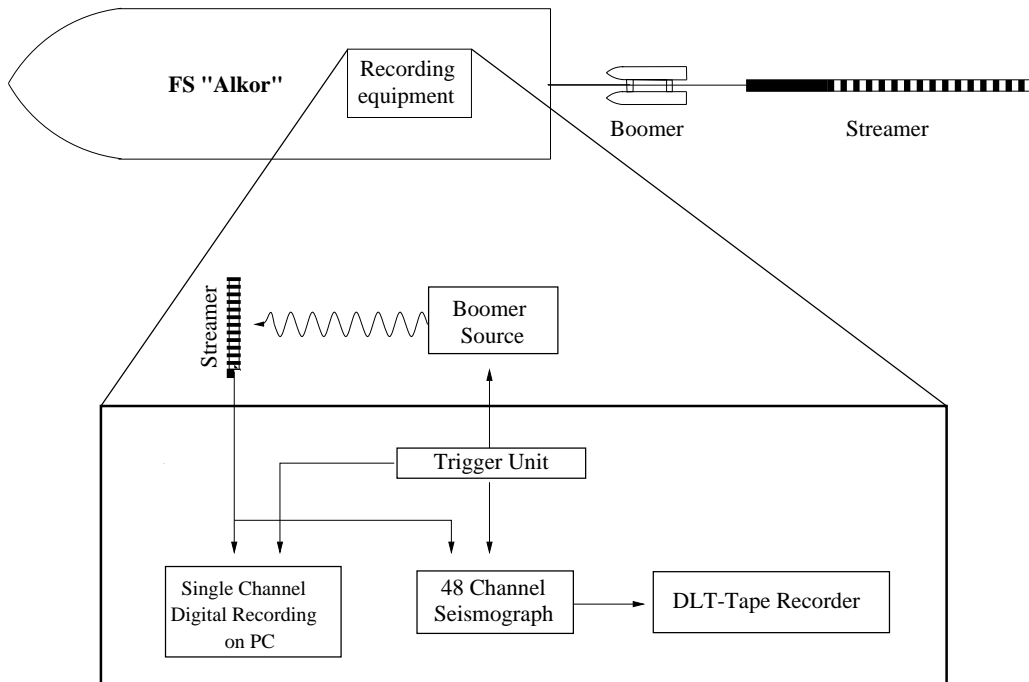


Figure 4.8: Acquisition geometry and recording equipment setup used during the wide grid 2D seismic investigation. For multichannel recordings a 48 channel BISON seismograph was used. Near trace control profiles were recorded on a PC unit.

correct for array characteristics has been applied. One explanation for this effect might be the existence of a real double layer that is only resolved with increasing offset.

For the offset range corresponding to supercritical reflection angles $\kappa_i > \kappa_c$ changes in phase of the reflected signal would also have to be expected. κ_c for the present case can be estimated to be $\kappa_c \approx 55^\circ$, assuming a water layer velocity of 1550 m/s and a reflector velocity of 1900 m/s (Riedel, 1998). This would correspond to source receiver offsets greater than approximately 56 m. In order to avoid destructive interference in stacking, for conventional reflection seismic processing the offset range of the acquired data was thus limited.

Further data processing towards the stacked zero offset section included, deconvolution, CDP-sorting, velocity analysis, NMO correction and stacking. Figure 4.10a shows part of the finally processed zero offset section for profile 18.

In order to illustrate the enhancement in data quality achieved by multichannel seismic data acquisition and processing, a single receiver seismic section is plotted in figure 4.10b. The data were extracted from the multichannel data set. The zero offset sections are characterized by six main features (please refer to figure 4.10). The sea floor is either represented by a strong till-layer reflection (1) (Pleistocene, clay, silt, sand and gravel, deposited during the end of the Weichsel glaciation (Atzler, 1995)) or by a weaker reflecting mud horizon (2) built from Holocene unconsolidated sediments, (Hinz *et al.*, 1971), which fills up the till layer basins whenever they submerge significantly below 20 m water depth. A prominent reflector situated between the mud and till horizon (3) generates a reflection

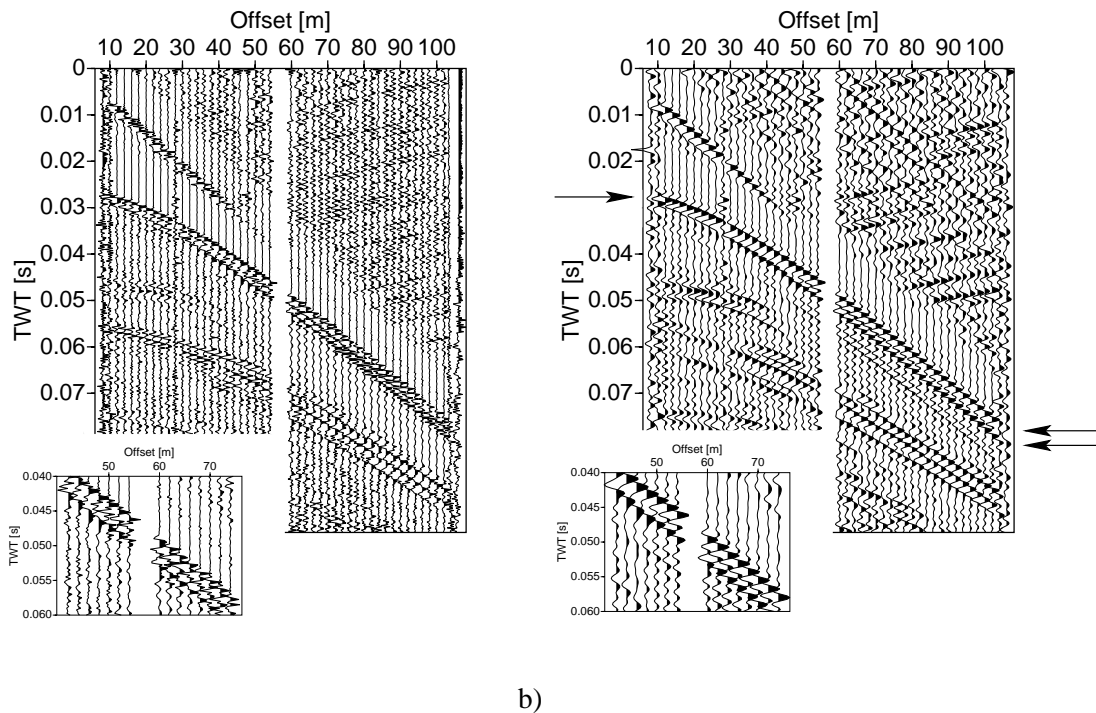


Figure 4.9: Example of a single shot seismogram to illustrate general data quality. a) Raw data. Panel (b) is filtered with a bandpass filter ($f_i = (100, 200, 600, 700)$ Hz) to suppress the effect of the streamer characteristics. The seafloor response splits up into a double pulse with increasing offset (enlargements in (a) and (b)) albeit a band limit to correct for array characteristics has been applied. It can either be explained by a real double layer that is only resolved with increasing offset or supercritical reflection.

with an inverted signal phase. Due to the observable high reflection coefficient and phase characteristics the corresponding reflector is interpreted to be a gas layer. Due to its location it can be assumed, that the gas is generated by bacteria living within the unconsolidated sediments (Lemke, 1994; Whiticar, 1978). One would usually expect the gas to migrate upwards and into the water column, since the unconsolidated sediments that built the mud do not provide a barrier for the gas. The horizon albeit seems to be quite stable and well defined in depth. This effect might be explained if we assume that the gas is either bound to the bacteria producing it, or gets caught in a e.g. biological horizon which could be built from algae. There is no proof however, that the gas is not persistently migrating upwards and supplied by a deeper source of possibly hydrocarbon origin. Figure 4.11 shows another enlargement of profile 18 (further to the east) where this horizon can be observed (3'). Besides these three main reflectors, the sections are also characterized by a second till-layer (4), which is broken up and might consist of coarser material than the sea floor till. With increasing travel times in the section we find strongly dipping features which could not be classified (5). All sections show prominent multiples (6), which aggravate the interpretation of deeper geological features.

In addition to the laterally continuous events described above, diffracted and scattered

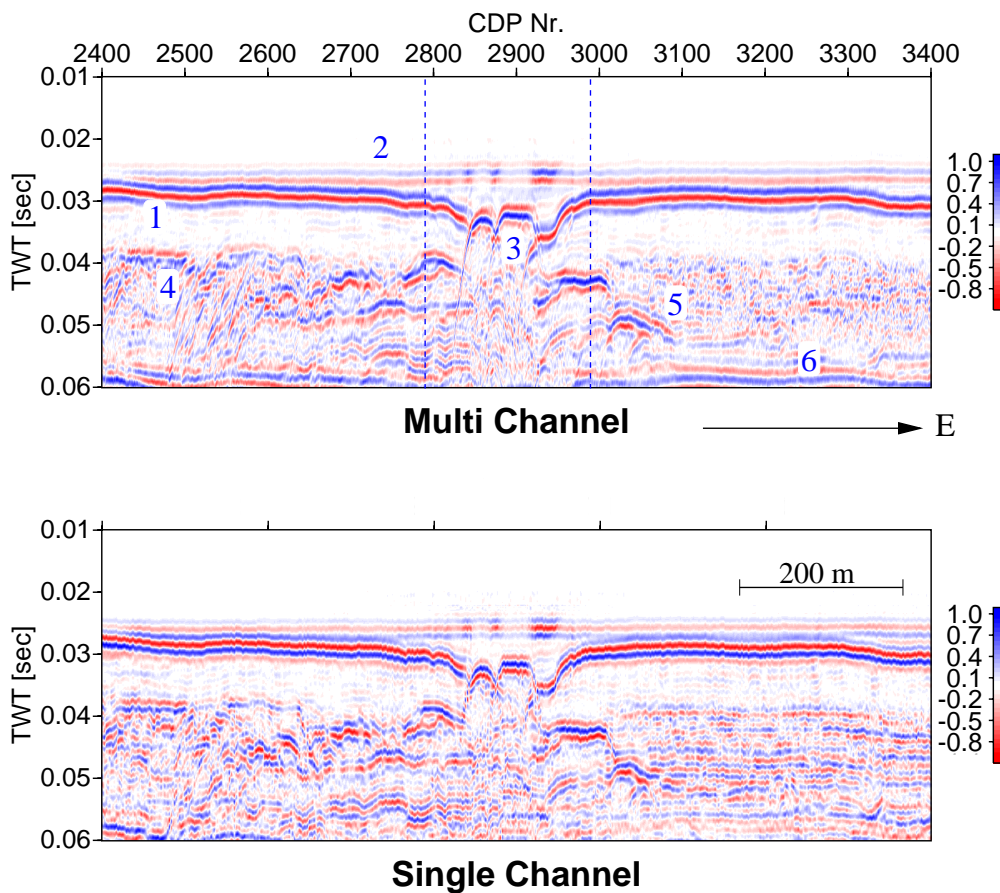


Figure 4.10: Finally processed zero offset section of profile 18 compared with single channel section of profile 18. The seafloor is either represented by a strong till layer reflection (1) or by a weaker reflecting mud horizon (2). Between the mud and till horizon a gas reflection is observed (3). The sections are also characterized by a second till-layer (4) and strongly dipping features with longer travel times which could not be classified (5). Strong multiples aggravate the interpretation of later seismic events (6).

seismic energy can be observed characterized by hyperbolic signatures in the sections (e.g. in figure 4.11 (4)).

The data collected along the profiles displayed in figure 4.7 were integrated in a coarse grid seismic interpretation as a first approach towards 3D-seismic investigations with high frequency seismic sources. With an average inter profile distance of 500 m it was not possible to compose a seismic data cube. Profiles were thus interpreted individually by picking the most prominent horizons. The travel time picks were used to generate horizon maps. Only East-West profiles, displayed as red lines in figure 4.7 were used since they were acquired in sequence under comparable weather, tide and acquisition geometry conditions. Including profiles sailed in North-South direction into the interpretation caused interpolation artefacts

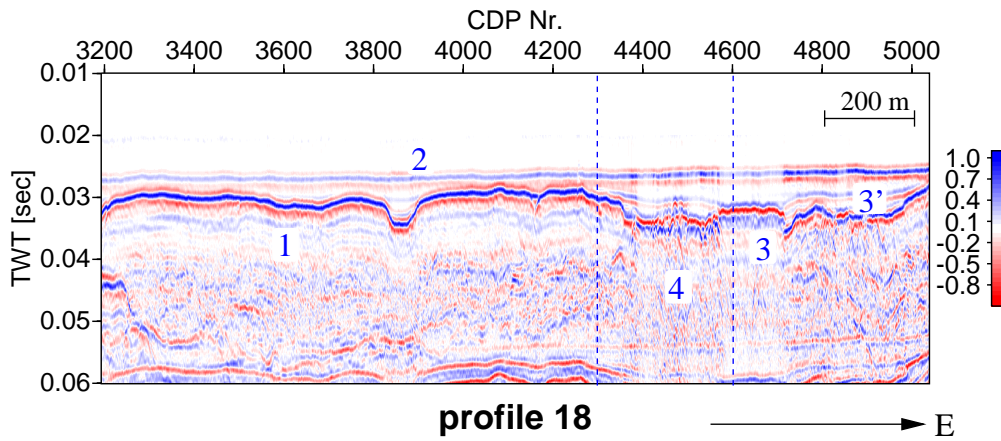


Figure 4.11: The gas related feature observed on several of the recorded sections, is well defined in depth. It seems to be generated somewhere between the till horizon and the mud layer that builds the seafloor, where a weak reflection can be observed that serves as a barrier for the upwards migrating gas (3'). In this section, gas has accumulated at the till horizon (1) and within the mud (2). We can clearly observe the phase reversal of the gas layer reflection and the shielding effect (3) of the gas. Characteristic scattering/diffraction hyperbolae are generated by small scale gas accumulations (4).

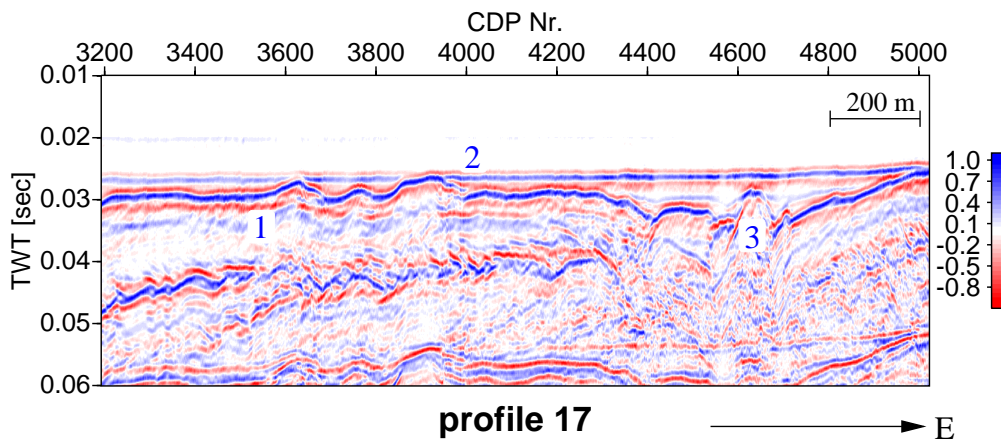


Figure 4.12: In order to illustrate the lack of continuity in horizon features from profile to profile a section of profile 17 was plotted here for comparison with figure 4.11. Several features, like distribution of gas (3) or till layer topography (1) show dramatic changes from profile to profile. Only the mud horizon building the seafloor (2) is sufficiently continuous to built a bathymetrical map (figure 4.13).

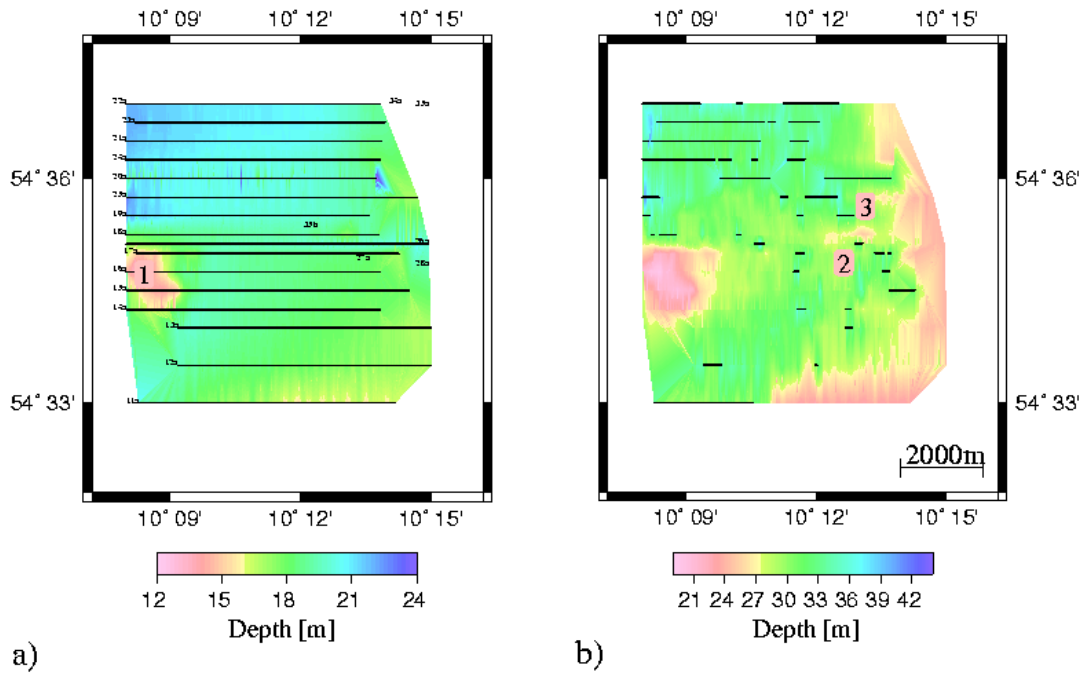


Figure 4.13: Panel a) shows a bathymetrical map composed from seafloor travel time picks (converted to depth assuming a water velocity of $v_w = 1500\text{m/s.}$; (Brughmans, 2000)). Only profiles sailed in sequence and thus under comparable weather, tide and acquisition geometry conditions were used. The water depth minimum observed at E $10^\circ 8.5'$, N $54^\circ 34.8'$ corresponds with the "Plattengrund" seafloor high (1) (please compare with figure 4.14). Panel b) shows a map composed from till-layer travel time picks. The map is dominated by a number of artefacts (2) (3), which are due to insufficient inter profile continuity of the till horizon (please compare figures 4.11 and 4.12).

facts that might be due to navigational problems.

Figure 4.13a shows the resulting maps for the sea floor horizon combining mud and till horizon, depending on whichever locally builds the sea floor. Two way travel times were converted to depths assuming a water velocity of $v_w = 1500\text{ m/s.}$ A pronounced water depth minimum is observed at coordinates E $10^\circ 8.5'$, N $54^\circ 34.8'$ which perfectly corresponds with the well documented "Plattengrund" sea floor high. Figure 4.14 shows a bathymetrical map provided by the "Bundesamt für Seeschifffahrt und Hydrographie" (Hamburg, Germany) for comparison.

Panel b of figure 4.13 shows a map composed from till-layer travel time picks. The map is dominated by a number of artefacts facts, which are due to insufficient inter profile continuity of the till horizon (Brughmans, 2000). Figure 4.12 in comparison with figure 4.11 illustrates insufficient lateral continuity of the till layer horizon as observed on profile 17 and profile 18. In order to compose a 3D seismic data cube the inter profile distance

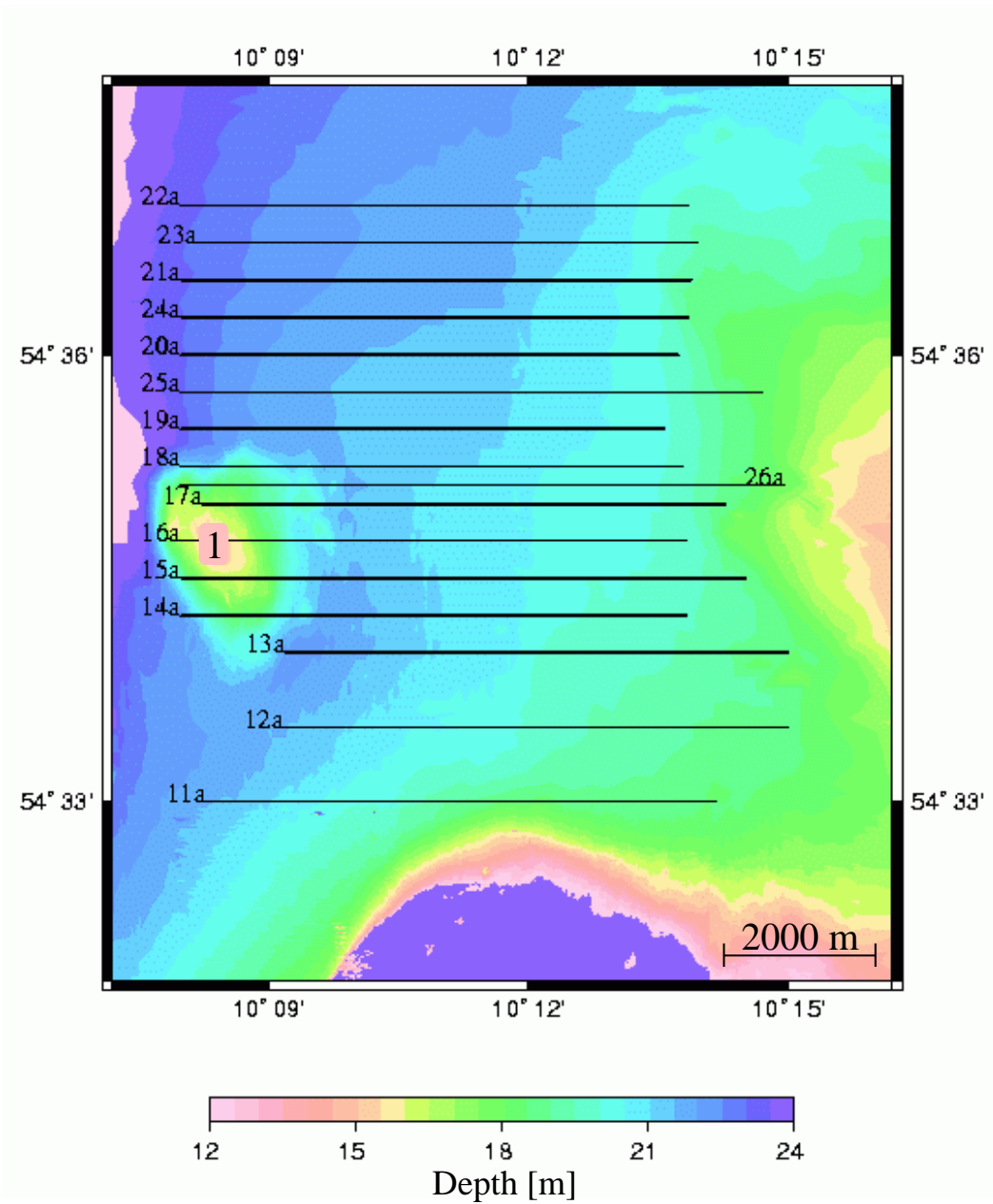


Figure 4.14: The bathymetrical map shown here was provided by the "Bundesamt für Seeschifffahrt und Hydrographie" in Hamburg, Germany. In comparison with figure 4.13a we find rather good agreement in the calculated seafloor topography. Figure 4.13b, however, still shows obvious artefacts. The profiles used to compose figure 4.13 are plotted for convenience. (1: "Plattengrund" seafloor high)

thus had to be significantly reduced. The enhancements achieved in seismic imaging and interpretation as well as experience that was gained with the deployed acquisition layouts will be discussed in the following section.

High Frequency 3D Seismic Survey

In May and August of 1999 two additional marine surveys were conducted in order to overcome the interpretation drawbacks encountered during the coarse grid investigations described in section 4.1.2. It was intended to collect seismic data on densely spaced profiles in order to provide sufficient lateral continuity between seismic lines. The investigation was now focussed on the area in close vicinity to the diffracting gas accumulations observed in earlier surveys e.g. on line 18 as shown in figure 4.10. As an enhancement to the acquisition pattern already shown in figure 4.7 the inter profile distance was significantly reduced and chosen to be 20 m. It is worth noting, that with a vessel like the "FS Alkor" it is not a simple task to sail such tightly spaced profiles. As shown in figure 4.15 in each survey a different acquisition pattern was used.

In May 1999 data were acquired by sailing patterns of propagating rectangles, like it is quite common in marine 3D-seismic acquisition (figure 4.15 (A)). Due to the small inter profile distance this acquisition scheme proved to be not very efficient. Only slow progress was made in covering a significant area of connected profiles and much time was lost on the transit from one set of profiles to the other (a-a'). In August it was thus decided to sail a "weaving" pattern¹ as displayed in panel B of figure 4.15 which was much more efficient. For transit (b-b') the vessel just turned on a tight circular course.

In state of the art marine 3D seismic surveying it is common to use a combination of several sources and streamer arrays in order to acquire as many profiles as possible while sailing one acquisition line. Thus two different acquisition layouts were tested using

1. two sources and one streamer array, and
2. one boomer source and two streamers.

Figure 4.16 illustrates these two designs along with a schematic of the recording equipment that was used.

Layout A was used in April and layout B was used in May (see also figure 4.15):

For layout A two boomer sources, each mounted on a small catamaran that served as a buoyancy device, were towed to the side of the vessel. Cables were connected in a way that each catamaran would drift to a distance of approximately 10 m side ways from the boat. During acquisition there was severe wave action. The sources tended to dive and were difficult to stabilize in a well defined position. In addition there was strong tension on the cables and on the power lead in. As the sensor a 48 channel streamer array was used (please refer to table 4.1 for streamer parameters). It was positioned on the center line off the boat and was quite stable.

¹This pattern was suggested by the captain of "FS Alkor".

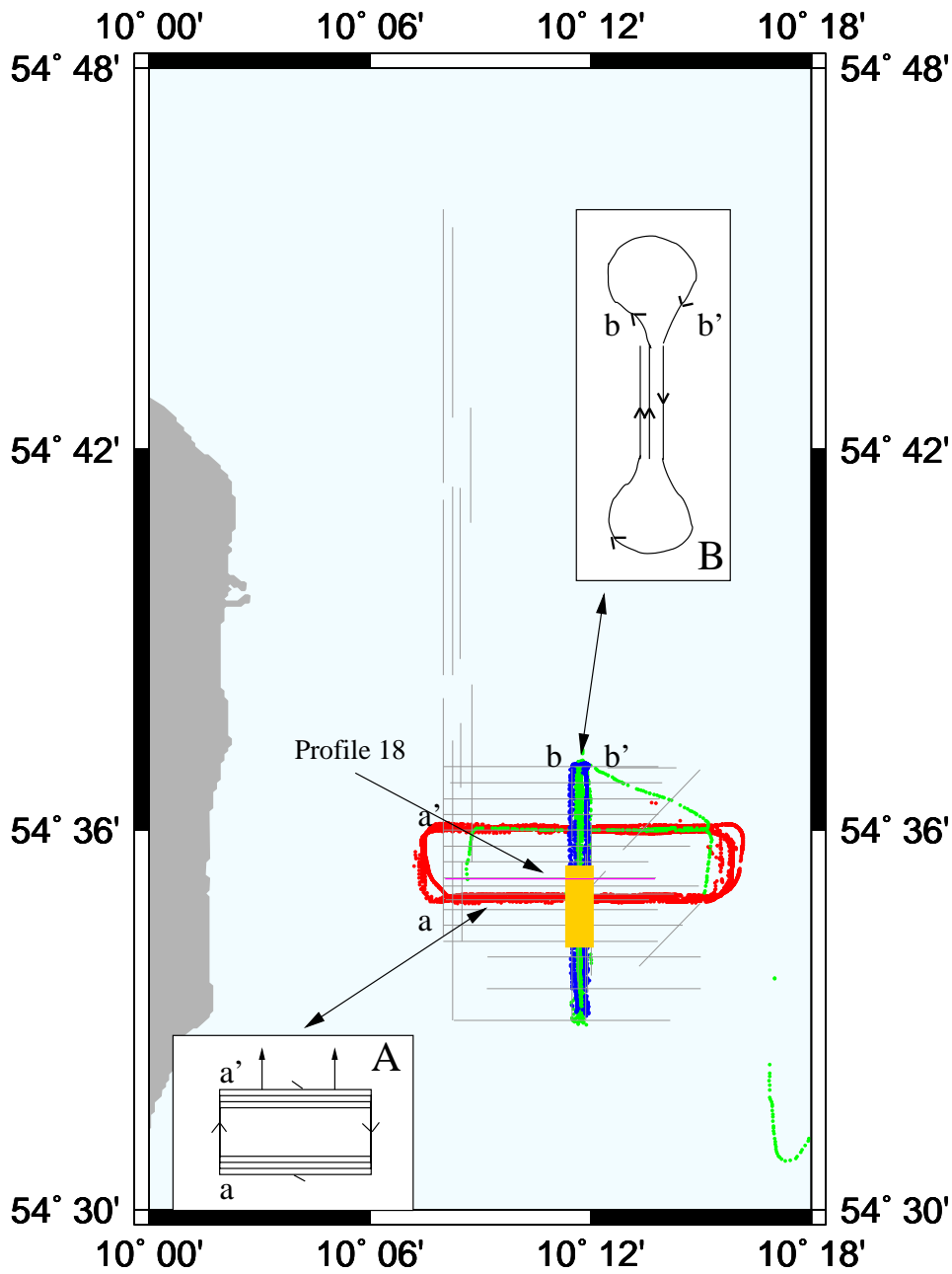


Figure 4.15: Shot positions of three individual data sets acquired for a $2\frac{1}{2}D$ -survey in May and August of 1999 (red, green and blue). Profiles sailed for the wide grid analysis are plotted in light gray for comparison. A pattern of propagating rectangles was less efficient in covering a connected area of dense profiles (A) than the "weaving" pattern (B), as shown in the inlaid panels. The area shown in yellow was used to compose a first $2\frac{1}{2}D$ -seismic cube.

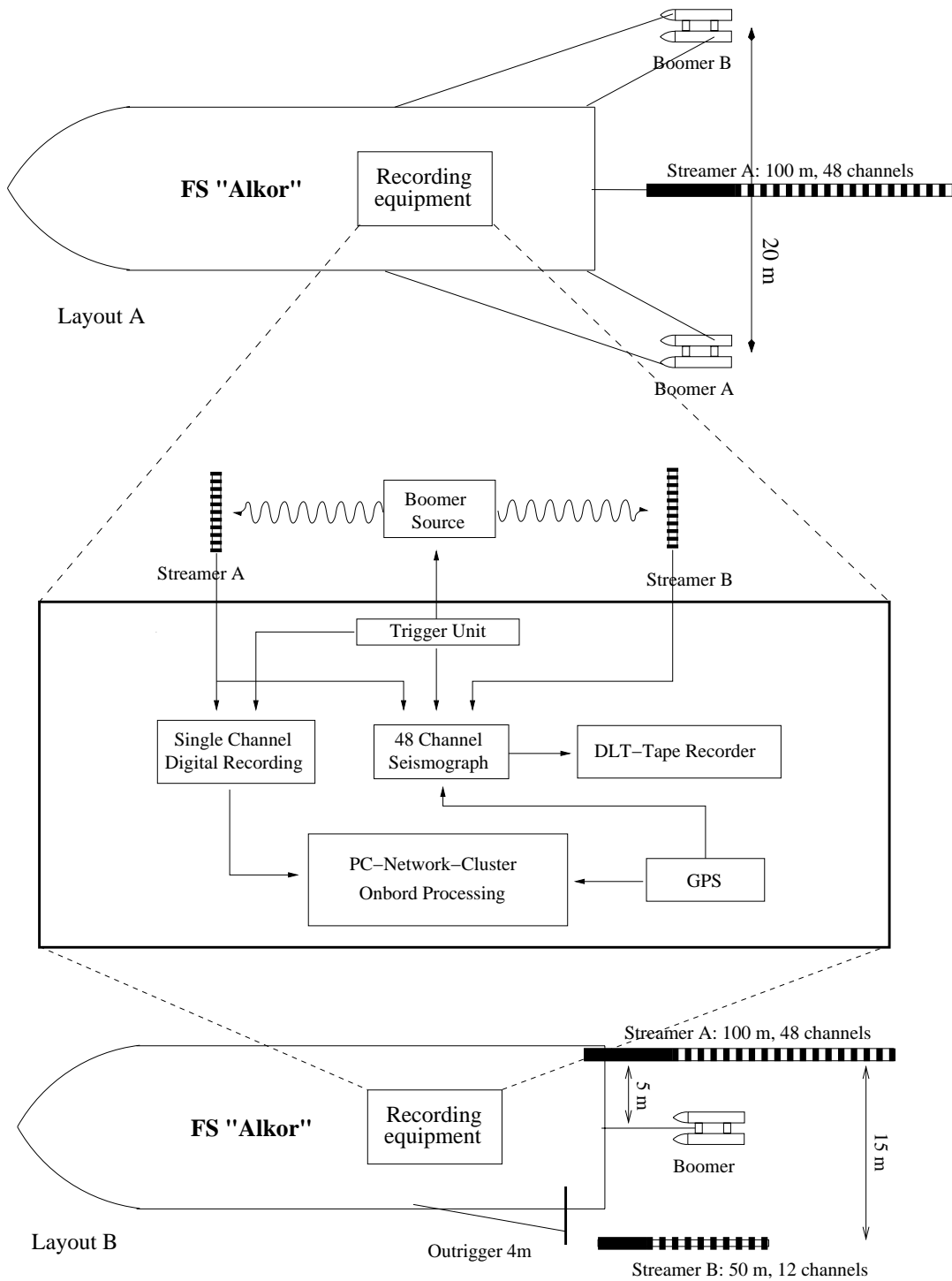


Figure 4.16: Acquisition geometry and recording equipment setup used for the high frequency 3D seismic survey. For multichannel recordings a 48 channel BISON seismograph was used. Near trace control profiles were recorded on a PC unit. Layouts A was used when sailing the pattern of propagating rectangles and B for the "weaving" acquisition pattern as shown in figure 4.15.

Initially it was intended to use two equally designed streamers for layout B. But due to delivery problems and a lag of other choice two streamers different design had to be deployed. By using an outrigger the 12 channel streamer (streamer B in table 4.1) was shifted 4 m away from the vessel. The 48 channel streamer (streamer A) was simply fastened on starboard. The source was towed directly behind the vessel. Layout B proved to be much more stable than layout A. It provided well defined positions for both, source and sensors. It was thus decided to only use data acquired with layout B to compose the 3D seismic cube.

Figure 4.17 schematically illustrates the two different acquisition layouts and defines the notions *acquisition line* and *acquisition profile*. They will be used now to explain problems of lateral first Fresnel zone coverage as were faced with both layouts:

In both cases seismic traces were acquired with a shot rate of $R_s=1$ /s and a vessel speed of $v_v=2$ m/s resulting in a shot to shot distance of 2 m. The first Fresnel zone for a seismic signal with a center frequency of 500 Hz at 20 m depth is $2R_f=15.6$ m. It was thus clearly covered in direction of the sailed acquisition profiles.

For both layouts the sources (layout A) and streamers (layout B) were separated 20 m and 15 m, respectively. The minimum acquisition profile distance thus amounts to 10 m (layout A) and 7.5 (layout B) along one acquisition line. Acquisition lines however had to be sailed with at least 50 m separation due to limits in navigational resolution of the vessels GPS system. The maximum distance between acquisition profiles thus tended to be larger then the first Fresnel zone and lateral continuity was not fully provided.

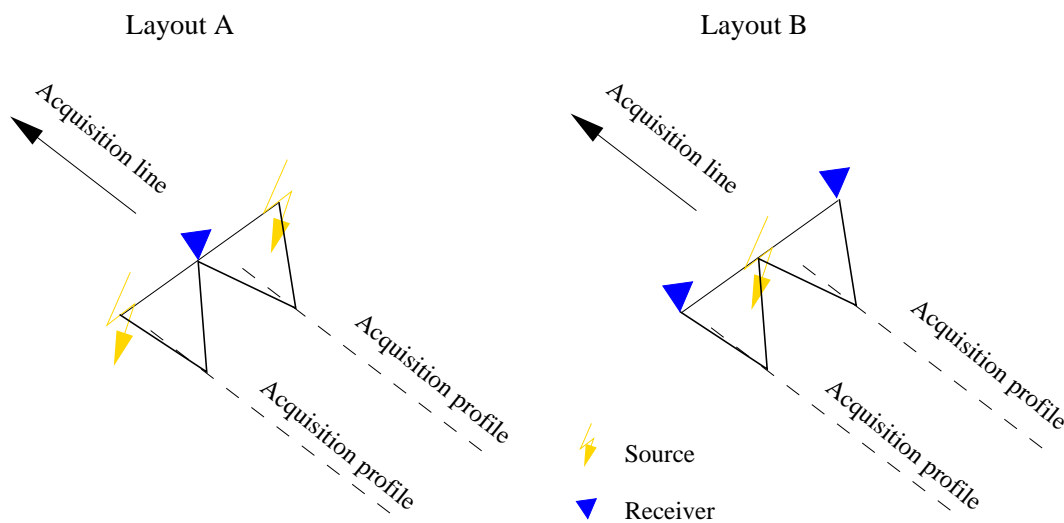


Figure 4.17: Acquisition lines and acquisition profiles were not equally spaced in neither of both surveys (layout A, B). Due to navigation accuracy the distance between two acquisition lines was not smaller than 20 m. The inter profile distance for layout A was 10 m and for layout B was 7.5 m.

In order to reduce the amount of acquired data to a handable size the area of investigation was further confined, as indicated by the yellow rectangle in figure 4.15.

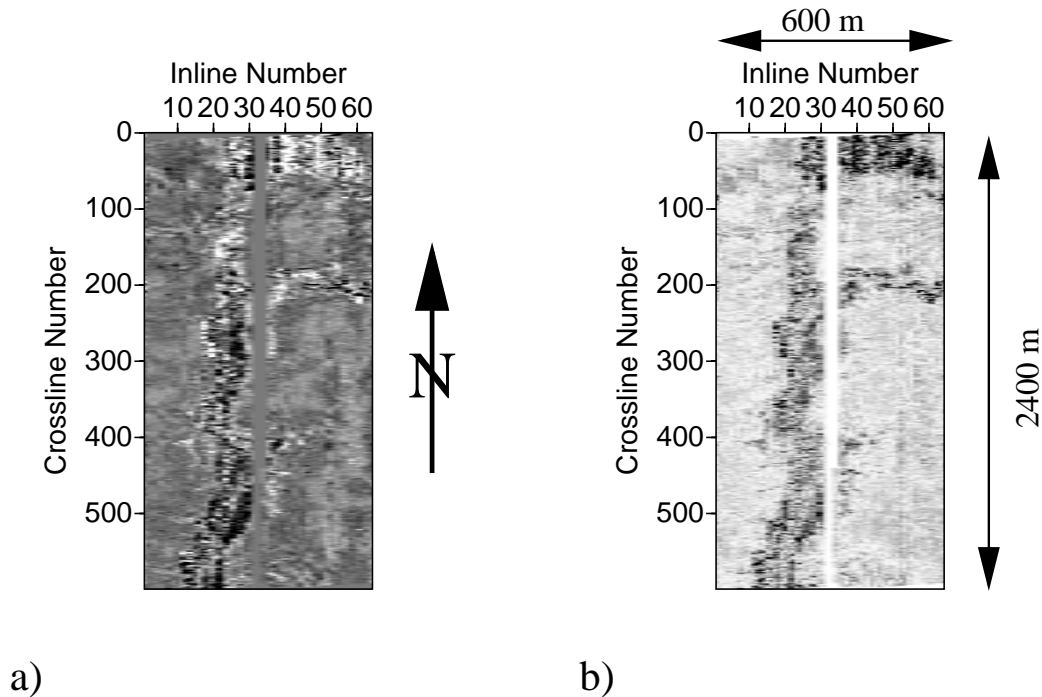


Figure 4.18: a) Time slice at 0.034s two way travel time (approx. 25m depth), after filtering, binning and signal equalization. b) Geological structures become more distinct due to increased contrast after building envelope traces.

The data set that was used to built the 3D seismic cube had a size of 1.7 Gbyte and the final cube 80 Mbytes. Traces were transformed to a grid of regular bins. Due to insufficient coverage of the first Fresnel zone as described above binning was only applied along each acquisition profile and not transverse to it. The binned profiles were combined to build a single channel seismic cube. Seismic data processing included filtering in order to avoid streamer array effects, phase shifting to equalize signals recorded with different streamers and mixing of neighbored profiles to smooth inter profile discontinuities. 3D seismic data has to be displayed in several different ways in order to gain complete understanding of the structures observed in a seismic cube. One possible kind of display is the "time slice", a map view of data samples with equal two way travel time values. Figure 4.18a shows a time slice that was processed as described above. Structured geology can clearly be observed. The contrast of the image could be increased by taking the envelope instead of the amplitude of seismic data as shown in figure 4.18b.

Figure 4.19 shows a sequence of time slices cut from the 3D seismic cube of envelope traces. Each time slice is labeled with its corresponding depth value, which was calculated by assuming a homogeneous background medium with water velocity ($v_w=1500$ m/s). At 0.025 s two way travel time which corresponds to 19 m depth, the sea floor reflection can be observed as a nearly completely flat and featureless seismic event. The sea floor is build from unconsolidated sediments that behave like a dense fluid with shear wave velocities as low as $v_s = 9-47$ m/s and compressional wave velocities close to that of water (Ayres &

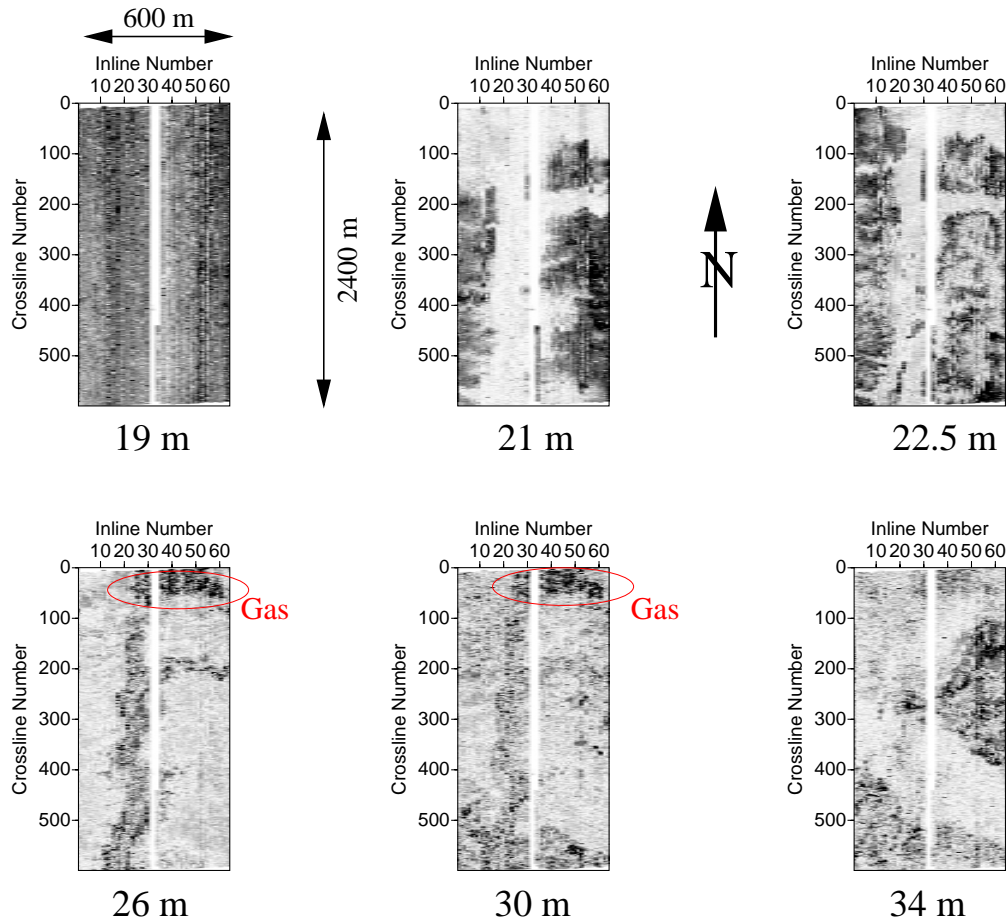


Figure 4.19: The panels show time slices generated from the 3D seismic cube. Depth values are calculated assuming water velocity for the background medium. At $TWT=0.025$ s (19 m) the featureless seafloor build from unconsolidated sediments is clearly documented. Slight amplitude variations are interpreted as tidal acquisition footprint. Beginning at a two way travel time of $TWT=0.03$ s (21-22 m) clearly structured geology can be observed, which up to $TWT=0.035$ (25 m) forms a prominent channel system. Due to its location in the till it is interpreted as a glacial fluvial system probably build at the end of the Weichsel glaciation period. The amplitude anomaly in the north-east corner of the area corresponds to gas accumulations as already observed on individual 2D profiles (e.g. figure 4.11). At $TWT=0.045$ s (32 m) we observe a sudden change in geological features. Beneath the channel an older anticlinale geological structure is observed, but could not be classified.

Theilen, 1999). It thus forms a perfectly flat horizon. Slight travel time variations are most likely due to very small tidal activity during acquisition, and thus are interpreted as a static acquisition footprint. Please note that the sea floor horizon would build a natural barrier for side scan sonar investigations. It would not be possible to penetrate significantly beyond this interface. 3D seismic however enables us to not only perform area wide mapping of the sea floor but also of the deeper sediments.

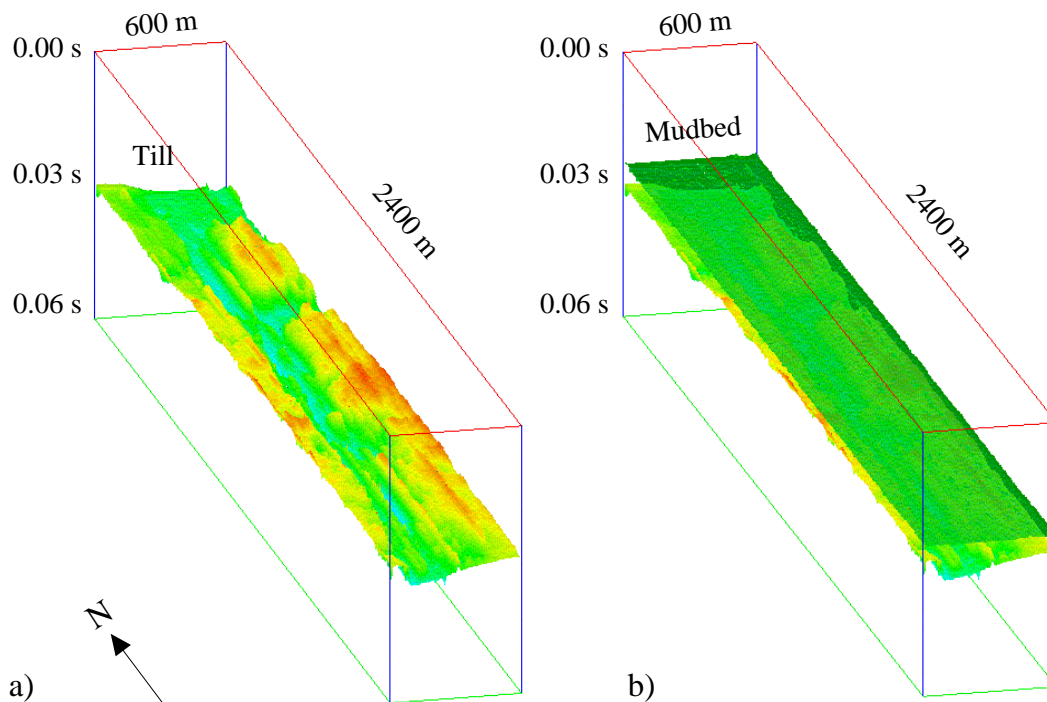


Figure 4.20: a) In order to support the interpretation of the geological situation two way travel time values of the till and mudbed horizons were picked to generate a 3D display of their topography. The riverbed is covered by the completely flat and featureless mud layer (b). With conventional side scanning sonar investigations only this cover of unconsolidated sediments would be observed. The mudbed would obscure the interesting geological imprints found underneath, which can only be investigated by utilizing 3D seismics.

At 0.03 s two way travel time, just a few meters below the sea floor (≈ 20 m depth), pronounced geological features are revealed. A river like channel structure with distinctive side arms can be observed. It is interpreted as a glacial fluvial system that most probably has built during the end of the Weichsel glacial period. Within the north east corner of the time slice, gas accumulations produce an amplitude anomaly which was already observed on individual 2D profiles (please see e.g. figure 4.11).

Towards higher travel time values, a sudden change in the geological setting can be observed at $TWT=0.045s$ (32 m). An anticlinale structure is emerging which is obviously older than the channel system and must have built during one of the earlier glacial periods in the area. It could not be classified.

The interpretation of 3D seismic data sets is often supported by the use of "seismic interpretation" displays. Figure 4.20 shows a 3D topographic display of picked travel time values that correspond to the till horizon (A) and to the mud-bed cover building the sea floor (B). By means of seismic interpretation it is now possible to even calculate an estimate of the depth of the river-bed beneath the sea floor, which corresponds to the thickness of the mud-bed cover (Figure 4.21). The volume of the mud layer can thus be estimated. In a more complex situation preferably a depth migrated seismic cube would serve as interpre-

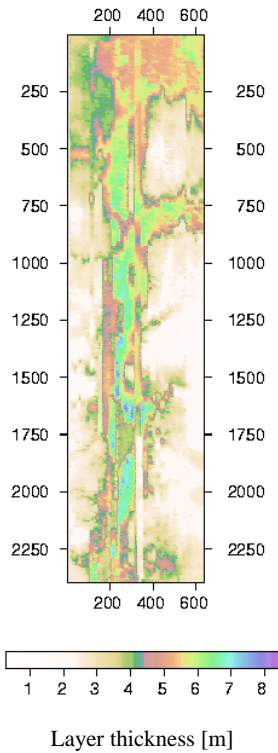


Figure 4.21: *Depth of channel system beneath the seafloor or thickness of mud cover as calculated from the two way traveltime difference between mudbed and till horizon. Assuming 1500m/s background velocity for the mudlayer, the volume of the channel filling can be estimated to be $V = 5.5 \cdot 10^6\text{m}^3$.*

tation basis. In this case, however, it should be a valid approximation to assume that the velocity of seismic waves traveling through the mud is comparable to that in water (Ayres & Theilen, 1999; Riedel, 1998). The volume of the river-bed filling can be estimated to be $V = 5.5 \cdot 10^6\text{ m}^3$ in the investigated area. With a density of 1220 kg/m^3 this amounts to $6.72 \cdot 10^9\text{ kg}$ of mud.

4.1.3 Imaging of Marine Scatterers Using Diffraction Coherency Migration

The newly developed processing approach of diffraction coherency migration (section 3.2.2) (DCM) shall now be applied to an example selection from the marine seismic data sets presented in the preceding sections. I will investigate the performance of processing as proposed in appendix B and will focus on profile 18 which was already described in more detail in section 4.1.2:

First example:

Step one:

Figure 4.22a shows a zero offset section of profile 18 as an enlargement of the region between CDP no. 2790 to CDP no. 2990 (CDP distance is one meter; see scale). The section shows the sea floor mud horizon (1) and the till horizon forming the river channel system beneath it (2), as identified by the 3D seismic survey (section 4.1.2). Gas has migrated in between

those two horizons (3) and produces pronounced diffractions (4). Thus, like pointed out in section B the CDP stacked zero offset section yields first indications for the presence of scattering/diffraction.

Step two:

As a second step towards imaging of scattering centers it is proposed to suppress as much seismic energy from primary events, i.e. the direct arrival and reflections, as possible. I thus applied the common offset domain filter ("difference filter" (DF)) as introduced in section 3.1.4. In order to illustrate the performance of the DF in figure 4.22b the CDP stacked section is shown after applying difference filtering prior to stacking. The length of the filter window was set to be twenty shots. Please note that horizontal events, e.g. the flat sea floor horizon, are now effectively suppressed. Only dipping events and diffraction signatures remain in the section. The performance of the filter is thus in perfect agreement with the synthetic tests performed in section 3.1.4.

Step three:

The DF is applied to unstacked seismic data. Prestack migration of difference filtered seismic data thus yields a depth section which enhances the image of scattering centers and dipping interfaces on the cost of the image of horizontal reflectors. This is illustrated in figures 4.22c and 4.22d. A DSM result with and without difference filtering prior to migration is shown for comparison.

Step four:

As explained in detail in section 3.2.2 "Diffraction Coherency Migration" (DCM) takes advantage of the characteristic travel time behavior of scattered/diffracted seismic energy in order to further highlight the subsurface position of scattering centers. It is thus proposed as the next necessary step in the imaging approach. Figures 4.23a,b,c,d show results for DCM applied to the example data using either unnormalized cross correlation (CC) (panels A and B) and semblance (NE) (panels C and D) as coherency measure. Panels B and D display difference filtered results which show less contributions from reflecting interfaces ("reflector noise"). In addition we find that the image of discontinuity locations, i.e. scattering centers or diffracting edges, are enhanced in the difference filtered sections (1, 2). The image resulting from CC-DCM shows less highlights indicating scattering centers than that obtained from NE-DCM. Due to the normalizing character of the semblance coefficient the strength of individual scattering centers is balanced compared to the image obtained by CC-DCM. The NE-DCM image thus emphasizes more scattering center positions than CC-DCM which can be regarded as an advantage for finding weak scatterers. A drawback of this performance however is the fact that "reflector noise" is stronger in the NE-DCM compared to CC-DCM. In individual applications one will have to decide which quality of the migrated image is to be preferred.

Second example:

In order to illustrate the advantage that DCM provides in finding scattering centers on seismic sections, I selected an additional example data set from profile 18. Further to the east of the area described above (please compare with figure 4.11) an extended region of gas accumulations is found. Figure 4.24a shows a CDP stacked section as an enlargement of that area. A continuous gas layer reflection characterized by its high reflection amplitudes

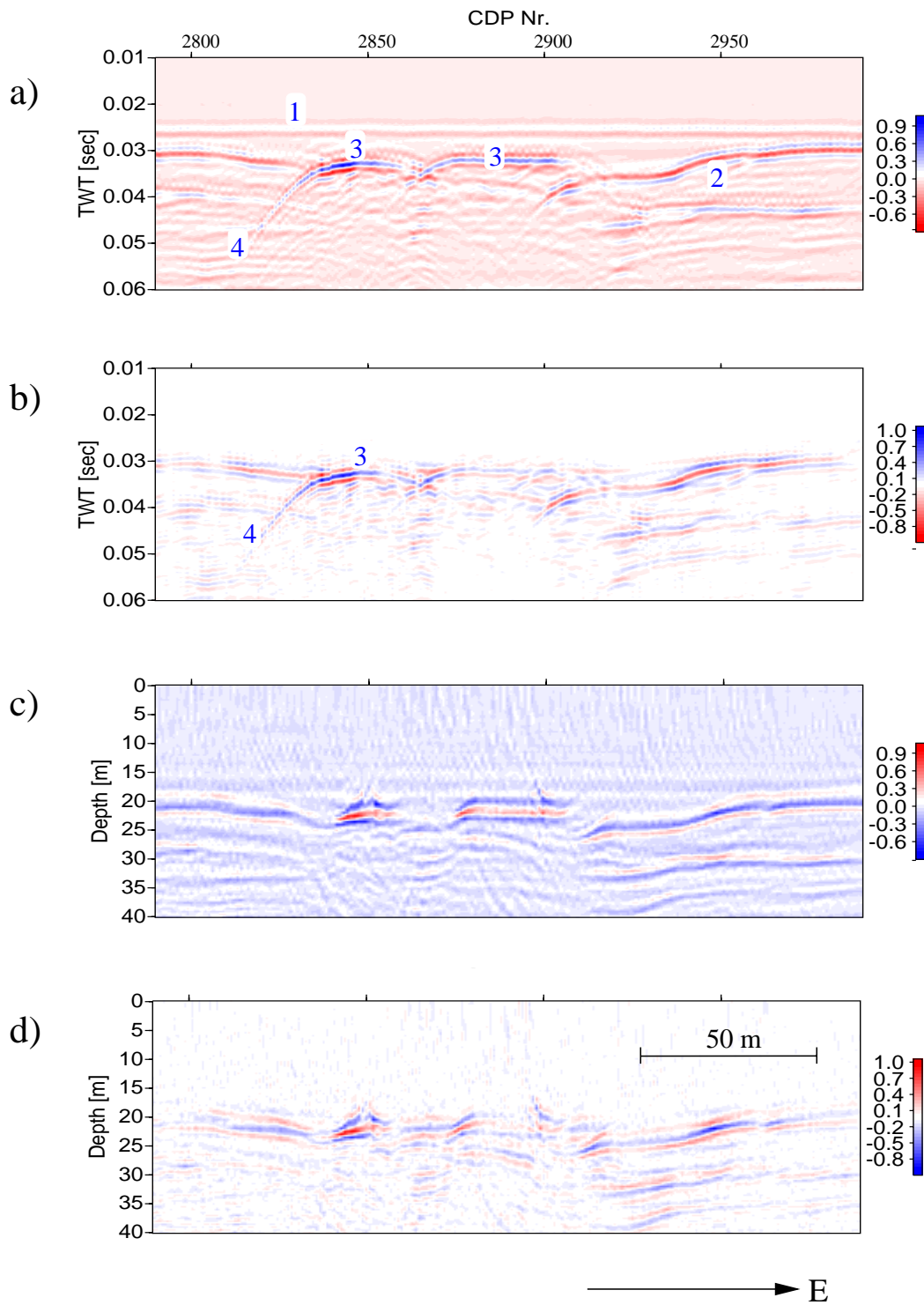


Figure 4.22: Data example from profile 18 displayed as CDP stacked (a,b) and DSM section (c,d) respectively. The data shown in panel b and d have been difference filtered prior to stacking, migration. Difference filtering effectively suppresses the seismic response from horizontal reflectors and direct arrivals, while diffracted energy and reflections from dipping events remain (see also section 3.1.4).

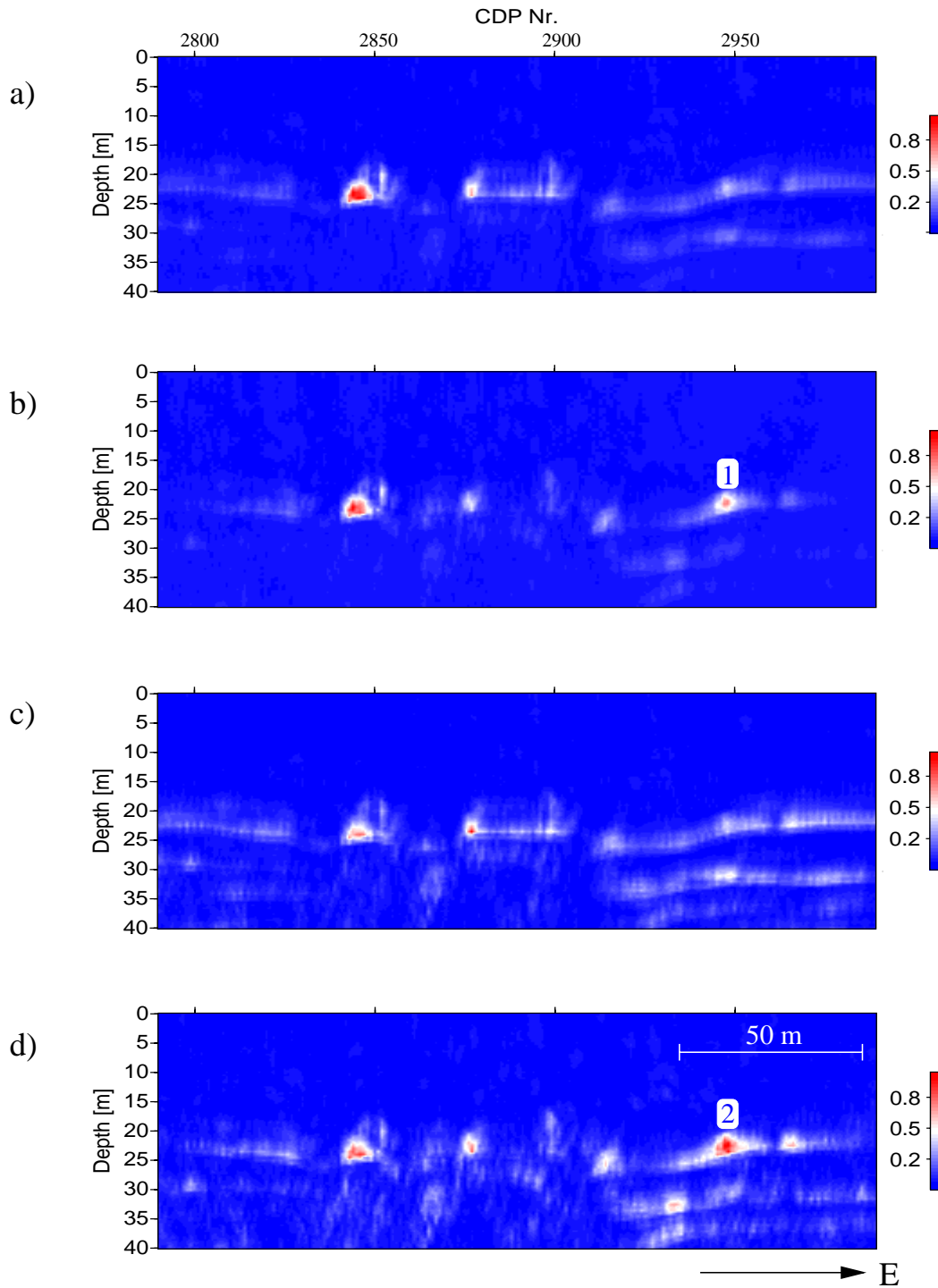


Figure 4.23: Data example from profile 18 displayed as CC-DCM (a,b) and NE-DCM section (c,d) respectively. Like in figure 4.22 panels b and d show section with data that were difference filtered prior to migration. Reflected seismic energy is suppressed whereas scattering centers are pronounced by DCM taking advantage of the characteristic travel time behavior of scattered/diffracted seismic energy. Difference filtering prior to migration assists in further suppressing images of reflectors. NE-DCM shows a more detailed image of scattering centers compared to CC-DCM but also preserves stronger contributions from reflecting interfaces.

and phase reversal can be observed (1). The layer breaks up into a field of smaller non connected gas accumulations that scatter the seismic wave field (2). These small scale gas accumulations are in a process of upward migration to be finally caught at an interface between the till and the sea floor horizon (3). In the section shown here it is difficult to tell e.g. how many scattering centers are observed. A diffraction stack migrated section of this area (figure 4.24b) maps the connected part of the gas layer (1) and also indicates that the gas layer is broken up into several individual units further to the west (2). But it is undoubtedly difficult to determine the number of discontinuities. By applying difference filtering and NE-DCM, CC-DCM to the data set the sections shown in figure 4.24c, d are obtained. Events that on a conventionally migrated seismic section easily might have been ignored, as e.g. indicated by the circles in figure 4.24c and d, are now clearly visible. DCM provides the means of enhancing the image of scattering centers in the subsurface. It suppresses primary seismic energy like reflection responses. It is efficiently assisted by applying "difference filtering" prior to migration.

Given the positions of the scattering centers, further analysis is proposed to follow (please refer to appendix B). A CSA stack investigation e.g. would only apply to the case of pure scattering from an object of sufficient spherical symmetry and not to the case of diffraction or scattering from an object of complex shape.

For the examples discussed above, by comparison of DSM and DCM results, it can be concluded that observed scattering, diffraction responses are predominantly caused by the interrupted layer of a biogenic gas accumulation. Only if the extend of the continuous part of the gas layer gets as small as the dominant seismic wave length, pure scattering occurs. In any other case the observed characteristic hyperbolas in CDP stacked sections are due to diffractions (figure 4.10). A CSA investigation will then not be applicable. In the second example discussed (figure 4.11), scattering is generated by a large number of closely spaced small gas reflector elements. Due to the close vicinity of the individual scatterers, their scattering response will interfere and CSA analysis will fail as well.

4.1.4 Conclusions

The Boomer source showed sufficient repeatability to be applied in multichannel marine seismic acquisition and processing. Since streamer arrays are generally constructed to be used with airguns their inherent array characteristics can generate severe distortion of the recorded Boomer signal. Either single hydrophone streamers or streamers with a grouping geometry adapted to high frequency seismic sources should thus be used.

Multichannel seismic acquisition significantly extends the possibilities of seismic processing. The signal to noise ratio, as well as, the lateral resolution in the CMP processed zero offset sections was increased. The conducted seismic surveys were especially aimed towards finding and classifying single scattering objects. The marine processing sequence proposed in appendix B was successfully applied to the acquired marine data sets. Difference filtering and subsequent diffraction coherency migration proved to efficiently suppress reflections and enhance the image of subsurface scattering centers and discontinuities.

CSA gather analysis strictly applies only to the case of scattering from spherically symmetric objects. This requirement was not met in the discussed examples and thus CSA analysis had to be omitted.

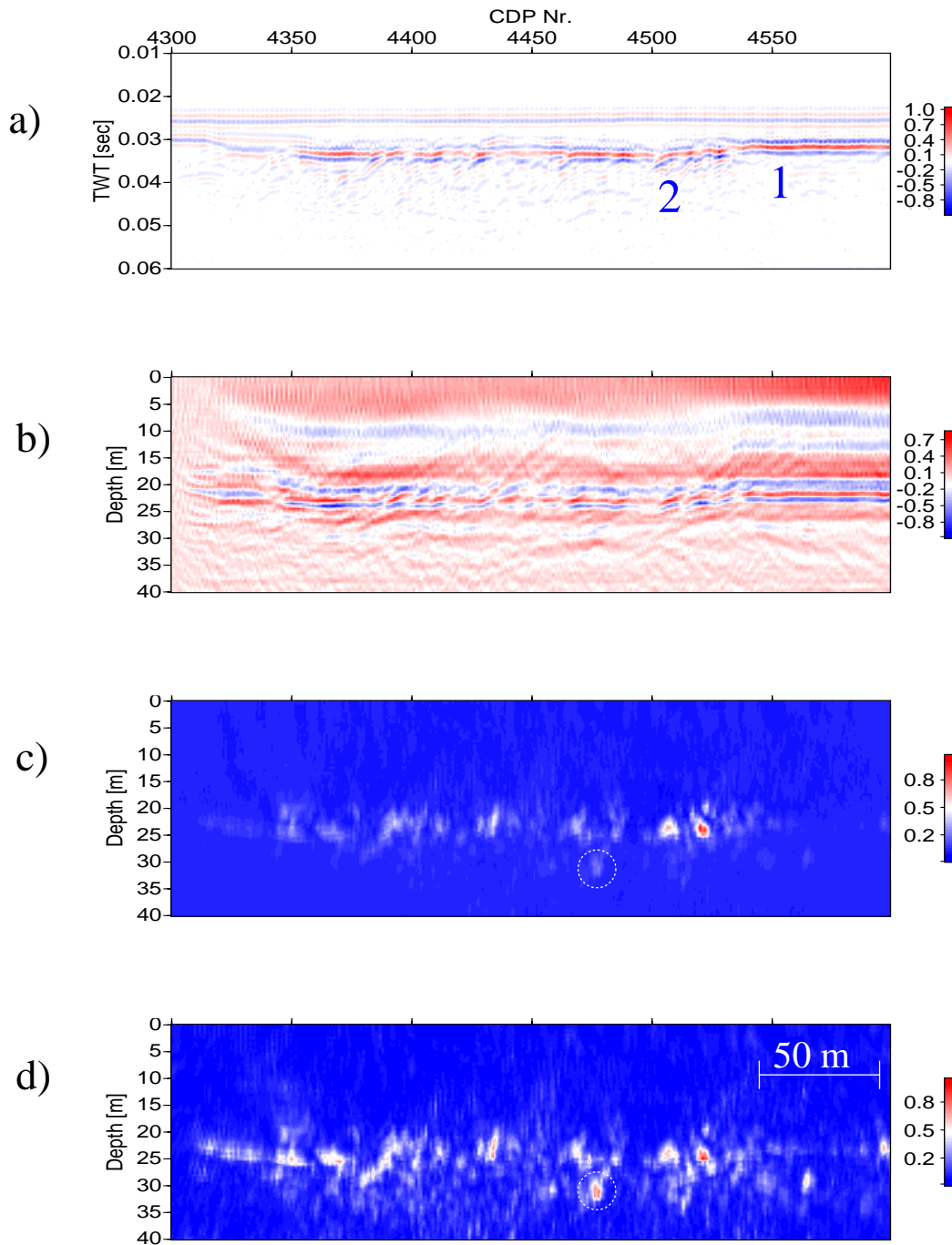


Figure 4.24: Data example from profile 18 further to the east from the preceding example. Displayed are: A CDP-stacked seismic section (a), a section resulting from conventional DSM (b), difference filtered results from CC-DCM (c) and NE-DCM (d). The CDP-stacked section provides first indication for scattering present at a gas layer (1) that breaks up into several individual units (2). It is difficult to identify individual scattering centers in the migrated section. CC-DCM and NE-DCM draw a clearer picture of the distribution of scattering centers.

For the first time it was possible to conduct a high resolution multichannel $2\frac{1}{2}$ D seismic survey in the Baltic Sea, revealing a Pleistocene fluvial channel system situated below a flat mudbed cover which locally builds the seafloor. Penetration up to 40 m was achieved showing deeper anticlinale structures within the seismic cube which could not be classified. Gas features are clearly visible in seismic time slices, but scattering signatures were not observed due to a lag lateral coverage in the $2\frac{1}{2}$ D seismic survey, and the applied binning procedure.

4.2 Crustal Seismic Case Histories

High frequency seismic reflection profiles have been acquired in various Canadian mining camps as part of the Abitibi-Grenville Lithoprobe project. The usefulness of the seismic method regarding imaging of massive sulphide ore deposits and mineral exploration was tested. Comprehensive in situ measurements have been conducted in numerous deep boreholes. Laboratory measurements have been made on extensive sets of rock and ore samples from several Canadian mining camps (figure 4.25).

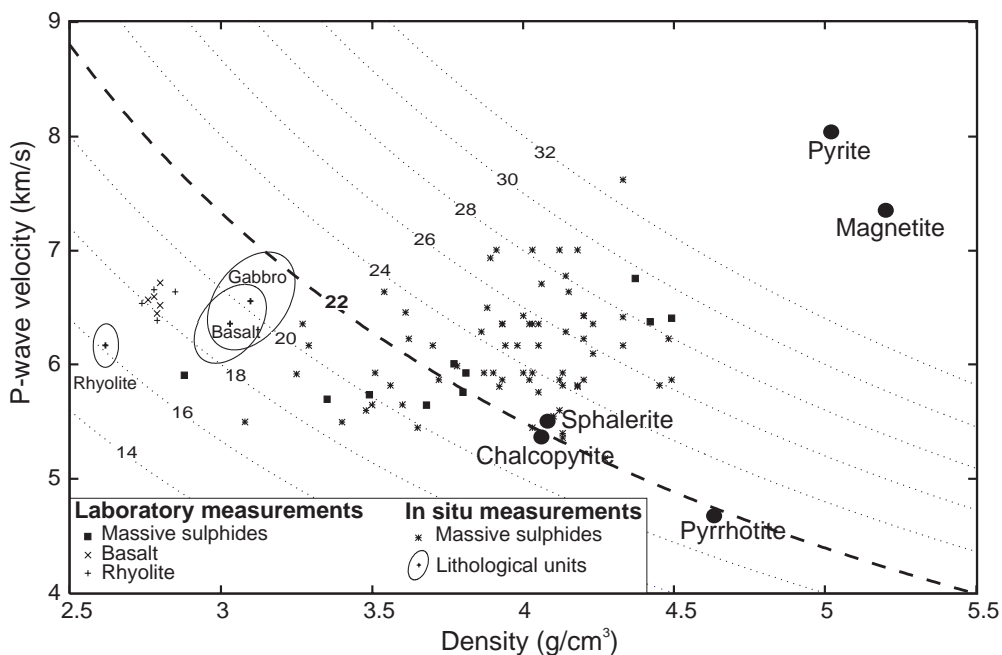


Figure 4.25: Physical rock properties of typical sulphide and orebody host minerals plotted along with those of the rocks of the crystalline crust background (from Adam et al., 1996). Most ore minerals show significant impedance contrast compared to the background rocks. Massive sulphide ore deposits should thus be reflective to seismic waves. (Dotted lines indicate constant impedance values ($v_p\rho = const$)).

The results to date clearly indicate that surface seismic reflection profiling, when combined with borehole geophysics, is a viable tool to map the deep stratigraphy of mining camps in

two and three dimensions. The success of Lithoprobe high-frequency (up to 140 Hz) surveys has raised the interest of several mining companies, resulting in a series of follow-up studies above known locations of massive volcanogenic sulphide ore mineralizations. The mining industry has long relied on traditional mapping, drilling and potential field techniques to locate base metal deposits. With shallow deposits already discovered and exploited, there is growing interest in deep exploration techniques, in order to maintain long term profitability. A promising new approach is to search for base metal deposits using high-resolution seismic techniques as very successfully employed for exploration by the petroleum industry.

Surface seismic profiling confirms that massive sulphide can be highly reflective (Milkereit *et al.*, 1996; Adam, 2000). Geologic settings characterized by steep dips are problematic for surface seismic methods, however. In this case vertical seismic profiling provides a logical alternative to surface seismics. Eaton *et al.* (1996), demonstrated that steeply dipping deposits can be imaged using borehole seismic methods.

Ore deposits most often rather scatter than reflect seismic energy due to their small size compared to the wavelength applied in crustal seismic exploration. Thus downhole seismic imaging (DSI) has to account for contributions from all three spatial dimensions.

I will now review the geological setting, acquisition and preprocessing of two VSP data sets that have been acquired in Canadian mining camps between 1992 and 1999. The newly developed 3D imaging concepts of DCM and DPM were applied to these example data sets. The performance of both methods will be discussed. The first example focuses on a three component single shot VSP data set acquired at the Matagami mining camp in Quebec, Canada. The exact position and shape of the massive volcanogenic ore mineralization that was target to the investigation, i.e. the Bell-Allard orebody, is known (Adam, 2000). The data set serves as a benchmark example for the performance of DCM and DPM for crustal seismic data.

In 1999 a three component multi source VSP survey was conducted on the Norman West property of the Sudbury mining area in Ontario, Canada (Perron, 2000). The performance of DCM in case of this very recent acquisition project of the DSI consortium, will be discussed. Only the vertical component was used for migration since DCM is a scalar migration technique. Since no polarization information was used an imaging ambiguity investigation will also be subject to the discussion.

4.2.1 Single Shot 3C VSP Survey in Matagami.

Currently the Bell Allard mine is producing zinc from a 6 Mt orebody. The deposit is rich in zinc sulphide minerals which show a strong perturbation in density compared to the crystalline host rock background (Salisbury *et al.*, 1996; Adam *et al.*, 1996, see also figure 4.25). The mining camp and the area of the Bell Allard mineralization have a significant record of geophysical investigations (Adam, 2000). Since 1990 several seismic reflection studies have been conducted including surface seismic surveys that were part of the Lithoprobe program, several VSP's and a complete 3D seismic survey that were directly addressed towards imaging of the orebody structure (Adam, 2000). These investigations and additional rock properties studies, in situ as well as core sample measurements, had proven that the Bell-Allard mineralization is reflective to seismic waves and can be imaged using seismic methods. The extent of the orebody is well known from drill hole sampling

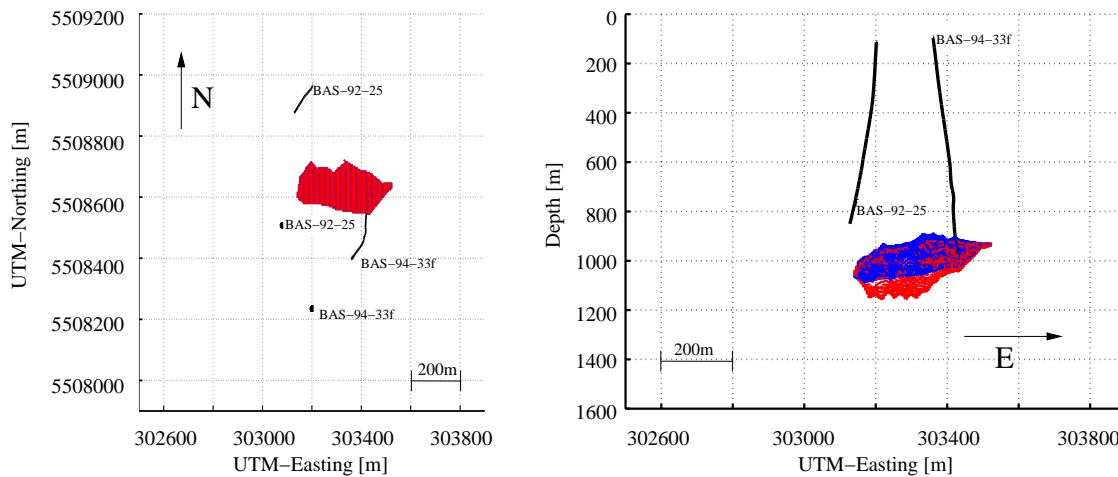


Figure 4.26: Locations of the shot points and boreholes used in VSP/DSI surveys conducted at the Matagami mining camp and outline of the orebody. Data collected in borehole BAS-92-25 was used to test DCM and DPM performance.

and due to its shape and size it is understood that the deposit behaves like a scatterer rather than a reflector. It is thus well suited to serve as an example in this investigation. In 1992 and 1994 two vertical seismic profiling surveys were conducted at boreholes situated at the site named "BAS-94-33f" and "BAS-92-25" respectively. Figure 4.26 shows a map and side view of shot and borehole locations of these surveys along with an outline plot of the orebody.

The data was acquired by the Continental Geoscience Division of the GSC, Ottawa, Ontario. Processing and interpretation has already been conducted by Adam (2000), who showed, that the seismic response of Bell Allard decreases so rapidly with distance from the orebody that it could only be identified directly on the VSP section of BAS-94-33f and not on VSP data acquired in BAS-92-25. Since it was still uncertain at the beginning of the current investigation, if and up to what distance an orebody like Bell Allard could be imaged using VSP methods, seismic data acquired in BAS-92-25 was used as a test input to the DCM and DPM imaging algorithms. In the following I will briefly review the geological and structural setting of the Bell Allard ore deposit. I will then introduce the acquisition geometry and preprocessing of the BAS-92-25 data set regarding subsequent DCM and DPM migration. Finally the migration results will be presented and discussed.

Matagami Orebody: Geological and Structural Setting

Following the description given in Adam et. al (2001 (in preparation)), I will now summarize the geological and structural setting in the Matagami mining camp area. The overall geological setting is depicted in the map displayed in figure 4.27. Figure 4.28 shows the structural setting of the ore deposit itself:

The Matagami volcanic complex was formed by two major phases of predominantly tholei-

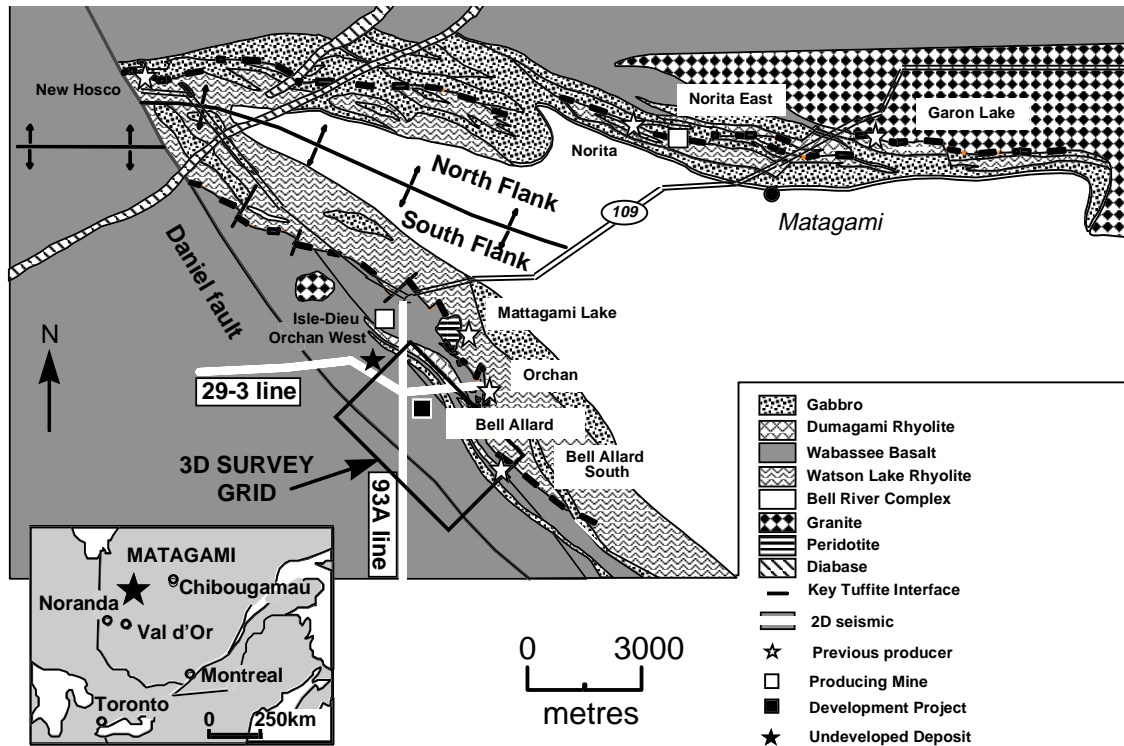


Figure 4.27: General geology of the Matagami mining camp area. (reproduced from Adam, 2000)

itic² volcanism. The early phase produced dacites and rhyolites of the Watson lake group, whereas the younger phase, which produced the Wabasseé Group, was dominated by basaltic volcanism with subordinate felsic activity, and was accompanied by mafic dominated sub-concordant intrusions (Piché et al., 1993; Beaudry and Gaucher, 1986). A cherty³, sulphidic chemical sediment⁴ known as the Key Tuffite marks the contact and hiatus between the two formations and is traceable for many kilometers along strike and down-dip on the South Flank of the mining camp (Sharpe, 1968). This thin horizon (0.6-6 m of thickness) was deposited during a period of intense hydrothermal circulation and represents the primary exploration target in the camp because it is host to most of the ore bodies discovered to date (Piché et al., 1993).

Bell Allard is a typical Matagami mining camp south flank VMS deposit. It is located at the Watson Lake-Wabasseé groups interface atop a synvolcanic fracture zone, characterized by classic hydrothermal alteration. A weakly transposed concordant lens of sulphide mineralization directly overlies a discordant pipe, or conduit, hosting massive or stringer mineralization. The deposit is bounded to the south by a synvolcanic fault system (Bound-

²Sub-group of the basalts, low in alkali elements. On Earth, olivine tholeiites and quartz tholeiites are the main divisions, depending on the proportion of SiO₂. Surplus SiO₂ appears as fine-grained quartz.

³A sedimentary form of amorphous or extremely fine-grained silic, partially hydrous, found in concretions and beds.

⁴One that is formed at or near its place of deposition by chemical precipitation, usually from sea water.

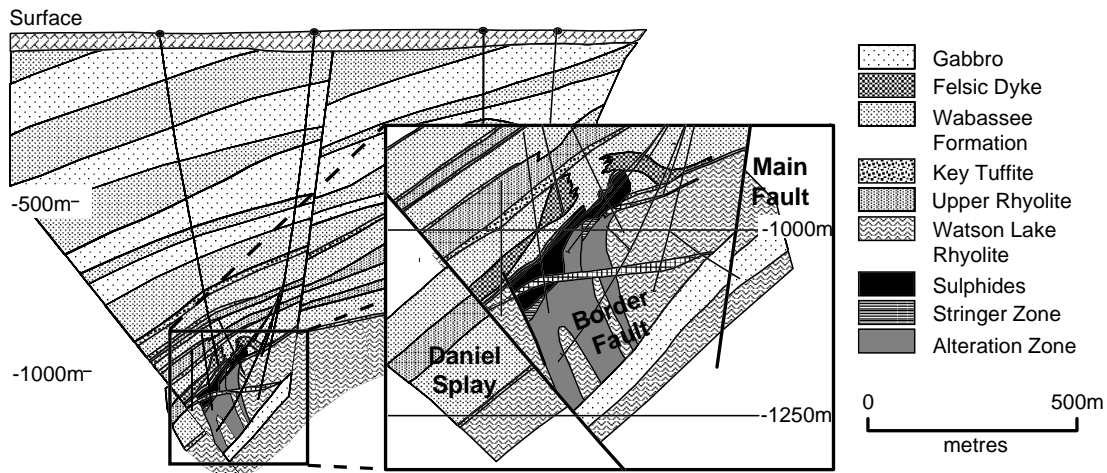


Figure 4.28: Structural and geological setting of the Matagami orebody (reproduced from Adam, 2000).

ary Fault) oriented 095° relative to north. The orebody consists of two lenses, and is approximately 370 m long and 165 m wide down-dip along the Key Tuffite interface with an overall east-west orientation in plan. The North lens is composed primarily high-grade Zn-rich massive sulphides whereas the south lens is of lower grade and comprised, in part, of conduit-type mineralization. Sulphide mineralization consists of pyrite, Fe-rich sphalerite, minor chalcopyrite and pyrrhotite. Thickness averages about 30 m, but can change up to 60 m in portions of the south lens. The deposit dips 50° to 55° degrees towards the south between depths of 900 and 1150 m below the surface. A global resource in excess of 6 Mt makes Bell Allard the second largest deposit discovered in the Matagami (Adam, 2000).

Acquisition and Preprocessing

The data set serving as a field example was acquired in borehole BAS-92-25 which location is shown in figure 4.26 along with the shot position used. The borehole is located approximately 200 m away from the orebody and gently dipping towards the south west. It is deviating from vertical by about 100 m along its depth range of 750 m. As source a 227 g pentolite booster was used which, in order to provide good source coupling, was pushed 0.3 m into the clays of a water filled pit. A single level downhole receiver unit with 14 Hz geophones was used to collect 3 component data along the borehole. Receiver spacing was chosen to be 10 m between 113 m and 465 m and 5 m from 465 m to 850 m depth. The maximum depth of 850 m was enforced by a blockade within the borehole. No data was collected at the Key Tuffite level at 1021 m where the orebody is located (Adam *et al.*, 2001 (in preparation)). Processing steps applied to the VSP data as preparation for final Diffraction Coherency and Diffraction Polarization migration were chosen following those documented in Adam *et al.*, 2000. For the removal of downgoing waves an f-k filter was applied, in contrast to the median filter used by Adam *et al.* (2000):

- band pass filter (20,40,160,200)
- notch filter around 50 Hz
- trace editing
- static corrections
- determination of geophone orientations from direct P-wave
- residual orientation correction
- rotation into N-E- system
- f-k filter for removal of downgoing wave field

The removal of the downgoing p- and s-wave arrival is the most critical step in DCM, DPM preparation processing, like it is in any kind of VSP processing. Direct arrivals often obscure the weak scattering response and great care has to be taken not to destroy it in this processing step. For DPM it is also important not to influence the polarization characteristic of the recorded signals. An extensive investigation on the performance of different methods to remove the downgoing wave field in VSP sections was conducted by Duveneck, 2000.

The receiver coordinate system was finally rotated into a N-E-system. Figure 4.29 compares the rotated three component data set prior to and after f-k-filtering. The range of input traces was limited to the densely sampled portion in the depth range of 465 m to 850 m in order to avoid aliasing effects in f-k-filtering (Duveneck, 2000).

Figure 4.30a compares the processed portion of the BAS-92-25 data set (vertical component) with a 3D finite difference pure scattering response seismogram (b) (Adam, 2000). The straight line in panel b indicates the modeled $p \rightarrow p$ scattering response of the orebody. An event of equal slowness (arrows in panel a) but slightly lower intercept time can be observed on the real data seismic section. In contrast to the result obtained by Adam, et al., 2000 this event can be interpreted to originate from the orebody.

The finally processed sections were chosen as input to the migration algorithms. For DCM only the vertical component was used.

Migration Results

In order to apply diffraction coherency or diffraction polarization migration, the velocity field of the background medium has to be known. The crystalline crust like in the current example provides the fortunate situation, that the distribution of seismic velocities is very small (Adam *et al.*, 2001 (in preparation)) so that a constant velocity model can be assumed. The data set acquired and processed as described above was migrated using either DCM and DPM. Figure 4.31a shows the migration result for DCM using semblance as the coherency measure (NE-DCM) displayed as planar vertical and horizontal cross section through the 3D image space. For migration a depth sampling interval of $dx=dy=dz=10$ m was chosen,

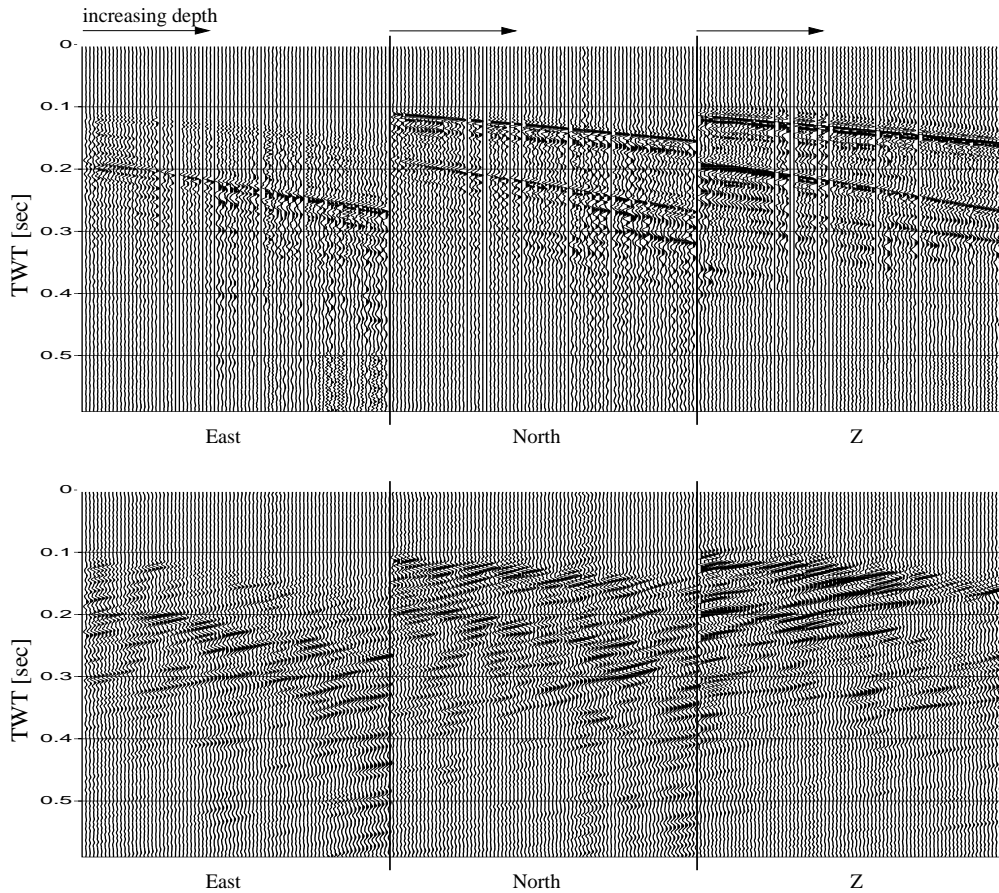


Figure 4.29: Data as rotated to a North-East coordinate system. Traces were limited to the densely sampled portion in the depth range between 465 m and 850 m of the borehole (data clipped at 99% maximum amplitude) (Duvenceck, 2000).

migration velocity was $v_{mig} = 6175$ m/s and the gate for the semblance investigation was set to be $t_w = 0.01$ s, approximately corresponding to the length of the source signal. The outline of the orebody and the deeper portion of the borehole are plotted as a reference. The coherency values are normalized and color coded by the scale shown along side. The UTM coordinate system as given in figure 4.26 was transposed to provide smaller numbers for convenience. Due to the acquisition layout using only one shot point the migrated image is ambiguous (see section 3.2.3). The DCM image itself would not provide any confidence about the existence of an orebody but proves that the seismic response coming from a distance as far as 200 m away from the borehole can readily be detected using VSP methods. This result is in contrast to that obtained by Adam et al., 2000. DCM provides the means of finding coherent seismic events and revealing their possible spatial origin. In addition to DCM, DPM was also applied to the sample data set, using the same spatial range and sampling intervals as described above (Duvenceck, 2000). Polarization alignment measure function h_{III} was used for DPM (section 3.2.4, equation 3.48). In figure 4.32a the migration result is plotted as an ISO surface plot (equal data values are connected by

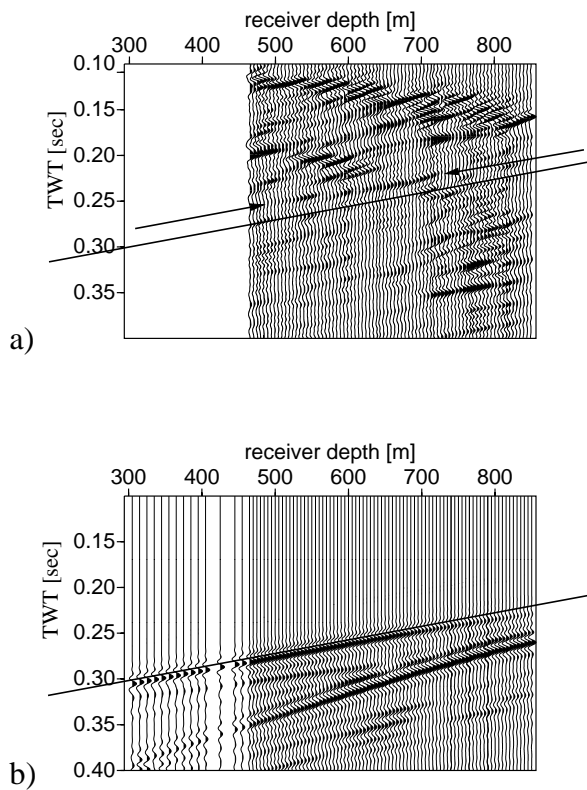


Figure 4.30: a) Deeper portion of the BAS-92-25 finally processed data set (vertical component) in comparison with b) 3D finite difference pure scattering response seismogram as discussed by Adam et al., 2000 (seismograms normalized to maximum amplitudes). The straight line in panel b indicates the modeled $p \rightarrow p$ scattered orebody response. An event of equal slowness (arrows in panel a) but slightly lower intercept time can be interpreted as the same response in the real data set (Adam, 2000).

a surface, which is virtually illuminated by optical ray tracing). Figure 4.32b again shows the outline of the Bell Allard ore deposit along with the lower part of the borehole for comparison. We clearly can observe a localized high of the polarization alignment measure sum Σ_{PAM} at the position of the orebody. The data shown here is limited to values of exactly $\Sigma_{PAM} = -0.4$ (normalized PAM values) in order to provide a three dimensional transparent view of the migration image. In the vicinity of the borehole additional features of the migration image can be observed, which are of the same strength, but not more wide spread than the orebody response. Please note that the ambiguity in the image is significantly reduced, even though only one shot point was used. The image obtained is comparable to that found after migrating a realistic 3D finite difference model data set (section 3.2.4, figure 3.29).

In this benchmark example the exact position of the orebody is known and reproduced in good agreement with not only its real depth but also in azimuth and borehole distance. However, in the case of any other field experiment, i.e. when the position and extent of the scattering object is unknown, it would still be impossible to decide, if features imaged by migration correlate with massive sulphide ore deposit scattering centers. Only a subsequent investigation of the dynamical behavior, like in a CSA stack analysis (3.1.3), of the scattered wave field would allow for a classification of the scattering situation. As discussed in section 2.3.1 significant phase reversals in the scattered seismic wave field can

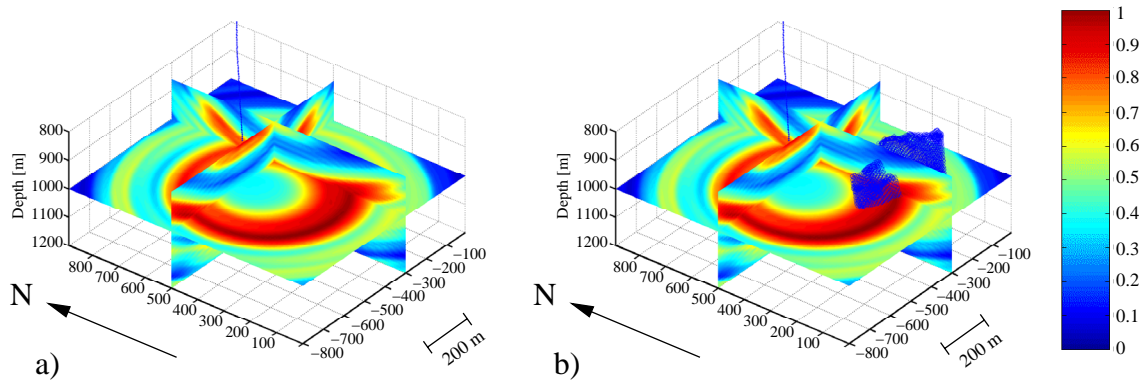


Figure 4.31: Resulting NE-DCM image for the data set collected in BAS-92-25. a) The image is highly ambiguous as expected from previous investigations. b) The outline of the orebody is plotted along with the data to evaluate migration accuracy.

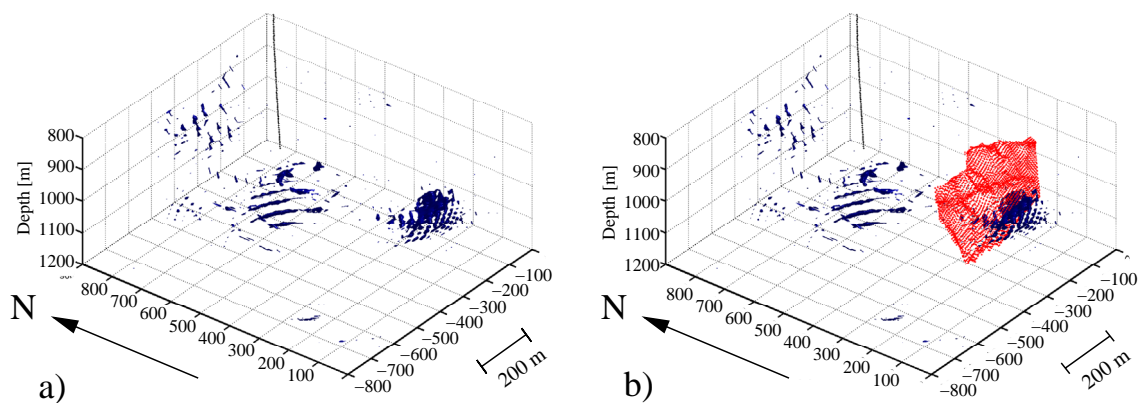


Figure 4.32: Migration result from DPM ($PAM=h_{III}$, equation 3.48) as applied to the VSP data set acquired in BAS-92-25. An isosurface display was chosen in order to provide a transparent view into the image space. DPM significantly reduced imaging ambiguity and performs superior to DCM. The outline of the orebody is plotted in panel b for comparison (Duvenceck, 2000).

be regarded as the most robust criterion of a given scattering situation. In the current example angular coverage, fold and range is not sufficient to conduct a CSA stack analysis and thus was not applied.

4.2.2 Multi Source VSP Survey in Sudbury

The Sudbury Igneous Complex (SIC) is the richest nickel-producing area in the world. In order to guarantee for continued use of the infrastructure of this mining district the discovery of new ore deposits is an important economical and political issue. There is significant interest in locating new nickel deposits to depths much deeper than 2100 m. In Sudbury it is planned to significantly increase the up to date mining depths limit⁵. An extensive database of new and existing geological mapping information, geophysical logs of existing drillholes, and physical rock property studies on core samples has been compiled, in the past few years. In situ logging and borehole seismic experiments have been conducted at multiple locations within the SIC (Adam *et al.*, 1999).

The investigations carried out in Matagami mining camp (previous section) served as a benchmark to test the ability of DSI methods to detect massive sulphide ore deposits. Several other DSI surveys have been conducted since these first approaches. The downhole seismic survey discussed in the current section was conducted in 1999 in Sudbury's Norman West mining camp and shall serve as a very recent example. The Norman West data were collected, processed and provided by the DSI consortium in order to investigate the performance of several different imaging approaches. In this context diffraction coherency migration was applied to the data set. In the following I will briefly summarize the geological setting in Sudbury and Norman West and subsequently describe data acquisition. I will review seismic processing as preparation for subsequent DCM. Since diffraction coherency migration is a scalar migration method only the vertical component of the data set was used. Imaging ambiguity is thus an important question with regard to interpretation of the obtained DCM images (please compare with section 3.2.3). The performance of the migration method and significance of the obtained subsurface images will be discussed.

Sudbury Igneous Complex and Norman West: Geological and Structural Setting

The geological setting in the Sudbury Igneous Complex will now be summarized, putting a focus on the Norman West area of the Sudbury mining camp. The description closely follows that given by Perron, 1999.

The mineralization of massive ore deposits mainly took place at the base of the SIC which outcrops as an elliptical ring. Figure 4.33 shows a geological map of the area and the location of Sudbury.

⁵ Falconbridge Ltd. is spending \$640-million to expand its Kidd Creek copper and zinc mine in Timmins, Ont., creating the world's deepest base metal mine. The project involves sinking a new mine shaft to the 3,100-metre level – 3.1 kilometers or nearly two miles beneath the surface – down from current mine workings 2,100 metres below ground" (from 'News from The Globe and Mail - globeinvestor.com', Thursday, July 20, 2000)

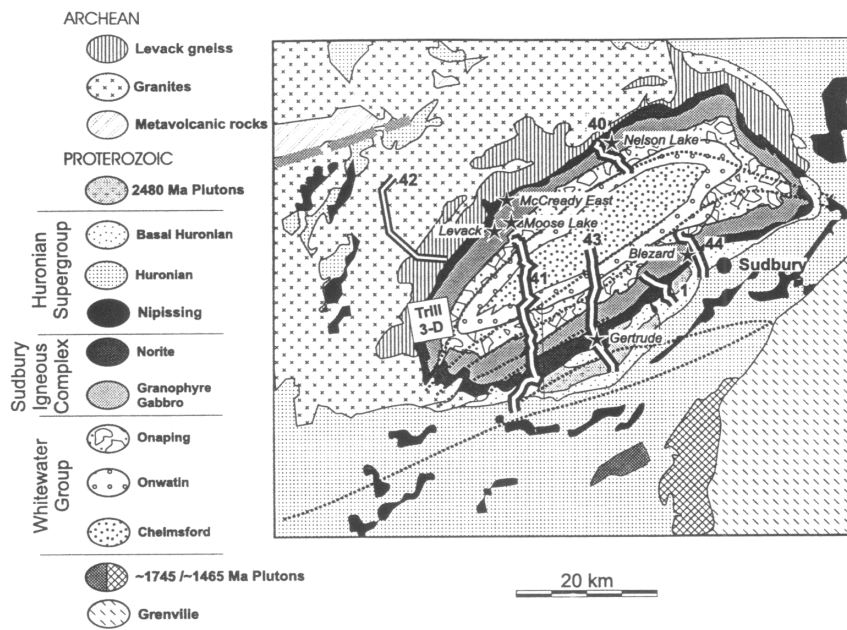


Figure 4.33: Geological map of Sudbury structure with Lithoprobe seismic profile locations (1, 40-44) and the Trill 3D seismic survey area (Milkereit et al., 2000). Stars indicate collar locations of boreholes that were used for geophysical logging (modified from Boerner et al., 2000)

The SIC is a tripartite igneous sequence of norite, gabbro and granophyre overlain by breccias and meta sedimentary rocks of the Whitewater group. Footwall rocks consist of Archean granitic and mafic igneous rocks. Initially generated by a high-energy meteorite impact (Dressler *et al.*, 1992) it was shortened in its northwest-southeast extent by brittle thrust faulting resulting in its elongated shape. Figure 4.34 shows a composite north-south cross section of the Sudbury structure along Lithoprobe seismic profile 40 and 41. The asymmetry of the geological setting is indicated by the overlaid interpretation (WU *et al.*, 1995; Adam, 2000).

Figure 4.35 shows an enlargement of the northeast corner of the SIC with locations of the shots and boreholes used to acquire the data considered here. Principal lithologies of the Norman West property include the upper granophyre unit (GRPH), Transition Zone (TRZN), Felsic Norite (FNOR), Mafic Norite (MNOR) and a basal zone of sub layer (SLN). The foot wall rocks consist of Granite (GR), Felsic Gneiss, Mafic Gneiss, Migmatites (MIG), Mafic Volcanics (BSLT), Gabbro and Diabase Dikes. The transition zone (TRZN) contact is cut by northwest trending faults, commonly occupied by late, post SIC event, olivine diabase dikes (OD).

Velocity and density borehole logs acquired at the SIC (figure 4.33) suggest, a narrow range of seismic velocities as well as density variations within the impact structure varying from 6200 to 6400 m/s for p-wave velocities and 2.75 g/cm³ to 2.8 g/cm³ for densities. The sub layer and footwall velocities and densities show much larger variations from 6000 to

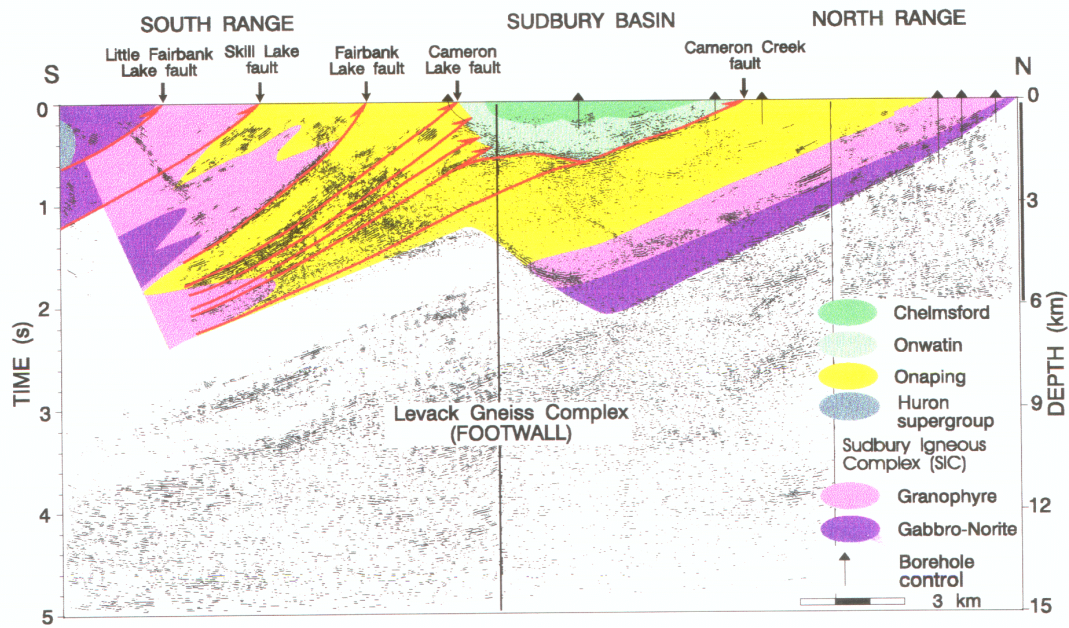


Figure 4.34: Composite north-south cross-section of the SIC along Lithoprobe reflection seismic profiles 40 and 41 (see figure 4.33). The overlaid interpretation reveals the asymmetry of the structure at depth, generated by thrust faulting (from Wu et al. 1995).

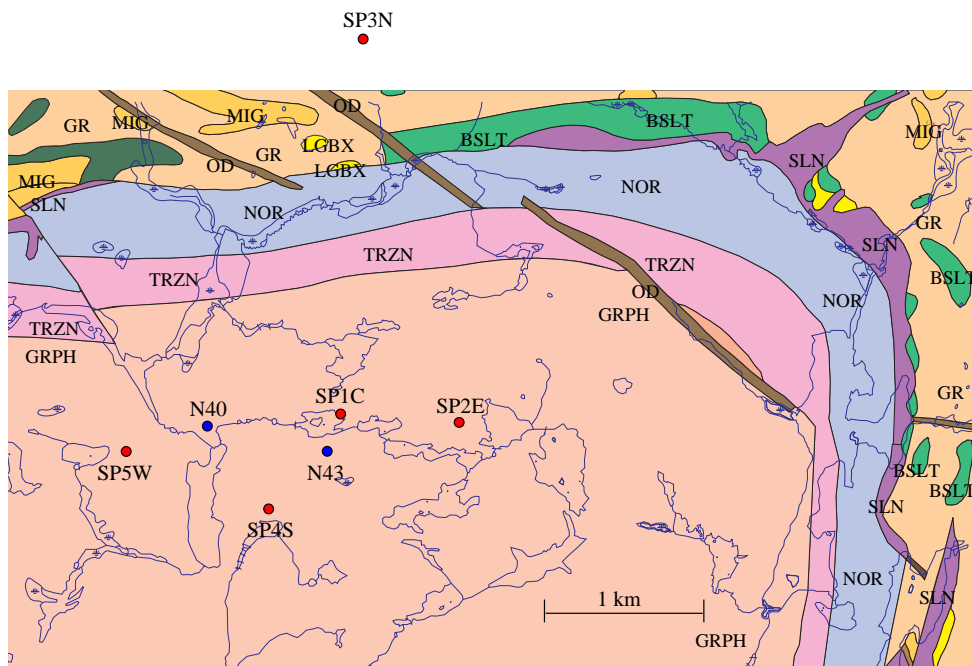


Figure 4.35: Geological setting of the north eastern corner of the SIC (description in text). Superimposed on the geological map the locations of shot and borehole positions used for the VSP/DSI survey considered here, are plotted (DSI Consortium).

6700 m/s and 2.75 g/cm^3 to 3.0 g/cm^3 respectively (Milkereit *et al.*, 1998). The SIC can thus be regarded as a relatively seismically transparent homogeneous medium, whereas the interface to the footwall complex provides a reflective marker horizon. The Pyrrhotite hosted Ni,Cu and Co ores are found at a depth of about 1700 m and lie within the sub layer norite.

Acquisition and Preprocessing

The data set was acquired in a typical DSI acquisition geometry using five shot point positions as indicated on the location map in figure 4.35. Receivers were deployed in two boreholes, N40 and N43. Shot point SP1C and SP4S were placed in vicinity to the boreholes, of which SP1C was intended to serve as a near offset shot point to provide information on the velocity field. The other three shot points were located to the north, east and west, with offsets ranging from 400 m (west) up to 2500 m (north). For each shot point three shot holes were drilled to a depth of 5 m and water filled to provide good coupling. At SP5W, SP1C and SP2E a 227 g Pentolite booster was used as the source. The source charge had to be increased for SP4S and SP3N to compensate for large offset and poor shot hole conditions respectively (Perron, 2000).

Borehole N40 is drilled rather straight and vertical down to 1419 m depth, whereas N43 bends to the north finally deviating 200 m from vertical at 1705 m depth. The data was collected using an eight level 3-component geophone chain from Vibrometric Oy Inc., Finland. In borehole N43 a 4 level geophone chain had to be used for the first 280 m as a backup due to technical problems with the 8 level tool. Five VSP surveys per recording hole were collected. The recording depths range from 350 m to the end of each borehole. During acquisition the receivers were kept at the same position for a specific recording depth, providing constant geophone orientation, until traces from all shot points were recorded. The recording interval was 5 m for the entire survey. The sampling interval was $250 \mu\text{s}$, to ensure for good reconstruction of the source signal wavelet, with a total recording length of 3 seconds. The shooting stations and the recording units were triggered using clocks, which were synchronized at the beginning and the end of each recording day. A surface Geophone that was kept at the same position during each survey, was placed in the vicinity to the borehole collar, in order to record first arrivals for each shot. It was later used to correct for drifts in the timing clocks (Perron, 2000).

Figure 4.36 displays raw data from shot point SP2E recorded with the vertical component of the geophone chain in borehole N43. The energy balanced seismogram documents electrical noise and discontinuities in the first arrival times caused by trigger clock drift. Preprocessing was done by G. Bellfleur (Bellfleur & Perron, 2000) and is summarized in table 4.2:

Electrical noise was removed at 60, 180 and 300 Hz using a time domain adaptive filtering module (Butler and Russel, 1993). Bandpass filtering between 50 and 250 Hz was applied with low and high-cut frequencies of 25 and 300 Hz. The data set was rotated so that the first horizontal (H1) component was pointing towards the shot position. Predictive deconvolution had to be applied in order to remove short period reverberations of the first arrival seismic events, which obscured near first break reflection and scattering responses.

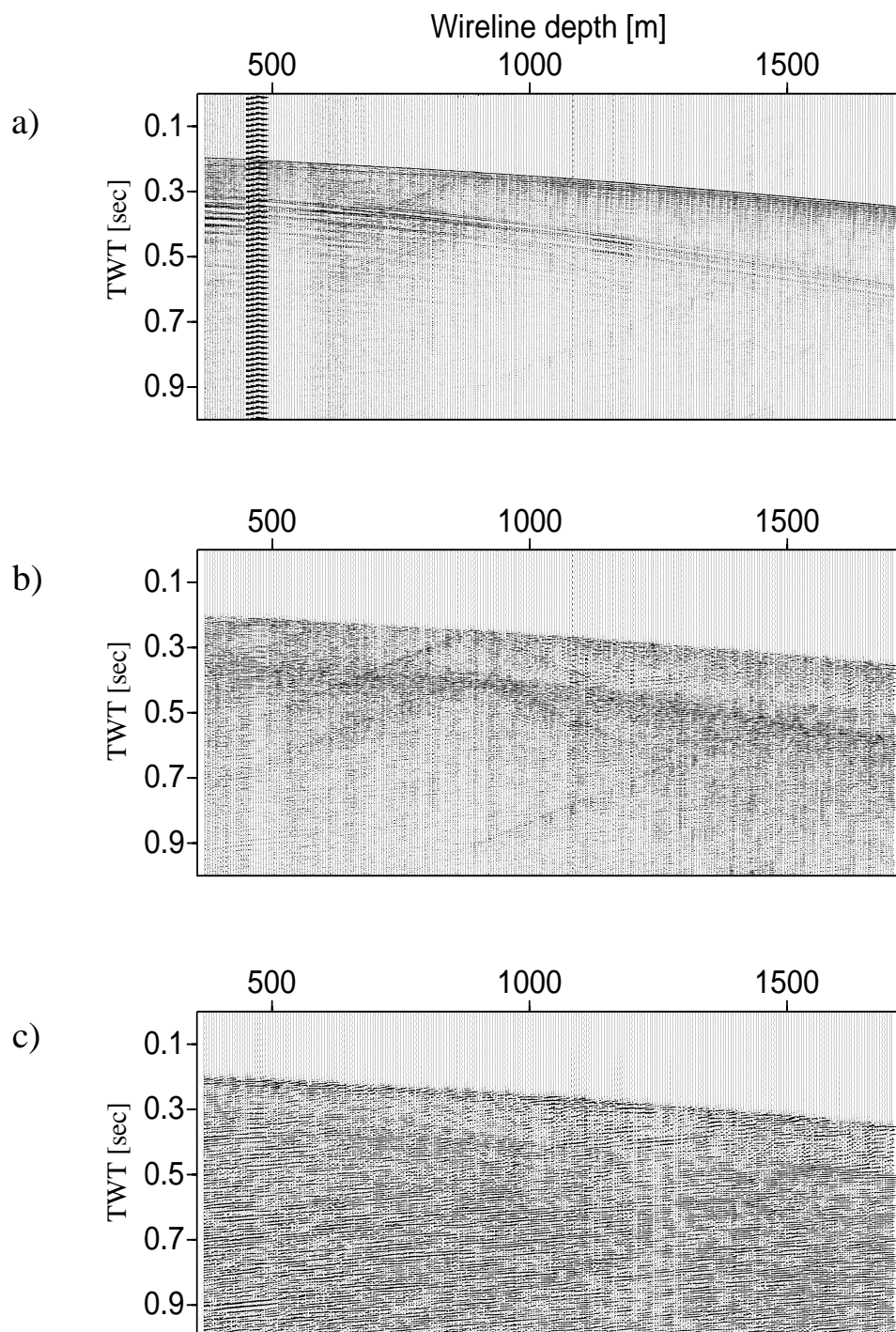


Figure 4.36: Sample VSP sections shot from SP2E and recorded on the vertical receiver component in borehole N43. Shown are three major processing steps: a) raw data after clock drift correction and rotation of the H1 horizontal component towards the shot point; b) same section after removal of downgoing p- and s-waves; c) after removal of tubewave. Trace balancing was applied (Bellfleur & Perron, 2000).

Geometry	
Sort	Wireline Depth
Timing clock drift corrections	
Monofrequency electrical noise removal	Adaptive filter (60, 180, 300 Hz)
Rotation to maximize energy in H1	Based on energy from 6 ms before first breaks to 8 ms after first breaks
Predictive deconvolution of vertical component	Start of window = 50 ms before first breaks End of window = 150 ms after first breaks Operator lag = 2.75 ms Operator length = 3 ms Prewhitening = 1%
Predictive deconvolution of horizontal components	Start of window = 0 s End of window = 2 s Operator lag = 7.50 ms Operator length = 3 ms Prewhitening = 1%
Resample	Sample rate = 0.5 ms (original 0.1 ms)
Removal of downgoing P-wave	median velocity filter (15 points)
Removal of downgoing S-wave	median velocity filter (19 points)
Removal of tubewave energy	f-k filters (N43) Tube_time (N40)
Removal of other downgoing energy	f-k velocity filter
agc 3 components	
Bandpass filtering	40Hz-70Hz-160Hz-190Hz

Table 4.2: Summary of processing flow for DSI datasets recorded in boreholes N40 and N43 (Bellfleur, 2000). Description in text

The horizontal and vertical components showed different ringing characteristics, so that different parameter sets had to be used for deconvolution (table 4.2).

In order to to remove downgoing P- and S-wave direct arrivals from the sections a median filter was applied. The wavelet shape of the direct arrival was effected by the recording characteristic of each individual geophone. Thus seismic traces were sorted by geophone numbers and median filtered after horizontal alignment of the first breaks in a first step. After resorting traces to wire line depth a second pass of a 13 trace median filter had to be applied to properly remove downgoing p-wave energy. Energy balancing that had been applied prior to median filtering was reverted afterwards, to guarantee for true amplitude processing. S-waves were removed in a similar fashion. Remaining tube waves had to be suppressed by f-k-filtering.

In a final processing step the data were bandpass filtered again after analyzing the frequency content of the upgoing wave field. Cutoff frequencies were set to 40 and 190 Hz. The spectrum was passed between 70 and 160 Hz. A three component AGC was used to display the finally processed section (Bellfleur & Perron, 2000).

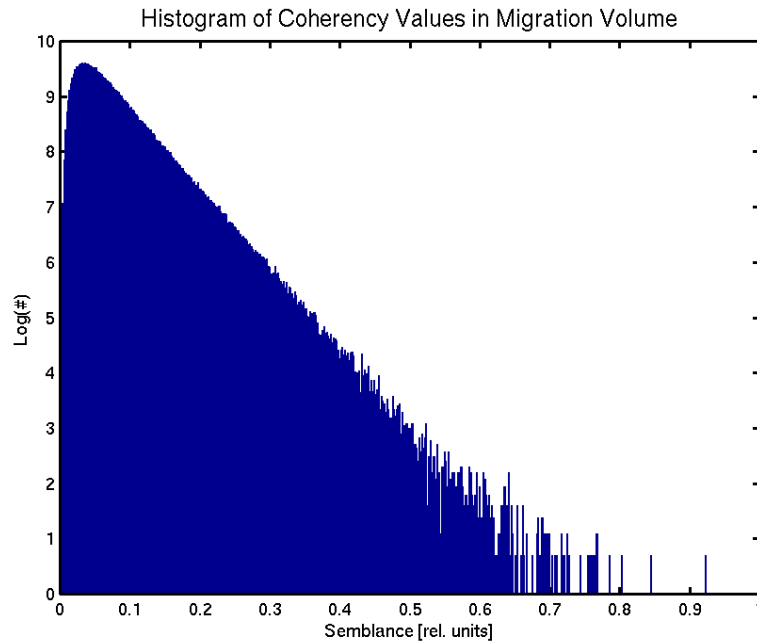


Figure 4.37: *The histogram of semblance values in the migrated data cube expresses the noisy character of the migration result.*

Migration Results

Diffraction coherency migration using semblance as the coherency measure (NE-DCM) was applied to the vertical component of the finally processed seismic sections of the data collected in N40 and N43. For migration a constant velocity background medium was assumed, as indicated by the borehole logging information available for the SIC. The assumption is supported by a linear regression analysis of the first break travel time picks conducted by Bellfleur, 2000. The background compressional wave velocity was found to be 6140 m/s as the best fit for the regression. Spatial sampling for migration was set to $dx=dy=dz=20$ m. The migrated cube covers a volume ranging from 5177200 (Nm) to 5178800 (Nm) northing, 505500 (Em) to 508000 (Em) easting (UTM coordinates) and 500 to 2000 m depth. Figure 4.37 shows a histogram of the semblance values obtained for the image cube.

The noisy character of the data would make interpretation difficult when displaying the three dimensional subsurface image as slices through the cube, like e.g. in the Matagami example. Instead an ISO surface display was chosen (equal data values are connected by a surface, which is virtually illuminated by optical ray tracing) and is plotted in figures 4.38 through 4.40. In each figure a sequence of migration images with increasing threshold for the ISO surface is displayed as seen from a different view position. High semblance values that remain stable in the noisy background can be interpreted as contributions from edges or scatterers in the subsurface (A,B,C). The circular distribution of events is due to imaging ambiguity as discussed in section 3.2.3.

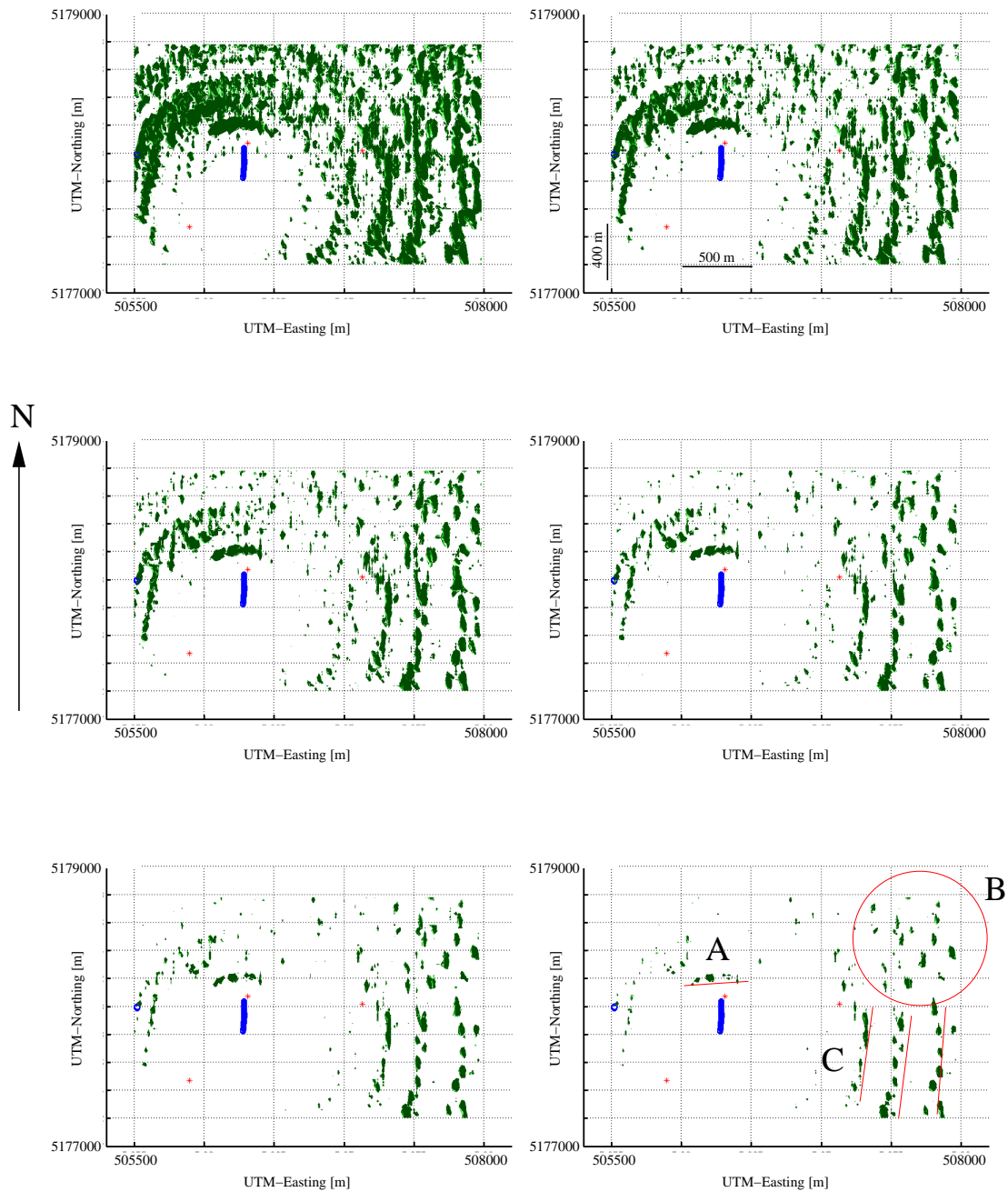


Figure 4.38: Norman West NE-DCM result as a sequence of figures with increasing isosurface threshold. Events that are stable with increasing threshold (A, B, C) can be interpreted as scattering/diffraction centers. The circular structures in the resulting image are due to migration ambiguity (please compare with figure 4.41). As migration input only the vertical component was used.

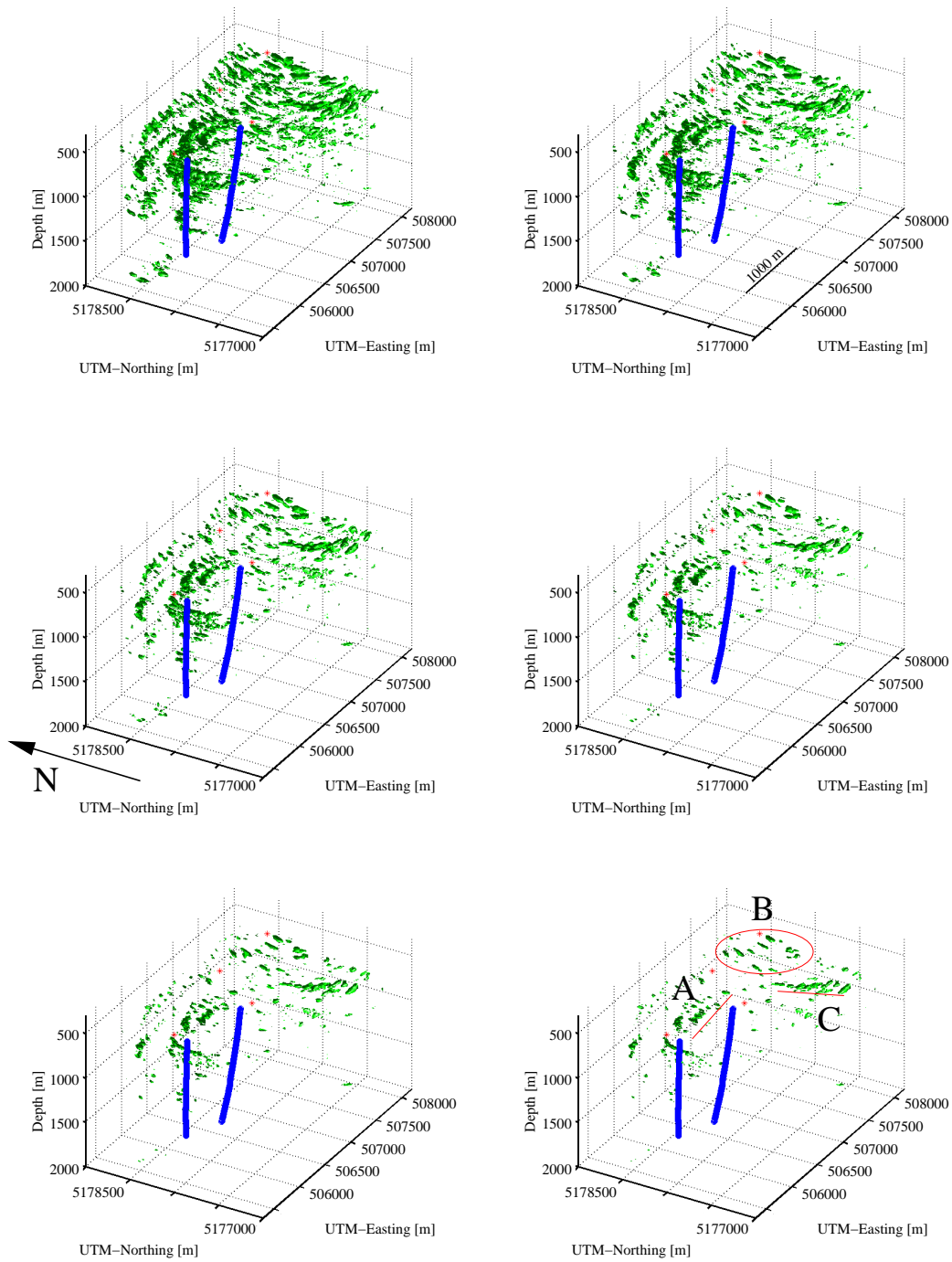


Figure 4.39: Same as in figure 4.38 but as seen from the south-west. To gain the correct understanding of the distribution of events within the migration cube several different view points have to be selected. An even better insight is given by displaying this sequence of images with increasing isosurface values as a movie.

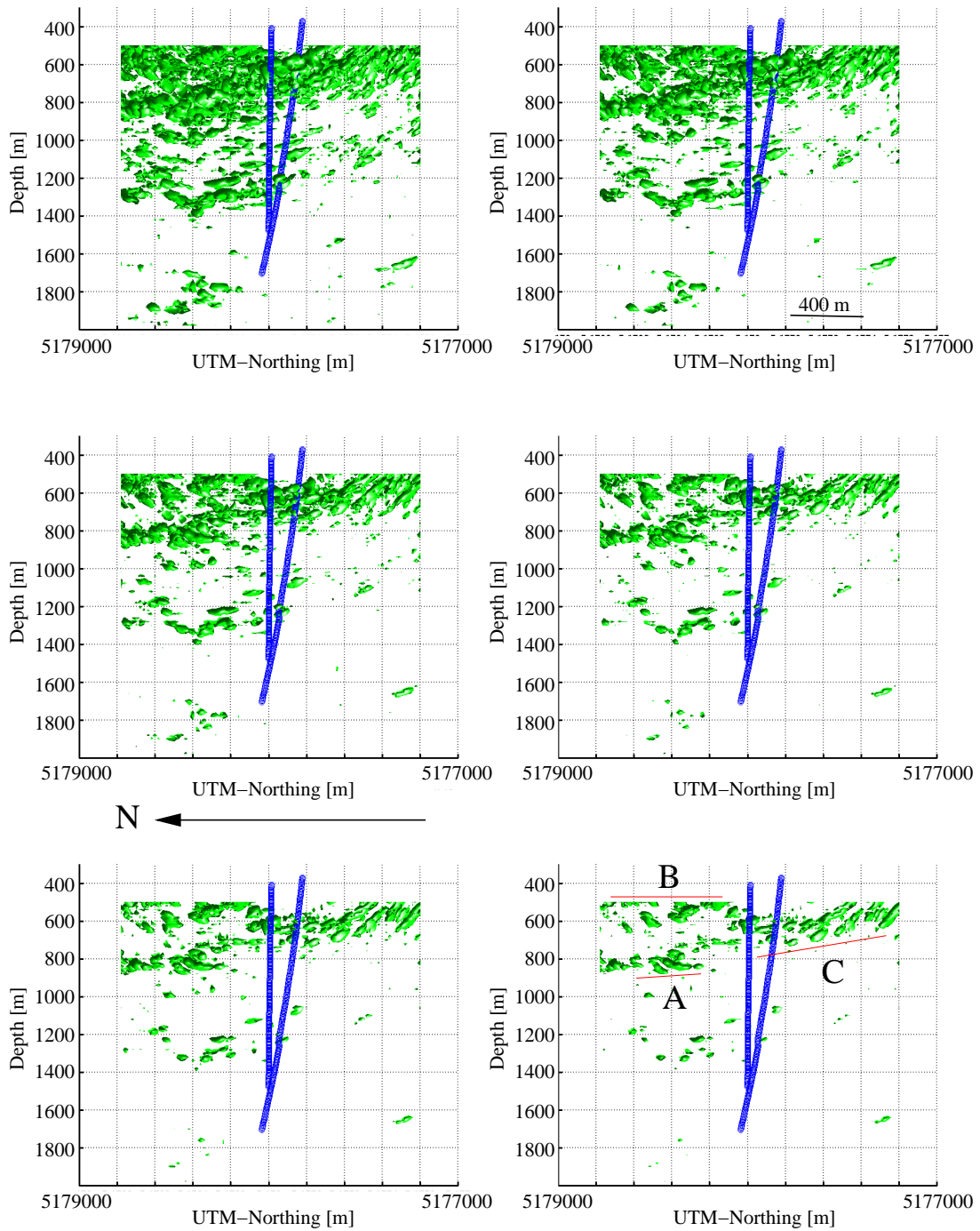


Figure 4.40: Same as in figure 4.38 but as seen from the west. Migration ambiguity highly effects the azimuthal distribution of the migrated events. Depth information shows a high degree imaging certainty.

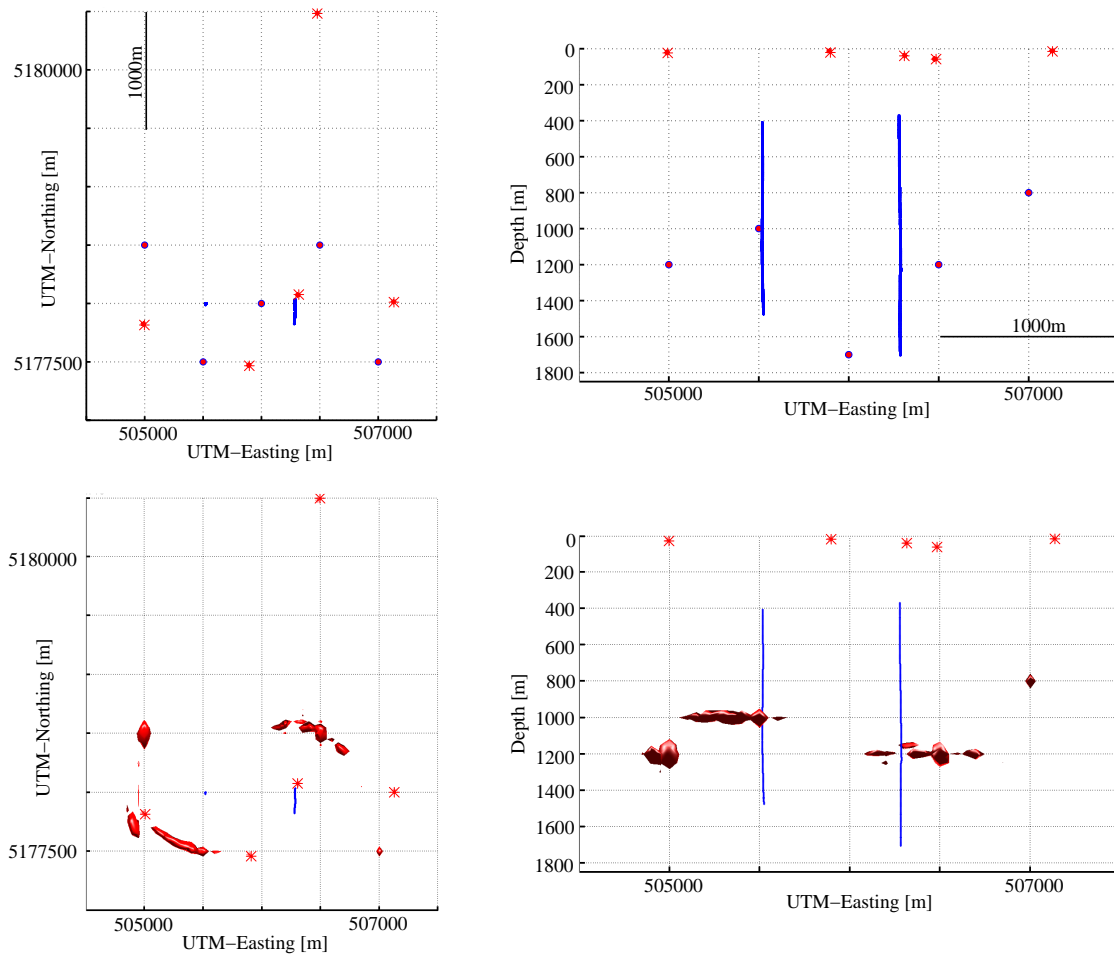


Figure 4.41: Results from the ambiguity investigation carried out for the acquisition geometry used in the Norman West survey. Seismic responses from point scatterers (upper panel) were modeled using simple travel time seismograms as input to the DCM algorithm. Azimuthal ambiguity is apparent, whereas the depth of the scatterers could be reconstructed with great accuracy. The scatterer located between borehole N40 and N43 was not imaged because the east-west orientated horizontal component of the modeled data set was used (lower panel).

An ambiguity investigation for the Norman West acquisition geometry was carried out in order to verify this interpretation (figure 4.41). Simple three component travel time modeling, using the original shot and receiver positions from the field experiment and placing point scatterers at several positions within the volume was conducted. DCM migration was subsequently applied to the synthetic data set. The input model (upper panel) and the DCM result (lower panel) are shown in figure 4.41.

An ISO surface threshold of $ISO=0.3$ was chosen in order to illustrate migration ambiguity effects. The lower left panel of figure 4.41 shows a map view of the migration image volume. The circular distribution of semblance values is apparent and comparable to the

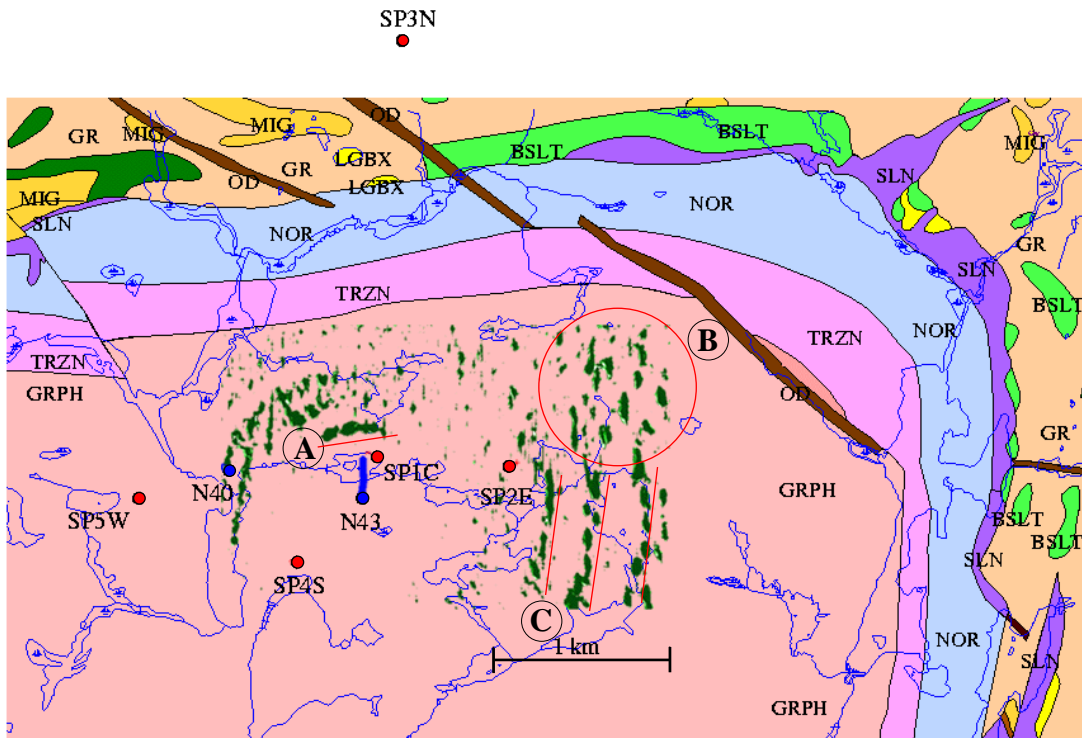


Figure 4.42: Migration result superimposed on the geological map of the north-east area of the SIC. Features (A, B, C) in the migration image that are stable in the noisy background signal show comparable strike as regional features (indicated by red lines). Interpretation, however, is difficult, since imaging ambiguity imprints a circular appearance on the image which leads to comparable directional trends (DSI Consortium).

pattern observed in figure 4.38. It must thus be concluded that even for the Norman West experiment, which utilizes five shot points and two boreholes DCM images still suffer from some azimuthal ambiguity. The side view (lower right panel) clearly documents, that depth information gained from this type of acquisition geometry is reliable. Please note, that the point scatterer situated exactly between the boreholes was not imaged, because for migration the horizontal component was used. Imaging ambiguity is not effected by this choice, but some regions of the subsurface will probably not be imaged.

Figure 4.42 shows a map view of the migration image as superimposed to the regional geology map of the Norman West area.

Unfortunately the elliptical structure of the SIC as it outcrops in this area is comparable to the migration ambiguity pattern that is imprinted on the migration image. It is thus difficult to correlate the migration result with regional structural features of the SIC and has to be done with great caution. Striking of image features characterized by high semblance values, is comparable to the striking of the transition zone and sublayer norite units. The features labeled A and C could thus probably indicate scattering or diffraction from terraced lithological structures. Features A and C are found in a depth range between 800 m and 900 m and are thus too shallow to be interpreted as seismic responses from massive sulphide

ore deposits. The same is valid for the image feature labeled C. The seismically reflective units of the SIC are located in the area north and east from the boreholes N40 and N43. The south-western part should be relatively seismically transparent. The distribution of high semblance values in the migration image follows this trend and gives some confidence, that the observed features are generated by lithological contacts. The isolated features at approx. 1700 m depth close to borehole N40 can probably be interpreted as seismic response from the footwall contact.

4.2.3 Conclusions

Two crustal VSP data sets served as examples for the performance of DCM, DPM with regard to detecting massive sulphide ore deposits in the crystalline crust. In a first example DCM as well as DPM were applied to a single shot three component VSP conducted in Matagami, which was aimed towards measuring the seismic response from the Bell-Allard massive sulphide ore deposit.

Due to a lag in azimuthal shot position coverage it was not possible to detect the orebody by DCM and consequently imaging ambiguity is severe. High semblance values observed on the migration image correlate however quite well with the depth position of the ore deposit. DPM highly reduced imaging ambiguity and performed superior to DCM regarding the task of localizing a possible scattering, diffraction center in close vicinity to the known position of the Bell Allard orebody. The obtained results have to be treated with some caution, since several assumption that have to be made in order to perform DPM are probably not completely fulfilled:

The borehole used to acquire the Matagami VSP data set is slightly deviating from vertical. If the vertical component of the deployed geophone tool was aligned along the axis of the borehole, the inclination of expected polarization is not correctly estimated. A misplacement of features in the migration image results.

Polarization quality most probably decreases with increasing length of the seismic ray path, which also could lead to wrong estimates on expected polarization.

Provided this is the case, scattering could possibly also have been generated by deeper structures. The Pyrite rich alteration zone located directly below the Bell Allard deposit most probably exhibits a much higher impedance contrast than the deposit itself (figure 4.28) and could thus produce prominent scattering.

DCM was applied to a crustal multisource VSP data example. Since DCM was developed to be applied to scalar seismic data, only the vertical component of a three component data set was used for migration. The obtained image shows significant background noise and ambiguity is apparent in the resulting subsurface image even though an acquisition layout with five shot points and two boreholes was used. Nevertheless, depth information deduced from migration is reliable, as was confirmed by imaging ambiguity investigation. Correlation with regional geology is aggravated by similarities between geological structures and the imaging ambiguity imprint on the migration result. Only image features that, with increased ISO surface threshold, remain constant in the background noise can be interpreted as images from coherent seismic events. The low impedance contrast of pyrrhotite compared to the

felsic and mafic background rocks of the SIC suggest a lower reflectivity than that expected for pyrite hosted ore bodies like in Matagami (figure 4.25). This could be another possible reason for imaging difficulties encountered in migrating the Norman West VSP data set.

Despite the problems mentioned above, DCM and DPM provide a reasonable approach towards imaging of scattering centers in the crystalline crust.

As proposed in appendix B a dynamic analysis of the scattering response might follow if a scattering center can be localized. Finding the position of an SPR, however, poses high demands on data quality, angular fold, coverage and range. The analysis was omitted because neither of these demands were fulfilled for the example data sets.

Modeling studies regarding loss in polarization quality of seismic wave fields traveling through random media should follow the current investigation.

In general, significant portions of incident compressional wave energy is converted into shear wave energy by scattering. DCM and DPM migration algorithms should thus account for different travel times for rays going to and coming from the scatterer.

DCM and DPM use different characteristic features of the scattered seismic wave field in order to enhance the migration image over that of reflectors. Combining both approaches into one migration algorithm should thus improve this quality of the methods.

Chapter 5

Conclusions

The nature of seismic scattering was investigated by elastic scattering theory and numerical experiment. Knowledge gained from this investigation was used to develop new processing and interpretation methods that are capable of enhancing the signature or image of seismic scatterers on seismic section and assist in classifying a given scattering situation.

The newly developed methods of DCM and DPM migration were applied to different marine and crustal seismic data sets. Marine data were acquired as part of a feasibility study which was conducted in order to test multichannel seismic surveying using boomer sources as a first step in developing a high resolution 3D seismic acquisition technique. The crustal seismic data was acquired within the scope of the DSI development program which is aimed towards detecting massive volcanogenic ore deposits in the crystalline crust using seismic methods.

I will now summarize and discuss the main results of this study and point out necessary follow-up investigations.

5.1 Seismic Wave Scattering

Scattering from small scale seismic inclusions not only depends on their composition, but also on the composition of the background medium situated in. This *scattering situation* can be classified by analyzing the amplitude versus scattering angle behavior of the scattered seismic wave field. Such an interpretation, inversion approach can possibly be applied, whenever classical AVO analysis breaks down due to the non continuity of the subsurface structure being subject to seismic investigation. When observed on seismic sections, a significant phase reversal (SPR) within the first arriving scattered seismic wave field can be utilized as a robust criterion in order to classify the current scattering situation.

The concept of SPR classification can in part be extended to the case of scattering from large complex objects. It can be assumed that scattering takes place at *scattering centers*, i.e. areas with strong curvature. The shape of large objects has a significant impact on the dynamic of the scattered wave field. Also scattering and diffraction can be intertwined and dynamical analysis may be difficult. An analysis of amplitude variations with scattering angle demands the knowledge about the position of the scattering center, for which it is necessary to image the scatterer as such.

Diffractions from interrupted, otherwise continuous seismic reflectors is possibly stronger than scattering from structures with comparable parameter perturbations. Due to their equal kinematics, it is difficult to distinguish between scattered and diffracted seismic energy.

5.2 Acquisition, Processing and Interpretation

Seismic acquisition and processing aimed towards resolving, position, shape and composition of a single scatterer has to focus on gaining and preserving as much scattered energy as possible, since the scattered seismic signal is weak by nature. In any case the phase information of the scattered wave field has to be preserved in order to provide the possibility of AVSA analysis.

The CDP processing approach does not account for the kinematic and dynamic characteristics of the scattered wave field. Due to the NMO correction applied in individual CDP gathers prior to stacking, only near offset scattered or diffracted energy will be enhanced. Several new, gather oriented as well as prestack processing methods that are capable of enhancing the seismic response of isolated scattering objects were introduced.

For most of the gather orientated methods, such as the SES, CPP and CSA approaches, the position of the scatterer has to be known a priori. In all the cases discussed in detail a reliable velocity model of the background medium has to be given in order calculate the travel time of scattered energy and to apply static travel time corrections.

A new 3D migration technique based on diffraction stack migration (DSM) was introduced. The method uses either coherency (DCM) or polarization information (DPM) of the scattered wave field.

In case of scalar wave field registration, coherency measured along reflection time surfaces in the dataset, detects scattered energy (DCM). The resulting migrated cube enhances images of scattering centers over those of reflector elements. The image obtained by applying DSM to scalar VSP and surface seismic surveying data is ambiguous. Entropy is introduced as an ambiguity measure. Imaging ambiguity is greatly reduced if polarization information is included into the concept of DSM (DPM).

Given the position of the scattering center amplitude versus scattering angle analysis can be applied in order to interpret the scattering situation in question. Traces of common scattering angle are stacked in order to enhance the signal to noise ratio of the scattering response. The acquisition layout should be tailored to provide sufficient fold, resolution and range of scattering angles when aimed towards interpretation of scattered seismic energy.

5.3 Marine and Crustal Seismic Case Histories

Boomer sources show sufficient repeatability to be applied in multichannel marine seismic acquisition and processing. Since streamer arrays are generally constructed to be used with airguns either single hydrophone streamers or streamers with a grouping geometry adapted to high frequency seismic sources should be used.

Multichannel seismic acquisition significantly extends the possibilities of seismic processing. The signal to noise ratio, as well as, the lateral resolution in the CMP processed zero offset sections is increased. The conducted seismic surveys were especially aimed towards finding

and classifying single scattering objects. Difference filtering and subsequent diffraction coherency migration proved to efficiently suppress reflections and enhance the image of subsurface scattering centers and discontinuities.

Analysis of the scattering response dynamics in a CSA gather and search for an SPR strictly applies only to the case of scattering from spherically symmetric objects. This requirement was not met in the discussed examples and thus CSA analysis had to be omitted.

For the first time it was possible to conduct a high resolution multichannel $2\frac{1}{2}$ D seismic survey in the Baltic Sea. A Pleistocene fluvial channel system situated below a flat cover of unconsolidated sediments was revealed in Kiel Bay. Penetration up to 40 m was achieved showing deeper anticlinale structures within the seismic cube which could not be classified. Gas features are clearly visible in seismic time slices, but scattering signatures were not observed due to a lag lateral coverage in the $2\frac{1}{2}$ D seismic survey, and the applied binning procedure.

In a first benchmark example DCM as well as DPM were applied to a single shot three component crustal VSP conducted in Matagami, where the position as well as the reflectiveness of the ore deposit are well documented. Due to a lag in azimuthal shot position coverage and resulting severe imaging ambiguity it was not possible to detect the Bell Allard orebody by DCM. High semblance values observed on the migration image correlate however quite well with the depth position of the ore deposit.

DPM highly reduced imaging ambiguity and performed superior to DCM regarding the task of localizing a possible scattering, diffraction center in close vicinity to the known position of the orebody.

DCM was applied to the vertical component of a crustal multi source VSP data example acquired at the Norman West area of the Sudbury impact structure. The obtained image shows significant background noise and ambiguity is apparent in the resulting subsurface image. Depth information deduced from migration is reliable, however, as was confirmed by imaging ambiguity investigation. Correlation with regional geology is aggravated by similarities between geological structures and the imaging ambiguity imprint on the migration result.

As in the marine example, analysis of the scattered wave field dynamics was omitted, since data quality as well as angular fold, coverage and range was not sufficiently provided by the investigated data sets.

Despite the problems mentioned above, DCM and DPM provide a reasonable approach towards imaging of scattering centers in marine sediments or the crystalline crust.

5.4 Future Work

The progress made in imaging subsurface discontinuities is promising. The aim of inverting the composition of a scattering object by using seismic methods, however, could not be met. In part caused by a lag of suitable seismic data future work should focus on applying the imaging and interpretation methods developed in this study to other seismic data sets. Since scattering is a three dimensional phenomenon by nature, the development of new high resolution 3D marine seismic acquisition techniques should be continued.

Modeling studies regarding loss in polarization quality of seismic wave fields traveling through random media should follow the current investigation. It is still uncertain, to which degree the polarization quality of scattered seismic energy is affected by randomly scattering background media, such as the crystalline crust. Especially regarding DSI problems it would be interesting to investigate how polarization of the scattered wave field is altered as a function of travel time.

In general, significant portions of incident compressional wave energy is converted into shear wave energy by scattering. DCM and DPM migration algorithms should thus account for different ray travel times going to and coming from the scatterer.

DCM and DPM use different characteristic features of the scattered seismic wave field in order to enhance the migration image over that of reflectors. Combining both approaches into one migration algorithm should thus improve this quality of the methods.

References

- ADAM, E. 2000. *Détection Directe D'un Gisement de Sulfures Massifs Volcanogènes Pas Sismique Réflexion (in English)*. Ph.D. thesis, École Polytechnique de Montréal.
- ADAM, E., MILKEREIT, B., ARNOLD, G., & PINEAULT, R. 1996. Seismic Response of the Bell Allard Orebody, Matagami, Québec. *Pages 634–637 of: 66 th Annual Meeting Expanded Abstracts*. Denver, Colorado: Society of Exploration Geophysicists.
- ADAM, E., PERRON, G., MILKEREIT, B., WU, J., SALISBURY, M., VERPAELST, PL., DION, D.J., & CALVERT, A. 1999. High-Resolution Seismic Profiling Across the Sudbury, Selbaie, Noranda, and Matagami Mining Camps. *Canadian Journal of Earth Sciences*, submitted.
- ADAM, E., BOHLEN, T., & MILKEREIT, B. 2001 (in preparation). *Vertical Seismic Profiling at the Bell Allard Orebody, Matagami, Quebec*. Denver, Colorado: Society of Exploration Geophysicists.
- AKI, K. 1980. Scattering and Attenuation of Shear Waves in the Lithosphere. *Journal of Geophysical Research*, **85**, 6496–6504.
- ASANO. 1979. Light Scattering Properties of Spheroidal Particles. *Appl. Opt*, **18**(5), 712–723.
- ATZLER, R. 1995. *Der pleistozäne Untergrund der Kieler Bucht und angrenzender Gebiete nach reflexionsseismischen Messungen*. Ph.D. thesis, Kiel University.
- AYRES, A., & THEILEN, F. 1999. Relationship Between P- and S-Wave Velocities and Geological Properties of Near-Surface Sediments of the Continental Slope of the Barents Sea. *Geophysical Prospecting*, **47**(4), 431–441.
- BEAUDRY, C., & GAUCHER, E. 1986. *Cartographie Géologique dans la Région de Matagami*. rapport MB 86-32. Ministère de l'Énergie et des Ressources.
- BELFER, I., BRUNER, I., KEYDAR, S., KRAVTSOV, A., & LANDA, E. 1998. Detection of Shallow Objects Using Refracted and Diffracted Seismic Waves. *J. Appl. Geophys.*, **38**, 155–168.
- BELLFLEUR, G., & PERRON, G. 2000. *Processing of Norman West '99 Data*. Tech. rept. Geological Survey of Canada, Continental Geoscience Division, Ottawa.

- BERRYHILL, J.R. 1977. Diffraction Response for Nonzero Separation of Source and Receiver. *Geophysics*, **42**(6), 1158–1176.
- BEYLKIN, G., & BURRIDGE, R. 1990. Linearized Inverse Scattering Problems in Acoustics and Elastics. *Wave Motion*, **12**, 15–52.
- BHATIA, A.B. 1959. Scattering of High Frequency Sound Waves in Polycrystalline Materials. *J. Acoust. Soc. Am.*, **31**, 16–23.
- BLANCH, J.O. 1995. *A Study of Viscous Effects in Seismic Modeling, Imaging, and Inversion: Methodology, Computational Aspects, and Sensitivity*. Ph.D. thesis, Rice University, Houston, Texas.
- BOERNER, D.E., MILKEREIT, B., & DAVIDSON, A. 2000. Geoscience Impact: A Synthesis of Studies of the Sudbury Structure. *Canadian Journal of Earth Sciences*, **37**(2/3), 477–501.
- BOHLEN, T. 1998. *Viskoelastische FD-Modellierung seismischer Wellen zur Interpretation gemessener Seismogramme*. Ph.D. thesis, Universität Kiel.
- BOHLEN, T., MÜLLER, CF., & MILKEREIT, B. 2000. *Elastic Wave Scattering from Massive Sulfide Orebodies: on the role of Composition and Shape*. Society of Exploration Geophysicists. Chap. accepted.
- BORN, M., & WOLF, E. 1980. *Principles of Optics*. Pergamon Pr.
- BRUGHMANS, N. 2000. *Study of Shallow Subsurface Structures in the Northern Kiel Bay (Germany) Based on High-Frequency Multi-Channel Seismic Surveying*. M.Phil. thesis, Kiel University.
- BUTLER, K.E., & RUSSELL, R.D. 1993. Subtraction of Powerline Harmonics from Geophysical Records. *Geophysics*, **58**, 898–903.
- CERVENY, V. 1987. *Ray Methods for Three-Dimensional Seismic Modelling*. Norwegian Institute of Technology.
- COSMA, C., & HEIKKINEN, P. 1996. Seismic Investigations for the Final Disposal of Spent Nuclear Fuel in Finland. *J. Appl. Geophys.*, 151–157.
- DEVANEY, A.J. 1981. Inverse-Scattering Theory Within the Rytov Approximation. *Optics letters*, **6**(8), 374–376.
- DEVANEY, A.J. 1984a. A Filtered Backpropagation Algorithm for Diffraction Tomography. *Ultrasonic Imaging*, **GE-22**(1), 3–13.
- DEVANEY, A.J. 1984b. Geophysical Diffraction Tomography. *IEEE Transactions on Geoscience and Remote Sensing*, **GE-22**(1), 3–13.
- DRESSLER, B.O., PEREDERY, W.V., & MIUR, T.L. 1992. *Ontario Geological Guidebook*. Chap. Geology and Mineral Deposits at the Sudbury Structure.

- DUVENECK, E. 2000. *Abbildung von Erzkörpern in VSP-Geometrie*. M.Phil. thesis, Kiel University.
- EATON, D., GUEST, S., MILKEREIT, B., BLEEKER, W., CRICK, D., SCHMITT, D., & SALISBURY, M. 1996. Seismic Imaging of Massive Sulfide Deposits: Part III. Borehole Seismic Imaging of Near Vertical Structures. *Economic Geology*, **91**, 829–834.
- EATON, D.W. 1997. *BMOD3D: A Program for Three-Dimensional Seismic Modelling Using the Born Approximation*. Geological Survey of Canada, GSC Open File 3357.
- EATON, D.W. 1999. Weak Elastic Scattering from Massive Sulfide Orebodies. *Geophysics*, 289–299.
- ECKER, C. 1998. *Seismic Characterization Of Methane Hydrate Structures*. Ph.D. thesis, Stanford University.
- FRENCH, W.S. 1975. Computer Migration of Oblique Seismic Reflection Profiles. *Geophysics*, **40**, 961–980.
- GELCHINSKI, B., LANDA, E., & SHTIVELMAN, V. 1985. Algorithms of Phase and Group Correlation. *Geophysics*, **50**(4), 596–608.
- GOLTZ, C. 1998. *Fractal and Chaotic Properties of Earthquakes*. Berlin, Heidelberg, New York: Springer.
- GRITTO, R., KORNEEV, V.A., & JOHNSON, L.R. 1995. Low-Frequency Elastic-Wave Scattering by an Inclusion; Limits of Applications. *Geophysical Journal International*, 766–692.
- GUBERNATIS, J. E., DOMANY, E., KRUMHANSL, J. A., & HUBERMAN, M. 1977a. The Born Approximation in the Theory of the Scattering of Elastic Waves by Flaws. *Journal of Applied Physics*, **48**, 2812–2819.
- GUBERNATIS, J. E., DOMANY, E., & KRUMHANSL, J. A. 1977b. Formal Aspects of the Theory of the Scattering of Ultrasound by Flaws in Elastic Materials. *Journal of Applied Physics*, **48**, 2804–2811.
- HADDON, R.A.W., & BUCHEN, P.W. 1981. Use of Kirchhoff's Formula for Body Wave Calculations in the Earth. *Geophys. J. R. astr. Soc.*, **67**, 587–598.
- HAJNAL, Z., ANNESLEY, I.R., WHITE, D., MATTHEWS, R.B., SOPUCK, V., KOCH, R., LEPPIN, M., & AHUJA, S. 1997. Sedimentary-Hosted Mineral Deposits: A High-Resolution Seismic Survey in the Athabasca Basin. *Pages 421–432 of: GUBINS, A.G. (ed), Proceedings of Exploration 97: Fourth Decennial International Conference on Mineral Exploration*.
- HILTERMAN, F.J. 1970. Three-Dimensional Seismic Modeling. *Geophysics*, **35**(6), 1020–1037.

- HINZ, K., KÖGLER, F., RICHTER, I., & SEIBOLD, E. 1971. Reflexionsseismische Untersuchungen mit einer pneumatischen Schallquelle und einem Sedimentecholot in der westlichen Ostsee. Teil II: Untersuchungsergebnisse und geologische Deutung. *Meyniana (Kiel University)*, **21**, 17–24.
- HOFFMANN, H.J. 1995. *Objektorientierte Analyse und Migration diffrakter Wellenfelder unter Verwendung der Strahlenmethode und der Edge-Wave-Theorie*. Ph.D. thesis, Kiel University.
- HUDSON, J., & HERITAGE, J.R. 1981. The use of the Born Approximation in Seismic Scattering Problems. *Geophys. J. R. astr. Soc.*, **66**, 221–240.
- HYNDMAN, R., & SPENCE, G. 1992. A Seismic Study of Methane Hydrate Marine Bottom Simulating Reflectors. *Geophys. Res.*, 6683–6698.
- IMHOF, M.G. 1996. *Scattering of Elastic Waves using Non-Orthogonal Expansions*. Ph.D. thesis, Massachusetts Institute of Technology.
- JÄGER, T. 1998. *Entwicklung und Anwendung neuer Datenbearbeitungsverfahren zur Interpretation von seismischen Streuantworten und deren Trennung von Reflexionen*. M.Phil. thesis, Kiel University.
- JÄHNE, B. 1997. *Digital Image Processing. Concepts, Algorithms, and Scientific Applications*. Berlin: Springer-Verlag.
- J.G., HAGEDORN. 1954. A Process of Seismic Reflection Interpretation. *Geophysical Prospecting*, 85–127.
- KAMPFMANN, W. 1988. A Study of Diffraction-Like Events on DEKORP 2-S by Kirchhoff Theory. *Journal of Geophysics*, 163–174.
- KANASEWICH, E.R., & PHADKE, S.M. 1988. Imaging Discontinuities on Seismic Sections. *Geophysics*, **53**, 334–345.
- KELLER, J.B. 1962. A Geometrical Theory of Diffraction. *Journal of the Optical Society of America*, **52**, 116–130.
- KLÄSCHEN, D. 1995. *Strahlenseismische Modellierung unter Berücksichtigung von Mehrfachdiffraktionen mit Hilfe der Edge-Waves: Theorie und Anwendungsbeispiele*. Ph.D. thesis, Kiel University.
- KLEM-MUSATOV, K.D., & AIZENBERG, A.M. 1985. Seismic Modelling by Methods of the Theory of Edge Waves. *Journal of Geophysics*, **57**, 90–105.
- KLEM-MUSATOV, K.D., & AIZENBERG, A.M. 1989. The Edge Wave Superposition Method (2-D Scalar Problem). *Geophysical Journal International*, 351–367.
- KNEIB, G., KASSEL, A., & LORENZ, K. 2000. Automated seismic prediction ahead of the tunnel boring machine. *First Break*, **18**(7), 295–302.

- KORNEEV, V.A., & JOHNSON, L.R. 1993a. Scattering of Elastic Waves by a Spherical Inclusion - I. Theory and numerical results. *Geophysical Journal International*, **115**, 230–250.
- KORNEEV, V.A., & JOHNSON, L.R. 1993b. Scattering of Elastic Waves by a Spherical Inclusion - II Limitations of Asymptotic Solutions. *GJI*, **115**, 251–263.
- LANDA, E., & KEYDAR, S. 1998. Seismic Monitoring of Diffraction Images for Detection of Local Heterogeneities. *Geophysics*, **63**, 1093–1100.
- LANDA, E., SHTIVELMAN, V., & GELCHINSKY, B. 1987. A Method for Detection of Diffracted Waves on Common-Offset Sections. *Geophysical Prospecting*, **35**(4), 359–373.
- LEMKE, W. 1994. Spät- und postglaziale Sedimente der westlichen Ostsee. (German). *Zeitschr. geol. Wiss.*, **22**, 275–286.
- LEVANDER, A.R. 1988. Fourth-order Finite-Difference P-SV seismograms. *Geophysics*, **53**(11), 1425–1436.
- MAYNE, W.H. 1962. Common Reflection Point Horizontal Data Stacking Techniques. *geo*, **27**(6), 927–938.
- MIE, G. 1908. Beiträge zur Optik trüber Medien, speziell kolloidaler Metallösungen. *Ann. Physik*, **25**, 377–445.
- MILES, J.M. 1960. Scattering of Elastic Waves by Small Inhomogeneities. *Geophysics*, **25**(3), 642–648.
- MILKEREIT, B. 1987. Migration of Noisy Crustal Seismic Data. *Journal of Geophysical Research*, **92**(B8), 7916–7930.
- MILKEREIT, B., EATON, D., WU, J., PERRON, G., SALISBURY, M., BERRER, E.K., & MORRISON, G. 1996. Seismic Imaging of Massive Sulfide Deposits: Part II. Reflection Seismic Profiling. *Economic Geology*, **91**, 835–840.
- MILKEREIT, B., ROBERTS, B., ADAM, E., & KING, A. 1998. Integrated Borehole Geophysical and 3-D Seismic Study of a Deep Massive Sulfide Deposit, Sudbury Basin, Canada. *Pages 768–771 of: 68th Annual Meeting Expanded Abstracts*. New Orleans, Louisiana: Society of Exploration Geophysicists.
- MILKEREIT, B., BERRER, K.E., KING, A.R., WATTS, A.H., ROBERTS, B., ADAM, E., EATON, D.W., WU, J., & SALISBURY, M.H. 2000. Development of 3-D Seismic Exploration Technology for Deep Nickel-Copper deposits— A Case History from the Sudbury Basin, Canada. *Geophysics*, **65**(4), 1–10.
- MILLER, D. 1983. Integral Transforms and the Migration of Multiple-Offset Borehole Seismic Profiles. *Research Note, Schlumberger-Doll Research*.

- MILLER, D., ORISTAGLIO, M., & G., BEYLKIN. 1984. A new Formalism and old Heuristic for Seismic Migration. *54th Ann. Int. Mtg. Soc. Explor. Geophys., Atlanta: abstracts and biographies*, 704–707.
- MILLER, D., ORISTAGLIO, M., & G., BEYLKIN. 1987. A new Slant on Seismic Imaging: Migration and Integral Geometry. *Geophysics*, **52**(7), 943–964.
- NEIDELL, N. S., & TANER, M. T. 1971. Semblance and Other Coherency Measures for Multichannel Data. *Geophysics*, **36**(3), 482–497.
- OSTRANDER, W. J. 1984. Plane-Wave Reflection Coefficients for gas Sands at Nonnormal Angles of Incidence. *Geophysics*, 1637–1649.
- PAO, Y.H., & VARATHARAJULU, V. 1976. Huygens' Principle, Radiation Conditions and Intergrals for the Scattering of Elastic Waves. *J. Acoust. Soc. Am.*, **59**(6), 1361–1371.
- PERRON, G. 2000. *Acquisition at Norman West '99, Sudbury, Ontario*. Tech. rept. Geological Survey of Canada, Continental Geoscience Division, Ottawa.
- PERRON, G., & SNYDER, D. 1998. *Downhole Seismic Imaging for Mineral Exploration Acquisition at Norman West 98, Sudbury, Ontario: Report for the Core Program of the DSI Consortium*. Tech. rept. Geological Survey of Canada, Continental Geoscience Division, Ottawa.
- PERRON, G., & SNYDER, D. 1999. *Downhole Seismic Imaging for Mineral Exploration. Acquisition at Norman West 98, Sudbury, Ontario. Report for the Core Program of the DSI Consortium*. Tech. rept. Geological Survey of Canada, Continental Geoscience Division, Ottawa.
- PETRASHEN, G.I. 1945. Solution of Vector Boundary Problems of Mathematical Physics in the Case of a Sphere. *Doklady Acad. Nauk USSR*, **46**(7).
- PETRASHEN, G.I. 1949. Symmetry of Rotation and Spherical Vectors. *Scientific Papers of Leningrad State University, Series in Mathematical Sciences*, **114**, 3–27.
- PICHÉ, M., GUHA, J., & DAIGNEAULT, R. 1993. Stratigraphic and Structural Aspects of the Volcanic Rocks of the Matagami Mining Camp, Québec: Implications for the Norita Ore Deposit. *Economic Geology*, **88**, 1542–1558.
- PRESS, W.H., TEUKOLSKY, S.A., VETTERLING, W.T., & FLANNERY, B.P. 1994. *Numerical Recipes in C - The Art of Scientific Computing*. Cambridge University Press.
- RABEL, W. 1987. *Seismische Erkundung oberflächennaher Störzonen: Strahlentheoretische Grundlagen und Feldbeispiele*. Ph.D. thesis, Kiel University.
- RADON, J. 1917. Über die Bestimmung von Funktionen durch ihre Integral-Werte längs gewisser Mannigfaltigkeiten. *Berichte über die Verhandlungen der Königlich Sächsischen Gesellschaft der Wissenschaften zu Leipzig, Math. Phys. Klasse*, **69**, 262–267.

- RECHENBERG, I. 1994. *Evolutionsstrategie '94*. Stuttgart: Frommann-Holzboog.
- RIEDEL, M. 1998. *AVO/AVA Untersuchungen an flachmarinen Sedimenten*. M.Phil. thesis, Universität Kiel.
- ROBERTSSON, J.O.A, BLANCH, J.O., & SYMES, W.W. 1994b. Viscoelastic Finite-Difference Modeling. *Geophysics*, **59**(9), 1444–1456.
- RONEN, J., & CLAERBOUT, J.F. 1985. Surface-Consistent Residual Statics Estimation by Stack-Power Maximization. *Geophysics*, **50**(12), 2759–2767.
- SALISBURY, M., MILKEREIT, B., & BLEEKER, W. 1996. Seismic Imaging of Massive Sulfide Deposites: Part I. Rock Properties. *Economic Geology and the Bulletin of the Soc. of Economic Geologists.*, **91**(5), 821–828.
- SALISBURY, M.H., MILKEREIT, B., ASCOUGH, G.L., ADAIR, R., SCHMITT, D., & MATTHEWS, L. 1997. Physical Properties and Seismic Imaging of Massive Sulphides. Pages 383–390 of: GUBINS, A.G. (ed), *Proceedings of Exploration 97: Fourth Decennial International Conference on Mineral Exploration*.
- SATO, H. 1982. Amplitude Attenuation of Impulse Plane Waves in Random Media Based on Traveltime Corrected Mean Wave Formalism. *J. Acoust. Soc. Am.*, **71**, 599–564.
- SCHÖN, J. 1996. *Handbook of Geophysical Exploration, Section: Seismic Exploration*. Vol. 18. Pergamon Press. Chap. Physical Properties of Rocks: Fundamentals and Principles of Petrophysics.
- SCHWEFEL, H.-P. 1995. *Evolution and Optimum Seeking*. New York: John Wiley & Sons.
- SHAPIRO, S.A., & KNEIB, G. 1993. Seismic Attenuation by Scattering: Theory and Numerical Results. *Geophysical Journal International*, 373–391.
- SHARPE, J.L. 1968. *Géologie et Gisements de Sulfures de la Région de Matagami, Comté d'Abitibi-Est*. Geological report 137. Ministère des Ressources Naturelles du Québec.
- SHERIFF, R.E., & GELDART, L.P. 1982. *Exploration Seismology: History, Theory, and Data Acquisition*. Cambridge University Press.
- STRUTT (LORD RAYLEIGH), J.W. 1871. Theory of Scattering. *Phil. Mag.*, **41**, 107–120, 274–9.
- VARADAN, V.V. 1978. Scattering Matrix for Elastic Waves. II. Application to Elliptic Cylinders. *J. Acoust. Soc. Am.*, **63**(4), 1014–1024.
- VARADAN, V.V., & VARADAN, V.K. 1979. Scattering Matrix for Elastic Waves. III. Application to Spheroids. *J. Acoust. Soc. Am.*, **65**(4), 896–905.
- VARADAN, V.V., LAKHTAKIA, A., & VARADAN, V.K. 1991. *Field Representations and Introduction to Scattering: Volume 1 in Acoustic, Electromagnetic and Elastic Wave Scattering*. North-Holland.

- ČERVENÝ, V., MOLOTKOV, I., & PŠENČÍK, I. 1977. *Ray Methods in Seismology*. University Karbva, Praha.
- VERBEEK, N. H., & MCGEE, T.M. 1995. Characteristics of High-Resolution Marine Reflection Profiling Sources. *Journal of Applied Geophysics*, **33**(4), 251–269.
- WHITICAR, M.J. 1978. Relationship of Interstitial Gases and Fluids During Early Diagenesis in some Marine Sediments. *Reports: Sonderforschungsbereich 95*, 152ff.
- WU, J., MILKEREIT, B., & BOERNER, D.E. 1995. Seismic Imaging of the Enigmatic Sudbury Structure. *Journal of Geophysical Research*, **100**, 4117–4130.
- WU, R.S. 1986. Seismic Wave Scattering. *Pages 1166–1187 of: JAMES, D.E. (ed), The Encyclopedia of Solid Earth Geophysics*.
- WU, R.S. 1989a. The Perturbation Method in Elastic Wave Scattering. *Pure and Applied Geophysics*, **131**, 605–637.
- WU, R.S. 1989b. Seismic Wave Scattering. *Pages 1166–1187 of: JAMES, D.E. (ed), Encyclopedia of Solid Earth Geophysics*.
- YILMAZ, Ö. 1987. *Seismic Data Processing*. Society of Exploration Geophysicists.
- ZOEPPRITZ, K. 1919. Erdbebenwellen VIII B, On the Reflection and Penetration of Seismic Waves Through Unstable Layers. *Göttinger Nachrichten*, 66–84.

Appendix A

Diffraction Stack and Kirchhoff Migration

The method of the weighted diffraction stack (section 3.2.1) closely relates to Kirchhoff migration, as can readily be seen by applying equation 3.37 to the case of a zero offset experiment. The rays from the source \mathbf{x}_s to the image point \mathbf{y}_0 and back to the receiver \mathbf{x}_r lie on the same straight line connecting $\mathbf{x}_s = \mathbf{x}_r$ and \mathbf{y}_0 . Thus we find for $\hat{\xi}$ (compare with figure A.1):

$$\hat{\xi}(\mathbf{x}_r, \mathbf{y}_0, \mathbf{x}_s) = \frac{\mathbf{y}_0 - \mathbf{x}_r}{|\mathbf{y}_0 - \mathbf{x}_r|} \quad (\text{A.1})$$

after applying a coordinate transform into the receiver coordinate system, equation 3.37 for the inversion of the GRT reads (Miller *et al.*, 1987):

$$\langle f(\mathbf{y}) \rangle = \frac{16}{c_0^3} \int_{r_3=0} d^2 \mathbf{x}_r \cos \phi u_s(\mathbf{x}_r, t = 2|\mathbf{y} - \mathbf{x}_r|/c_0) \quad (\text{A.2})$$

r_3 is set to zero, because equation A.2 is derived for a surface experiment. $\cos \phi$ is the obliquity factor depending on the angle ϕ between the image rays $\mathbf{y}_0 - \mathbf{x}_r$ and the surface normal \hat{n} . Zero offset Kirchhoff migration can thus be interpreted as an inversion of a GRT or a weighted diffraction stack for the case of a zero offset surface experiment.

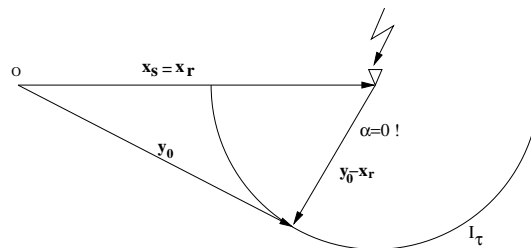


Figure A.1: Zero offset experiment (post stack kirchhoff migration).

Appendix B

Proposed Generic Processing Sequences

The aim of section 3 was to draw an outline of possible processing methods that are capable of enhancing the seismic response of single isolated scattering inclusions. A processing method that is aimed towards resolving shape and composition of a single scatterer has to focus on gaining and preserving as much scattered energy as possible, since the scattered seismic signal often is weak. The methods discussed above were newly developed from considerations regarding the characteristic dynamic and kinematic behavior of the scattered wave field.

Some of them demand a high amount of information on the scattering situation in question, like for most of the gather oriented method we need to know the position of the scatterer (CSA-stack) or have to iteratively determine it. In all the discussed cases a velocity model of the background medium has to be given.

In order to analyze the dynamic behavior of the scattered wave field, e.g. when applying inversion algorithms like diffraction tomography (Devaney, 1981; Devaney, 1984b; Devaney, 1984a), only the scattered field is of interest. It is then desirable to suppress events like the direct arrival or strong reflections on seismic sections.

The processing sequence decided on also depends on the available type of seismic data. As we have seen in section 3.2 using three component data provides much more possibilities in finding the position of a scatterer than the use of scalar data.

Even though an individual situation can lead to several different processing approaches there will always be certain requirements that have to be met, if we want to image and interpret the seismic response of single scatterers. Thus I will now propose two generic processing sequences for marine seismic and VSP data that may serve as a blueprint. In both cases the following general concept was used, but implemented in the specific way demanded by the acquisition layout:

1. Construct a background velocity model from standard seismic processing, i.e. CDP velocity analysis or migration
2. suppress as much primary energy (direct arrival, reflections) as possible

3. Image the location of possible scattering centers
4. Analyze the dynamic behavior of the scattering response (CSA-stack, if applicable)

Since scattering is a three dimensional phenomenon, seismic imaging often can be ambiguous. Apart from finding the right processing sequence there are minimum requirements for the acquisition layout that should generally be met, when trying to image seismic scatterers. The achievable processing result will consequently also depend on the type of acquisition geometry used. I thus will include recommendations for such layout requirements.

B.1 A generic processing sequence for marine seismic surveys

- In order to reduce imaging ambiguity the survey should utilize two-streamer array
- The CDP, CMP-stacked section often shows first indications for scattering. It can provide the lateral position of the scatterer and a reliable background velocity model derived from velocity analysis in the CDP section. This information serves as a good starting point for further processing/inversion steps
- In order to remove reflected energy from horizontal geological interfaces and the direct arrival the difference filter described in section 3.1.4 can be applied to the prestack data set.
- Subsequently diffraction coherency migration, using either semblance or unnormalized cross correlation as coherency measure can be applied in order to locate the scatterer. If data from both streamers is used we not only can determine the lateral but also the off line position of the scatterer.
- By comparison of the DCM with a prestack Kirchhoff migration result we can now decide which scattering center are the origin of edge diffractions and which are single isolated inclusions.
- In the case that scatterers are located in the migrated volume, a dynamic investigation applying CSA analysis can be carried out. Even for scatterers of non spherical symmetry detecting a phase reversal could help in classifying the given scattering situation.

B.2 A generic processing sequence for VSP surveys

- In order to reduce imaging ambiguity in VSP surveys preferably up to six shot point positions should be distributed to cover a maximum azimuthal range together with three component geophones deployed in the bore hole. The acquisition layout should provide sufficient angular coverage and fold for possible subsequent CSA-stack analysis

- First break picks can be used to estimate the velocity distribution in the subsurface. Often information from other surface seismic and geological surveys is available to enhance the model.
- The downgoing wave field including the direct arrival can be removed by applying a moving window median filter or filtering in the fk -domain.
- The position of possible scattering centers can subsequently be delineated by applying DCM and/or DPM.
- As above: In the case that scatterers are located in the migrated volume, a dynamic investigation applying CSA analysis can be carried out. Even for scatterers of non spherical symmetry detecting a phase reversal could help in classifying the given scattering situation.

Appendix C

List of Symbols

α	: complementary scattering angle
α, β	: slowness
γ	: v_s/v_p
θ	: scattering angle
κ	: reflection angle
λ	: wavelength
λ, μ	: Lamé parameter
ρ	: density
σ_N	: normalized scattering cross section
ω	: frequency

a	: characteristic extent
c, v_p, v_s	: wave speed
f	: trace gather
h	: polarization alignment measure
\hat{i}, \hat{o}	: ray direction
\mathbf{k}	: wavenumber
\hat{n}	: normal vector
\hat{p}	: expected polarization
t	: travelttime
t_r	: traction
\mathbf{u}^t	: total wave field
\mathbf{u}_o	: outer scattered wave field
\mathbf{u}'	: inner scattered wave field
\mathbf{u}^0	: incident wave field
\mathbf{x}, \mathbf{y}	: subsurface-, image space position
$\mathbf{x}_0, \mathbf{y}_0$: scatter point, image point
$\mathbf{x}_s, \mathbf{x}_r$: source-, receiver position

Γ : diffraction-, reflection signature
 Ξ : image space

C_{jklm} : stiffness tensor
 F : stacked section
 H : entropy
 P_l^m : Legendre function
 R, R' : regions, sphere radius
 V : volume
 Y_{lm} : spherical harmonic function

Appendix D

List of Abbreviations

<i>AE</i>	:	streamer array effect
<i>CC</i>	:	unnormalized cross correlation sum
<i>CDP</i>	:	common depth point
<i>CFP</i>	:	common fault point
<i>CMP</i>	:	common midpoint
<i>CPP</i>	:	common profile point
<i>CSA</i>	:	common scattering angle
<i>DCM</i>	:	diffraction coherency migration
<i>DF</i>	:	difference filter
<i>DPM</i>	:	diffraction polarization migration
<i>DSM</i>	:	diffraction stack migration
<i>DSI</i>	:	downhole seismic imaging
<i>ECC</i>	:	energy normalized cross correlation sum
<i>GRT</i>	:	generalized Radon transform
<i>GSC</i>	:	Geological Survey of Canada
<i>NCC</i>	:	normalized cross correlation sum
<i>NE</i>	:	semblance
<i>NMO</i>	:	normal moveout correction
<i>PAM</i>	:	polarization alignment measure
<i>RI</i>	:	repeatability index
<i>RTS</i>	:	reflection time surface
<i>SES</i>	:	scattering enhancement stack
<i>SPR</i>	:	significant phase reversal
<i>VSP</i>	:	vertical seismic profiling

Acknowledgements

Ich danke Professor Dr. Bernd Milkereit, der es mir ermöglichte den Weg in die Geophysik einzuschlagen, und an mehreren sehr interessanten Forschungsprojekten mitzuarbeiten. Er stand mir stets mit gutem Rat zur Seite und sicherte meine Finanzierung.

Mein Dank gilt ebenfalls Professor Dr. Wolfgang Rabbel, für u.a. die wichtigen Diskussionen über seismische Strahlverfolgung und Diffraktion, sowie seine wertvollen und detaillierten Korrekturvorschläge zu dieser Arbeit.

Bedanken möchte ich mich ganz besonders bei Dr. Thomas Bohlen, der mir nicht nur ein lieber Zimmergenosse, sondern auch ein geschätzter Diskussionspartner für viele meiner Probleme mit der Streuung war. Er hat oftmals wertvolle Anregungen zum weiteren Verlauf unserer Forschungsarbeiten gemacht, die mir sehr geholfen haben. Danke auch für das gute Arbeitsklima.

Gedankt sei Eric Duveneck, von dem ich (auch) sehr viel gelernt habe und der mit seiner Arbeit zur Polarisations-Migration einen sehr wichtigen weiteren Ansatz zur Abbildung von Streukörpern geliefert hat. Auch für viele wertvolle Diskussionen sei ihm gedankt.

Ich möchte mich bei Thorsten Jäger und Natasja Brughmanns bedanken, deren Arbeiten wertvolle Aspekte der hier behandelten Problematik beleuchtet haben.

Gedankt sei Dr. Christian Goltz, der mit mir die tieferen Aspekte der Entropy diskutierte. Auch für seine Korrekturvorschläge zu dieser Arbeit sei ihm gedankt.

Patrick Musmann sei gedankt für seine Unterstützung bei der Bearbeitung der marine-seismischen 3d Daten, sowie allen Studenten die auf See geholfen haben. Ohne sie wäre diese Arbeit nicht durchführbar gewesen.

Ich möchte mich ebenfalls ganz herzlich bei Holger Busche bedanken, der diese Arbeit Korrektur gelesen hat und wichtige Vorschläge zur Formulierung anbrachte.

Auch Thies Beilecke sei Dank. Er nahm uns in seiner Wohnung auf, wo wir noch so manche Frage zur allgemeinen Geophysik diskutiert haben.

An dieser Stelle sei Herrn Wolf-Dietrich Grahl gedacht und gedankt, für seine wertvollen technischen Arbeiten zu den Geräten, die auf See eingesetzt wurden.

My special thanks goes to Dr. Erick Adam and Gervais Perron from the GSC. I would like to thank Erick for his discussion of scattering phenomena and aspects regarding processing of scattered seismic waves, which was always very inspiring. My thanks goes to Gervais for discussion of my work on ambiguity and who had the idea of using statistical measures to

distinguish scatterers from reflectors. I also like to thank both and their families for their great hospitality in Canada.

The support of the DSI Consortium is highly acknowledged. I especially like to thank Noranda Inc. and Falconbridge Limited for granting permission to use the Sudbury DSI data set in this thesis.

Mein Dank geht ebenfalls an den DAAD, für die Gewährung eines Kurzzeit-Stipendiums in Canada. Der Aufenthalt dort war für mich persönlich und für die Entstehung dieser Arbeit sehr wertvoll.

Ich danke allen meinen Freunden und den Kollegen am Institut, die mich in dieser Zeit unterstützt haben.

Mein ganz besonderer Dank gilt meiner lieben Susi, die mir in der manchmal beschwerlichen Zeit so viele alltägliche Probleme vom Hals gehalten hat, obwohl sie selbst in der Promotion stand. Sie unterstützte mich wo immer sie konnte. Ich danke ihr ganz besonders für Ihre Liebe und Freundschaft die mich immer begleiten.

Mein Dank gilt vor allem auch meinen Eltern, die mir stets ermöglichten und mich darin unterstützten, meiner Neigung zur Naturwissenschaft nachzugehen.

Curriculum Vitae

Name: Christof Müller

Geburtsdatum/-ort: 26.06.67 Eschweiler

Staatsangehörigkeit: deutsch

Schulbildung: 1973-1977 Grundschule Kinzweiler
1977-1986 Gymnasium: Liebfrauenschule Eschweiler

Zivildienst: 1986-1988 Schule für geistig Behinderte, Stolberg

Studium: 1988-1990 Grundstudium Physik: RWTH Aachen
1990-1996 Hauptstudium Physik: TU Berlin
1997-2000 Promotion an der Christian-Albrechts-Universität Kiel

Berufstätigkeit: 1997-2000 wissenschaftlicher Mitarbeiter am Institut für
Geowissenschaften der CAU Kiel.